Electrochemical and Spectroscopic Studies of Graphene Nanoflakes with Functionalised Edges

Mailis Maria Lounasvuori

Thesis submitted in partial fulfilment of the requirements for the degree of

Doctor of Philosophy

UNIVERSITY COLLEGE LONDON

February 2017

Declaration

I, Mailis Maria Lounasvuori, confirm that the work presented in this thesis is my own. Where information has been derived from other sources, I confirm that this has been indicated in the thesis.

Signature: ……

Date: ……

Abstract

The influence of surface functional groups on the electrochemical performance of carbon electrodes was studied by using graphene nanoflakes (GNF), a well-defined carbon nanomaterial. After characterisation with different techniques, GNF were used to modify a boron-doped diamond (BDD) electrode and the influence of different edge terminations on various redox probes was investigated using cyclic voltammetry (CV).

The outer-sphere redox probe ferrocenemethanol (FcMeOH) was found to be unaffected by the presence of GNF at the electrode surface, confirming that GNF do not inhibit electron transfer. When proton-coupled electron transfer was investigated, it was shown that the acid-terminated GNF acted as a non-solution proton source and sink.

The $[Fe(CN_6)]^{3-/4-}$ redox couple was found to be quasi-reversible and independent of electrolyte pH at clean BDD and BDD modified with amide-terminated GNF. When GNF were decorated with COOH functionalities, the reaction became less reversible and pH-dependent. The reaction was also directly influenced by the electrolyte concentration, with low concentrations causing the reaction to become more irreversible.

Potential-induced dissociation of the carboxylic acid edge groups on GNF was investigated with in situ spectroelectrochemistry combining potentiostatic control with attenuated total reflectance Fourier transform infrared spectroscopy (ATR-FTIR). Applying a negative electrode potential led to the deprotonation of both electrode-immobilised groups and species in solution. Acid dissociation was driven by an increase in interfacial cation activity at the electrode surface that lowered the apparent pK_a of all species at or near the electrode.

Different methods of GNF attachment on the electrode surface were explored, including direct attachment to gold via thiol edge groups and EDC-mediated amidation reaction to form covalent bonds with a self-assembled monolayer (SAM) on gold. Scanning tunnelling microscopy (STM) was used to verify the presence and probe the orientation of GNF at the surface.

Contents

Declaration 2
Abstract 3
Contents 4
List of Symbols 9
List of Abbreviations 11
List of Figures 13
List of Schemes 19
List of Tables 20
List of Appendix Figures 22
List of Publications 23
1 Introduction 24
1.1 Graphene 24
1.1.1 Graphene synthesis 28
1.1.2 Graphene Oxide 30
1.1.3 Graphene Functionalisation 32
1.2 Electrochemistry of Graphene 33
1.3 Graphene Nanoflakes 36
1.4 Acid-base Properties of Graphene-related Materials 40
1.4.1 Controlling the Protonation State of Electrode-Immobilised Species 41
1.5 Methods of immobilising GNF on Electrode 43
1.5.1 Drop-coating 43

1.5.2 Spin-coating 43
1.5.3 Self-assembly 44
1.6 Aim and Scope of the Thesis 45
References for Chapter 1 47
2 Experimental Theory and Techniques 56
2.1 Electrochemistry 56
2.1.1 Cyclic Voltammetry 59
2.1.2 Differential Pulse Voltammetry 61
2.2 Infrared Spectroscopy 64
2.2.1 Attenuated Total Reflectance 66
2.3 Scanning Tunnelling Microscopy 68
2.4 X-ray Photoelectron Spectroscopy 70
2.5 Transmission Electron Microscopy 71
References for Chapter 2 73
3 Characterisation of GNF 74
3.1 Introduction 74
3.2 Experimental Methods 75
3.2.1 Preparation of Complexed GNF 76
3.2.2 X-ray Photoelectron Spectroscopy 76
3.2.3 Transmission Electron Microscopy 76
3.2.4 pH Titration 77
3.2.5 Electrochemical Experiments 77
3.2.6 ATR-FTIR 79
3.2.6.1 Stability of Aqueous Suspension of GNF 79
3.2.6.2 Solution-Phase Characterisation of GNF 79
3.3 Results and Discussion 80
3.3.1 Transmission Electron Microscopy 80
3.3.2 X-ray Photoelectron Spectroscopy 81
3.3.3 Infrared Spectroscopy 83

3.3.3.1 Stability ... 86
3.3.4 pH Titration ... 86
3.3.5 In Situ pH Studies Monitored with Infrared Spectroscopy ... 89
3.3.6 Electrochemistry of GNF without Redox Probes ... 91
3.3.7 Electrochemistry of FcMeOH at GNF-Modified Electrode ... 95
3.3.8 Electrochemistry of Hydroquinone/Benzoquinone at GNF-Modified Electrode ... 100
3.3.8.1 pH-Dependence of the Q/H_2Q Reaction ... 102
3.3.8.2 Exploring the Mechanism for Hydroquinone Oxidation ... 107
3.3.9 Electrochemistry of $[Ru(NH_3)_6]^{2+/3+}$ at GNF-Modified Electrode ... 112
3.4 Conclusion ... 121
References for Chapter 3 ... 123
4 GNF-COOH and Ferri/Ferrocyanide ... 125
4.1 Introduction ... 125
4.2 Experimental Methods ... 127
4.2.1 Electrochemical Experiments ... 127
4.2.2 Infrared Spectroscopy Experiments ... 127
4.2.3 Spectroelectrochemical Experiments ... 128
4.3 Results and Discussion ... 129
4.3.1 The Effect of Solution pH ... 129
4.3.2 The Effect of Background Electrolyte Concentration ... 133
4.3.3 Cyclic Voltammetric Studies of $[Fe(CN)_6]^{3-/4-}$ Redox Couple in the Presence of GNF-COOH in Solution ... 137
4.3.4 Isotope Effect of H_2O and D_2O on $[Fe(CN)_6]^{3-/4-}$ Redox Couple at GNF-COOH Modified Electrode ... 138
4.3.5 Spectroelectrochemical Studies of $[Fe(CN)_6]^{3-/4-}$ ... 140
4.3.6 Stability of $[Fe(CN)_6]^{3-/4-}$ in the Presence of GNF-COOH ... 142
4.3.6.1 Identity of decomposition product ... 145
4.4 Conclusion ... 146
References for Chapter 4 ... 148

5 Potential-Induced Dissociation of Acid Groups 150

5.1 Introduction 150

5.2 Experimental Methods 152

5.2.1 Construction of Calibration Curves 154

5.3 Estimating the Distance between the Electrode Surface and the ATR Internal Reflection Element 155

5.4 Penetration Depth of IR Evanescent Wave 157

5.5 Proposed Mechanism for Potential-Induced Deprotonation of Acid Edge Groups 159

5.6 Evidence of Electrolyte Ion Migration 163

5.7 Quantifying Changes in Ion Activity 168

5.8 Ruling Out pH Change at Interface 171

5.9 Investigating the Effect of Electrolyte Cation 173

5.10 Estimating the Number of Acid Groups Undergoing Potential-Induced Changes 175

5.11 Predicting Potential-Dependent Changes in Solution Species 180

5.11.1 Sulphate 181

5.11.2 Phosphate 184

5.12 Conclusion 188

References for Chapter 5 191

6 Immobilisation of GNF on Electrode Surface 193

6.1 Introduction 193

6.1.1 Thiol-Functionalised GNF 198

6.1.2 Electrochemistry of Ferrocene Derivatives 200

6.2 Experimental Methods 201

6.2.1 Substrate Preparation 201

6.2.2 SAM Deposition 202

6.2.3 Attaching GNF onto SAM 202

6.2.4 Labelling GNFs with Ferrocene Derivatives 204

6.2.5 X-ray Photoelectron Spectroscopy 204

6.2.6 Scanning Tunnelling Microscopy 205
6.2.7 Electrochemical Experiments 205
6.3 Results and Discussion 205
6.3.1 Thiol-Functionalised GNF 205
6.3.1.1 STM 209
6.3.2 GNF Attached onto SAM-functionalised Gold 215
6.3.2.1 Electrochemical Studies of Au + SAM + GNF Assembly 220
6.4 Conclusion 225
References for Chapter 6 227
7 Concluding Remarks 230
7.1 Influence of GNF on the Electrochemistry of Redox Probes 231
7.2 Potential-Driven Deprotonation of Acid Groups 232
7.3 Immobilisation of GNF 233
7.4 Future Work 233
References for Chapter 7 235
Appendix 1: Additional Figures for Chapter 4 237
Appendix 2: Derivation of Equation (5.9) 240
Appendix 3: Calculation of the values presented in Table 5.6 242
Appendix 4: Calculation of the values presented in Table 5.7 246

List of Symbols

Symbol	Meaning	Units
A	Area	
a	Activity	
c	Speed of light	m s^{-1}
C_j^*	Bulk concentration of species j	M, mol dm^{-3}
$(C_j^*)_{app}$	Apparent bulk concentration of species j	M, mol dm^{-3}
d	Distance between STM tip and substrate	Å
d_e	Effective penetration depth	µm
d_p	Penetration depth	µm
e	Elementary charge	C
E	Energy of electron	eV
E_B	binding energy	eV
E_K	Kinetic energy	eV
E	Potential	V
E^0	Standard potential	V
$E^{0'}$	Formal potential	V
E_{pa}	Anodic peak potential	V
E_{pc}	Cathodic peak potential	V
ΔE_p	Peak potential separation	V
F	Faraday constant	C
h	Planck constant	J s
$\hbar$	Reduced Planck constant	J s
h	Solution thickness in thin-layer electrochemical cell	µm
i	Current	A
i_p	Peak current	A
I_t	Tunnelling current	A
I	Integrated peak area	
I	Intensity	
I^0	Intensity at distance z = 0	
k^0	Standard heterogeneous electron transfer rate constant	
K_a	Dissociation constant of an acid	

Symbol	Meaning	Units
n	Refractive index	
m_e	Mass of electron	kg, u, J, MeV
O	Oxidised species; used as subscript to denote quantities pertaining to O	
p	Momentum	
$pK_a(app)$	Apparent pKa of acid	
q	Charge	C
R	Reduced species; used as subscript to denote quantities pertaining to R	
r	Angle of refraction	
S	Atomic sensitivity factor	
T	Temperature	K
t	Time	s
v	Scan rate	$V\ s^{-1}$
z	Distance normal to the ATR surface	μm
Γ_j^*	Initial amount of adsorbed species j	
γ_j	Activity coefficient of species j	
δ	Bend	
θ	Angle of incidence	
θ_c	Critical angle of incidence	
κ	Force constant	
λ	Wavelength	nm
μ	Reduced mass	
v	Wavenumber	cm^{-1}
ν	Frequency	Hz
v	Stretch	
v_{as}	Asymmetric stretch	
v_s	Symmetric stretch	
φ	Surface potential	V
φ	Work function	eV
φ_{sp}	Calibrated spectrometer work function	eV

List of Abbreviations

AFM	Atomic force microscopy
ATR	Attenuated total reflectance
BDD	Boron-doped diamond
CNT	Carbon nanotube
CPET	Concerted proton-electron transfer
CV	Cyclic voltammetry
CVD	Chemical vapour deposition
DME	Dropping mercury electrode
DPV	Differential pulse voltammetry
EDC	1-ethyl-3-[3-dimethylaminopropyl]carbodiimide
FcCHO	Ferrocenealdehyde
FcCOOH	Ferrocenecarboxylic acid
FcMeOH	Ferrocenemethanol
FTIR	Fourier transform infrared
FTO	Fluorine-doped tin oxide
FWHM	Full width at half maximum
GL(30)	Line shape that is 70% Gaussian and 30% Lorentzian
GNF	Graphene nanoflakes
GNF-amide	Amide-terminated graphene nanoflakes
GNF-COOH	Carboxylic acid -terminated graphene nanoflakes
GNF-thiol	Thiol-terminated graphene nanoflakes
GO	Graphene oxide
H_2Q	Hydroquinone
HET	Heterogeneous electron transfer
HOPG	Highly oriented pyrolytic graphite
IHP	Inner Helmholtz plane
IR	Infrared
IRE	Internal reflection element
LBE	Liquid-based direct exfoliation
MWCNT	Multi-walled carbon nanotube
OHP	Outer Helmholtz plane
PAD	Plane of acid dissociation

PAH	Polycyclic aromatic hydrocarbon
PCET	Proton-coupled electron transfer
PCTFE	Polychlorotrifluoroethylene
PEEK	Polyether ether ketone
PMMA	Polymethyl methacrylate
Q	1,4-benzoquinone
QCM	Quartz crystal microbalance
RGO	Reduced graphene oxide
SAM	Self-assembled monolayer
SEM	Scanning electron microscopy
SPM	Scanning probe microscopy
STM	Scanning tunnelling microscopy
Sulfo-NHS	N-hydroxysulfosuccinimide
TEM	Transmission electron microscopy
UHV	Ultra-high vacuum
XPS	X-ray photoelectron spectroscopy
XRD	X-ray diffraction

List of Figures

Figure 1.1 Graphene is a two-dimensional building material for other carbon materials; it can be wrapped up into 0D buckyballs, rolled into 1D nanotubes or stacked into 3D graphite. Reproduced from [5] with permission. 25

Figure 1.2 (a) Comparison of Raman spectra at 514 nm for bulk graphite and graphene. They are scaled to have similar height of the 2D peak at ~2700 cm^{-1}. (b) Evolution of the spectra at 514 nm with the number of layers. (c) Evolution of the Raman spectra at 633 nm with the number of layers. Adapted from [7] with permission. 26

Figure 1.3 (a) X-ray photoelectron survey spectra of graphene oxide (blue) and GNF (black). Inset: High resolution XPS spectra of the C1s region of GO (blue) and GNF (black). (b) AFM image of GNF spin-coated onto highly oriented pyrolytic graphite. (c) Height and (d) diameter distribution of GNF. (e) ^{13}C solid state NMR and (f) Raman spectra of GO (black) and GNF (blue). Adapted from [107] with permission. 38

Figure 1.4 (a) Electrostatic potential distribution across a metal/acid monolayer/solution interface. (b) Schematic representation of a mixed monolayer of 11-mercaptoundecanoic acid and 1-decanethiol in contact with an electrolyte solution as a function of electrode potential (E) and pH. Reproduced from [121] with permission. Copyright 1998 American Chemical Society. 42

Figure 2.1 A schematic representation of the electric double layer at the electrode-solution interface and the potential profile across the double layer region in the absence of specific adsorption. Adapted from [1] with permission. 57

Figure 2.2 Waveforms in cyclic voltammetry. (a) Potential as a function of time, (b) current as a function of potential. Adapted from [1] with permission. 60

Figure 2.3 (a) Potential waveform for a differential pulse voltammetric experiment showing two full potential steps. (b) Differential current plotted against potential for reaction $O + ne \rightleftharpoons R$. Adapted from [1] with permission. 62

Figure 2.4 Stretching and bending modes of (a) water and (b) CO_2 molecule. Reproduced from [2] with permission. 66

Figure 2.5 (a) Graphical representation of the evanescent wave. (b) Variation of the angle of refraction (r) with the angle of incidence (θ). The critical angle θ_c is the angle of incidence that leads to r = 90°. Adapted from [2] and [3] with permission..... 67

Figure 3.1 A schematic of the electrochemical cell used in this Chapter. 77

Figure 3.2 TEM images of the GNF. (a), (b): GNF-COOH. (c), (d): GNF-Ba..... 80

Figure 3.3 Wide scan survey spectra of GNF-COOH (black) and GNF-COOH complexed with Ca^{2+} (red); Ba^{2+} (green); $[Ru(NH_3)_6]^{3+}$ (blue). Relevant elements are highlighted with circles. Spectra are offset for clarity..... 82

Figure 3.4 ATR-FTIR spectra of (a) GNF-COOH; (b) GNF-amide; (c) GNF-Ca..... 85

Figure 3.5 Titration curve of GNF-COOH (black), first derivative (red). Adapted from [6]. 88

Figure 3.6 Changes in IR absorption of GNF upon addition of 0.1 M KOH. GNF with no added base at pH 2 (black), pH 3 (red), pH 5 (green), pH 7 (blue). Reproduced from [11]. 91

Figure 3.7 (a) pH 4.6 PBS with oxygen and (b) pH 4.6 PBS without oxygen; clean BDD (black), acid-terminated GNF (red) and amide-terminated GNF (blue). Adapted from [6]. 92

Figure 3.8 Cyclic voltammograms of BDD modified with (a) carboxylic acid-terminated GNF and (b) amide-terminated GNF in pH 4.6 (red) and 9.2 (blue). Electrolyte concentration 0.1 M. Scan rate 50 mV/s. Adapted from [6]. 94

Figure 3.9 Cyclic voltammograms in 0.1 PBS at pH 7. Working electrode: clean BDD (black); BDD modified with GNF-Ca (blue). Red curve shows the response of BDD modified with GNF-Ca in deoxygenated electrolyte..... 95

Figure 3.10 Cyclic voltammograms of 0.5×10^{-3} M ferrocenemethanol at different electrode modifications. (a) At clean BDD (black), GNF-COOH modified BDD (red) and GNF-amide modified BDD (blue) in 0.1 M KH_2PO_4 pH 4.6, scan rate 100 mV s^{-1}. (b) At clean BDD (black), GNF-COOH modified BDD (red) and GNF-amide modified BDD (blue) in 0.1 M K_2HPO_4 pH 9.2, scan rate 100 mV s^{-1}. Adapted from [6]..... 96

Figure 3.11 Cyclic voltammograms of 0.5×10^{-3} M ferrocenemethanol at GNF-amide modified BDD. Supporting electrolyte: (a) 0.1 M KH_2PO_4 pH 4.6; (b) 0.1 M K_2HPO_4 pH 9.2. Scan rate 100 mV s^{-1} (black, blue), 1 (red, orange) V s^{-1}. Adapted from [6]..... 97

Figure 3.12 (a) Cyclic voltammograms of 0.5×10^{-3} M ferrocenemethanol at GNF-COOH modified BDD in 0.1 M KH_2PO_4 pH 4.6: scan rate 50 (black), 100 (red), 250 (green), 500 (blue), 1000 (light blue) mV s^{-1}; (b) peak currents i_{pa} (red) and i_{pc} (blue) plotted against square root of scan rate v; (c) log i_{pa} (red) and log $|i_{pc}|$ (blue) plotted against log v. 98

Figure 3.13 Cyclic voltammograms of 0.5×10^{-3} M hydroquinone in 0.1 M PBS: (a) at pH 5; (b) at pH 8.5. Working electrode: clean BDD (black), BDD modified with GNF-COOH (red) and BDD modified with GNF-amide (blue). Scan rate 50 mV s^{-1}. First scans shown. Adapted from [6]..... 101

Figure 3.14 (a) Peak potential of hydroquinone oxidation (circles) and benzoquinone reduction (squares); (b) peak separation; (c) $E_{1/2}$ as a function of pH at clean BDD

electrode (black), GNF-COOH modified BDD (red) and GNF-amide modified BDD (blue). Adapted from [6]. 104

Figure 3.15 (a) CVs of 0.5 × 10^{-3} M hydroquinone at clean BDD electrode (black line) and GNF-COOH modified electrode (red line) in unbuffered H_2O pH 6.6. (b) Peak potential of hydroquinone oxidation in unbuffered KCl electrolyte as a function of pH at a clean BDD electrode (black) and GNF-COOH modified electrode (red). (c) CVs of 0.5 × 10^{-3} M hydroquinone at clean BDD electrode in unbuffered H_2O pH 6.5 (black line) and D_2O pD 6.6 (red line). Supporting electrolyte: 0.1 M KCl. Scan rate: 50 mV s^{-1}. First scans shown. Adapted from [27]. 109

Figure 3.16 (a) CV of 0.5 × 10^{-3} M hydroquinone at clean BDD electrode (black line) and GNF-COOH modified electrode (red line) in unbuffered H2O. The pH of the H2O electrolyte solution was adjusted to 8.21 with KOH. Supporting electrolyte: 0.1 M KCl. Scan rate: 50 mV s^{-1}. Second scans shown. (b) Ratio of peak heights of hydroquinone oxidation as a function of pH at clean BDD electrode (black) and GNF-COOH modified electrode (red). Adapted from [27]. 111

Figure 3.17 Cyclic voltammograms of 0.5 × 10^{-3} M $[Ru(NH_3)_6]Cl_3$ in 0.1 M PBS pH 7 at (a) clean BDD and (b) GNF-COOH modified BDD. Scan rates 50 mV s^{-1} (black), 250 mV s^{-1} (red) and 500 mV s^{-1} (blue). 113

Figure 3.18 (a) Cyclic voltammograms of 0.5 × 10^{-3} M $[Ru(NH_3)_6]Cl_3$ in 0.1 M PBS pH 3 at GNF-Ca modified BDD. Scan rates 5 (black), 25 (red), 50 (green), 250 (blue) and 500 (light blue) mV s^{-1}. (b) Cyclic voltammograms from (a) with normalised current. 114

Figure 3.19 (a) Peak current i_{pa} of peak Ia determined from **Figure 3.18**(a) plotted against the square root of scan rate v. (d) i_{pa} of peak IIa determined from **Figure 3.18**(a) plotted against v. 116

Figure 3.20 log i_{pa} of (a) peak Ia and (b) peak IIa determined from **Figure 3.19**(a) plotted against log v. 117

Figure 3.21 (a) Cyclic voltammograms recorded at a BDD modified with $[Ru(NH_3)_6]^{3+}$ complexed GNF. Scan rates 5 (black), 25 (red), 100 (green), 325 (blue) and 500 (light blue) mV s^{-1}. Electrolyte: 0.1 M K_2HPO_4. (b) A plot of oxidation peak current i_{pa} against scan rate v. (c) log i_{pa} plotted against log v. 119

Figure 4.1 Spectroscopy cell used in this Chapter. 127

Figure 4.2 (a) Spectroelectrochemical setup used in this Chapter. (b) Schematic of the cell viewed from the top. 129

Figure 4.3 Cyclic voltammograms of 0.5 × 10^{-3} M $K_3[Fe(CN)_6]$ recorded in 0.1 M PBS. Working electrode: (a) BDD; (b) BDD modified with GNF-COOH; (c) BDD modified with GNF-amide. Solution pH 4.6 (black, blue, light blue); 9.2 (red, orange, pink). Scan rate 50 mV s^{-1}. First scans shown. Adapted from [14]. 132

Figure 4.4 Cyclic voltammograms of 0.5 × 10^{-3} M $K_3[Fe(CN)_6]$ recorded in different concentrations of KCl: (a) 1 M; (b) 0.1 M; (c) 0.01 M. Working electrode: BDD (black); BDD modified with GNF-COOH (red); BDD modified with GNF-amide (blue). Scan rate 50 mV s^{-1}. First scans shown. Adapted from [14]. 135

Figure 4.5 Cyclic voltammograms of 0.5 × 10^{-3} M $K_3[Fe(CN)_6]$ (dashed blue); 0.5 × 10^{-3} M $K_3[Fe(CN)_6]$ and 34 µg ml^{-1} GNF (solid blue); 0.5 × 10^{-3} M $K_4[Ru(CN)_6]$ (dashed red); 0.5 × 10^{-3} M $K_4[Ru(CN)_6]$ and 34 µg ml^{-1} GNF (solid red); 34 µg ml^{-1} GNF only

(black). Working electrode: BDD. Supporting electrolyte: 10^{-3} M KCl. Scan rate: 50 mV s^{-1}. First scans shown. Reproduced from [11]..... 138

Figure 4.6 Cyclic voltammograms of 0.5 × 10^{-3} M $K_3[Fe(CN)_6]$ recorded at GNF-COOH modified BDD in (a) H_2O; (b) D_2O. First scans (black) and 10th scans (red) shown. Supporting electrolyte 0.01 M KCl. Scan rate 50 mV s^{-1}. Adapted from [11]. 139

Figure 4.7 (a) Difference spectra of $[Fe(CN)_6]^{3-}$ and $[Fe(CN)_6]^{4-}$. After reduction of $[Fe(CN)_6]^{3-}$, the IR spectrum shows a negative $[Fe(CN)_6]^{3-}$ band and positive $[Fe(CN)_6]^{4-}$ band (solid line). Oxidation of $[Fe(CN)_6]^{4-}$ results in a positive $[Fe(CN)_6]^{3-}$ band and negative $[Fe(CN)_6]^{4-}$ band (dashed line). (b) Height of the $[Fe(CN)_6]^{4-}$ CN stretch band at 2036 cm^{-1} relative to the intensity of absorption at full conversion as a function of time. Blue squares: 1 × 10^{-3} M $K_3[Fe(CN)_6]$; red squares: 1 × 10^{-3} M $K_3[Fe(CN)_6]$ and 3.2 µg ml^{-1} of GNF. Electrolyte: 0.01 M KCl. Potentials: 0 V (reduction), +350 mV (oxidation). Reproduced from [11]..... 141

Figure 4.8 Infrared spectra of 2 × 10^{-3} M $K_3[Fe(CN)_6]$ and 2 × 10^{-3} M $K_4[Fe(CN)_6]$ in H_2O at *t* = 0 h (solid blue) and at *t* = 24 h (dashed blue); with 30 µg ml^{-1} GNF at *t* = 0 h (solid red) and at *t* = 24 h (dashed red). Spectra are offset for clarity. Reproduced from [11]. 143

Figure 4.9 ATR-FTIR spectra of 2 × 10^{-3} M $K_3[Fe(CN)_6]$ and 2 × 10^{-3} M $K_4[Fe(CN)_6]$ with 30 µg ml^{-1} GNF In H_2O at *t* = 0 h (solid red) and *t* = 4 h (dashed red), in D_2O at *t* = 0 h (solid blue) and *t* = 4 h (dashed blue). Spectra are offset for clarity. Reproduced from [11]. 144

Figure 5.1 Experimental setup in in situ spectroelectrochemical experiments. Adapted from [9] 154

Figure 5.2 Cyclic voltammograms of 1.13 × 10^{-3} M FcMeOH in 0.1 M NaCl in IR setup. (a) Black line: BDD positioned 5 mm above ATR prism. Red line: BDD positioned against ATR prism, creating thin-layer conditions. Scan rate 5 mV s^{-1}. (b) CVs recorded in the thin-layer geometry with scan rates 5, 8 10, 12, 14 and 17 mV s^{-1}. Reproduced from [9]. 156

Figure 5.3 Difference spectra of BDD modified with GNF-Ca in 0.1 M NaCl electrolyte at pH 7. Initial application of +1 V, background spectrum recorded without applied potential (light blue); spectrum after subsequent application of −0.5 V (black); spectrum after subsequent application of +1 V (red). Arrows on top spectrum indicate direction of spectral features relative to baseline as a guide to the eye. Reproduced from [9]..... 159

Figure 5.4 Potential-induced changes in cation activity in the electrode-electrolyte interfacial region drive protonation and deprotonation of acidic surface groups. 162

Figure 5.5 GNF-Ca modified electrode immersed in 2 ml of 0.1 M K_2SO_4 electrolyte in spectroelectrochemical setup after 0 minutes (black line), 5 minutes (red line) and 35 minutes (blue line). Background: electrolyte only. Reproduced from [9]..... 164

Figure 5.6 Difference spectra of BDD modified with GNF-Ca in 0.1 M Na_2SO_4 pH 7. Background recorded at the beginning of experiment before the application of potential. Potentials: +1 V (light blue); −0.5 V (black); +1 V (red); −0.5 V (blue); +1 V (orange). The sulphate band at 1100 cm^{-1} is highlighted in green. Reproduced from [9]..... 165

Figure 5.7 Difference spectra in different concentrations of supporting electrolyte Na_2SO_4 at pH 7. BDD modified with GNF-Ca in 0.1 M: application of −0.5 V (black); application of +1 V (red). BDD modified with GNF-Ca in 1×10^{-3} M: application of −0.5 V

(orange); application of +1 V (blue). A background spectrum was collected at each potential immediately prior to switching the applied potential. Reproduced from [9].. 167

Figure 5.8 (a) Infrared spectra of aqueous solutions of K_2SO_4 at different concentrations. The pH of all solutions was ca. 7. Inset: Magnification of the SO_4^{2-} absorption bands. (b) Peak fit of the sulphate absorption band from 0.075 M K_2SO_4 spectrum. (c) Peak areas from Fig 1.1 plotted against concentration of K_2SO_4 and a linear fit of data points. Error bars represent one standard deviation. Reproduced from [9]. 169

Figure 5.9 (a) Cyclic voltammograms in 0.1 M PBS at pH 7 with and without oxygen present in solution. Clean BDD with O_2 (black); BDD modified with GNF-Ca with O_2 (blue); BDD modified with GNF-Ca without O_2 (red). (b) Cyclic voltammograms in different ionic strength solutions. BDD modified with GNF-Ca in 1×10^{-3} M PBS at pH 7 (red); in 0.1 M PBS at pH 7 (blue). Reproduced from [9]. 172

Figure 5.10 Difference spectra of BDD modified with GNF-Ca in 0.1 M K_2SO_4 pH 3.5. Application of −0.5 V (black); application of +1 V (red). Difference spectra under same conditions but electrolyte deoxygenated with argon for 20 minutes. Application of −0.5 V (blue); application of +1 V (orange). Reproduced from [9]. 173

Figure 5.11 Difference spectra of BDD modified with GNF-Ca in 0.1 M K_2SO_4 pH 7; application of −0.5 V (black); subsequent application of +1 V (red). Difference spectra of BDD modified with GNF-Ca in 0.1 M Na_2SO_4 pH 6.8; application of −0.5 V (blue); subsequent application of +1 V (orange). Reproduced from [9]. 174

Figure 5.12 Difference spectra of BDD modified with GNF-Ca in 0.1 M NaCl electrolyte at pH 3.5. Application of −0.5 V (black); subsequent application of +1 V (red).Difference spectra of BDD modified with GNF-Ca in 0.1 M $CaCl_2$ pH 3.5. Application of −0.5 V (blue); subsequent application of +1 V (orange)..... 175

Figure 5.13 (a) Peak fit of drop-coated potassium acetate film containing 5.38×10^{-9} moles of acetate groups. Experimental data (black), baseline (green), peak fits (red), cumulative peak fit (blue). (b) Asymmetric stretch peak areas at 1565 cm^{-1} plotted against number of acetate groups and a linear fit of data points. (c) Symmetric stretch peak areas at 1415 cm^{-1} plotted against number of acetate groups and a linear fit of data points. Error bars represent one standard deviation. Reproduced from [9]..... 177

Figure 5.14 Peak fitted difference spectrum in 0.1 M K_2SO_4 pH 7 when applying −0.5 V to GNF-Ca modified BDD. Experimental data (black), baseline (green), peak fits (red), cumulative peak fit (blue). Reproduced from [9]. 178

Figure 5.15 IR difference spectra of the GNF-Ca modified electrode interface in: 0.1 M pH 7 K_2SO_4, −0.5 V (pink), +1.0 V (light blue); 0.1 M pH 3.5 K_2SO_4, −0.5 V (blue), +1.0 V (orange); 0.1 M pH 3 K_2SO_4, −0.5 V (black), +1.0 V (red). Reproduced from [9].... 182

Figure 5.16 Difference spectra of BDD modified with GNF-Ca in 0.1 M KH_2PO_4/K_2HPO_4 electrolytes of different pH: pH 3 at +1 V (red) and −0.5 V (black); pH 7 at +1 V (orange) and −0.5 V (blue); pH 9 at +1 V (light blue) and −0 5 V (pink). Reproduced from [9]. 186

Figure 6.1 Infrared spectrum of GNF-thiol. 199

Figure 6.2 (a) Survey spectra of unmodified Au (black) and Au+GNF-thiol (red). (b) High-resolution spectrum of the N1s region of unmodified Au (black) and Au+GNF-thiol (red). Spectra are offset for clarity. 206

Figure 6.3 High-resolution XPS spectra of the C1s region of (a) Au and (b) Au+GNF-thiol. Experimental data is shown in black, background in green, peak fits in red and the cumulative peak fit in blue..... 208

Figure 6.4 STM images of (a) clean Au(111); (b) GNF-thiol spin-coated onto Au(111). Suspension concentration 72 μg ml^{-1}. 210

Figure 6.5 STM images of GNF-thiol spin-coated onto Au(111). Suspension concentration (a) 8 μg ml^{-1}; (b) 124 μg ml^{-1}. (c) Height profile from (a) along green line. (d) Height profile from (b) along green line..... 212

Figure 6.6 (a) STM image of Au(111) substrate after drop-coating distilled water. (b) Height profile from (a) along green line. 213

Figure 6.7 (a) STM image of 2 μg ml−1 GNF-thiol drop-coated on Au(111). (b) Height profile from (a) along green line. 214

Figure 6.8 High-resolution spectra of (a) S2p and (b) N1s regions. Au (black), Au+cysteine (red), Au+cysteine+GNF-amide (blue), Au+cysteamine (green), Au+cysteamine+GNF-COOH (light blue). Spectra are offset for clarity. 216

Figure 6.9 Narrow scan XPS spectra of the C1s region. (a) Unmodified Au; (b) Au+cysteine; (c) Au+cysteine+GNF-amide; (d) Au+cysteamine; (e) Au+cysteamine+GNF-COOH. Black squares: experimental data; green: baseline; red: peak fits; blue: cumulative peak fit. 217

Figure 6.10 Narrow scans of the Fe2p regions of Au+cysteamine+GNF-COOH (black) and Au+cysteine+GNF-amide+FcCHO (red). Spectra are offset for clarity. 219

Figure 6.11 Differential pulse voltammograms of (a) Au+cysteamine+GNF-COOH (red) and Au+cysteamine+GNF-COOH+FcCOOH (blue); (b) Au+cysteine (red) and Au+cysteine+GNF-amide+FcCHO (blue). Solid line: oxidation; line and symbols: reduction..... 221

Figure 6.12 (a) Cyclic voltammograms at Au+cysteine+GNF-amide+FcCHO in 0.1 M PBS pH 7; scan rate 50 (black), 100 (red), 250 (blue), 500 (green), 750 (light blue) and 1000 (pink) mV s^{-1}; 5th scans shown; (b) i_{pa} (red) and i_{pc} (blue) plotted against v; (c) log i_{pa} (red) and log $|i_{pc}|$ (blue) plotted against log v..... 223

List of Schemes

Scheme 1.1 Schematic representation of different edge configurations. A defect in the basal plane is shown in orange. Reproduced from [11] with permission. 27

Scheme 1.2 Schematic depiction of edge-carboxylated (left) and amide-functionalised GNF. The images are not to scale; the aromatic region at the core of the flakes is significantly larger than is depicted here. Reproduced from [110]. 39

Scheme 3.1: 1,4-Benzoquinone undergoes a two-proton, two-electron reduction to hydroquinone. 100

Scheme 6.1 (a) Cystamine dihydrochloride; (b) cysteamine SAM formed by cystamine on gold; (c) GNF-COOH attached onto cysteamine SAM on gold; ((d) ferrocene carboxylic acid attached onto Au-cysteamine-GNF-COOH. 195

Scheme 6.2 (a) Cysteine molecule; (b) cysteine SAM on gold; (c) GNF-amide attached onto cysteine SAM on gold; (d) ferrocene carboxaldehyde attached onto Au-cysteine-GNF-amide. 196

Scheme 6.3 Schematic depiction of edge-thiolated GNF. The image is not to scale; the aromatic region at the core of the flakes is significantly larger than is depicted here. 198

Scheme 6.4 Reaction scheme illustrating activation of carboxylate with EDC and formation of reaction intermediate after addition of sulfo-NHS. Adapted from [32]. ... 203

List of Tables

Table 1.1: Summary and comparison of some methods for graphene synthesis. Modified from [13] with permission. 28

Table 2.1: Tabulated values of d_p at a diamond ATR crystal-water interface when θ = 45°. The values of n_1 were found in [4] and the values of n_2 in [5]. 68

Table 3.1: Fraction of carboxylic acid groups that are complexed in different materials calculated from the atomic percentages of oxygen and complexing cation. 83

Table 3.2: Peak parameters of FcMeOH redox reaction from cyclic voltammetry experiments at GNF-COOH modified BDD in 0.1 M KH_2PO_4 pH 4.6. 99

Table 3.3: Scan rates, oxidation peak currents and oxidation peak potentials extracted from **Figure 3.21** 121

Table 4.1: Calculated values of peak potential separation ΔE_p in various concentrations of supporting electrolyte KCl. 134

Table 5.1: Scan rates, peak currents for forward and backward scans, calculated volumes of the thin-layer cell and distance *h* between electrode and IRE. Adapted from [9]. 157

Table 5.2: Penetration depth d_p and the effective penetration d_e calculated at different wavenumbers. Values of n_1 were found in ref [12] and values of n_2 in ref [13]. Reproduced from [9]. 158

Table 5.3: Peak areas from difference spectra obtained at different potentials and the calculated activity change in sulphate ion at the electrode surface. Reproduced from [9]. 170

Table 5.4: Carboxylate asymmetric and symmetric stretch peak areas from difference spectra obtained at different potentials. Reproduced from [9]. 179

Table 5.5: Values used to calculate change in the number of carboxylate groups at the electrode surface when a potential is applied. Reproduced from [9]. 179

Table 5.6: Predicted changes in activity of HSO_4^- and SO_4^{2-} on application of −0.5 V calculated from Equation (5.9). Reproduced from [9]. 183

Table 5.7: Changes in activity of H_3PO_4, $H_2PO_4^-$ and HPO_4^{2-} on application of −0.5 V calculated from Equation (5.9). Reproduced from [9]. 186

Table 6.1: XPS binding energies of some carbon species. 197

Table 6.2: Elemental composition calculated from peak areas in survey spectra in **Figure 6.2**..... 206

Table 6.3: Peak parameters from peak fit of C1s spectra in **Figure 6.3**..... 208

Table 6.4: Peak parameters extracted from peak fits in **Figure 6.9**. 218

Table 6.5: Peak currents found from cyclic voltammograms in **Figure 6.12**(b), amount of charge q calculated by integrating peak areas under CV curve in Coulombs and corresponding number of FcCHO molecules in moles. 224

List of Appendix Figures

Figure A1.1 Cyclic voltammograms of 0.5×10^{-3} M $K_3[Fe(CN)_6]$ at a BDD modified with GNF-COOH in different concentrations of pH 5 PBS: 1 M (blue); 0.1 M (red); 0.01 M (black). Scan rate 50 mV s^{-1}. First scans shown. 237

Figure A1.2 Cyclic voltammograms of 0.5×10^{-3} M $K_4[Ru(CN)_6]$ at (a) clean BDD; (b) BDD modified with GNF-COOH. Supporting electrolyte: 0.1 M PBS at pH 6 (black), pH 7 (red), pH 8 (blue). Scan rate 50 mV s^{-1}. First scans shown. 238

Figure A1.3 Cyclic voltammograms of 0.5×10^{-3} M $K_3[Fe(CN)_6]$ at a BDD modified with GNF-COOH in 0.01 M NaCl at pH 5 (black) and pH 8.4 (red). Scan rate 50 mV s^{-1}. First scans shown. 239

Figure A1.4 UV Vis spectra of 2×10^{-3} M $K_3[Fe(CN)_6]$ and 2×10^{-3} M $K_4[Fe(CN)_6]$ with 30 µg ml^{-1} GNF in H_2O at *t* = 0 h (black), *t* = 7 h (red) and *t* = 24 h (blue). 239

List of Publications

Lounasvuori, M. M.; Rosillo-Lopez, M.; Salzmann, C. G., et al., Electrochemical Characterisation of Graphene Nanoflakes with Functionalised Edges. *Faraday Discussions* **2014,** *172* ( ), 293-310.

Lounasvuori, M. M.; Rosillo-Lopez, M.; Salzmann, C. G., et al., The Influence of Acidic Edge Groups on the Electrochemical Performance of Graphene Nanoflakes. *J. Electroanal. Chem.* **2015,** *753*, 28-34.

Lounasvuori, M. M., Holt, K. B., Acid Deprotonation Driven by Cation Migration at Biased Graphene Nanoflake Electrodes. *Chem. Commun.* **2017**, Advance Article. **DOI:** 10.1039/C6CC09418J.

1 Introduction

1.1 Graphene

For decades, carbon nanomaterials, such as fullerenes and carbon nanotubes, have been the subject of intense research due to their exceptional electrical and mechanical properties (for reviews see [1-4]). The building block of these carbon materials is graphene [5], a one-atom thick sheet of sp^2-hybridised carbon arranged in six-membered rings (**Figure 1.1**). Graphene has long been studied theoretically, but it was not isolated experimentally until 2004, when it was successfully prepared by Geim and Novoselov [6] by peeling thin layers off a graphite surface using Scotch tape. This method, termed micromechanical cleavage, resulted in samples with few defects as shown by field effect experiments.

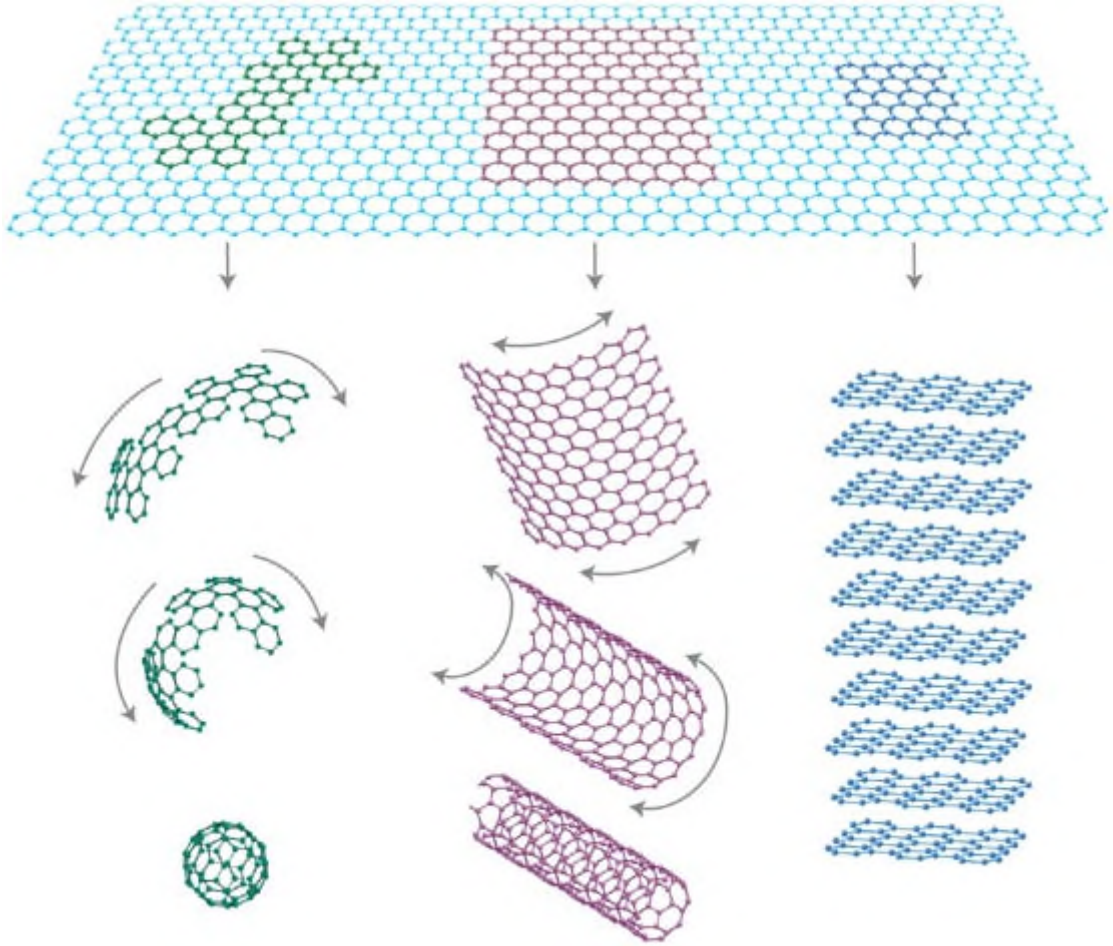

Figure 1.1 Graphene is a two-dimensional building material for other carbon materials; it can be wrapped up into 0D buckyballs, rolled into 1D nanotubes or stacked into 3D graphite. Reproduced from [5] with permission.

Raman spectroscopy is widely used to characterise graphitic materials. The two most intense Raman bands in graphite are the G peak at ~1580 and 2D peak at ~2700 cm^{-1} (with 514 nm excitation) resulting from the doubly degenerate zone centre E_{2g} mode and a second-order two-phonon process of zone-boundary phonons, respectively [7]. Raman spectra of graphite and graphene are presented in **Figure 1.2**(a). Defects in graphitic materials give rise to a Raman band termed the D peak at ca. 1350 cm^{-1}, thus allowing the use of Raman spectroscopy to assess the number of defects in graphene. Ferrari et al. [7] were the first to show that Raman spectroscopy also produces unique fingerprints depending on the number of layers in graphene samples. The 2D band,

sometimes referred to as the G′ band, changes significantly in shape and intensity going from single-layer graphene to graphite as shown in **Figure 1.2**(b-c).

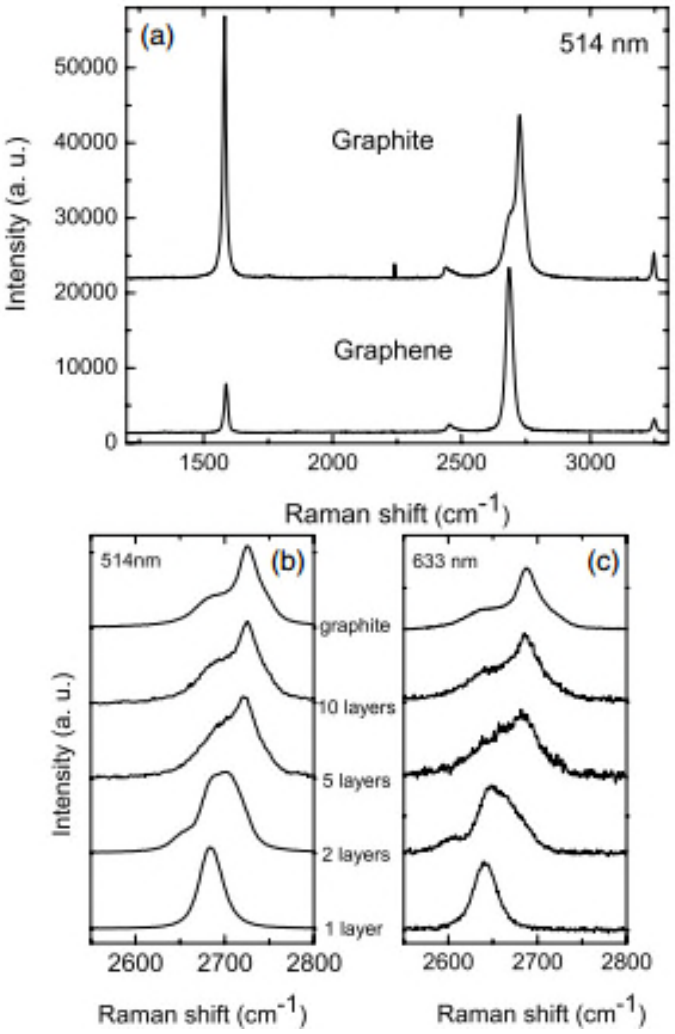

Figure 1.2 (a) Comparison of Raman spectra at 514 nm for bulk graphite and graphene. They are scaled to have similar height of the 2D peak at ~2700 cm^{-1}. (b) Evolution of the spectra at 514 nm with the number of layers. (c) Evolution of the Raman spectra at 633 nm with the number of layers. Adapted from [7] with permission.

The remarkable electronic properties of graphene, such as high carrier mobility and high transport velocity, stem from the sp^2-hybridisation of the carbon atoms, where the p_z orbitals remain perpendicular to the graphene lattice and form a conjugated π-bond network extending across the basal plane [8]. This electronic structure is disrupted at

defect sites – which is why pristine graphene is desirable for electronic applications – and at the edges of the graphene sheets.

Graphene edges can adopt two different configurations, referred to as armchair and zigzag, with an edge often consisting of alternating segments of the two types referred to as a chiral edge [8] (**Scheme 1.1**). The zigzag and armchair edges have very different electron configurations: the armchair edge is more stable due to a triple covalent bond between the two open edge carbon atoms [9], whereas the zigzag edge is higher in energy because of the p_z electrons confined on each outer carbon atom [8]. Due to these edge states, the zigzag edge is metastable and undergoes planar reconstruction to pentagonal or heptagonal structures [10].

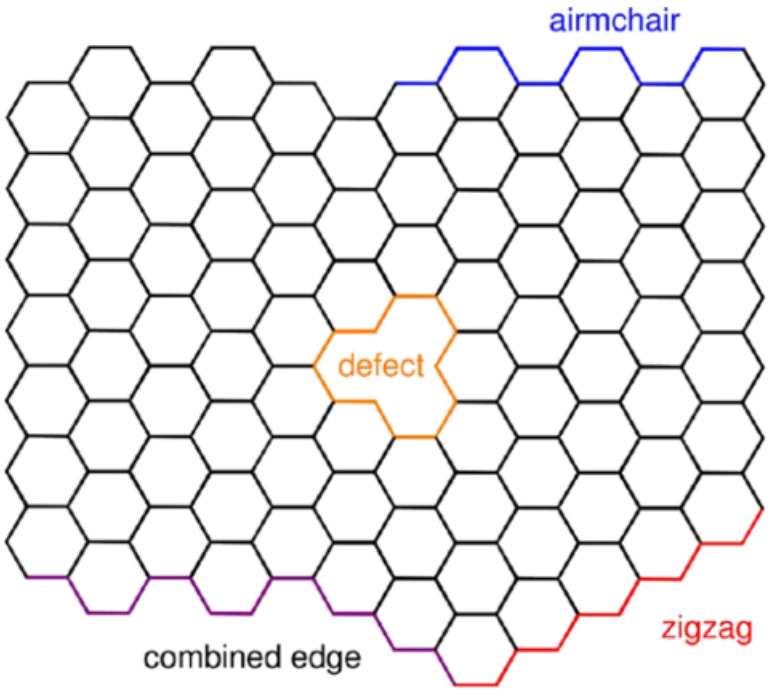

Scheme 1.1 Schematic representation of different edge configurations. A defect in the basal plane is shown in orange. Reproduced from [11] with permission.

1.1.1 Graphene synthesis

As mentioned above, the first successful reported experiment to prepare graphene made use of Scotch tape, which was used to mechanically exfoliate sheets from bulk graphite [6]. This simple method is cheap to operate but suffers from low throughput as well as small and irregular sample size, making this method currently not relevant for commercial electronic applications [12]. More techniques have since been devised and a selection of the most commonly used methods are summarised in **Table 1.1**.

Table 1.1: Summary and comparison of some methods for graphene synthesis. Modified from [13] with permission.

Method	Precursor	Advantages	Disadvantages	Ref
Mechanical exfoliation	Graphite	Low cost, high electronic quality	Low throughput, broad size distribution, small size	[6, 14-16]
Liquid-based direct exfoliation	Graphite	Scalable, versatile, mild conditions	Low monolayer content, broad size distribution	[17-23]
CVD	Methane, ethane, acetylene	Large-area graphene, relatively high electronic quality	Polycrystalline, damaging transfer process required	[24-34]
Electrochemical/ Chemical/ Thermal reduction of GO	Graphene oxide (from oxidation of graphite)	Low cost, high throughput	Low electronic quality	[35-37]

Chemical vapour deposition (CVD) has become the method of choice to prepare graphene for electronic applications (for a review see [38, 39]). CVD growth utilises heat, light or electric discharge [38] to deposit carbon onto a substrate from hydrocarbon precursors, usually methane [32-34]. The thermal decomposition of methane occurs at a very high temperature, and therefore a substrate that can simultaneously act as a catalyst is used [38]. The most common substrate is Cu [30,

31], although the use of Pt [27, 34], Ni [29, 40] and Cu-Ni alloys [32, 33] have also been reported. CVD allows the fabrication of large-area graphene of relatively high quality, although not as high as that achieved by mechanical exfoliation due to bilayer domains and grain boundaries [28, 38]. In addition to the requirement of high temperature and high vacuum, the major drawback of graphene grown by the CVD method is the need to transfer the graphene film from the conductive metal substrate onto an insulating substrate. The conventional wet chemical transfer method involves attaching a temporary support layer onto the graphene film, etching the metal substrate off, transferring the film onto the targeted substrate and removing the temporary support. Commonly used temporary supports are polymers such as polymethyl methacrylate (PMMA) [25, 26]. This transfer process can be damaging to the structural integrity of the graphene film due to water trapped underneath the graphene, and leave behind residue from the etching reagents and the polymer support [28]. Alternative methods of transfer are the subject of intense research and recent reports of PMMA-free CVD graphene have been published [28, 41].

Liquid-based direct exfoliation (LBE) is an emerging collection of synthetic methods for preparing high quality graphene using mild conditions (for a review see [42]). In LBE, graphite is directly exfoliated into 2D nanosheets in liquid media using ultrasonic, electrochemical or shear exfoliation. Ultrasonic exfoliation can make use of organic solvent only [43]; surfactants [17], polymers [19] or polycyclic aromatic hydrocarbons (PAHs) [20] can be added as stabilisers; and different intercalants such as Li^+ [18] or acids [21] can be used to facilitate exfoliation. In electrochemical exfoliation, a potential bias is used to achieve intercalation of ionic species into graphite, thus making the subsequent ultrasonic exfoliation more facile (for a review see [44]). Shear exfoliation can be performed by ball milling [23] or by rotor and stator [22] in stabilising liquids.

1.1.2 Graphene Oxide

Aside from electronic applications where large, single-crystalline graphene is needed, there are various other potential applications for graphene-related materials that don't require high electronic quality, defect-free graphene, allowing for cheaper, higher-throughput synthesis techniques to be used. One method for graphene synthesis producing high yields is the reduction of graphene oxide (GO). GO has been known and studied since Brodie first oxidised graphite using potassium perchlorate and fuming nitric acid more than 150 years ago [45]. Staudenmaier improved on Brodie's method but employed the same oxidising agents, with the addition of sulphuric acid to increase the acidity of the reaction mixture [46]. Later, Hummers replaced $KClO_3$ and fuming HNO_3 with potassium permanganate and sulphuric acid [47]. These three methods are the main routes to GO [48]. The products show great variation depending not only on the oxidising agent but also the starting material, which is most commonly naturally occurring flake graphite, purified to remove heteroatomic contamination but containing an abundance of inherent localised defects in the π-structure [48]. The resulting graphite oxide can be easily exfoliated in many solvents [49], giving individual sheets of GO which can then be chemically [36], thermally [37] or electrochemically [35] reduced to give the final product.

The chemical structure of GO is difficult to determine because of its inherently nonstoichiometric structure and dependence on synthesis method and parameters [50]. Earlier models were based on regular lattices, such as Hofmann and Holst's structure consisting of epoxy groups spread across the basal plane of graphite [51] and Ruess' model based on an sp^3-hybridised carbon backbone incorporating hydroxyl groups in addition to epoxy groups [52]. In current models, the discrete repeat units of regular lattices are rejected in favour of non-stoichiometric amorphous structures [48]. The model proposed by Lerf and Klinowski consists of both aromatic regions with

unoxidised benzene rings and regions with sp^3-hybridised 6-membered rings of carbon, with hydroxyl groups and epoxides above and below the plane and carboxyl and hydroxyl groups terminating the edges [53]. The supporting evidence for the model came from NMR and CP/MAS experiments [53]. The main issue with this model, as pointed out by Szabó and Dékány [54], is the assumption of edge-terminating carboxylic acid groups being the only carbonyl species, which is not supported by spectroscopic data and does not explain the planar acidity of GO. A new model presented by Szabó and Dékány [54] introduces phenolic groups into the bulk of the layers through carbon-carbon bond cleavage to account for the spectroscopic data and the acidity; also, the presence of 1,3-ethers is assumed rather than epoxides. The carbon backbone has a periodic structure of trans-linked cyclohexane chairs and ribbons of flat hexagons with C=C double bonds; aromaticity is lost early in the oxidation process [54].

Dimiev et al. [55] have introduced a new dynamic structural model in which interaction with water, rather than existing acidic functional groups, is the main factor in the acidity of GO and the functional groups evolve continuously as water incorporates into GO, transforms it, generates protons and then leaves *via* different reactions. In this model, reaction with water results in carbon-carbon bond cleavage, formation of vinylogous carboxylic acids and generation of protons. The reaction proceeds faster in alkaline solution. Based on experimental results, Dimiev's group combine elements from the two conflicting models: the main functional groups on the basal plane proposed by Lerf and Klinowski, namely tertiary alcohols and epoxides [53], and the idea of carbonyl group formation through C-C bond cleavage suggested by Szabó and Dékány [54]. Recent direct imaging experiments support the dynamic interpretation of the structural evolution of GO [50].

1.1.3 Graphene Functionalisation

Pristine graphene exhibits remarkable electronic properties. Experimental results show high charge carrier mobilities at ambient temperatures over a technologically relevant range of carrier concentrations [16]. Additionally, due to the ambipolarity of graphene, the charge carriers can be tuned continuously between electrons and holes [5]. This means that the adsorption of both electron withdrawing and donating groups can lead to chemical gating of graphene, making graphene a potential material for resistive-type sensors [56]. These electronic properties, combined with a high surface area, suggest tantalising possibilities for graphene in applications such as optoelectronic devices [57-59], supercapacitors [60-62] and electrochemical sensing [63-65].

However, pristine graphene suffers from low solubility in polar solvents and a tendency to restack irreversibly, making its use problematic in many practical applications. To improve the water solubility and to prevent restacking of the graphene layers, various approaches to introduce functionalities onto graphene have been reported, such as covalent modification [66, 67], π–π interactions [68, 69] and hydrophobic interactions [70, 71].

Although covalent functionalisation will in most cases disrupt the π-bonding system of graphene, Jeong et al. [66] suggest existing defects can be used as active sites to minimise introduction of sp^3 carbon. They modified thermally exfoliated graphene with ethanolamine and butyl bromide to introduce cationic ammonium functionalities onto the graphene basal plane and obtained a product that was stable in solution for months despite a particle size of around 7 μm. Aminoethyl acrylate –functionalised graphene nanosheets bearing cationic functional groups were also shown to effectively resist restacking and agglomeration [67]. To preserve the electronic structure of the graphene basal plane, non-covalent methods of functionalisation are needed. Pyrene derivatives such as 4-(pyren-1-yl)butanal [68] or 1-pyrenebutyric acid hydroxysuccinimide ester

[69] can be used to functionalise graphene as the pyrene moiety has the ability to form π–π interactions with the graphene sheet while the end groups introduce a polar functionality, thus improving water solubility and preventing stacking due to steric effects from the bulky molecules.

Non-covalent modification of graphene can also be achieved by exploiting hydrophobic interactions, for example between the graphene basal plane and the butyl chains in poly-L-lysine [70] or the PTFE backbone of Nafion [71]. Both graphene hybrid materials exhibited good stability and dispersibility in aqueous solutions.

1.2 Electrochemistry of Graphene

Traditional consensus has been that electron transfer on graphitic materials is dominated by the edge plane [72-74], and it has been shown that the intentional generation of oxygen-containing defects increases the reactivity [72]. However, recently it has been shown that the basal plane of highly oriented pyrolytic graphite (HOPG) can exhibit fast electron transfer for outer-sphere redox couples [72, 75-79]. High resolution electrochemical surface imaging studies have shown that electron transfer at carbon nanotube walls and the graphene basal plane surfaces is fast and reversible and limited only by available density of states [78, 80-82]. This contrasts with previous and indeed very recent studies [74, 83] reporting exceedingly sluggish kinetics at the basal plane of graphitic materials. One possible explanation for these discrepancies is in preparation of the materials before electrochemical investigation. Adsorption of organic impurities onto freshly prepared graphene has been shown to take place within minutes on exposure to a typical laboratory atmosphere [84] and such a surface layer may lead to inhibition of electron transfer at carbon surfaces.

Notwithstanding the conflicting reports of basal plane activity, it is accepted that the edge plane of graphitic materials shows enhanced electrochemical activity due to the

presence of high energy defects such as dangling bonds and oxygen functionalities. The interaction of various redox species with oxygen functionalities at carbon electrodes has been investigated extensively by McCreery and co-workers [85-87]. Common redox probes can be classified roughly into three categories: those which are insensitive to surface termination (FcMeOH, $[Ru(NH_3)_6]^{3+/2+}$); those which interact with specific oxygen functionalities (such as $Fe^{3+/2+}$ with C=O) and those which are surface sensitive but apparently do not interact with specific oxygen-containing groups ($[Fe(CN)_6]^{3-/4-}$) [88].

Graphene has been studied as electrode material using several different redox probes, such as ferrocenemethanol [41, 89], $[Fe(CN)_6]^{3-/4-}$ [14, 74, 90] and 1,4-benzoquinone/hydroquinone [91, 92]. Due to the variation in the methodology of graphene synthesis and electrode preparation, comparing the results is not straightforward. For example, Dryfe's group [14] fabricated electrodes from mechanically exfoliated graphene with a well-defined exposed area and controlled level of defects, thus being able to compare defect-free graphene and graphene with defects. In contrast with reports of defects improving HET kinetics at basal plane of graphite [72], Dryfe et al. found no significant difference in the electrochemical response of $[Fe(CN)_6]^{3-}$ reduction at graphene regardless whether defects were present [14]. Abruña and Ralph's group [89] employed a similarly rigorous electrode fabrication method to both mechanically exfoliated and CVD-grown graphene. Amemiya's group [41] reported significantly faster electron transfer kinetics for ferrocenemethanol at PMMA-free CVD-grown graphene compared to conventionally transferred CVD graphene contaminated with PMMA residue. Banks and co-workers [74], on the other hand, used commercially available graphene platelets directly from the ethanol dispersion in which the platelets were supplied and modified an edge-plane graphite electrode by the drop-coating method. This method gives very little control over surface area and coverage of the underlying electrode. Chemically, thermally and

electrochemically reduced GO samples are also widely employed by immobilisation onto a glassy carbon electrode surface [93-95]. Aksay et al. [96] have pointed out that the effect of roughness and porosity of drop-coated films on electrodes can often dominate the electrochemical response. In some cases, effects stemming from electrode morphology are unwittingly being measured, rather than effects related to specific surface chemistry and differences in the HET rates [90, 96].

In addition to variations in oxygen content, defect density and electrode morphology, the presence of impurities also plays a role in the electrochemistry of graphene-related materials. The identity of impurities varies from sample to sample and is often overlooked when results are reported. Exciting electrochemical properties originally attributed to graphene have subsequently been shown to originate from metallic impurities [97, 98]. Metallic impurities are inherent in natural graphite and introduced to both natural and synthetic graphite during milling [99]; they persist in reduced GO despite the extensive oxidative treatment graphite is subjected to [99]. Additionally, the use of permanganate in the Hummers method of graphite oxidation has been shown to lead to Mn impurities at high ppm levels in the graphene oxide product [98]. Different carbonaceous impurities include the presence of multiple layers due to incomplete exfoliation [97]; amorphous carbon impurities that persist from precursors to synthetic graphite [99] and are created during digestion of graphite with strong oxidants [97]. The use of hydrazine as reducing agent introduces significant amounts of covalently bonded nitrogen into reduced GO [100-102] with a number of possible configurations leading to differences in the electronic structure [103].

Different oxygen-containing impurities arise from the oxidation of graphite and its subsequent incomplete reduction [104] depending on the synthesis method. The identity of the different oxygen-containing functionalities that remain on reduced GO and may develop during atmospheric exposure on any graphene material remains unclear. The presence of carbonyls, epoxy groups and carboxylic acid functionalities

has been detected by XPS [100]. Epoxy and hydroxyl groups have been suggested without experimental evidence [105], and IR spectra have been reported without attempts to assign the observed bands [106]. The amount of oxygen in graphene samples also varies depending on the preparation steps, with 4.96 % atomic oxygen reported in commercially available graphene platelets [74] and 6.25 % in “highly reduced GO” [102].

Given that even the most carefully prepared graphene samples may have some oxygen content, it seems important to determine the influence of these functionalities on the electrochemical response. As graphene is increasingly being manufactured via reduction of graphene oxide, where an array of oxygen groups persist in the final product, the interaction of oxygen moieties with solution species will influence how well the material performs in electrochemical applications.

1.3 Graphene Nanoflakes

The work presented in this report was conducted using graphene nanoflakes (GNF) provided by Dr Salzmann’s group, who have reported the synthesis and characterisation of this novel graphene-related nanomaterial [107]. The method involves chemical oxidation of multi-walled carbon nanotubes grown by CVD using sulphuric and nitric acids, followed by neutralisation with KOH, dialysis and freeze-drying.

Whereas graphene is defined as “a single carbon layer of the graphite structure, describing its nature by analogy to a polycyclic aromatic hydrocarbon of quasi infinite size” [108], the GNF synthesised by Salzmann’s group were, on average, only 30 nm in diameter [107]. In comparison, commercially available pristine graphene flakes, used by Banks et al. [74], have an average lateral dimension of 550 nm. Graphene grown

epitaxially and by CVD is usually aimed for applications in which large areas of pristine aromatic carbon is desirable.

After purification and dialysis, XPS confirmed the purity of GNF, detecting only carbon and oxygen [107] (**Figure 1.3**(a)). The carbon-carbon bonding in GO is only 60 % sp^2-hybridised [109] due to increased defect density leading to sp^3-hybridisation. In contrast, ^{13}C solid state NMR studies by Salzmann's group show that only COOH and sp^2-hybridised carbon are present [107], indicating that the GNF contain fewer oxygenated defects on the basal plane and that the oxygen content is concentrated around the edges. High-resolution spectrum of the C1s region showed the presence of COOH groups and a complete lack of any alcohol or epoxide groups in GNF [107] which are often found on the basal plane in GO materials [48], providing further evidence that the GNF consist of a pristine basal plane with carboxylic acid groups decorating the edges.

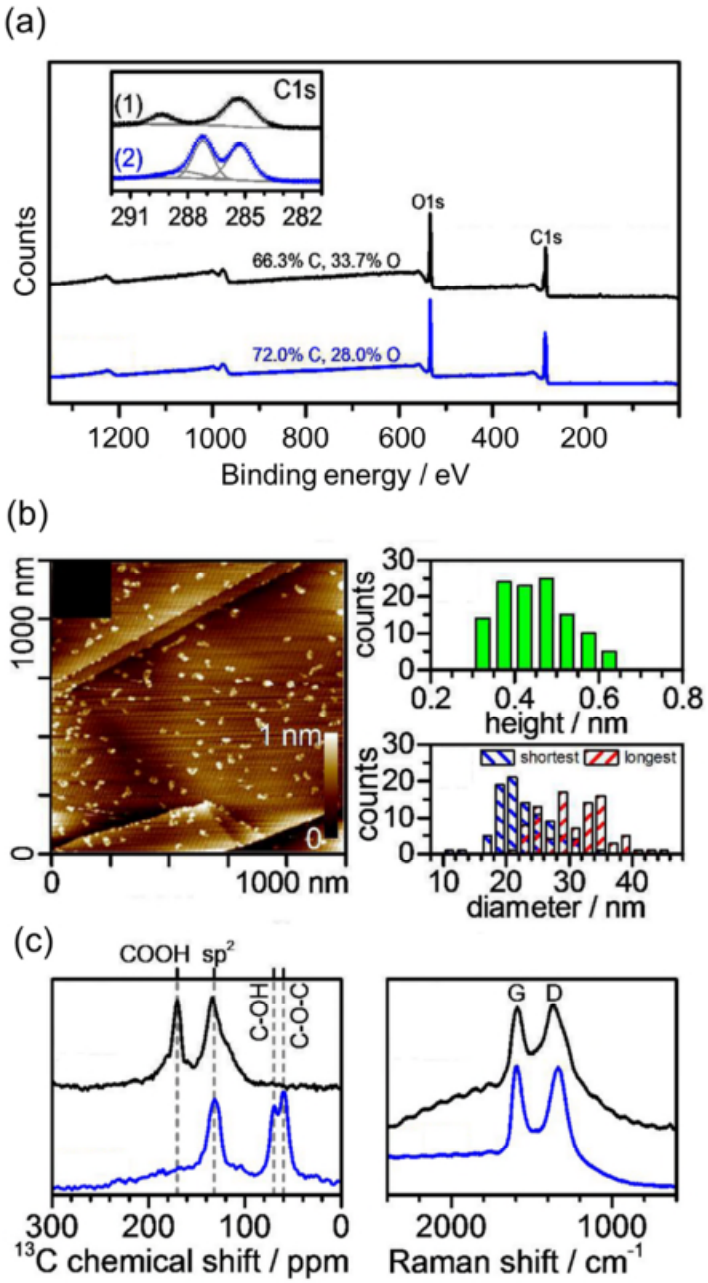

Figure 1.3 (a) X-ray photoelectron survey spectra of graphene oxide (blue) and GNF (black). Inset: High resolution XPS spectra of the C1s region of GO (blue) and GNF (black). (b) AFM image of GNF spin-coated onto highly oriented pyrolytic graphite. (c) Height and (d) diameter distribution of GNF. (e) ^{13}C solid state NMR and (f) Raman spectra of GO (black) and GNF (blue). Adapted from [107] with permission.

The carboxylic acid groups offer useful synthetic routes to flakes terminated with different functionalities. The experiments included in this report were conducted using carboxyl-functionalised GNF and amide-functionalised GNF. Schematic representations of these two functionalities are given in **Scheme 1.2**.

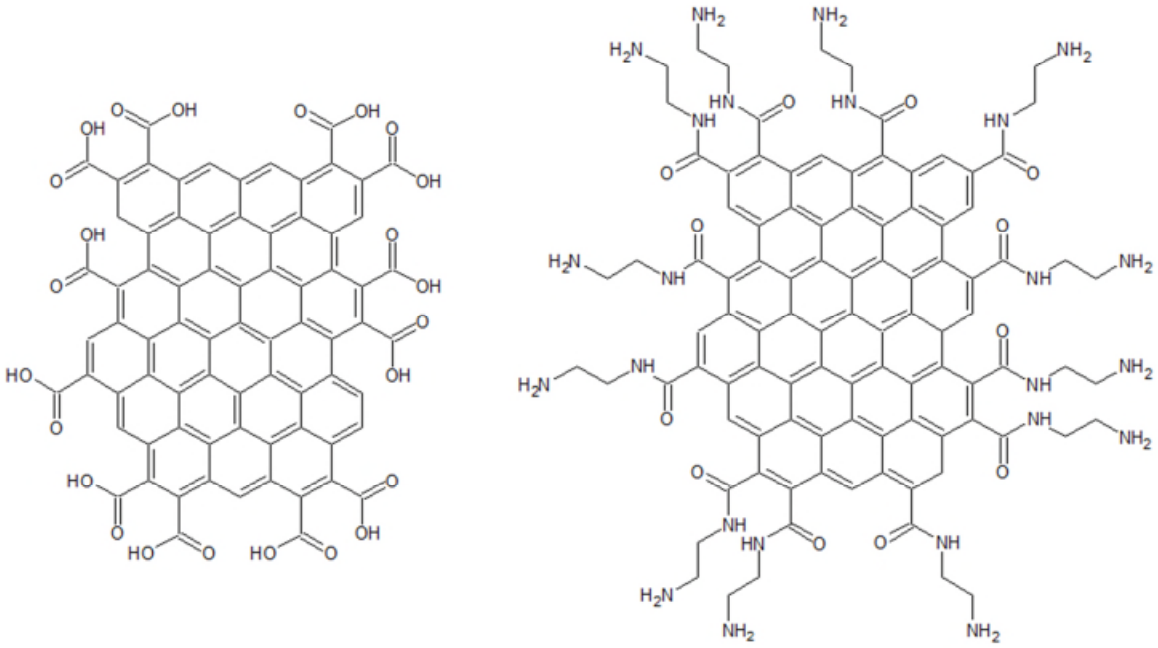

Scheme 1.2 Schematic depiction of edge-carboxylated (left) and amide-functionalised GNF. The images are not to scale; the aromatic region at the core of the flakes is significantly larger than is depicted here. Reproduced from [110].

In addition to acting as a precursor to other functionalities, the acid groups in GNF-COOH form strong complexes with divalent cations. This is achieved by deprotonating the carboxylic acid edge groups of GNF-COOH and subsequently adding an aqueous solution of a chloride salt of an alkali earth metal. Reaction of the water-soluble GNF with Ca^{2+} results in a porous precipitate where the loss of solubility indicates a strong interaction between the COO^- edge groups and the Ca^{2+} cation.

The use of GNF distinguishes this project from work done by other groups on graphene-related materials. The small size of the flakes amplifies the importance of the edge groups. GNF will also bridge pristine graphene and GO in a manner similar to reduced GO while providing a unique starting point in terms of uniform small size, controlled introduction of functionalities and low defect density, all of which are absent from reduced GO.

1.4 Acid-base Properties of Graphene-related Materials

Many ionisable functionalities are present in GO, such as carboxylic acids and phenols [48-50, 55, 111-114]. Carboxylic acid groups are commonly found on carbon electrode surfaces, especially after use at high anodic potentials. Their presence has been shown to greatly influence the electron transfer kinetics of common redox species at graphene-modified [110] and BDD [115] electrodes, although the exact nature of the influence is unclear.

The ability of acidic functional groups to dissociate and carry negative charge means that they can interact electrostatically with cationic species to form complexes, and this can be exploited in applications where relatively weak interactions are desirable. For instance, Loh's group [116] used the carboxylic acid groups on graphene oxide to create a charge transfer complex through electrostatic interaction between the negatively charged GO and a positively charged dye. Additional π–π interactions led to fluorescence quenching of the dye through charge transfer. The fluorescence could be recovered by extracting the dye from the GO-dye complex and DNA was found to be very efficient in achieving this as DNA formed a stronger electrostatic bond than GO with the positively charged dye. By monitoring the intensity of the fluorescence, the GO-dye complex could then be used to detect the presence of DNA in biological mixtures.

The pK_a of a functional group determines the pH at which protonation takes place. pH differences in biological systems can therefore be exploited to achieve selective release of molecules from complexes, as demonstrated by Qiu et al. [117]. They used graphene quantum dots (GQD) functionalised with NH_2 groups as a fluorescent carrier for a common anti-cancer drug. The increased acidic conditions inside cancer cells compared to healthy tissue caused protonation of the NH_2 groups on both the GQDs and the drug, weakening the interaction and promoting release of the drug.

1.4.1 Controlling the Protonation State of Electrode-Immobilised Species

Organic acids do not undergo reversible redox reactions and potentials exceeding +2 V vs. SCE are required to achieve their irreversible oxidation [118], while reduction occurs at potentials exceeding −2 V vs. SCE [119]. Even though less extreme potentials have been reported to partially reduce graphene oxide electrochemically [112, 120], COOH groups may not be fully reduced at these potentials. There are, however, reports of reversible non-Faradaic peaks being observed in CV and electrochemical impedance spectroscopy (EIS) studies of electrode-confined carboxylic acid –terminated SAMs [121-124]. Theoretical treatment of this phenomenon attributes the CV peaks to the change in interfacial differential capacitance induced by the change in protonation state of the acid, the protonation/deprotonation being driven by the electric field at the electrode [125-128]. The interfacial potential distribution for a monolayer of an acid-terminated alkanethiol at a gold electrode is depicted in **Figure 1.4** showing the plane of acid dissociation (PAD) [125], the common plane on which all the acid groups lie. This electrochemically driven reversible acid protonation reaction has recently been exploited to fabricate a novel supercapacitor electrode material, making use of the fast charge-discharge response of the electric field driven protonation of 3,4,9,10-perylene tetracarboxylic acid [129].

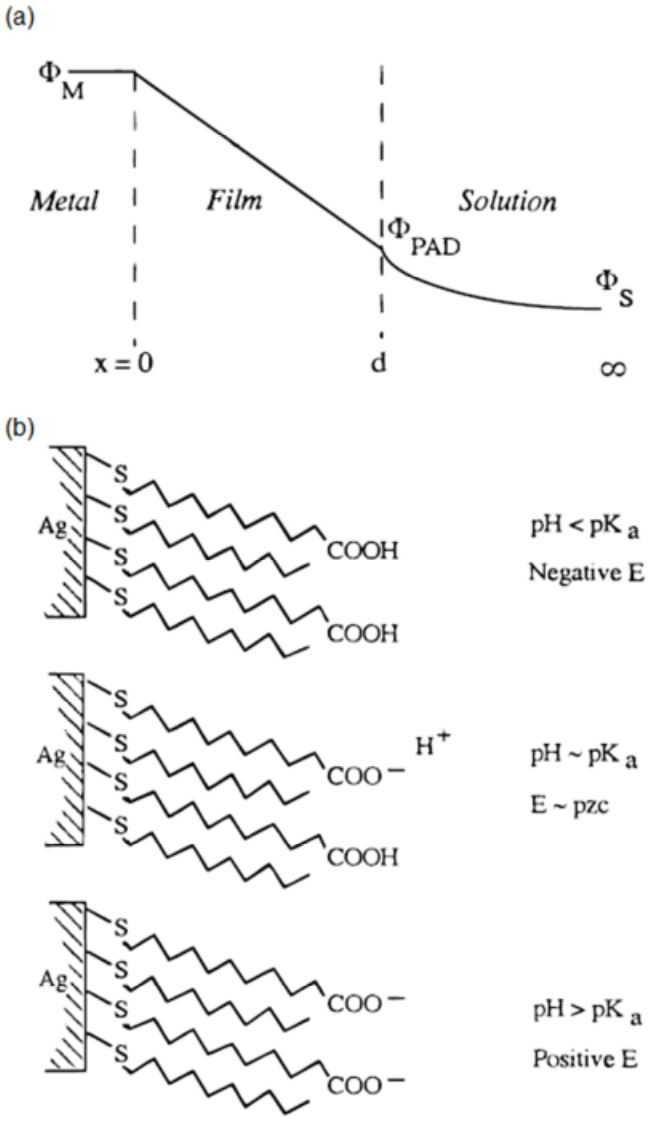

Figure 1.4 (a) Electrostatic potential distribution across a metal/acid monolayer/solution interface. (b) Schematic representation of a mixed monolayer of 11-mercaptoundecanoic acid and 1-decanethiol in contact with an electrolyte solution as a function of electrode potential (E) and pH. Reproduced from [121] with permission. Copyright 1998 American Chemical Society.

Other studies have used in situ quartz crystal microbalance (QCM) [130] and IR spectroscopy [131-133] to determine the protonation/deprotonation behaviour of carboxylic acid –terminated SAMs on gold electrodes and have observed protonation taking place at positive potentials and deprotonation at negative potentials. Instead of being driven by the electric field, the acid dissociation was thought to be governed by the concentration of electrolyte cations near the surface that affected the apparent pK_a of the acid groups [130-133].

Based on these conflicting reports, the nature and response of carboxylic acid groups at the electrode surface seems quite complex and not entirely understood. Given their ubiquity, not only as defect sites on carbon electrodes, but also in the polymer electrolytes employed in solid supercapacitors, the response of organic acids to applied electrode potential is an essential area of study.

1.5 Methods of immobilising GNF on Electrode

In order to use GNF in an electrochemical investigation, they must be fabricated into an electrode. Various ways of constructing electrodes from nanomaterials exist, such as incorporating the sample in a compact paste [134, 135] or screenprinting the sample as an ink [136, 137], but these methods involve the addition of binders. An alternative method is immobilisation on the surface of commercially available solid electrodes, and this is the route chosen for my work. The surface modification can be achieved by drop-coating, spin-coating or self-assembly.

1.5.1 Drop-coating

In drop-coating, a sample is first suspended in a desired solvent. A known volume of the suspension is then applied onto the substrate and the solvent is allowed to evaporate either under atmospheric conditions or under inert atmosphere. Drop-coating is a quick and easy method of modifying electrodes, and it is widely used in electrochemical research to immobilise graphene-related materials on electrode surfaces [93-95]. However, it doesn’t give much control over the structure of the deposited layer.

1.5.2 Spin-coating

Spin-coating is a technique for depositing thin films on flat substrates. The coating material in a solution form is applied onto the substrate and the substrate is rotated at

high speed, which causes the coating material to spread by centrifugal force. Spin-coating offers many advantages, such as the ability to obtain uniform coatings and the ability to control the thickness of the film by altering the speed of rotation. However, the wastage is high in this process as >95% of the solution is wicked off the substrate [138]. Spin-coating is a commonly used technique in microfabrication of solar cells [139, 140], OLEDs [141] and field-effect transistors [142].

1.5.3 Self-assembly

Self-assembly of molecules at interfaces is a common phenomenon. It is exhibited by surfactant molecules and lipids that consist of a polar head group and a hydrophobic tail. Due to this ambiphility they aggregate and form micelles in emulsions and lipid bilayers in living organisms.

Spontaneous adsorption on a substrate can occur if the substrate environment is energetically more favourable than solution environment [143]. This process can be exploited in surface engineering to tailor the interfacial properties of a surface. Self-assembled monolayers carry several benefits compared to ultra-thin films made by molecular beam epitaxy (MBE) or CVD. Firstly, they can be formed without expensive equipment or the use of ultra-high vacuum (UHV). Secondly, highly ordered monolayers can be formed using self-assembly on substrates of different shapes and sizes [144]. Thirdly, there is a large variety of molecular structures available in terms of head groups (thiols [145], silanes [146] and phosphonates [147]); tail groups (alkyl chains [148], aromatic chains [144]); and end groups (non-polar [149], polar [133], electroactive [150]).

SAMs of thiols on gold are a good example of spontaneous adsorption due to a very strong gold-sulphur interaction. Gold is the most studied substrate due to, in part, the great affinity with which it binds sulphur, but also because gold has many useful

characteristics: thin films and nanoparticles of gold are straightforward to prepare; it can be handled in atmospheric conditions due to its inert nature and ability to withstand oxidation by atmospheric oxygen; it is a commonly used substrate in various spectroscopic and analytical techniques; and it is compatible with cells [145].

The self-assembly occurs in two distinct kinetic steps: in the first, fast step, the head groups chemisorb onto the Au substrate, followed by a slow reorganisation of the alkyl chain tail groups to form a tightly packed, ordered monolayer [151].

In applications, the alkyl chain tail is often functionalised with an end group. Thiols with a variety of different end groups are commercially available and synthesis procedures are reported for many others, such as ferrocenyl-terminated alkanethiols [152] for molecular diodes [150]. The identity of the end group affects interfacial properties [153], but they can also be tailored to enable attachment of large, complex ligands after SAM formation either covalently (antibodies for immunosensing [148], polymers for solar cells [154]) , or *via* adsorption (proteins for cell adhesion [155], polyelectrolytes for water purification [156]).

1.6 Aim and Scope of the Thesis

This thesis has three objectives: to examine the effect of specific surface functionalities present at carbon electrodes on common redox probes; to study the potential-dependent dissociation of acidic surface functionalities; and to explore different ways of attaching functionalised carbon nanomaterials onto a surface.

The structure of this thesis is as follows: The main techniques used in this work are briefly introduced in Chapter 2. Existing literature on GNF was summarised in Section 1.3 and further characterisation is presented in Chapter 3. Transmission electron microscopy (TEM) was used to image the flakes, while attenuated total reflectance Fourier transform infrared spectroscopy (ATR-FTIR) was employed to verify the identity

of functional groups present, and to explore the acid/base properties of the material. Cyclic voltammetry (CV) was also used to determine the electrochemical properties of GNF immobilised onto an electrode surface. After characterising the GNF, their influence on a standard outer-sphere redox couple was studied. Ferrocenemethanol (FcMeOH) was used as a probe to ascertain whether electrode-immobilised GNF would inhibit or improve electron transfer. Inner-sphere redox probes and redox couples exhibiting proton-coupled electron transfer were also investigated to further elucidate the influence on different electron transfer processes.

Chapter 4 focuses on the redox couple $[Fe(CN)_6]^{3-/4-}$ and examines how it is affected by the presence of GNF both in solution and immobilised on the electrode surface. CV, IR and in situ spectroelectrochemical techniques were employed to gain information on the stability of $[Fe(CN)_6]^{3-/4-}$.

In Chapter 5, the effect of potential on the carboxylic acid groups present at the GNF edge is studied in depth. A new experimental protocol was developed for in situ spectroelectrochemistry that involves applying a series of potential steps to the GNF-modified electrode and monitoring possible changes to the GNF edge groups. A range of different solution conditions were examined, including changing the identity of the electrolyte cation and anion, varying the pH of the electrolyte and changing the ionic strength of the electrolyte.

Chapter 6 explores different ways of attaching GNF onto a surface. Cysteine and cystamine were used to form self-assembled monolayers on Au substrates that offered two different types of head groups onto which GNF were attached. Thiol-functionalised GNF were also assembled directly onto Au(111). CV, differential pulse voltammetry (DPV), X-ray photoelectron spectroscopy (XPS) and scanning tunnelling microscopy (STM) were used to verify the presence of GNF on the surface.

References for Chapter 1

1. Wu, Y.; Wang, J.; Jiang, K., et al., Applications of Carbon Nanotubes in High Performance Lithium Ion Batteries. *Frontiers of Physics* **2014,** *9* (3), 351-369.
2. Barsan, M. M.; Ghica, M. E.; Brett, C. M. A., Electrochemical Sensors and Biosensors Based on Redox Polymer/Carbon Nanotube Modified Electrodes: A Review. *Anal. Chim. Acta* **2015,** *881*, 1-23.
3. Kirner, S.; Sekita, M.; Guldi, D. M., 25th Anniversary Article: 25 Years of Fullerene Research in Electron Transfer Chemistry. *Adv. Mater.* **2014,** *26* (10), 1482-1493.
4. Coro, J.; Suárez, M.; Silva, L. S. R., et al., Fullerene Applications in Fuel Cells: A Review. *Int. J. Hydrogen Energy* **2016,** *41* (40), 17944-17959.
5. Geim, A. K.; Novoselov, K. S., The Rise of Graphene. *Nature Materials* **2007,** *6* (3), 183-191.
6. Novoselov, K. S.; Geim, A. K.; Morozov, S. V., et al., Electric Field Effect in Atomically Thin Carbon Films. *Science* **2004,** *306* (5696), 666-669.
7. Ferrari, A. C.; Meyer, J. C.; Scardaci, V., et al., Raman Spectrum of Graphene and Graphene Layers. *Phys. Rev. Lett.* **2006,** *97* (18), 187401.
8. Bellunato, A.; Arjmandi Tash, H.; Cesa, Y., et al., Chemistry at the Edge of Graphene. *ChemPhysChem* **2016,** *17* (6), 785-801.
9. He, K.; Lee, G.-D.; Robertson, A. W., et al., Hydrogen-Free Graphene Edges. *Nature Communications* **2014,** *5*, 3040.
10. Koskinen, P.; Malola, S.; Häkkinen, H., Evidence for Graphene Edges Beyond Zigzag and Armchair. *Physical Review B* **2009,** *80* (7), 073401.
11. Quintana, M.; Vazquez, E.; Prato, M., Organic Functionalization of Graphene in Dispersions. *Acc. Chem. Res.* **2013,** *46* (1), 138-148.
12. Avouris, P.; Dimitrakopoulos, C., Graphene: Synthesis and Applications. *Mater. Today* **2012,** *15* (3), 86-97.
13. Guo, S.; Dong, S., Graphene Nanosheet: Synthesis, Molecular Engineering, Thin Film, Hybrids, and Energy and Analytical Applications. *Chem. Soc. Rev.* **2011,** *40* (5), 2644-2672.
14. Valota, A. T.; Kinloch, I. A.; Novoselov, K. S., et al., Electrochemical Behavior of Monolayer and Bilayer Graphene. *ACS Nano* **2011,** *5* (11), 8809-8815.
15. Zhang, Y.; Tan, Y.-W.; Stormer, H. L., et al., Experimental Observation of the Quantum Hall Effect and Berry's Phase in Graphene. *Nature* **2005,** *438* (7065), 201-204.
16. Morozov, S. V.; Novoselov, K. S.; Katsnelson, M. I., et al., Giant Intrinsic Carrier Mobilities in Graphene and Its Bilayer. *Phys. Rev. Lett.* **2008,** *100* (1), 016602-016604.
17. Smith, R. J.; Lotya, M.; Coleman, J. N., The Importance of Repulsive Potential Barriers for the Dispersion of Graphene Using Surfactants. *New Journal of Physics* **2010,** *12* (12), 125008.

18. Zhou, K.; Shi, Y.; Jiang, S., et al., A Facile Liquid Phase Exfoliation Method to Prepare Graphene Sheets with Different Sizes Expandable Graphite. *Mater. Res. Bull.* **2013,** *48* (9), 2985-2992.
19. Xu, L.; McGraw, J.-W.; Gao, F., et al., Production of High-Concentration Graphene Dispersions in Low-Boiling-Point Organic Solvents by Liquid-Phase Noncovalent Exfoliation of Graphite with a Hyperbranched Polyethylene and Formation of Graphene/Ethylene Copolymer Composites. *The Journal of Physical Chemistry C* **2013,** *117* (20), 10730-10742.
20. Schlierf, A.; Yang, H.; Gebremedhn, E., et al., Nanoscale Insight into the Exfoliation Mechanism of Graphene with Organic Dyes: Effect of Charge, Dipole and Molecular Structure. *Nanoscale* **2013,** *5* (10), 4205-4216.
21. Kovtyukhova, N. I.; Wang, Y.; Berkdemir, A., et al., Non-Oxidative Intercalation and Exfoliation of Graphite by Brønsted Acids. *Nat Chem* **2014,** *6* (11), 957-963.
22. Paton, K. R.; Varrla, E.; Backes, C., et al., Scalable Production of Large Quantities of Defect-Free Few-Layer Graphene by Shear Exfoliation in Liquids. *Nat Mater* **2014,** *13* (6), 624-630.
23. Del Rio-Castillo, A. E.; Merino, C.; Díez-Barra, E., et al., Selective Suspension of Single Layer Graphene Mechanochemically Exfoliated from Carbon Nanofibres. *Nano Research* **2014,** *7* (7), 963-972.
24. Kibena, E.; Mooste, M.; Kozlova, J., et al., Surface and Electrochemical Characterisation of CVD Grown Graphene Sheets. *Electrochem. Commun.* **2013,** *35*, 26-29.
25. Kumar, K.; Kim, Y.-S.; Yang, E.-H., The Influence of Thermal Annealing to Remove Polymeric Residue on the Electronic Doping and Morphological Characteristics of Graphene. *Carbon* **2013,** *65*, 35-45.
26. Park, J.-H.; Jung, W.; Cho, D., et al., Simple, Green, and Clean Removal of a Poly(Methyl Methacrylate) Film on Chemical Vapor Deposited Graphene. *Appl. Phys. Lett.* **2013,** *103* (17), 171609.
27. Ma, T.; Ren, W.; Liu, Z., et al., Repeated Growth–Etching–Regrowth for Large-Area Defect-Free Single-Crystal Graphene by Chemical Vapor Deposition. *ACS Nano* **2014,** *8* (12), 12806-12813.
28. Deokar, G.; Avila, J.; Razado-Colambo, I., et al., Towards High Quality CVD Graphene Growth and Transfer. *Carbon* **2015,** *89*, 82-92.
29. Cabrero-Vilatela, A.; Weatherup, R. S.; Braeuninger-Weimer, P., et al., Towards a General Growth Model for Graphene CVD on Transition Metal Catalysts. *Nanoscale* **2016,** *8* (4), 2149-2158.
30. Li, X.; Colombo, L.; Ruoff, R. S., Synthesis of Graphene Films on Copper Foils by Chemical Vapor Deposition. *Adv. Mater.* **2016,** *28* (29), 6247-6252.
31. Ta, H. Q.; Perello, D. J.; Duong, D. L., et al., Stranski–Krastanov and Volmer–Weber CVD Growth Regimes to Control the Stacking Order in Bilayer Graphene. *Nano Lett.* **2016,** *16* (10), 6403-6410.
32. Wu, T.; Zhang, X.; Yuan, Q., et al., Fast Growth of Inch-Sized Single-Crystalline Graphene from a Controlled Single Nucleus on Cu-Ni Alloys. *Nat Mater* **2016,** *15* (1), 43-47.
33. Cho, J. H.; Gorman, J. J.; Na, S. R., et al., Growth of Monolayer Graphene on Nanoscale Copper-Nickel Alloy Thin Films. *Carbon* **2017,** *115*, 441-448.
34. Nam, J.; Kim, D.-C.; Yun, H., et al., Chemical Vapor Deposition of Graphene on Platinum: Growth and Substrate Interaction. *Carbon* **2017,** *111*, 733-740.
35. Wang, N.; Lin, M.; Dai, H., et al., Functionalized Gold Nanoparticles/Reduced Graphene Oxide Nanocomposites for Ultrasensitive Electrochemical Sensing of Mercury Ions Based on Thymine–Mercury–Thymine Structure. *Biosens. Bioelectron.* **2016,** *79*, 320-326.
36. Zhan, T.; Wang, X.; Li, X., et al., Hemoglobin Immobilized in Exfoliated Co_2Al LDH-Graphene Nanocomposite Film: Direct Electrochemistry and

Electrocatalysis toward Trichloroacetic Acid. *Sensors and Actuators B: Chemical* **2016,** *228*, 101-108.
37. Zhang, B.; Xiao, C.; Xiang, Y., et al., Nitrogen-Doped Graphene Quantum Dots Anchored on Thermally Reduced Graphene Oxide as an Electrocatalyst for the Oxygen Reduction Reaction. *ChemElectroChem* **2016,** *3* (6), 864-870.
38. Muñoz, R.; Gómez-Aleixandre, C., Review of CVD Synthesis of Graphene. *Chem. Vap. Deposition* **2013,** *19* (10-11-12), 297-322.
39. Geng, D.; Wang, H.; Yu, G., Graphene Single Crystals: Size and Morphology Engineering. *Adv. Mater.* **2015,** *27* (18), 2821-2837.
40. Lin, L.; Liu, Z., Graphene Synthesis: On-the-Spot Growth. *Nat Mater* **2016,** *15* (1), 9-10.
41. Chen, R.; Nioradze, N.; Santhosh, P., et al., Ultrafast Electron Transfer Kinetics of Graphene Grown by Chemical Vapor Deposition. *Angew. Chem.* **2015,** *127* (50), 15349-15352.
42. Niu, L.; Coleman, J. N.; Zhang, H., et al., Production of Two-Dimensional Nanomaterials Via Liquid-Based Direct Exfoliation. *Small* **2016,** *12* (3), 272-293.
43. Khan, U.; Porwal, H.; O'Neill, A., et al., Solvent-Exfoliated Graphene at Extremely High Concentration. *Langmuir* **2011,** *27* (15), 9077-9082.
44. Abdelkader, A. M.; Cooper, A. J.; Dryfe, R. A. W., et al., How to Get between the Sheets: A Review of Recent Works on the Electrochemical Exfoliation of Graphene Materials from Bulk Graphite. *Nanoscale* **2015,** *7* (16), 6944-6956.
45. Brodie, B. C., Sur Le Poids Atomique Du Graphite. *Annales de Chimie et de Physique* **1860,** *59*, 466-472.
46. Staudenmaier, L., Verfahren Zur Darstellung Der Graphitsaure. *Berichte der Deutschen Chemischen Gesellschaft* **1898,** *31*, 1481.
47. Hummers, W. S.; Offeman, R. E., Preparation of Graphitic Oxide. *J. Am. Chem. Soc.* **1958,** *80* (2), 1339-1348.
48. Dreyer, D. R.; Park, S.; Bielawski, C. W., et al., The Chemistry of Graphene Oxide. *Chem. Soc. Rev.* **2010,** *39* (1), 228-240.
49. Zhu, Y. W.; Murali, S.; Cai, W. W., et al., Graphene and Graphene Oxide: Synthesis, Properties, and Applications. *Adv. Mater.* **2010,** *22* (35), 3906-3924.
50. Dave, S. H.; Gong, C.; Robertson, A. W., et al., Chemistry and Structure of Graphene Oxide Via Direct Imaging. *ACS Nano* **2016,** *10* (8), 7515-7522.
51. Hofmann, U.; Holst, R., Über Die Säurenatur Und Die Methylierung Von Graphitoxyd. *Berichte der deutschen chemischen Gesellschaft (A and B Series)* **1939,** *72* (4), 754-771.
52. Ruess, G., Über Das Graphitoxyhydroxyd (Graphitoxyd). *Monatshefte für Chemie und verwandte Teile anderer Wissenschaften* **1947,** *76* (3-5), 381-417.
53. Lerf, A.; He, H. Y.; Forster, M., et al., Structure of Graphite Oxide Revisited. *The Journal of Physical Chemistry B* **1998,** *102* (23), 4477-4482.
54. Szabó, T.; Berkesi, O.; Forgó, P., et al., Evolution of Surface Functional Groups in a Series of Progressively Oxidized Graphite Oxides. *Chem. Mater.* **2006,** *18* (11), 2740-2749.
55. Dimiev, A. M.; Alemany, L. B.; Tour, J. M., Graphene Oxide. Origin of Acidity, Its Instability in Water, and a New Dynamic Structural Model. *ACS Nano* **2013,** *7* (1), 576-588.
56. Green, N. S.; Norton, M. L., Interactions of DNA with Graphene and Sensing Applications of Graphene Field-Effect Transistor Devices: A Review. *Anal. Chim. Acta* **2015,** *853*, 127-142.
57. Lin, L.; Liao, L.; Yin, J., et al., Building Graphene P–N Junctions for Next-Generation Photodetection. *Nano Today* **2015,** *10* (6), 701-716.
58. Singh, E.; Nalwa, H. S., Stability of Graphene-Based Heterojunction Solar Cells. *RSC Advances* **2015,** *5* (90), 73575-73600.

59. Sun, Y.; Zhang, W.; Chi, H., et al., Recent Development of Graphene Materials Applied in Polymer Solar Cell. *Renewable and Sustainable Energy Reviews* **2015,** *43*, 973-980.
60. Choi, H.; Yoon, H., Nanostructured Electrode Materials for Electrochemical Capacitor Applications. *Nanomaterials* **2015,** *5* (2), 906.
61. Fan, X.; Chen, X.; Dai, L., 3D Graphene Based Materials for Energy Storage. *Current Opinion in Colloid & Interface Science* **2015,** *20* (5–6), 429-438.
62. Mombeshora, E. T.; Nyamori, V. O., A Review on the Use of Carbon Nanostructured Materials in Electrochemical Capacitors. *International Journal of Energy Research* **2015,** *39* (15), 1955-1980.
63. Adhikari, B.-R.; Govindhan, M.; Chen, A., Carbon Nanomaterials Based Electrochemical Sensors/Biosensors for the Sensitive Detection of Pharmaceutical and Biological Compounds. *Sensors* **2015,** *15* (9), 22490.
64. Kumar, S.; Ahlawat, W.; Kumar, R., et al., Graphene, Carbon Nanotubes, Zinc Oxide and Gold as Elite Nanomaterials for Fabrication of Biosensors for Healthcare. *Biosens. Bioelectron.* **2015,** *70*, 498-503.
65. Wang, Z.; Yu, J.; Gui, R., et al., Carbon Nanomaterials-Based Electrochemical Aptasensors. *Biosens. Bioelectron.* **2016,** *79*, 136-149.
66. Dao, T. D.; Lee, H.-i.; Jeong, H. M., et al., Direct Covalent Modification of Thermally Exfoliated Graphene Forming Functionalized Graphene Stably Dispersible in Water and Poly(Vinyl Alcohol). *Colloid. Polym. Sci.* **2013,** *291* (10), 2365-2374.
67. Hsiao, S.-T.; Ma, C.-C. M.; Tien, H.-W., et al., Effect of Covalent Modification of Graphene Nanosheets on the Electrical Property and Electromagnetic Interference Shielding Performance of a Water-Borne Polyurethane Composite. *ACS Applied Materials & Interfaces* **2015,** *7* (4), 2817-2826.
68. Myung, S.; Yin, P. T.; Kim, C., et al., Label-Free Polypeptide-Based Enzyme Detection Using a Graphene-Nanoparticle Hybrid Sensor. *Adv. Mater.* **2012,** *24* (45), 6081-6087.
69. Chia, J. S. Y.; Tan, M. T. T.; Khiew, P. S., et al., A Bio-Electrochemical Sensing Platform for Glucose Based on Irreversible, Non-Covalent Pi–Pi Functionalization of Graphene Produced Via a Novel, Green Synthesis Method. *Sensors and Actuators B: Chemical* **2015,** *210*, 558-565.
70. Wang, J.; Zhao, Y.; Ma, F.-X., et al., Synthesis of a Hydrophilic Poly-L-Lysine/Graphene Hybrid through Multiple Non-Covalent Interactions for Biosensors. *Journal of Materials Chemistry B* **2013,** *1* (10), 1406-1413.
71. Yangqiao, L.; Lian, G.; Jing, S., et al., Stable Nafion-Functionalized Graphene Dispersions for Transparent Conducting Films. *Nanotechnology* **2009,** *20* (46), 465605.
72. Lim, C. X.; Hoh, H. Y.; Ang, P. K., et al., Direct Voltammetric Detection of DNA and pH Sensing on Epitaxial Graphene: An Insight into the Role of Oxygenated Defects. *Analytical Chemistry* **2010,** *82* (17), 7387-7393.
73. Sharma, R.; Baik, J. H.; Perera, C. J., et al., Anomalously Large Reactivity of Single Graphene Layers and Edges toward Electron Transfer Chemistries. *Nano Lett.* **2010,** *10* (2), 398-405.
74. Brownson, D. A. C.; Munro, L. J.; Kampouris, D. K., et al., Electrochemistry of Graphene: Not Such a Beneficial Electrode Material? *RSC Advances* **2011,** *1* (6), 978-988.
75. Edwards, M. A.; Bertoncello, P.; Unwin, P. R., Slow Diffusion Reveals the Intrinsic Electrochemical Activity of Basal Plane Highly Oriented Pyrolytic Graphite Electrodes. *The Journal of Physical Chemistry C* **2009,** *113* (21), 9218-9223.

76. Lai, S. C. S.; Patel, A. N.; McKelvey, K., et al., Definitive Evidence for Fast Electron Transfer at Pristine Basal Plane Graphite from High-Resolution Electrochemical Imaging. *Angew. Chem. Int. Ed.* **2012,** *51* (22), 5405-5408.
77. Patel, A. N.; Collignon, M. G.; O'Connell, M. A., et al., A New View of Electrochemistry at Highly Oriented Pyrolytic Graphite. *J. Am. Chem. Soc.* **2012,** *134* (49), 20117-20130.
78. Ebejer, N.; Gueell, A. G.; Lai, S. C. S., et al., Scanning Electrochemical Cell Microscopy: A Versatile Technique for Nanoscale Electrochemistry and Functional Imaging. *Annual Review of Analytical Chemistry, Vol 6* **2013,** *6*, 329-351.
79. Patel, A. N.; Tan, S.-y.; Unwin, P. R., Epinephrine Electro-Oxidation Highlights Fast Electrochemistry at the Graphite Basal Surface. *Chem. Commun.* **2013,** *49* (78), 8776-8778.
80. Gueell, A. G.; Ebejer, N.; Snowden, M. E., et al., Structural Correlations in Heterogeneous Electron Transfer at Monolayer and Multilayer Graphene Electrodes. *J. Am. Chem. Soc.* **2012,** *134* (17), 7258-7261.
81. Miller, T. S.; Ebejer, N.; Gueell, A. G., et al., Electrochemistry at Carbon Nanotube Forests: Sidewalls and Closed Ends Allow Fast Electron Transfer. *Chem. Commun.* **2012,** *48* (60), 7435-7437.
82. Gueell, A. G.; Meadows, K. E.; Dudin, P. V., et al., Mapping Nanoscale Electrochemistry of Individual Single-Walled Carbon Nanotubes. *Nano Lett.* **2014,** *14* (1), 220-224.
83. Rowley-Neale, S. J.; Brownson, D. A. C.; Banks, C. E., Defining the Origins of Electron Transfer at Screen-Printed Graphene-Like and Graphite Electrodes: MoO_2 Nanowire Fabrication on Edge Plane Sites Reveals Electrochemical Insights. *Nanoscale* **2016,** *8* (33), 15241-15251.
84. Li, Z.; Wang, Y.; Kozbial, A., et al., Effect of Airborne Contaminants on the Wettability of Supported Graphene and Graphite. *Nat Mater* **2013,** *12* (10), 925-931.
85. McDermott, C. A.; Kneten, K. R.; McCreery, R. L., Electron Transfer Kinetics of Aquated $Fe^{+3/+2}$, $Eu^{+3/+2}$, and $V^{+3/+2}$ at Carbon Electrodes: Inner Sphere Catalysis by Surface Oxides. *J. Electrochem. Soc.* **1993,** *140* (9), 2593-2599.
86. Chen, P.; Fryling, M. A.; McCreery, R. L., Electron Transfer Kinetics at Modified Carbon Electrode Surfaces: The Role of Specific Surface Sites. *Analytical Chemistry* **1995,** *67* (18), 3115-3122.
87. Chen, P.; McCreery, R. L., Control of Electron Transfer Kinetics at Glassy Carbon Electrodes by Specific Surface Modification. *Analytical Chemistry* **1996,** *68* (22), 3958-3965.
88. McCreery, R. L., Advanced Carbon Electrode Materials for Molecular Electrochemistry. *Chem. Rev.* **2008,** *108* (7), 2646-2687.
89. Li, W.; Tan, C.; Lowe, M. A., et al., Electrochemistry of Individual Monolayer Graphene Sheets. *ACS Nano* **2011,** *5* (3), 2264-2270.
90. Punckt, C.; Pope, M. A.; Liu, Y. M., et al., Structure-Dependent Electrochemistry of Reduced Graphene Oxide Monolayers. *J. Electrochem. Soc.* **2016,** *163* (7), H491-H498.
91. Zhang, H.; Bo, X.; Guo, L., Electrochemical Preparation of Porous Graphene and Its Electrochemical Application in the Simultaneous Determination of Hydroquinone, Catechol, and Resorcinol. *Sensors and Actuators B: Chemical* **2015,** *220*, 919-926.
92. Li, S.-J.; Xing, Y.; Deng, D.-H., et al., A Comparative Study of Different Types of Reduced Graphene Oxides as Electrochemical Sensing Platforms for Hydroquinone and Catechol. *J. Solid State Electrochem.* **2015,** *19* (3), 861-870.
93. Robledo, S. N.; López, J. C.; Granero, A. M., et al., Characterization of the Surface Redox Process of Caffeic Acid Adsorbed at Glassy Carbon Electrodes

Modified with Partially Reduced Graphene Oxide. *J. Electroanal. Chem.* **2016,** *783*, 258-267.
94. Bagheri, H.; Hajian, A.; Rezaei, M., et al., Composite of Cu Metal Nanoparticles-Multiwall Carbon Nanotubes-Reduced Graphene Oxide as a Novel and High Performance Platform of the Electrochemical Sensor for Simultaneous Determination of Nitrite and Nitrate. *J. Hazard. Mater.* **2017,** *324, Part B*, 762-772.
95. Haldorai, Y.; Yeon, S.-H.; Huh, Y. S., et al., Electrochemical Determination of Tryptophan Using a Glassy Carbon Electrode Modified with Flower-Like Structured Nanocomposite Consisting of Reduced Graphene Oxide and SnO_2. *Sensors and Actuators B: Chemical* **2017,** *239*, 1221-1230.
96. Punckt, C.; Pope, M. A.; Aksay, I. A., High Selectivity of Porous Graphene Electrodes Solely Due to Transport and Pore Depletion Effects. *The Journal of Physical Chemistry C* **2014,** *118* (39), 22635-22642.
97. Pumera, M.; Ambrosi, A.; Chng, E. L. K., Impurities in Graphenes and Carbon Nanotubes and Their Influence on the Redox Properties. *Chemical Science* **2012,** *3* (12), 3347-3355.
98. Wang, L.; Chua, C. K.; Khezri, B., et al., Remarkable Electrochemical Properties of Electrochemically Reduced Graphene Oxide Towards Oxygen Reduction Reaction Are Caused by Residual Metal-Based Impurities. *Electrochem. Commun.* **2016,** *62*, 17-20.
99. Ambrosi, A.; Chua, C. K.; Khezri, B., et al. In *Chemically Reduced Graphene Contains Inherent Metallic Impurities Present in Parent Natural and Synthetic Graphite*, Proc Natl Acad Sci U S A, Aug 7; 2012; pp 12899-904.
100. Stankovich, S.; Dikin, D. A.; Piner, R. D., et al., Synthesis of Graphene-Based Nanosheets Via Chemical Reduction of Exfoliated Graphite Oxide. *Carbon* **2007,** *45* (7), 1558-1565.
101. Si, Y.; Samulski, E. T., Synthesis of Water Soluble Graphene. *Nano Lett.* **2008,** *8* (6), 1679-1682.
102. Ren, P. G.; Yan, D. X.; Ji, X., et al., Temperature Dependence of Graphene Oxide Reduced by Hydrazine Hydrate. *Nanotechnology* **2011,** *22* (5).
103. Fujimoto, Y.; Saito, S., Formation, Stabilities, and Electronic Properties of Nitrogen Defects in Graphene. *Physical Review B* **2011,** *84* (24), 245446.
104. Compton, O. C.; Nguyen, S. T., Graphene Oxide, Highly Reduced Graphene Oxide, and Graphene: Versatile Building Blocks for Carbon-Based Materials. *Small* **2010,** *6* (6), 711-23.
105. Kim, Y.-R.; Bong, S.; Kang, Y.-J., et al., Electrochemical Detection of Dopamine in the Presence of Ascorbic Acid Using Graphene Modified Electrodes. *Biosens. Bioelectron.* **2010,** *25* (10), 2366-2369.
106. Du, H.; Ye, J.; Zhang, J., et al., A Voltammetric Sensor Based on Graphene-Modified Electrode for Simultaneous Determination of Catechol and Hydroquinone. *J. Electroanal. Chem.* **2011,** *650* (2), 209-213.
107. Rosillo-Lopez, M.; Lee, T. J.; Bella, M., et al., Formation and Chemistry of Carboxylic Anhydrides at the Graphene Edge. *RSC Advances* **2015,** *5* (126), 104198-104202.
108. McNaught, A. D.; Wilkinson, A., *IUPAC. Compendium of Chemical Terminology (the "Gold Book")*. 2nd ed.; Blackwell Scientific Publications: Oxford, 1997.
109. Mkhoyan, K. A.; Contryman, A. W.; Silcox, J., et al., Atomic and Electronic Structure of Graphene-Oxide. *Nano Lett.* **2009,** *9* (3), 1058-1063.
110. Lounasvuori, M. M.; Rosillo-Lopez, M.; Salzmann, C. G., et al., Electrochemical Characterisation of Graphene Nanoflakes with Functionalised Edges. *Faraday Discussions* **2014,** *172* ( ), 293-310.

111. Veerapandian, M.; Lee, M.-H.; Krishnamoorthy, K., et al., Synthesis, Characterization and Electrochemical Properties of Functionalized Graphene Oxide. *Carbon* **2012,** *50* (11), 4228-4238.
112. Kauppila, J.; Kunnas, P.; Damlin, P., et al., Electrochemical Reduction of Graphene Oxide Films in Aqueous and Organic Solutions. *Electrochim. Acta* **2013,** *89*, 84-89.
113. Krishnamoorthy, K.; Veerapandian, M.; Yun, K., et al., The Chemical and Structural Analysis of Graphene Oxide with Different Degrees of Oxidation. *Carbon* **2013,** *53* (0), 38-49.
114. Zhang, C.; Dabbs, D. M.; Liu, L.-M., et al., Combined Effects of Functional Groups, Lattice Defects, and Edges in the Infrared Spectra of Graphene Oxide. *The Journal of Physical Chemistry C* **2015,** *119* (32), 18167-18176.
115. Hutton, L. A.; Iacobini, J. G.; Bitziou, E., et al., Examination of the Factors Affecting the Electrochemical Performance of Oxygen-Terminated Polycrystalline Boron-Doped Diamond Electrodes. *Analytical Chemistry* **2013,** *85* (15), 7230-7240.
116. Balapanuru, J.; Yang, J.-X.; Xiao, S., et al., A Graphene Oxide–Organic Dye Ionic Complex with DNA-Sensing and Optical-Limiting Properties. *Angew. Chem. Int. Ed.* **2010,** *49* (37), 6549-6553.
117. Qiu J, Z. R., Li J, Sang Y, Tang W, Rivera Gil P, Liu H, Fluorescent Graphene Quantum Dots as Traceable, pH-Sensitive Drug Delivery Systems. *International Journal of Nanomedicine* **2015,** *10* (1), 6709—6724.
118. Cañizares, P.; García-Gómez, J.; Lobato, J., et al., Electrochemical Oxidation of Aqueous Carboxylic Acid Wastes Using Diamond Thin-Film Electrodes. *Industrial & Engineering Chemistry Research* **2003,** *42* (5), 956-962.
119. Coleman, J. P., The Electrochemistry of Carboxylic Acids and Derivatives: Cathodic Reductions. In *Acid Derivatives: Volume 2 (1979)*, Patai, S., Ed. John Wiley & Sons, Ltd.: Chichester, UK, 1979; pp 781-824.
120. Shao, Y.; Wang, J.; Engelhard, M., et al., Facile and Controllable Electrochemical Reduction of Graphene Oxide and Its Applications. *J. Mater. Chem.* **2010,** *20* (4), 743-748.
121. White, H. S.; Peterson, J. D.; Cui, Q., et al., Voltammetric Measurement of Interfacial Acid/Base Reactions. *The Journal of Physical Chemistry B* **1998,** *102* (16), 2930-2934.
122. Burgess, I.; Seivewright, B.; Lennox, R. B., Electric Field Driven Protonation/Deprotonation of Self-Assembled Monolayers of Acid-Terminated Thiols. *Langmuir* **2006,** *22* (9), 4420-4428.
123. Rosendahl, S. M.; Burgess, I. J., Electrochemical and Infrared Spectroscopy Studies of 4-Mercaptobenzoic Acid SAMs on Gold Surfaces. *Electrochim. Acta* **2008,** *53* (23), 6759-6767.
124. Wang, M.; Xiao, F.-N.; Wang, K., et al., Electric Field Driven Protonation/Deprotonation of 3,4,9,10-Perylene Tetracarboxylic Acid Immobilized on Graphene Sheets Via Π–Π Stacking. *J. Electroanal. Chem.* **2013,** *688*, 304-307.
125. Smith, C. P.; White, H. S., Voltammetry of Molecular Films Containing Acid/Base Groups. *Langmuir* **1993,** *9* (1), 1-3.
126. Andreu, R.; Fawcett, W. R., Discreteness-of-Charge Effects at Molecular Films Containing Acid/Base Groups. *The Journal of Physical Chemistry* **1994,** *98* (48), 12753-12758.
127. Fawcett, W. R.; Fedurco, M.; Kovacova, Z., Double Layer Effects at Molecular Films Containing Acid/Base Groups. *Langmuir* **1994,** *10* (7), 2403-2408.
128. Luque, A. M.; Mulder, W. H.; Calvente, J. J., et al., Proton Transfer Voltammetry at Electrodes Modified with Acid Thiol Monolayers. *Analytical Chemistry* **2012,** *84* (13), 5778-5786.

129. Gan, S.; Zhong, L.; Gao, L., et al., Electrochemically Driven Surface-Confined Acid/Base Reaction for an Ultrafast H^+ Supercapacitor. *J. Am. Chem. Soc.* **2016**.
130. Sugihara, K.; Shimazu, K.; Uosaki, K., Electrode Potential Effect on the Surface pK_a of a Self-Assembled 15-Mercaptohexadecanoic Acid Monolayer on a Gold/Quartz Crystal Microbalance Electrode. *Langmuir* **2000,** *16* (18), 7101-7105.
131. Futamata, M., Characterization of the First Layer and Second Layer Adsorbates on Au Electrodes Using ATR-IR Spectroscopy. *J. Electroanal. Chem.* **2003,** *550–551*, 93-103.
132. Goutev, N.; Futamata, M., Attenuated Total Reflection Surface-Enhanced Infrared Absorption Spectroscopy of Carboxyl Terminated Self-Assembled Monolayers on Gold. *Appl. Spectrosc.* **2003,** *57* (5), 506-513.
133. Luque, A. M.; Cuesta, A.; Calvente, J. J., et al., Potentiostatic Infrared Titration of 11-Mercaptoundecanoic Acid Monolayers. *Electrochem. Commun.* **2014,** *45*, 13-16.
134. Alizadeh, T.; Azizi, S., Graphene/Graphite Paste Electrode Incorporated with Molecularly Imprinted Polymer Nanoparticles as a Novel Sensor for Differential Pulse Voltammetry Determination of Fluoxetine. *Biosens. Bioelectron.* **2016,** *81*, 198-206.
135. Heidari, H.; Habibi, E., Amperometric Enzyme-Free Glucose Sensor Based on the Use of a Reduced Graphene Oxide Paste Electrode Modified with Electrodeposited Cobalt Oxide Nanoparticles. *Microchimica Acta* **2016,** *183* (7), 2259-2266.
136. Fu, K.; Wang, Y.; Yan, C., et al., Graphene Oxide-Based Electrode Inks for 3D-Printed Lithium-Ion Batteries. *Adv. Mater.* **2016,** *28* (13), 2587-2594.
137. Li, C.; Guo, B.; Guo, X. M., et al., The Electrochemical Sensor Based on Electrochemical Oxidation of Nitrite on Metalloporphyrin-Graphene Modified Glassy Carbon Electrode. *RSC Advances* **2016,** *6* (93), 90480-90488.
138. Madou, M. J., *Fundamentals of Microfabrication and Nanotechnology Volume II. Manufacturing Techniques for Microfabrication and Nanotechnology*. CRC Press: Boca Raton, 2011.
139. Krebs, F. C., Fabrication and Processing of Polymer Solar Cells: A Review of Printing and Coating Techniques. *Sol. Energy Mater. Sol. Cells* **2009,** *93* (4), 394-412.
140. Hanaei, H.; Assadi, M. K.; Saidur, R., Highly Efficient Antireflective and Self-Cleaning Coatings That Incorporate Carbon Nanotubes (CNTs) into Solar Cells: A Review. *Renewable and Sustainable Energy Reviews* **2016,** *59*, 620-635.
141. Eccher, J.; Zajaczkowski, W.; Faria, G. C., et al., Thermal Evaporation Versus Spin-Coating: Electrical Performance in Columnar Liquid Crystal OLEDs. *ACS Applied Materials & Interfaces* **2015,** *7* (30), 16374-16381.
142. Wang, D.; Noël, V.; Piro, B., Electrolytic Gated Organic Field-Effect Transistors for Application in Biosensors—a Review. *Electronics* **2016,** *5* (1), 9-32.
143. Bard, A. J.; Faulkner, L. R.; Leddy, J., *Electrochemical Methods : Fundamentals and Applications*. 2nd ed.; Wiley: New York ; Chichester, 2001; p xxi, 833 p.
144. Goldmann, C.; Lazzari, R.; Paquez, X., et al., Charge Transfer at Hybrid Interfaces: Plasmonics of Aromatic Thiol-Capped Gold Nanoparticles. *ACS Nano* **2015,** *9* (7), 7572-7582.
145. Love, J. C.; Estroff, L. A.; Kriebel, J. K., et al., Self-Assembled Monolayers of Thiolates on Metals as a Form of Nanotechnology. *Chem. Rev.* **2005,** *105* (4), 1103-1170.
146. Liu, L.; Mei, A.; Liu, T., et al., Fully Printable Mesoscopic Perovskite Solar Cells with Organic Silane Self-Assembled Monolayer. *J. Am. Chem. Soc.* **2015,** *137* (5), 1790-1793.

147. Hoque, E.; Derose, J. A.; Hoffmann, P., et al., Phosphonate Self-Assembled Monolayers on Aluminum Surfaces. *The Journal of chemical physics* **2006,** *124* (17), 174710.
148. Bhadra, P.; Shajahan, M. S.; Bhattacharya, E., et al., Studies on Varying n-Alkanethiol Chain Lengths on a Gold Coated Surface and Their Effect on Antibody-Antigen Binding Efficiency. *RSC Advances* **2015,** *5* (98), 80480-80487.
149. Srinivasan, U.; Houston, M. R.; Howe, R. T., et al., Alkyltrichlorosilane-Based Self-Assembled Monolayer Films for Stiction Reduction in Silicon Micromachines. *Journal of Microelectromechanical Systems* **1998,** *7* (2), 252-260.
150. Yuan, L.; Thompson, D.; Cao, L., et al., One Carbon Matters: The Origin and Reversal of Odd–Even Effects in Molecular Diodes with Self-Assembled Monolayers of Ferrocenyl-Alkanethiolates. *The Journal of Physical Chemistry C* **2015,** *119* (31), 17910-17919.
151. Ulman, A., Formation and Structure of Self-Assembled Monolayers. *Chem. Rev.* **1996,** *96* (4), 1533-1554.
152. Creager, S. E.; Rowe, G. K., Competitive Self-Assembly and Electrochemistry of Some Ferrocenyl-n-Alkanethiol Derivatives on Gold. *J. Electroanal. Chem.* **1994,** *370* (1), 203-211.
153. Laibinis, P. E.; Whitesides, G. M.; Allara, D. L., et al., Comparison of the Structures and Wetting Properties of Self-Assembled Monolayers of n-Alkanethiols on the Coinage Metal Surfaces, Copper, Silver, and Gold. *J. Am. Chem. Soc.* **1991,** *113* (19), 7152-7167.
154. Murugan, P.; Krishnamurthy, M.; Jaisankar, S. N., et al., Controlled Decoration of the Surface with Macromolecules: Polymerization on a Self-Assembled Monolayer (SAM). *Chem. Soc. Rev.* **2015,** *44* (10), 3212-3243.
155. Arima, Y.; Iwata, H., Preferential Adsorption of Cell Adhesive Proteins from Complex Media on Self-Assembled Monolayers and Its Effect on Subsequent Cell Adhesion. *Acta Biomaterialia* **2015,** *26*, 72-81.
156. Maroni, P.; Montes Ruiz-Cabello, F. J.; Cardoso, C., et al., Adsorbed Mass of Polymers on Self-Assembled Monolayers: Effect of Surface Chemistry and Polymer Charge. *Langmuir* **2015,** *31* (22), 6045-6054.

2 Experimental Theory and Techniques

2.1 Electrochemistry

Electrochemistry studies the relationship between electrical energy and chemical change. In electrochemical systems, a chemical reaction can be harnessed to produce electrical energy, or an external current can be supplied to a system to drive a chemical change. In order for an electrochemical reaction to happen, charge must be transferred across the interface between the different chemical phases of an electrode and an electrolyte. The electrode is a solid electronic conductor, typically metal, carbon or a semiconductor material, whereas the electrolyte is an ionic conductor and can be solid, liquid or plasma.

The electrode-solution interface behaves much like a capacitor. Due to the potential difference between the electrode and the solution, charge q^M accumulates on the electrode surface in the form of excess electrons or holes, depending on the potential

difference. At the same time, charge q^S accumulates in a thin layer of solution next to the electrode in the form of excess anions or cations so that $q^M = -q^S$ [1]. This arrangement of charged species and dipoles at the electrode-solution interface, illustrated in **Figure 2.1**, is called the electrical double layer. On the solution side, the structure of the layer changes with distance from the electrode surface, and this affects the potential profile across the double layer as shown in **Figure 2.1**. The region closest to the electrode is called the Helmholtz layer and it is defined by the inner Helmholtz plane (IHP), the plane through the electrical centres of specifically adsorbed ions. Solvent molecules will also reside in the inner layer. Solvated ions can only approach the electrode to a distance called the outer Helmholt plane (OHP) and they will only interact with the electrode through electrostatic forces. Due to the potential drop through the double layer, the potential experienced by these non-specifically adsorbed, solvated ions at the OHP is less than the potential difference between the electrode and the solution by $\varphi_2 - \varphi^S$. [1]

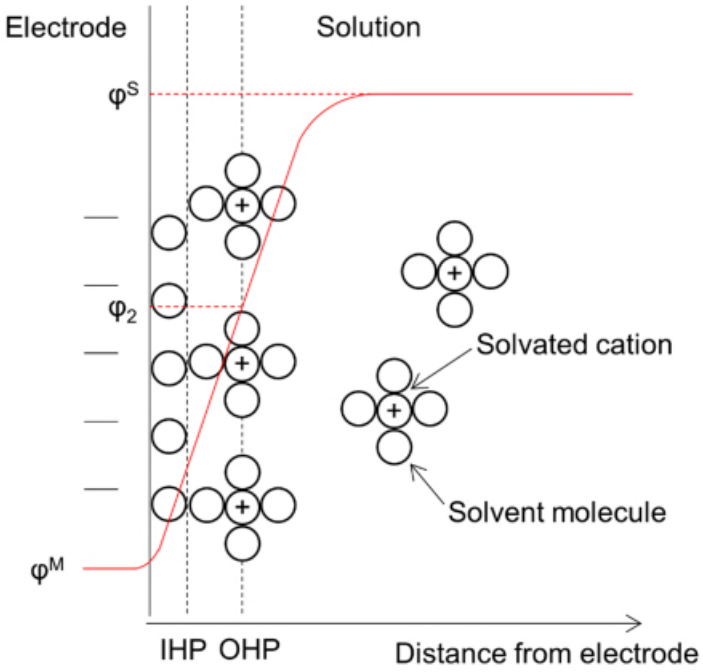

Figure 2.1 A schematic representation of the electric double layer at the electrode-solution interface and the potential profile across the double layer region in the absence of specific adsorption. Adapted from [1] with permission.

The equilibrium of an electrode reaction is characterised by the Nernst equation that relates the electrode potential to the bulk concentrations of the reduced and oxidised species C_{R}^{*} and C_{O}^{*}. For a reaction

$$\mathrm{O} + n\mathrm{e} \rightleftarrows \mathrm{R} \tag{2.1}$$

the Nernst equation is

$$E = E^{0\prime} + \frac{RT}{nF}\ln\frac{C_{\mathrm{O}}^{*}}{C_{\mathrm{R}}^{*}} \tag{2.2}$$

where $E^{0\prime}$ is the formal potential for the reaction. This quantity incorporates the standard potential, E^{0}, and activity coefficients of the reduced and oxidised species, γ_{R} and γ_{O}:

$$E^{0\prime} = E^{0} + \frac{RT}{nF}\ln\frac{\gamma_{\mathrm{O}}}{\gamma_{\mathrm{R}}} \tag{2.3}$$

Experimentally, charge transfer occurring at a single interface cannot be dealt with in isolation; instead, we must introduce multiple interfaces that together form an electrochemical cell [1]. An electrochemical cell usually consists of two or three electrodes and an electrolyte. The working electrode is the electrode at which the reaction of interest is taking place. To be able to define and control the potential of the working electrode, a reference electrode is used. The reference electrode must have a fixed, stable and well-known potential so that any changes in the cell can be ascribed to the working electrode [1]. In order to ensure that the potential of the reference electrode remains stable, a third electrode is introduced called the counter or auxiliary electrode through which the current is passed. A potentiostat is used to control the potential at the working electrode with respect to the reference electrode or the current that flows between the working electrode and the counter electrode.

A supporting electrolyte is used for several reasons. Firstly, it is used to increase the conductivity of the solution, which helps to reduce the so-called *i*R drop, a drop in the potential between the working and reference electrode caused by solution resistance. Secondly, using a supporting electrolyte in excess compared to the electroactive species of interest ensures that practically all current is transported by the electrolyte and thus the contribution of migration to the mass transport of the electroactive species is minimised. Thirdly, by using a suitable supporting electrolyte the ionic strength and pH of the solution can be maintained constant irrespective of reactions occurring at the electrodes. Fourthly, the use of a supporting electrolyte minimises the thickness of the electrical double layer, and therefore the potential drop, at the electrode interface. [1]

2.1.1 Cyclic Voltammetry

CV is a widely used electrochemical technique where the voltage is ramped linearly in time and the resulting current is recorded as a function of potential. A single cyclic voltammogram can give a multitude of information about the kinetics of heterogeneous electron transfer (HET), the thermodynamics of a redox reaction and adsorption processes occurring at the electrode.

Consider the redox couple in Equation (2.1). A CV experiment is carried out initially with only species R in solution. The potential is swept from E_i (usually E_i is chosen at which no electrode reactions occur, in this case sufficiently negative of $E^{0\prime}$ so that R isn't oxidised) to E_λ at rate v (usually in the range of mV s^{-1}). As the potential approaches $E^{0\prime}$, the current begins to increase rapidly as R is oxidised at the electrode to produce O. This depletes R from the vicinity of the electrode surface, creating a concentration gradient that causes R to diffuse towards the electrode. Up until a potential E_{pa} somewhat positive of $E^{0\prime}$, the mass transfer or R to the electrode surface can maintain the ratio of O and R to satisfy the Nernst equation. At E_{pa} the diffusion layer of R becomes so thick that the flux of R to the electrode is no longer fast enough

to support equilibrium concentration of R at the electrode surface. At this point the oxidation becomes controlled by the rate of mass transfer of R and the current begins to decay[1]. When E_λ is reached, the scan rate is switched to $-v$ and the potential is ramped back to E_i. In the reverse sweep, the current response has a similar shape to the forward sweep and can be explained by the same arguments of mass transfer rate and concentration gradient. The potential sweep and resulting cyclic voltammogram are depicted in **Figure 2.2**.

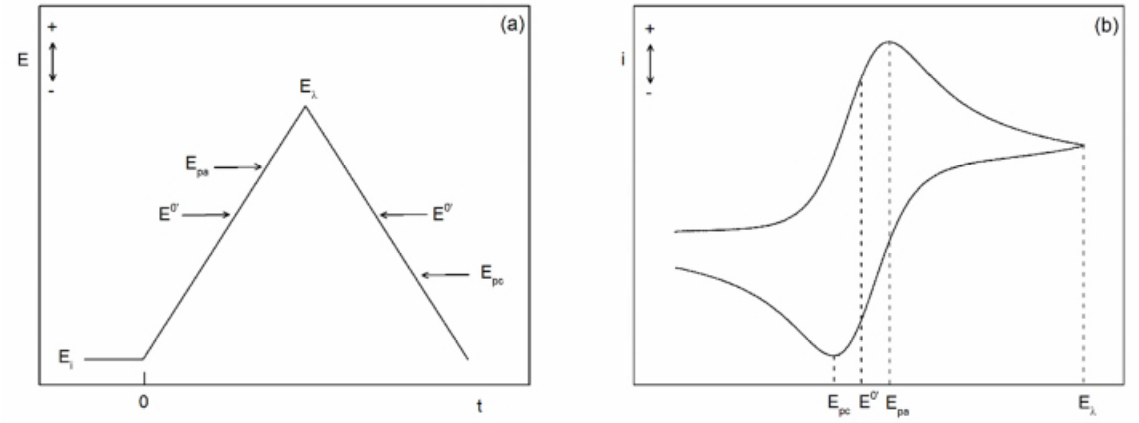

Figure 2.2 Waveforms in cyclic voltammetry. (a) Potential as a function of time, (b) current as a function of potential. Adapted from [1] with permission.

CV can be used to assess the reversibility of a reaction. For a Nernstian reaction, the separation of peak potentials, ΔE_p, is given by Equation (2.4)

$$\Delta E_p = | E_{pa} - E_{pc} | \approx \frac{2.3RT}{nF} \qquad (2.4)$$

Equation (2.4) gives $\Delta E_p = 59/n$ mV at 25 °C. If the standard heterogeneous electron transfer rate constant k^0 is very low, a large overpotential η is required before current begins to flow and the peak potentials are pushed further apart. Therefore, ΔE_p that increases with increasing scan rate is indicative of slow HET.

[1] At an electrode smaller than the scale of the diffusion layer the current will reach a steady state instead of decaying.

The scan rate is an important parameter not only in qualitative determination of kinetics but also in identifying adsorbed redox species. This can be done because the peak current, i_p, is a function of the scan rate. The Randles-Sevcik equation (2.5) describes i_p for the forward sweep of an electrode reaction involving dissolved species R:

$$i_p = (2.69 \times 10^5) n^{\frac{3}{2}} A C_R^* D_R^{\frac{1}{2}} v^{\frac{1}{2}} \tag{2.5}$$

where A is the electroactive electrode area, C_R^* is the bulk concentration of R, D_R is the diffusion constant of R. It can be seen from Equation (2.5) that for a dissolved species, i_p will vary linearly with $v^{1/2}$. In contrast, for adsorbed species, peak current is given by

$$i_p = \frac{n^2 F^2}{4RT} v A \Gamma_R^* \tag{2.6}$$

where Γ_R^* is the initial amount of adsorbed R. The peak current is now proportional to v and not $v^{1/2}$.

2.1.2 Differential Pulse Voltammetry

Pulse voltammetry techniques were developed as a mechanism to suppress charging currents arising from the expanding mercury drop at a dropping mercury electrode (DME). Pulse methods offer improved sensitivity by sampling the current at a point where the ratio of faradaic current to charging current is largest. In the context of DME, this would occur at the end of drop lifetime just before it is dislodged. Even though pulse techniques originated in a polarographic context, the potential waveforms and measurement strategies are applicable to stationary electrodes and therefore a similar sensitivity improvement can be seen at disc electrodes, making pulse voltammetry particularly suitable for trace analysis [1].

In differential pulse voltammetry, small amplitude pulses are superimposed on a stepped base potential and the current is sampled twice in each step: first at time $t = \tau'$

immediately before the pulse at potential *E* and second at *t* = τ towards the end of the pulse at potential *E* + *ΔE*. The potential waveform for a Nernstian reaction $\mathrm{O} + n\mathrm{e} \rightleftharpoons \mathrm{R}$ is shown in Figure 2.3(a). The current, shown in Figure 2.3(b), is plotted as the difference of the two sampled values:

$$\delta i = i(\tau) - i(\tau') \tag{2.7}$$

The potential step time τ′ is usually around 0.5 to 4 seconds and the pulse width τ − τ′ is 5 to 100 milliseconds [1]. Therefore a thick diffusion layer is established by *t* = τ′, and the pulse can only perturb a small part of it. In effect, the purpose of the base potential is to establish apparent bulk concentrations that vary from pure O to pure R for each potential step.

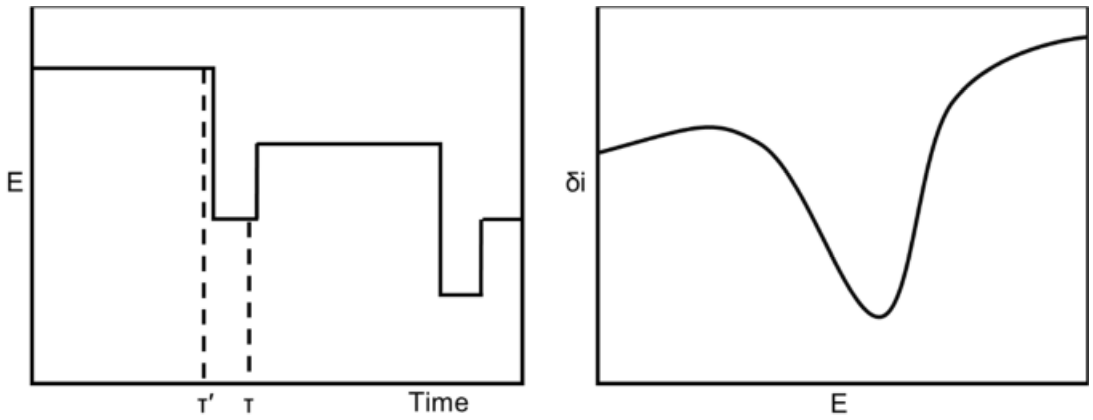

Figure 2.3 (a) Potential waveform for a differential pulse voltammetric experiment showing two full potential steps. (b) Differential current plotted against potential for reaction O + *n*e ⇌ R. Adapted from [1] with permission.

When R is initially absent, the apparent bulk concentrations for the pulse are the surface concentrations at potential *E*:

$$(C_{\mathrm{O}}^{*})_{\mathrm{app}} = C_{\mathrm{O}}(0,t) = C_{\mathrm{O}}^{*}\left(\frac{\xi\theta}{1+\xi\theta}\right) \tag{2.8}$$

$$(C_{R}^{*})_{\mathrm{app}} = C_{\mathrm{R}}(0,t) = C_{\mathrm{O}}^{*}\left(\frac{\xi}{1+\xi\theta}\right) \tag{2.9}$$

Where $\theta = \exp[\frac{nF}{RT}(E - E^{0\prime})]$ and $\xi = (D_{\mathrm{O}}/D_{\mathrm{R}})^{1/2}$. In a Nernstian system $(C_{\mathrm{O}}^{*})_{\mathrm{app}}$ and $(C_{\mathrm{R}}^{*})_{\mathrm{app}}$ are in equilibrium with potential *E*, so the faradaic current flow after a step from *E* to *E* + Δ*E* is:

$$i = \frac{nFAD_{\mathrm{O}}^{1/2}}{\pi^{1/2}t^{1/2}} \cdot \frac{\left[(C_{\mathrm{O}}^{*})_{\mathrm{app}} - \theta'(C_{\mathrm{R}}^{*})_{\mathrm{app}}\right]}{(1+\xi\theta')} \tag{2.10}$$

where $\theta' = \exp[\frac{nF}{RT}(E + \Delta E - E^{0\prime})]$. Substituting Equations (2.8) and (2.9) into (2.10):

$$i = \frac{nFAD_{\mathrm{O}}^{1/2}C_{\mathrm{O}}^{*}}{\pi^{1/2}t^{1/2}} \cdot \frac{(\xi\theta - \xi\theta')}{(1+\xi\theta)(1+\xi\theta')} \tag{2.11}$$

The differential faradaic current in Equation (2.7) is then:

$$\delta i = \frac{nFAD_{\mathrm{O}}^{1/2}C_{\mathrm{O}}^{*}}{\pi^{1/2}(\tau - \tau')^{1/2}} \cdot \frac{(\xi\theta - \xi\theta')}{(1+\xi\theta)(1+\xi\theta')} \tag{2.12}$$

DPV results in a peak current rather than limiting current. This is because the base potential is made more negative at each step. Clearly at the beginning of the experiment no faradaic current flows as $E >> E^{0\prime}$ and a small amplitude pulse is not able to stimulate the reduction of O. As the experiment proceeds past $E^{0\prime}$, the base potential *E* reaches the diffusion limited current region and O is reduced at a maximum rate. A small amplitude pulse is not able to increase the rate further, making the faradaic current component of $i(\tau) - i(\tau')$ equal to zero. Only close to $E^{0\prime}$ can a small Δ*E* stimulate a significant δ*i*.

The magnitude of ΔE controls the maximum δi, with larger $|\Delta E|$ giving higher δi_{max}. However, increasing $|\Delta E|$ also increases the width of the peak, meaning the resolution becomes objectionably poor at $|\Delta E| > 100$ mV [1].

2.2 Infrared Spectroscopy

Infrared is electromagnetic radiation extending from 1 mm to 750 nm and is further divided into far-, mid- and near-infrared regions. Higher energy near-infrared light is closer to visible light in frequency and can excite a molecule to a second or third excited state, referred to as an overtone, whereas at the lower end of the infrared region far-infrared is used for rotational spectroscopy. Mid-infrared frequencies, usually given in wavenumbers, span the region between 4000 and 400 cm^{-1} and are used to study fundamental vibrations.

Interatomic bonds in molecules have different modes of vibrations that absorb at specific frequencies. When IR light is passed through a sample, it may interact with a covalent bond in the sample and lose intensity as photons are absorbed by the sample. The resulting absorbance spectrum will show a peak at the wavenumber at which the absorption occurred.

Bond vibrations can be described in terms of a simple harmonic oscillator. The fundamental vibrational frequency ν is given by:

$$\nu = \frac{1}{2\pi c}\sqrt{\frac{\kappa}{\mu}} \tag{2.13}$$

where κ is the force constant and μ is the reduced mass of two atoms with masses m_1 and m_2:

$$\mu = \frac{m_1 m_2}{m_1 + m_2} \tag{2.14}$$

Transitions between the ground state and the first vibrational quantum level are virtually unaffected by anharmonicity, although when studying overtones at higher frequencies anharmonicity will begin to influence the transitions and must be taken into account.

The minimum set of fundamental vibrations, known as the normal modes, are described in terms of coordinate axes in three-dimensional space, and all possible variants of vibrational motion can be reduced to this minimum set. The number of normal modes of vibration for a molecule with N atoms is given by $3N - 5$ for linear molecules, and $3N - 6$ for non-linear molecules. According to this rule, a CO_2 molecule has 4 vibrations and a H_2O molecule has 3.

A vibrational mode is IR active if it causes a change in the dipole moment of the molecule. A symmetric diatomic molecule such as N_2 is not IR active as there is no change in the dipole moment, whereas H_2O and CO_2 have both IR active and IR inactive normal modes. These are illustrated in **Figure 2.4**. In **Figure 2.4**(a), the first two panels show the stretching modes and the panel on the right shows the bending mode of a water molecule. The out-of-plane stretch on the left causes a change in the dipole moment of the molecule and hence the vibration is IR active, whereas the in-plane stretching mode in the middle is IR inactive as there is no change in the dipole moment. The bending mode shown in the right-hand panel is also IR active due to the change in the dipole moment of the molecule. Correspondingly, the normal modes of CO_2 are shown in **Figure 2.4**(b). The first two panels from the left illustrate the IR active asymmetric stretching mode and the IR inactive symmetric stretching mode, respectively. The last two panels show the two IR active, mutually perpendicular bending modes.

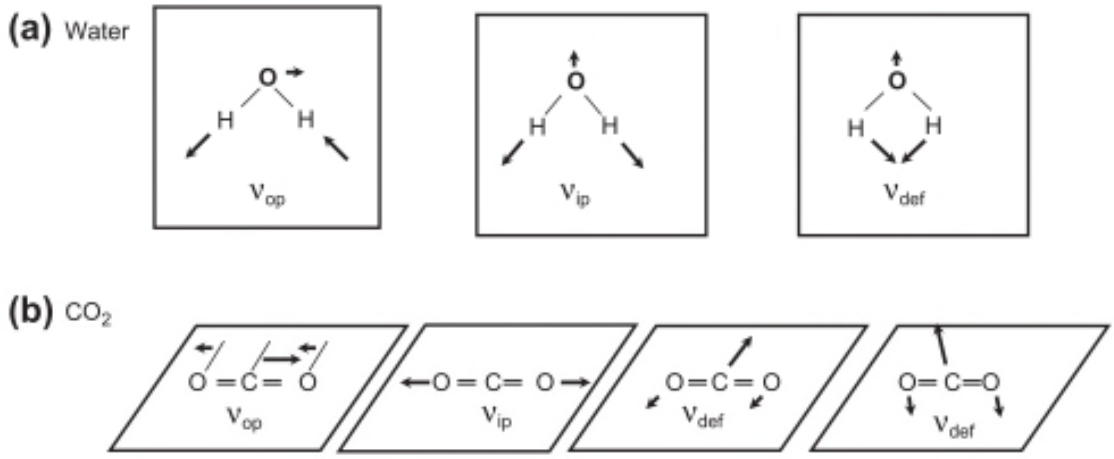

Figure 2.4 Stretching and bending modes of (a) water and (b) CO_2 molecule. Reproduced from [2] with permission.

2.2.1 Attenuated Total Reflectance

In the attenuated total reflectance configuration (**Figure 2.5**), an infrared beam is directed into a crystal made of a material that has a high refractive index. Due to the different refractive indices of the ATR crystal and the medium in contact with the crystal, the angle of the IR beam can be set so that it exceeds the critical angle at which total internal reflection occurs. The internal reflection creates an evanescent wave that extends orthogonally beyond the surface of the crystal. If a sample is placed into contact with the crystal, some of the energy in the evanescent wave is absorbed by the sample. The attenuated energy is passed back to the IR beam and back to the detector. By recording a background of a clean ATR crystal and subtracting that from the sample spectrum, an absorbance spectrum of the sample can be obtained.

The IR beam enters the ATR crystal with an angle of incidence, θ. Due to the differences in refractive indices, the angle of refraction, r, will differ from θ according to Snell's Law.

$$\frac{\sin\theta}{\sin r} = \frac{n_2}{n_1} \tag{2.15}$$

where n_1 and n_2 are the refractive indices of the ATR crystal and the sample, respectively. The critical angle θ_c is the angle at which r is equal to 90° and it follows from Equation (2.15) that

$$\theta_c = sin^{-1}\left(\frac{n_2}{n_1}\right) \tag{2.16}$$

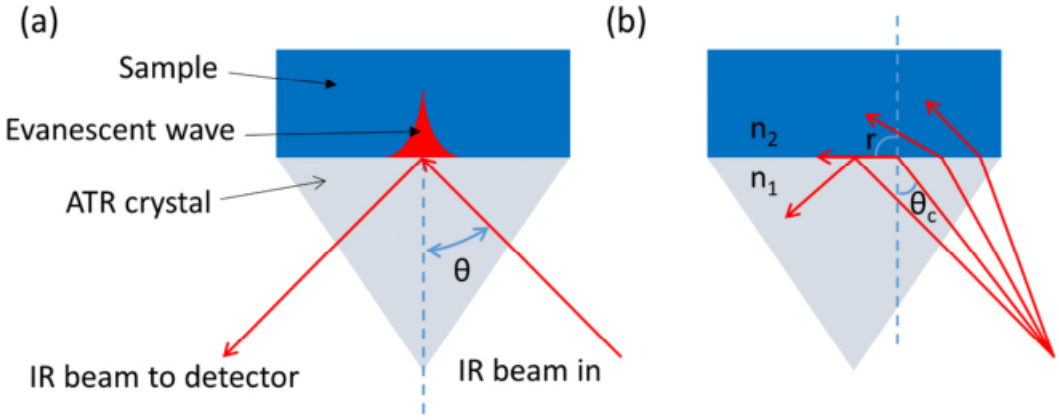

Figure 2.5 (a) Graphical representation of the evanescent wave. (b) Variation of the angle of refraction (r) with the angle of incidence (θ). The critical angle θ_c is the angle of incidence that leads to r = 90°. Adapted from [2] and [3] with permission.

Refractive indices are wavelength-dependent and are usually measured using the doublet sodium D line at 589 nm. For a diamond ATR crystal in contact with water, θ_c at mid-IR frequencies is ca. 34°.

The graphical depiction of the evanescent wave in Figure 2.5(a) shows that the wave doesn't extend very far from the ATR surface; instead, the intensity I of the wave decays exponentially with distance:

$$I = I_0^{-\frac{z}{d_p}} \tag{2.17}$$

where z is the distance normal to the ATR surface, I_0 the intensity at z = 0, and d_p is the penetration depth. d_p is defined as the distance at which the electric field amplitude

falls to 1/e of the value at the surface and it depends on the wavelength of the light (λ), θ, and the refractive indices of the two phases:

$$d_{\mathrm{p}} = \frac{\lambda}{2\pi(n_1^2 \sin^2\theta - n_2^2)^{\frac{1}{2}}} \tag{2.18}$$

Table 2.1 lists values of d_{p} at wavelengths in the mid-infrared region together with penetration depths at those wavelengths.

Table 2.1: Tabulated values of d_{p} at a diamond ATR crystal-water interface when θ = 45°. The values of n_1 were found in [4] and the values of n_2 in [5].

n_1	n_2	λ / nm	$\tilde{\nu}$ / cm^{-1}	d_{p} / µm
2.38	1.22	10000	1000	1.38
2.38	1.33	6667	1500	2.32
2.38	1.33	5000	2000	3.09
2.39	1.35	4000	2500	3.96
2.39	1.43	3333	3000	5.39

2.3 Scanning Tunnelling Microscopy

STM is part of a family of scanning probe microscopy (SPM) techniques. All SPM techniques use a sharp probe, with a radius of curvature typically in the nanometres or tens of nanometres, to study the surface properties of a sample. The probe may be in intermittent contact, constant contact, or near-contact with the sample surface, depending on the technique used.

In STM, a bias voltage is applied across the probe and the sample. As the probe approaches the sample, electrons can tunnel across the gap between the tip of the probe and the sample. For electron tunnelling to occur, both the probe and the sample must be made of a conductive or semi-conductive material. The tunnelling current, I_{t}, can be described by the following equation:

$$I_{\mathrm{t}} \propto eV_{\mathrm{b}}^{-\mathrm{c}d} \tag{2.19}$$

Where *e* is the electron charge, V_{b} is a bias voltage between the tip and the surface and *d* is the distance between the tip and the surface. c is a constant for a given material and is given by

$$\mathrm{c} = \frac{2\sqrt{2m_{\mathrm{e}}\phi}}{\hbar} \tag{2.20}$$

where m_{e} is the mass of the electron, φ is the work function and $\hbar$ is Planck's constant. Atomic resolution can be achieved in STM due to the exponential relationship of I_{t} with *d* in Equation (2.19) which means that a 0.1 nm increase in *d* leads to I_{t} decreasing by an order of magnitude.

STM is commonly operated in a constant current mode where a piezoelectric element controls the tip position and moves it along the *z* axis to maintain a constant current while also controlling the movement in the xy-plane for scanning the surface. Because the tunnelling current depends on not only the tip-to-sample distance but also the local density of states in the sample, STM images are a convolution of topography and electronic structure.

As tunnelling current decreases exponentially with distance, the resolution of STM depends on the ability to precisely control the tip-to-sample distance. The technique is therefore very sensitive to vibrations and experimental conditions must be carefully controlled to minimise interference. The tip and sample are placed on a vibration isolation table inside a solid box lined with contoured foam to reduce the impact of acoustic waves. The box is mounted on a table with air-damped feet to maximise isolation from floor vibrations.

2.4 X-ray Photoelectron Spectroscopy

XPS is a surface-sensitive ionisation technique that can be used in elemental, quantitative and surface structure analysis. Soft X-rays with energies in the range of 1-5 keV are used to ionise samples. The photons are sufficiently high in energy to eject core electrons. Since each core atomic orbital is associated with a characteristic binding energy, XPS is a chemically specific technique.

The surface-sensitivity of XPS arises from the emission and detection of the ejected electrons. Even though the penetration depth of the X-rays employed in XPS is measured in micrometres, the overwhelming majority of electrons ejected from the sample at those depths will collide with other atoms in the sample before reaching the surface. These collisions will lead to a loss of energy, making the electrons unable to escape from the sample. Only electrons from the top 4-5 monolayers are likely to be ejected and reach the detector without any energy loss.

When a photon of energy *hv* is incident upon the surface of a sample, the energy can be absorbed by an electron in the sample. If the frequency of excitation is above the work function *φ*, a threshold value representing the energy it takes to remove an electron from the Fermi level to vacuum, photoemission takes place and the electron is ejected with a specific kinetic energy E_K. For a spectrometer with a calibrated work function φ_{sp} and measuring kinetic energy E'_K, the binding energy of the electron, E_B, can be obtained from:

$$E_B = h\nu - \phi_{sp} - E'_K \tag{2.21}$$

If the photon energy is known and the kinetic energy of the ejected electron can be measured, the binding energy of the ejected electron can be calculated.

The observed binding energy of an electron depends on the chemical environment of the atom such as oxidation state and ligand electronegativity. The deviation in binding

energy caused by the environment is known as a chemical shift and it is readily observable in XPS. Therefore XPS can be used as a tool to identify not only elemental composition but also the oxidation state of the elements.

As the XPS signal at a given incident photon energy is proportional to the amount of species on the surface, the technique can be used for quantitative analysis. To determine the composition of the surface, the relative peak intensities are examined. For a homogeneous material with two components, A and B, the ratio of the concentrations is given by equation

$$\frac{[\mathrm{A}]}{[\mathrm{B}]} \approx \frac{I_{\mathrm{A}} S_{\mathrm{B}}}{I_{\mathrm{B}} S_{\mathrm{A}}} \tag{2.22}$$

where *I* is the integrated peak area and *S* is the atomic sensitivity factor. The atomic sensitivity factor is derived empirically for each spectrometer and the values are readily available in literature.

2.5 Transmission Electron Microscopy

The resolution of traditional light microscopes is limited by the wavelength of the light source. To image nanometre-scale specimens, electron microscopy is often used. The de Broglie equation gives a relationship between the wavelength *λ* and momentum *p* of a moving particle:

$$\lambda = \frac{h}{p} \tag{2.23}$$

where *h* is Planck's constant. As the electron velocity approaches the speed of light, the de Broglie equation must be corrected to account for relativistic effects [6]:

$$\lambda_e = \frac{h}{\sqrt{2m_0E\left(1+\frac{E}{2m_0c^2}\right)}} \tag{2.24}$$

where m_0 is the rest mass of the electron, E the energy of the accelerated electron and c the speed of light.

The source of electrons in electron microscopy is called an electron gun. When a high voltage is applied to the gun, electrons will be emitted either by thermionic emission or field emission. The resulting electron beam is accelerated further to achieve higher energy electrons as this shortens the wavelength and therefore improves resolution.

Electromagnetic lenses are used to focus the electron beam, and changes in magnification are achieved by changing the current flowing through the lenses. In TEM, the electron beam is transmitted through a sample, meaning that only very thin specimens can be imaged. The electrons interact with the sample as they pass through and the transmitted beam contains information about electron density, phase and periodicity in the sample. The de Broglie wavelength in a typical electron microscope is in the picometre range, but in practice it is not possible to achieve that kind of resolution due to the limitations of the focusing of the electron beam. The resolution of TEM is typically 2 nm.

References for Chapter 2

1. Bard, A. J.; Faulkner, L. R.; Leddy, J., *Electrochemical Methods : Fundamentals and Applications*. 2nd ed.; Wiley: New York ; Chichester, 2001; p xxi, 833 p.
2. Larkin, P., *Infrared and Raman Spectroscopy : Principles and Spectral Interpretation*. Elsevier: Waltham, MA, 2011.
3. Pike Technologies. ATR – Theory and Applications Application Note. 2011, Http://Www.Piketech.Com/Files/Pdfs/Atran611.Pdf (Accessed 29 May 2016).
4. Phillip, H. R.; Taft, E. A., Kramers-Kronig Analysis of Reflectance Data for Diamond. *Physical Review* **1964,** *136* (5A), A1445-A1448.
5. Hale, G. M.; Querry, M. R., Optical Constants of Water in the 200-nm to 200-µm Wavelength Region. *Appl. Opt.* **1973,** *12* (3), 555-563.

3 Characterisation of GNF

3.1 Introduction

One of the many advantages of carbon as electrode material is its relatively inert electrochemistry. However, carbon has a rich surface chemistry, and while this property is useful in that it allows the chemical modification of the electrode surface, it can also lead to unwanted oxidation in the presence of atmospheric oxygen and moisture [1, 2]. The interaction of various redox species with oxygen functionalities at carbon electrodes has been investigated extensively by McCreery et al. [3-5]. Common redox probes can be classified roughly into three categories: those which are insensitive to surface termination (FcMeOH, $[Ru(NH_3)_6]^{3+/2+}$); those which interact with specific oxygen functionalities (such as $Fe^{3+/2+}$ with C=O) and those which are surface sensitive but apparently do not interact with specific oxygen-containing groups

($[Fe(CN)_6]^{3-/4-}$) [1]. As higher surface area nanomaterials are used, the role of carbon surface chemistry becomes increasingly important.

A large variety of oxygen functionalities at the electrode surface makes it difficult to attribute changes in electrochemical response to specific functional groups. Our approach is to use novel GNF with average lateral dimension of just 30 nm. The basal plane of the GNF is predominantly defect free and hence contains negligible oxygen content. In this study we have two very clearly defined types of edge functionality with which to probe the interaction of different redox probes with carbon electrode surfaces. The high density of carboxylic acid groups available on the GNF-COOH allows us to study both the electrostatic interaction between the redox species and acid groups in different protonation states and the effect of acid/base equilibria on the redox response. The amide-terminated GNF allows us to probe the influence of the electronegative carbonyl moieties but in the absence of the deprotonation equilibria exhibited by the COOH groups. The high density of edge COOH groups makes this an ideal material with which to study the role of oxygen species on electrochemical response, as their influence is greatly amplified due to the small size of the flakes. Additionally, the acid-terminated GNF can be complexed with different cations. The use of divalent alkaline earth metal cations such as Ca^{2+} and Ba^{2+} allows the immobilisation of a thicker layer of GNF onto an electrode surface, thereby increasing the electroactive surface area. Complexation of GNF-COOH with redox-active counter cations increases the electroactive surface area and additionally allows the study of surface-immobilised redox probes at higher concentrations.

Some of the work presented in this Chapter has been published in [6].

3.2 Experimental Methods

All aqueous solutions were prepared with doubly deionised water, taken from a Milli-Q water purification system, with a resistivity of not less than 18.2 MΩ cm at 25 °C.

3.2.1 Preparation of Complexed GNF

For preparation of GNF complexed with divalent cations 2 mg of GNF dissolved in water was neutralised with dilute KOH to deprotonate all acidic groups. An aqueous solution of $CaCl_2$ or $BaCl_2$ was added dropwise and the mixture was agitated between additions. Addition of the divalent cation resulted in complexation of neighbouring GNF and hence a loss of solubility. The resulting precipitate suspension was centrifuged and washed four times.

For preparation of GNF complexed with $[Ru(NH_3)_6]^{3+}$ 2.5 mg of GNF dissolved in water was neutralised with dilute KOH to deprotonate all acidic groups. An aqueous solution of $[Ru(NH_3)_6]Cl_3$ was added dropwise and the mixture was agitated between additions. The resulting precipitate suspension was centrifuged and washed four times.

3.2.2 X-ray Photoelectron Spectroscopy

XPS was carried out on a Thermo Scientific K-Alpha spectrometer equipped with a monochromated Al K_α (hv = 1486.6 eV) X-ray source. All survey scans were scanned 3 times with a resolution of 1 eV, 400 µm spot size and 50 ms dwell time. Samples were either compacted into wells in a custom-built powder sample plate or pressed into a piece of indium that was then secured onto a sample plate. Elemental composition ratios were calculated from survey spectra using the element library function.

3.2.3 Transmission Electron Microscopy

TEM images were recorded using a Jeol JEM 2100 TEM with a 200 kV accelerating voltage using a LaB_6 filament. All nanoparticles were deposited from methanol dispersions. Holey carbon coated copper TEM grids were used as the nanoparticle support.

3.2.4 pH Titration

An equivalence point and approximate pK_a for the GNF-COOH was obtained by titration of an aqueous suspension of dispersed GNF-COOH with NaOH. The hydrophilic nature of the COOH edge groups means the GNF disperse readily in water and other polar solvents. The NaOH solution was standardised prior to titration using potassium hydrogen phthalate (KHP). NaOH and KHP were placed in a desiccator for 12 hours prior to use. Water was either boiled or deoxygenated with argon before use. All solutions were kept under argon throughout the experiment. A micropipette was used to measure the volume of NaOH additions.

3.2.5 Electrochemical Experiments

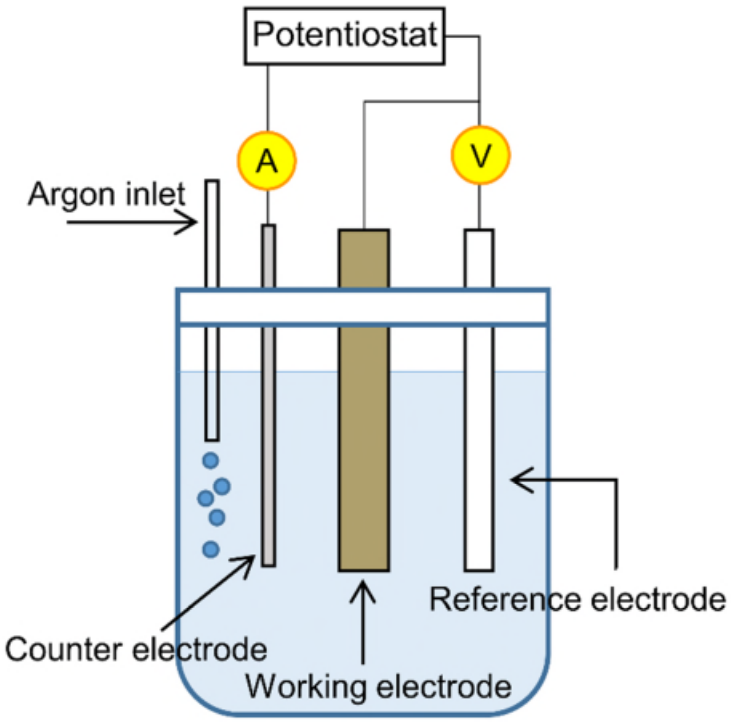

Figure 3.1 A schematic of the electrochemical cell used in this Chapter.

CV was carried out using a μ-Autolab potentiostat (Ecochemie, NL) coupled with GPES software. The electrochemical cell, depicted in **Figure 3.1** was a stoppered glass vial

with holes in the top to hold electrodes in place. A 3-mm diameter boron-doped diamond (BDD) disk sealed in polyether ether ketone (PEEK) (Windsor Scientific, UK) was used as the working electrode, either unmodified or modified with a layer of adsorbed GNF. A platinum wire, coiled at the end to increase the surface area, served as a counter electrode. The reference electrode was Ag/AgCl in saturated KCl and all potentials are reported relative to it. The BDD electrode was polished using successively finer grades of alumina suspension down to 0.05 µm, rinsed thoroughly with ultrapure water after each step and dried using an ambient air flow.

Complexed GNF precipitates were re-suspended in water and sonicated briefly before each use. The concentration of the suspensions, assuming full conversion of GNF and one Ca^{2+} per two carboxylate groups or one $[Ru(NH_3)_6]^{3+}$ per three carboxylate groups, is estimated to be 4.5 and 3.7 mg/ml for GNF-Ca and GNF-$[Ru(NH_3)_6]$, respectively. The GNF samples were drop-coated from aqueous suspensions of known concentration onto the freshly polished BDD electrode using a micropipette and allowed to dry under ambient conditions. After drying, the electrode was rinsed thoroughly with water to remove any poorly adhered material from the surface and dried using an ambient air flow. The resulting amount of GNF, GNF-Ca and GNF-$[Ru(NH_3)_6]$ on the electrode was estimated at (1.5 ± 0.5), (10 ± 2) and (7 ± 2) µg, respectively, in all experiments, and all CVs were recorded using a freshly modified electrode.

Redox probes hydroquinone (H_2Q), ferrocenemethanol (FcMeOH) and hexaammineruthenium(III) chloride were obtained from Sigma-Aldrich and used as received. For experiments in deoxygenated solutions and with air sensitive chemicals such as hydroquinone, high purity argon was bubbled through electrolyte solutions for 30 minutes to remove dissolved oxygen, and the gas flow was maintained over the surface of the solution during electrochemical experiments.

3.2.6 ATR-FTIR

3.2.6.1 Stability of Aqueous Suspension of GNF

The stability of GNF suspended in water was monitored over 6 months by recording mid-infrared spectra in ATR mode with a Bruker Tensor 27 spectrometer (Bruker, UK) fitted with a room temperature DLaTGS detector at 4 cm^{-1} resolution and a diamond crystal as the internal reflection element. A background was first collected of the clean ATR crystal. 0.50 µl of an aqueous suspension of the GNF was then applied directly onto the ATR crystal using a micropipette and allowed to dry.

3.2.6.2 Solution-Phase Characterisation of GNF

A droplet (volume ca. 50 µl) of an aqueous suspension of the GNF was applied directly onto the ATR crystal and 2 µl aliquots of 0.1 M KOH were added until the pH of the solution reached ca. 9 as determined with pH indicator paper. A spectrum was collected after each addition. Water bands were subtracted from the sample spectra by recording a background spectrum of water only prior to the experiment. The data was processed using the atmospheric compensation function of OPUS software. Changes in concentration due to the addition of aqueous aliquots of base were compensated by multiplying the spectra by the volume ratio.

To obtain spectra of the Ca^{2+}-complexed flakes 0.5 µl of GNF-Ca precipitate suspended in water was applied onto the ATR crystal and the solvent was allowed to evaporate. A droplet of water was then carefully added to ensure full hydration of the precipitate. Bulk water bands were subtracted from the sample spectra by recording a background spectrum of water prior to the experiment. The data was processed using the atmospheric compensation function of OPUS software.

3.3 Results and Discussion

3.3.1 Transmission Electron Microscopy

To gain information about the morphology of GNF, both in the acid-terminated form and when complexed with cations, TEM was employed.

TEM images of the acid-terminated GNF are shown in **Figure 3.2**(a)-(b). To reduce the degassing time in the chamber, the GNF were drop-coated onto a holey carbon covered copper TEM grid from a methanol dispersion. The acid-terminated GNF don't dissolve in methanol to the same extent as they do in water, so some aggregation and stacking of the particles is evident in the images. The flakes can be seen to curl up and form spherical shapes of concentric sheets.

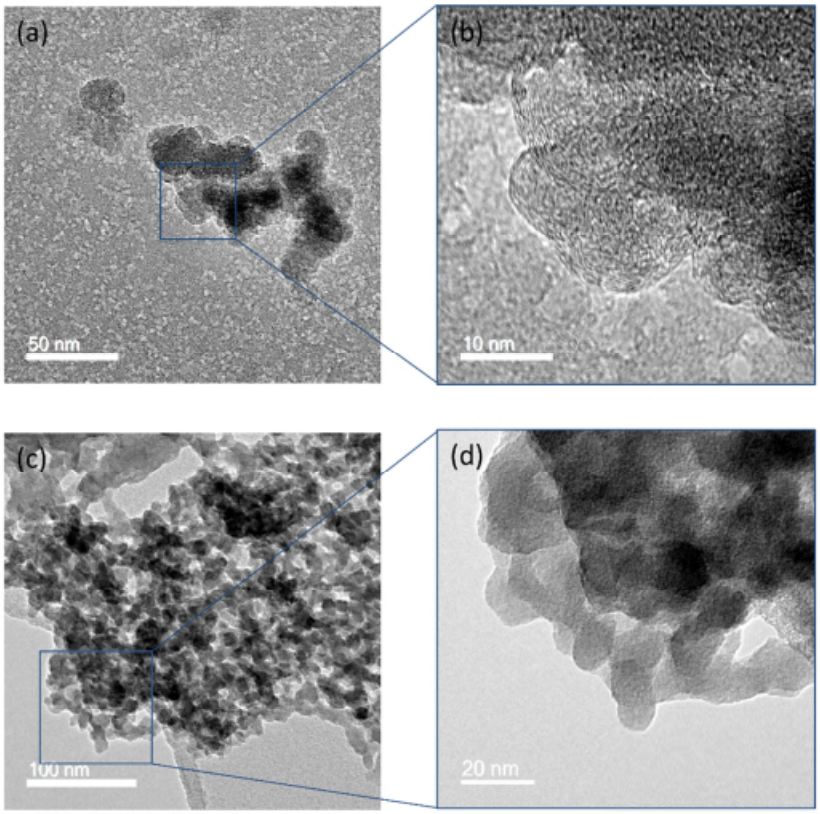

Figure 3.2 TEM images of the GNF. (a), (b): GNF-COOH. (c), (d): GNF-Ba.

GNF complexed with Ba^{2+} were also imaged with TEM and shown in **Figure 3.2**(c)-(d). When the divalent cations bind to carboxylate groups, it is sterically favourable for the flakes to cross-link through COO^- groups on two different flakes rather than adjacent groups on one flake. This is observed in the TEM images where chains of flakes can be seen at the edges of the clusters of particles. Also discernible in the image is the porous, three-dimensional nature of the resulting material. The crosslinking of the GNF leads to the formation of a disordered, three-dimensional structure that, due to its porosity and the small size of the flakes, possesses a large surface area.

3.3.2 X-ray Photoelectron Spectroscopy

XPS characterisation of GNF-COOH, GNF-amide and GNF-thiol has been reported previously [7, 8] and the high resolution spectrum of the C1s region of GNF-COOH is shown in **Figure 1.3**(a). The conversion of carboxylic acid edge groups was confirmed by the presence of nitrogen in GNF-amide and both nitrogen and sulphur in GNF-thiol. Additionally, components at binding energies corresponding to –C–N, –N–C=O and C–S appeared in the C1s region, further supporting the successful conversion of edge groups.

Carboxylic acid functional groups are versatile as precursors to other functionalities as demonstrated in [7, 8]. In addition to conversion to amides, the acid edge groups present in GNF-COOH can be exploited to form electrostatic complexes. In this thesis, GNF-COOH are complexed with divalent cations to construct a large surface area electrode for spectroelectrochemical experiments. GNF-COOH are also complexed with $[Ru(NH_3)_6]^{3+}$ to study the redox behaviour of the immobilised Ru(III) centre. XPS was used to confirm complexation of GNF and to estimate the number of edge groups that remain non-complexed.

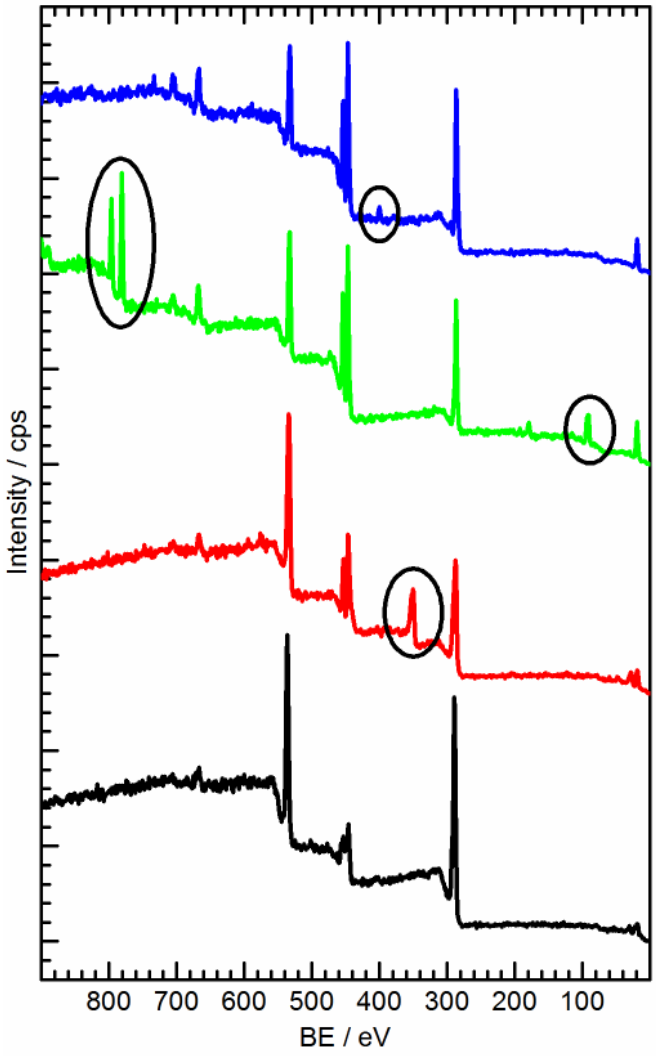

Figure 3.3 Wide scan survey spectra of GNF-COOH (black) and GNF-COOH complexed with Ca^{2+} (red); Ba^{2+} (green); $[Ru(NH_3)_6]^{3+}$ (blue). Relevant elements are highlighted with circles. Spectra are offset for clarity.

Survey spectra of GNF-COOH and GNF-COOH complexed with Ca^{2+}, Ba^{2+} and $[Ru(NH_3)_6]^{3+}$ are compared in **Figure 3.3**. The presence of calcium is evident in GNF-Ca (red line) from the appearance of a peak at 350 eV corresponding to calcium Ca2p. Complexation with Ba^{2+} leads to new peaks at 781 and 90 eV arising from Ba3f and Ba4d, respectively (green line). Although ruthenium was not detected in the survey spectrum of $[Ru(NH_3)_6]^{3+}$ complexed GNF (blue line), the presence of nitrogen in the survey scan at 400 eV shows that $[Ru(NH_3)_6]^{3+}$ is present in the sample. Additionally, clear peaks were seen in the Ru2d narrow scan. Because the Ru2d binding energies overlap with C1s, fitting of the region was not attempted.

From the atomic percentages of oxygen and the complexing cation, the ratio of COOH groups that are complexed was calculated. In the case of GNF-Ru, the atomic percentage of ruthenium was taken as 1/6 of the amount of nitrogen. To maintain charge neutrality, it is assumed that two carboxylate groups are complexed by one divalent cation and three COO^- by one $[Ru(NH_3)_6]^{3+}$ ion. The results are gathered in **Table 3.1**. Another method to estimate the ratio for GNF-Ca is presented in Section 5.10.

Table 3.1: Fraction of carboxylic acid groups that are complexed in different materials calculated from the atomic percentages of oxygen and complexing cation.

GNF-Ca	**O / atomic %**	**Ca / atomic %**	**COOH complexed / %**
	32.3	6.2	76 ± 6
GNF-Ba	**O / atomic %**	**Ba / atomic %**	**COOH complexed / %**
	27.6	2	28 ± 4
GNF-Ru	**O / atomic %**	**Ru / atomic %**	**COOH complexed / %**
	22.4	0.6	16.0 ± 0.1

Of the three cations tested, Ca^{2+} is most efficient at binding the carboxylate groups. This is probably due to the higher charge density and smaller size of the cation compared to Ba^{2+} and $[Ru(NH_3)_6]^{3+}$. The results show that even complex cations can be incorporated into the GNF material, thereby allowing the construction of high surface area redox active assemblies.

3.3.3 Infrared Spectroscopy

Carboxylic acid groups are well suited to characterisation by IR due to the strong absorption intrinsic to C–O bonds. The deprotonation process can also be followed using IR because the carbonyl band disappears and two new stretching modes appear arising from the carboxylate.

The IR spectrum of dry GNF (**Figure 3.4**(a)) shows a strong band at 1720 cm^{-1} assigned to the C=O stretching mode of carboxylic acid. Also present are the carboxylate asymmetric stretch at 1580 cm^{-1} and overlapping bands at 1435 and 1350 cm^{-1} assigned to the symmetric carboxylate stretch. The presence of two bands for the symmetric stretch is predicted by computational models for situations where the carboxylate groups occupy distinctly different environments within a molecule [9]. The feature at around 1220 cm^{-1} is a convolution of vibrational modes, but can be assigned partly to the C–O stretch in protonated COOH. The broad absorption features at 3700-2700 cm^{-1} are attributed to O–H stretches of adsorbed water (> 3000 cm^{-1}) and O–H stretches of the carboxylic acid edge groups (< 3000 cm^{-1}). The persistence of the water band even after lengthy drying suggests water is strongly associated with the GNF, most likely due to hydrogen bonding to the oxygenated edge groups. Adsorbed water associated with oxygen groups of graphene oxide is known to persist even after months of drying [10].

Figure 3.4(b) shows the IR spectrum of GNF-amide. The carbonyl stretch has moved from 1720 to 1640 cm^{-1} as the acid has been converted to an amide group. In addition to ν(C=O), δ(N–H) of the amide and amine groups and δ(O–H) of adsorbed water will contribute to the absorption band present at 1700–1500 cm^{-1}. The presence of water in the sample is clear from the broad absorption band above 3000 cm^{-1} that is attributed to O–H stretching of water. On top of this broad feature two bands can be discerned at 3380 and 3240 cm^{-1} that are assigned to the primary amine N-H stretches, although these are very broad and will probably include absorption by the secondary amide N-H stretch. Weak features arising from C–H stretches of the edge groups can be seen at 2925 and 2855 cm^{-1}. It is evident from the shoulder at 1720 cm^{-1} that some carboxylic acid groups remain in GNF-amide after reaction with ethylene diamine.

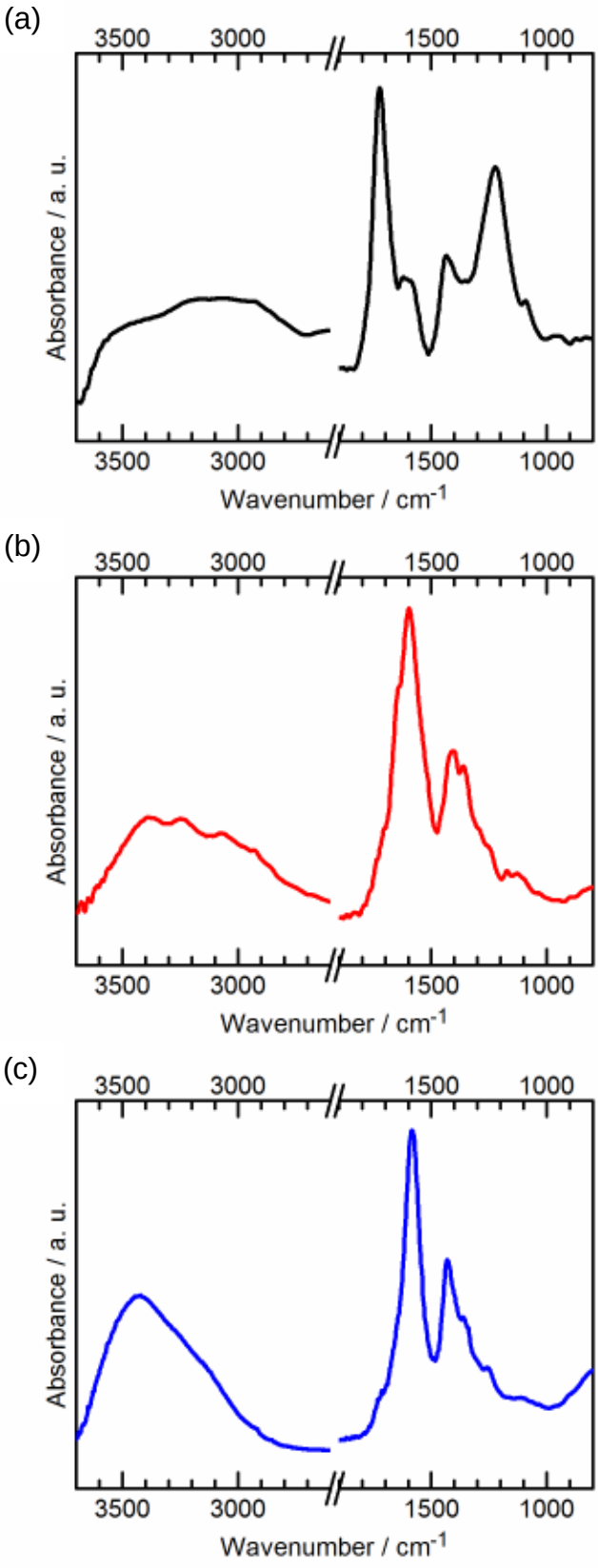

Figure 3.4 ATR-FTIR spectra of (a) GNF-COOH; (b) GNF-amide; (c) GNF-Ca.

Reaction of the water-soluble GNF with Ca^{2+} results in a porous precipitate where the loss of solubility indicates a strong interaction between the COO^- edge groups and the Ca^{2+} cation. IR spectrum of the dried GNF-Ca precipitate (**Figure 3.4**(c)) supports this observation, showing that the C=O stretching band at 1720 cm^{-1} and the C–O stretch at 1220 cm^{-1} are almost entirely absent and the majority of COOH groups are converted to carboxylate. The most intense peak for GNF-Ca at 1585 cm^{-1} is assigned to the asymmetric stretch in carboxylate and also contains a contribution from the bending mode of water at 1635 cm^{-1}; this peak is accompanied by the slightly weaker carboxylate symmetric stretch modes at 1430 and 1350 cm^{-1}. The presence of a strong stretching band for water at 3700–3000 cm^{-1} suggests that a significant number of water molecules remain in the sample. Absorption bands for acid O–H groups at 3000–2700 cm^{-1} are much reduced compared to the non-complexed GNF, which is consistent with the majority of acid groups being found as carboxylate and bound to Ca^{2+}.

3.3.3.1 Stability

The stability of GNF-COOH suspended in water was monitored over a period of six months. The sample was stored in a plastic Eppendorf vial in normal laboratory atmosphere, and no precautions were taken to exclude oxygen or to maintain a specific temperature. The temperature fluctuated between 18 and 25 °C over the course of the six months. No changes were observed to the IR spectrum over this time, suggesting that the GNF are stable in water under atmospheric conditions.

3.3.4 pH Titration

The acid/base properties of the acid-terminated GNF were investigated by pH titration. When a weak acid, HA, is dissolved in water, a dynamic equilibrium is established:

$$HA(aq) + H_2O(l) \rightleftharpoons H_3O^+(aq) + A^-(aq) \quad (3.1)$$

The dissociation constant, K_a, is given by

$$K_a = \frac{[H_3O^+][A^-]}{[HA]} \quad (3.2)$$

The dissociation constants of different acids span several orders of magnitude, and therefore it is common to work with pK_a values of acids. To get an estimate of the pK_a of the flakes, titrations were performed using a sodium hydroxide solution. When a strong base such as NaOH is added to a solution of a weak acid, the hydroxide ions react with the dissociated protons, perturbing the equilibrium and causing more of the weak acid to dissociate. When the number of moles of OH^- equals the number of moles of weak acid present, the pH of the solution will rise sharply. This point is the equivalence point, and after this any addition of OH^- will merely increase the pH. If the pH of the solution is monitored as a function of NaOH added, a titration curve can be constructed. By rearranging Equation (3.2) and taking logs, we arrive at Equation (3.3):

$$pH = pK_a + \log_{10}\left(\frac{[A^-]}{[HA]}\right) \quad (3.3)$$

Equation (3.3) is the Henderson-Hasselbalch equation, and it tells us that when [HA] = $[A^-]$, pK_a = pH. The pK_a can therefore be read from the titration curve at the point where half of the base required to reach the equivalence point is added.

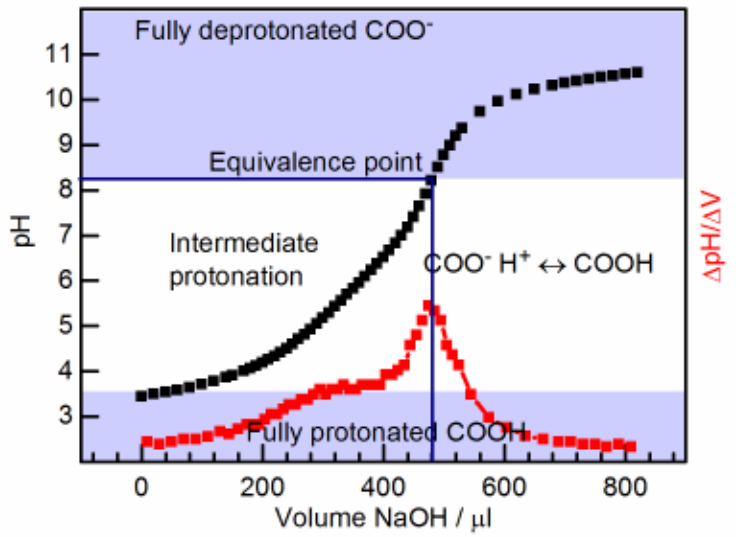

Figure 3.5 Titration curve of GNF-COOH (black), first derivative (red). Adapted from [6].

Figure 3.5 shows the titration curve for the addition of aliquots of (236 ± 6) × 10^{-4} M NaOH to an aqueous suspension of GNF-COOH. As the XPS and IR characterisation show no detectable concentration of other acidic functionalities present in the flakes, the observed behaviour can be attributed solely to the COOH edge groups.

When the weak acid COOH edge groups of the GNF-COOH are exposed to water a dynamic equilibrium is established, where the acid groups become deprotonated:

$$\text{GNF-COOH} + H_2O \rightleftharpoons \text{GNF-COO}^- + H_3O^+ \qquad (3.4)$$

Addition of a small amount of strong base to the solution results in reaction of OH^- with the solution protons and hence the equilibrium is perturbed. Once the number of moles of OH^- added is equal to the number of moles of weak acid groups (the equivalence point, found from the first derivative curve), further addition of base results in a rapid increase in pH. For GNF-COOH we observe more complex behaviour than would be expected for a single acid species dissolved in water. On addition of ca. 200–400 µl NaOH an increase in pH is observed, but this is not the sharp rise expected if all of the acid groups underwent deprotonation with the same pK_a. It is probable that different bonding environments or electrostatic/hydrogen-bonding interactions between

neighbouring groups result in a range of acid/base behaviours among the edge-group population. After addition of further NaOH an inflection point is observed in the first derivative curve, which we interpret as the point at which all COOH groups are fully deprotonated and which gives us an equivalence point of pH 8.3. This allows us to estimate the number of COOH groups as 7×10^{-3} mol of acid groups per gram of GNF material. The pK_a of a weak acid is defined as the pH at which half of the base required to reach the equivalence point is added and for the GNF-COOH pK_a is therefore estimated as 4.5. However given the wide pH range over which deprotonation is observed, the usefulness in reporting a single pK_a value for the GNF-COOH is questionable.

To understand the titration data, the spatial distribution of the groups must be considered. The flakes bear a large number of COOH functionalities that decorate the edges, making it very likely that these groups are found in close proximity to each other. In the beginning of the titration, as the added OH^- combine with H_3O^+, the COOH groups that dissociate to re-establish equilibrium would be located away from any existing negatively charged groups, and could also be stabilised by hydrogen bonding with neighbouring COOH functionalities. As deprotonation proceeds, the remaining COOH groups begin to experience the electrostatic effect of neighbouring negatively charged carboxylate groups. Consequently, these remaining COOH functionalities will be progressively more difficult to deprotonate, and more base needs to be added to achieve dissociation leading to deprotonation over a wide pH range.

3.3.5 In Situ pH Studies Monitored with Infrared Spectroscopy

The solution-phase IR spectra of solvated GNF are shown in **Figure 3.6**. Initially, when only water and GNF are present and no base has been added, the pH of the solution is approximately 2 as determined with pH indicator paper. Absorption bands can be seen at 1720 cm cm^{-1} (C=O stretch), 1590 cm^{-1} (asymmetric COO^- stretch), 1420 cm^{-1}

(symmetric COO^- stretch) and 1260 cm^{-1} (overlapping C–O stretch and O–H deformation). The GNF are partially deprotonated already before the addition of base, as indicated by the low pH of the solution and the peaks corresponding to both protonated and deprotonated forms of COOH. Adding increasing aliquots of KOH causes the signal from the C=O and C–O stretches associated with protonated carboxylic acid to decrease, whereas the two bands from COO^- gain intensity with added base. Changes can also be observed in the O–H stretch region where a decrease in absorption intensity is seen around 2900 cm^{-1} and increase around 3300 cm^{-1}. Because a background spectrum of pure water was recorded, the O–H stretch of water is subtracted from the sample spectra which initially leads to a negative feature centred at 3300 cm^{-1}. The increase in absorption at 3300 cm^{-1} upon addition of base is assigned to increased solvation of the deprotonated carboxylate groups. At the same time, the intensity of absorption around 2700 cm^{-1} decreases and this is attributed to the loss of hydrogen-bonded COOH groups. The final spectrum in is recorded at pH ca. 7. Thus these in situ pH studies agree with our former observations that the flakes occupy a range of protonation states in solutions of pH 3-7.

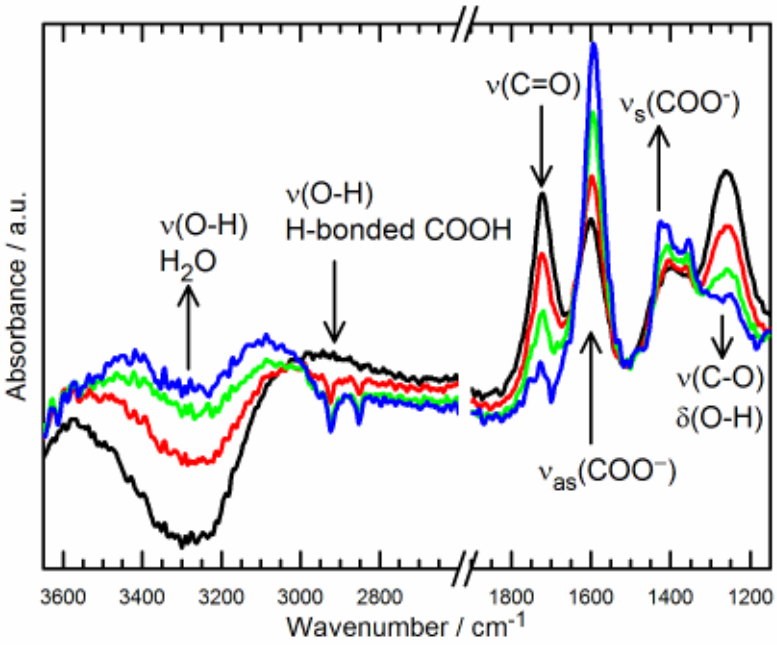

Figure 3.6 Changes in IR absorption of GNF upon addition of 0.1 M KOH. GNF with no added base at pH 2 (black), pH 3 (red), pH 5 (green), pH 7 (blue). Reproduced from [11].

3.3.6 Electrochemistry of GNF without Redox Probes

The edge-carboxylated GNF are very water-soluble, so there was a concern that they would not adhere to the surface of the BDD electrode when immersed in aqueous solution, and hence we would be unable to probe their electrochemical response using a drop-coating method. In order to establish the stability of a GNF layer immobilised on BDD, cyclic voltammetry in the absence of any redox probes was performed in the potential window −0.3 to +1 V in supporting electrolytes of varying pH. Additionally, these experiments show whether there is any inherent redox activity present in the flakes.

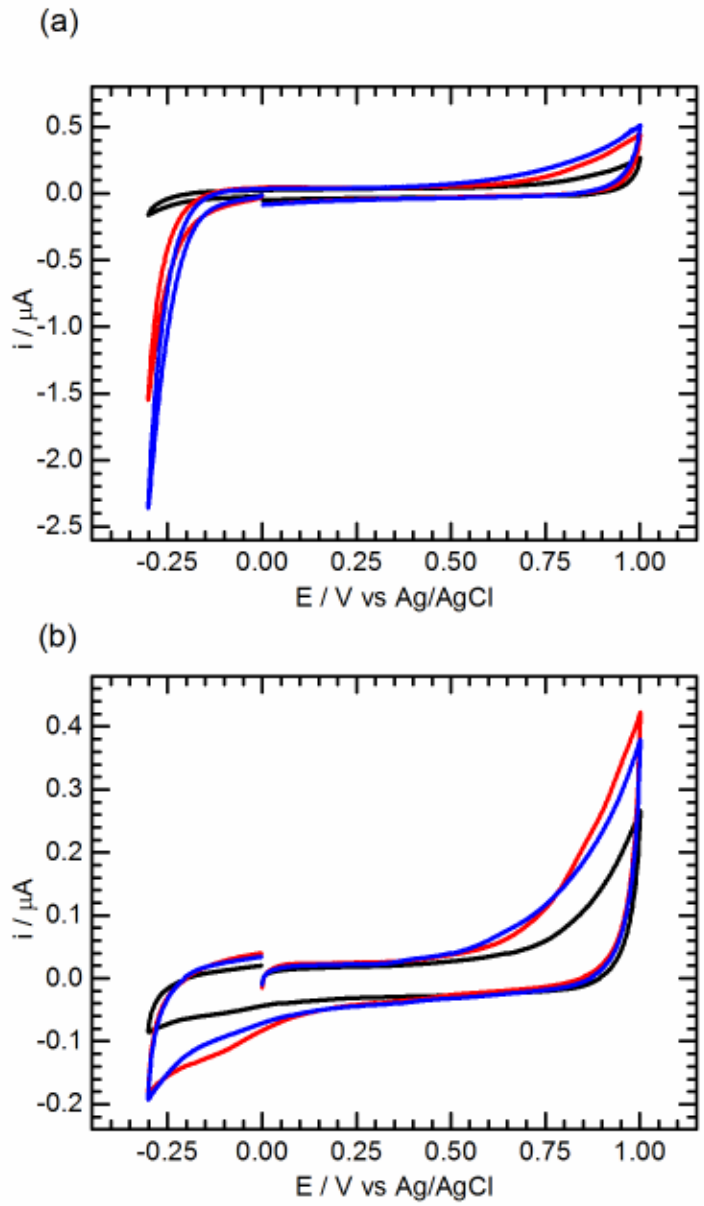

Figure 3.7 (a) pH 4.6 PBS with oxygen and (b) pH 4.6 PBS without oxygen; clean BDD (black), acid-terminated GNF (red) and amide-terminated GNF (blue). Adapted from [6].

Figure 3.7(a) shows the response of GNF-COOH, GNF-amide and clean BDD in 0.1 M KH_2PO_4 pH 4.6 electrolyte over the potential range −0.3 V to +1.0 V. **Figure 3.7**(b) shows the same but in degassed solution. In both solution conditions the response of the GNF layer can be observed over the background response of the BDD at potentials above ca. +0.4 V and below −0.2 V. Currents are larger for GNF-amide than GNF-COOH under the same conditions. No Faradaic peaks are observed for the GNF modified electrodes in the range 0 to +0.4 V. In deoxygenated solution the cathodic

currents below −0.2 V are greatly diminished, showing that the reduction currents in **Figure 3.7**(a) can be attributed to oxygen reduction. This indicates that both GNF samples can catalyse oxygen reduction better than BDD, which is a poor electrocatalyst for this reaction in comparison to sp^2 carbon materials.

These data show that despite their high solubility in water, a few monolayers of the GNF adhere to the surface of the BDD electrode for the duration of the experiment. At the present time it is unclear in what orientation the GNF are arranged on the electrode surface, as their small size and transparency makes the immobilised layer difficult to characterise. The capacitive current increases only slightly, which could be interpreted as the flakes adopting a horizontal conformation, lying flat on the electrode surface, as this orientation would not cause a significant increase the surface area. If the surface area would change markedly upon modification, a larger increase in the capacitance would be expected.

Figure 3.8(a) compares the response of GNF-COOH in pH 4.6 and pH 9.2, and (b) compares the response of GNF-amide in the same conditions. We found a pH-dependent increase in oxidation current at +0.6 V that closely resembles the response at a clean BDD electrode and is unaffected by the presence of oxygen in solution.

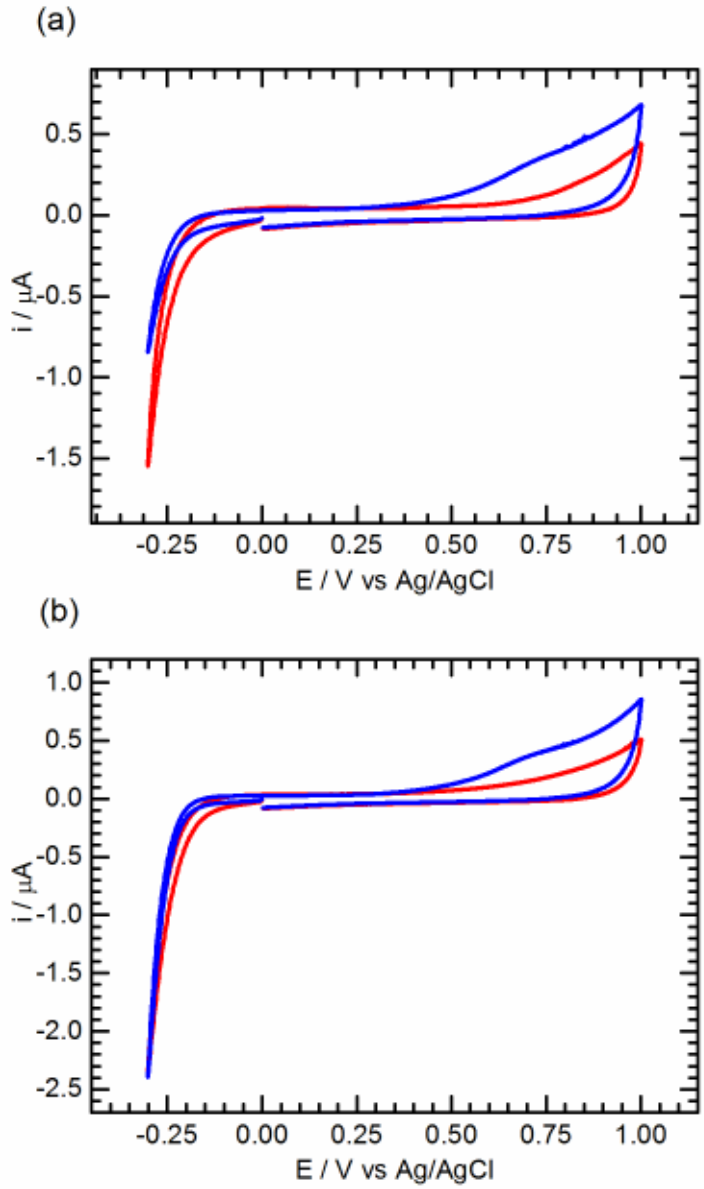

Figure 3.8 Cyclic voltammograms of BDD modified with (a) carboxylic acid-terminated GNF and (b) amide-terminated GNF in pH 4.6 (red) and 9.2 (blue). Electrolyte concentration 0.1 M. Scan rate 50 mV/s. Adapted from [6].

The CV response of GNF after complexation with Ca^{2+} was also studied (**Figure 3.9**). Again, there are no Faradaic peaks in the range 0 to 0.4 V. Significantly more current flows when the flakes are complexed with the precipitated flakes compared to acid-terminated flakes. This is due to the lower solubility of the complexed GNF that results in a higher coverage of the electrode surface and a larger electroactive surface area.

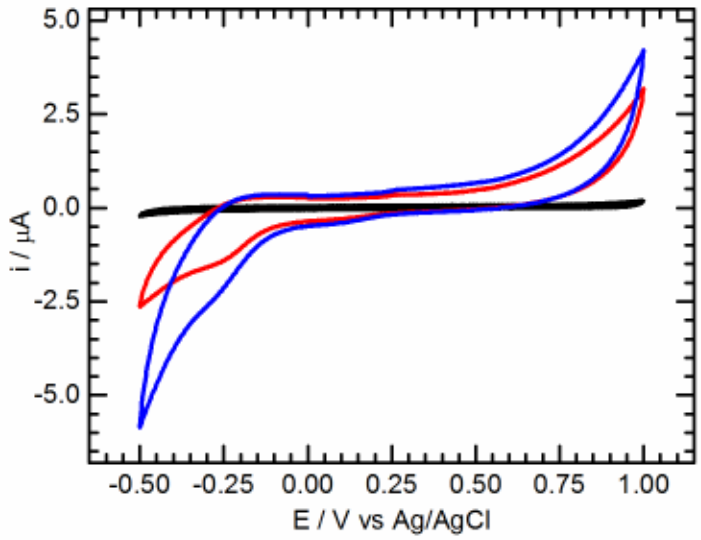

Figure 3.9 Cyclic voltammograms in 0.1 PBS at pH 7. Working electrode: clean BDD (black); BDD modified with GNF-Ca (blue). Red curve shows the response of BDD modified with GNF-Ca in deoxygenated electrolyte.

3.3.7 Electrochemistry of FcMeOH at GNF-Modified Electrode

Ferrocenemethanol was chosen as the first redox probe because it undergoes a reversible one-electron oxidation and exhibits near ideal outer-sphere behaviour. Unlike ferrocene, it is also soluble enough in water to allow its use in aqueous electrolyte.

Cyclic voltammograms of 0.5 × 10^{-3} M ferrocenemethanol were measured at a clean BDD electrode and BDD modified with either GNF-COOH or GNF-amide, and the results are shown in **Figure 3.10**. No difference in electrochemical response could be discerned between the BDD and the GNF-modified BDD under any conditions. Changing the pH of the supporting electrolyte from 4.6 (**Figure 3.10**(a)) to 9.2 (**Figure 3.10**(b)) did not affect the peak height or separation. ΔE_p calculated from the CVs in Figure 3.10(a)–(b) was approximately 65 mV at each electrode and in each pH, which is very close to the theoretical value for a reversible one-electron process.

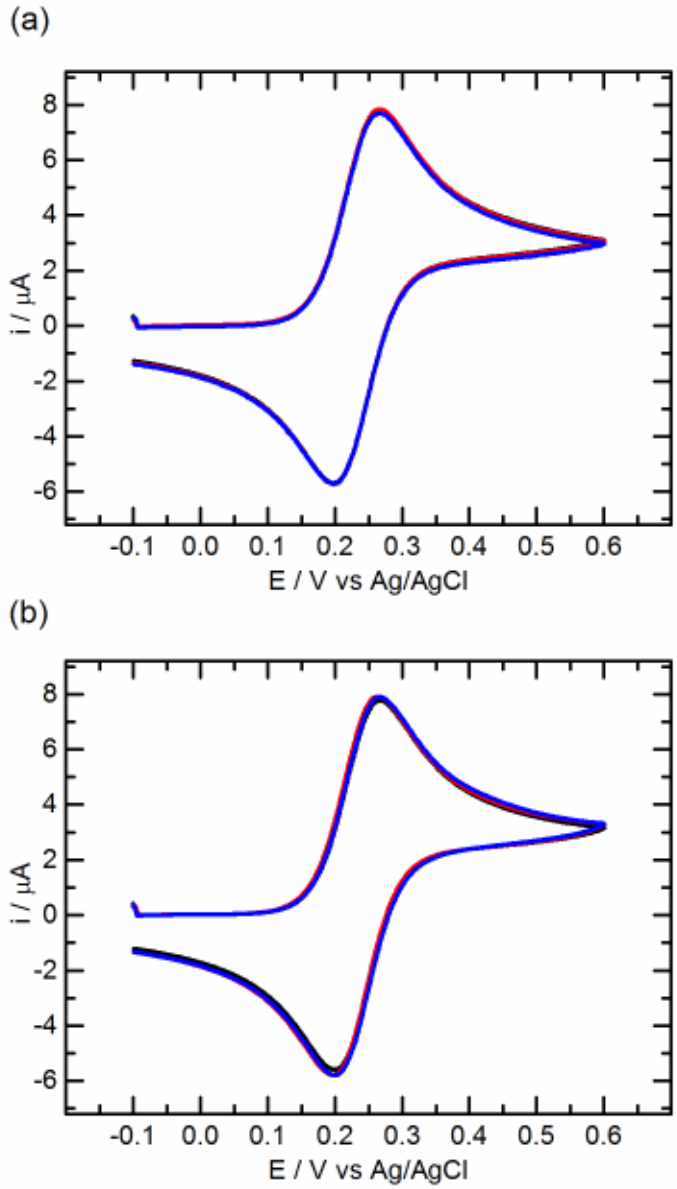

Figure 3.10 Cyclic voltammograms of 0.5×10^{-3} M ferrocenemethanol at different electrode modifications. (a) At clean BDD (black), GNF-COOH modified BDD (red) and GNF-amide modified BDD (blue) in 0.1 M KH_2PO_4 pH 4.6, scan rate 100 mV s^{-1}. (b) At clean BDD (black), GNF-COOH modified BDD (red) and GNF-amide modified BDD (blue) in 0.1 M K_2HPO_4 pH 9.2, scan rate 100 mV s^{-1}. Adapted from [6].

Figure 3.11 demonstrates that modification of BDD with GNF-amide resulted in reversible behaviour at a range of pH values and that scan rates up to 1 V s^{-1} could be used without significant increase to the peak separation.

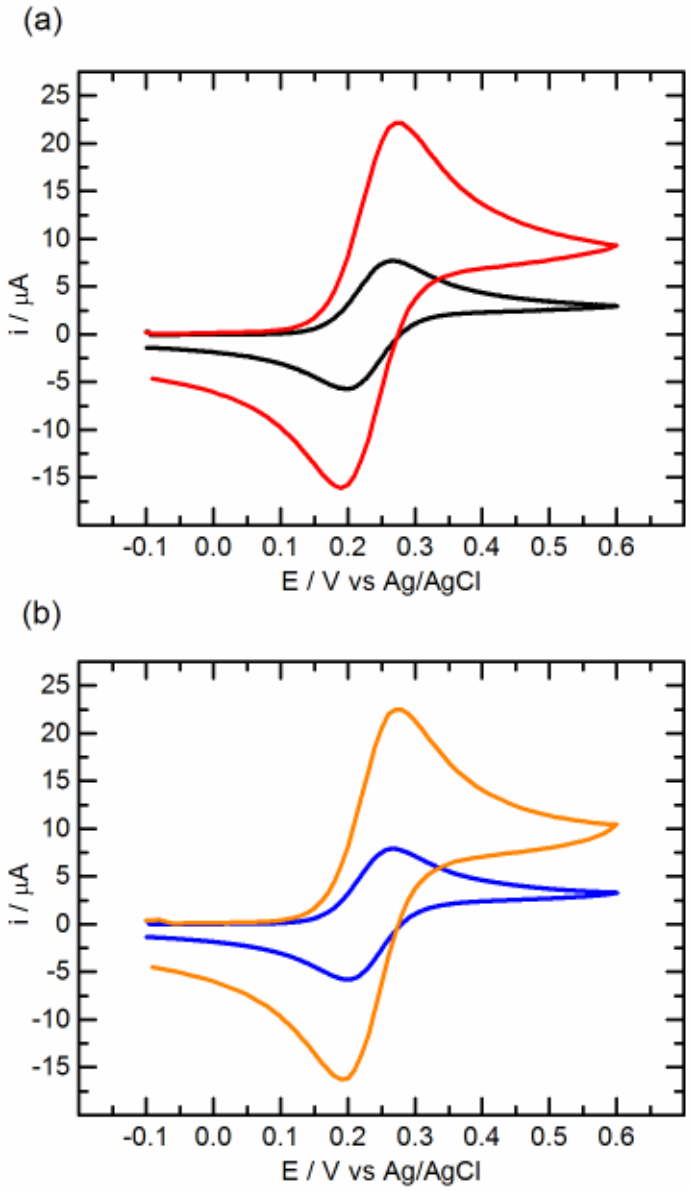

Figure 3.11 Cyclic voltammograms of 0.5 × 10^{-3} M ferrocenemethanol at GNF-amide modified BDD. Supporting electrolyte: (a) 0.1 M KH_2PO_4 pH 4.6; (b) 0.1 M K_2HPO_4 pH 9.2. Scan rate 100 mV s^{-1} (black, blue), 1 (red, orange) V s^{-1}. Adapted from [6].

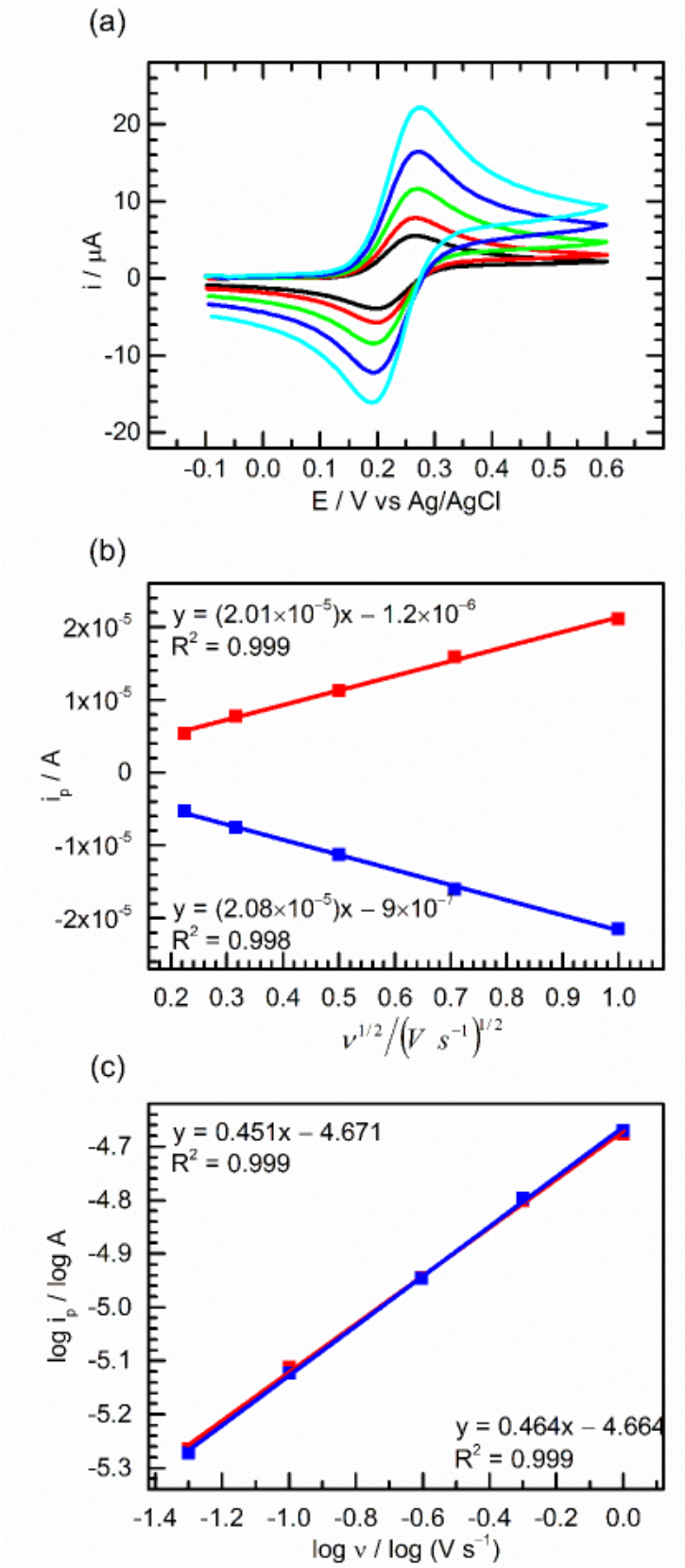

Figure 3.12 (a) Cyclic voltammograms of 0.5 × 10^{-3} M ferrocenemethanol at GNF-COOH modified BDD in 0.1 M KH_2PO_4 pH 4.6: scan rate 50 (black), 100 (red), 250 (green), 500 (blue), 1000 (light blue) mV s^{-1}; (b) peak currents i_{pa} (red) and i_{pc} (blue) plotted against square root of scan rate v; (c) log i_{pa} (red) and log $|i_{pc}|$ (blue) plotted against log v.

Figure 3.12(a) shows CVs of FcMeOH at GNF-COOH modified BDD recorded at different scan rates. As was seen for the GNF-amide modified BDD in **Figure 3.11**, scan rates up to 1 V s^{-1} could be utilised without significant irreversibility showing in the response (ΔE_p *ca*. 80 mV at both electrodes).

The peak currents from **Figure 3.12**(a) are plotted in **Figure 3.12**(b) against the square root of scan rate. The data can be fitted with a linear regression line, confirming that the redox reaction is diffusion controlled. The log-log plots in **Figure 3.12**(c) are also fitted with a linear regression line, and the regression coefficients for both the oxidation and reduction sweeps are very close to the theoretical value of 0.5 for a diffusion-controlled process. Selected parameters extracted from **Figure 3.12**(a) are tabulated in **Table 3.2**.

Table 3.2: Peak parameters of FcMeOH redox reaction from cyclic voltammetry experiments at GNF-COOH modified BDD in 0.1 M KH_2PO_4 pH 4.6.

v / mV s^{-1}	E_{pa} / V	i_{pa} / µA	E_{pc} / V	i_{pc} / µA	ΔE_p / V	i_{pa} / i_{pc}
50	0.267	5.43	0.198	−5.35	0.066	1.02
100	0.266	7.73	0.198	−7.54	0.065	1.03
250	0.270	11.3	0.195	−11.3	0.075	1.00
500	0.270	15.8	0.195	−16.0	0.075	0.989
1000	0.270	21.1	0.190	−21.4	0.083	0.984

It is not unexpected to find that the response of this redox probe is unchanged at the modified electrode, as the FcMeOH/$FcMeOH^+$ redox couple is known to be relatively surface-insensitive and outer-sphere in nature. However, adsorption of this species to graphene [12] has been reported, indicating some surface interaction that could influence the electrochemical response. In this case no evidence of adsorption is seen and also no indication that the protonation state of the GNF-COOH plays any role in the redox response of this probe. An outer-sphere reaction is not necessarily independent of electrode material and can be influenced by double-layer effects and effects of the energy and distribution of electronic states in the electrode [13]. In this

case, the changes in the degree of protonation of the functional groups on the electrode surface as a function of electrolyte pH do not affect the electron transfer kinetics. The GNF materials likewise show no electrode blocking effects that inhibit electrochemical response and no sign of limitation in electron transfer kinetics due to low density of states or lack of surface adsorption sites. On the other hand no enhancement in electron transfer kinetics is noted either, although the response at the underlying BDD is also close to reversible, so it would be difficult to determine any improvement.

3.3.8 Electrochemistry of Hydroquinone/Benzoquinone at GNF-Modified Electrode

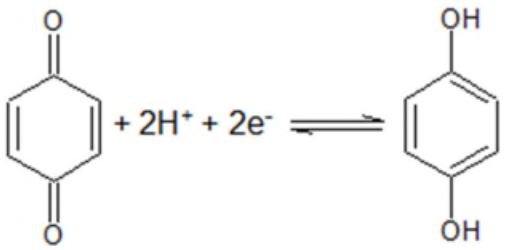

Scheme 3.1: 1,4-Benzoquinone undergoes a two-proton, two-electron reduction to hydroquinone.

After having established that GNF do not inhibit electron transfer for an outer-sphere redox couple, a more complex redox system was investigated. The 1,4-benzoquinone/hydroquinone (Q/H_2Q) redox couple (**Scheme 3.1**) was chosen to examine how the acidic groups at the GNF edge influence proton-coupled electron transfer (PET). Phenolic compounds are used in various industrial processes, including the preparation of petrochemicals [14], cosmetics and pharmaceutical products [15]. Phenols are non-biodegradable and toxic to many organisms, and their release into the environment from the waste streams of these industrial processes leads to soil and

water contamination [16]. Therefore, finding ways to detect and degrade phenolic compounds is of great importance.

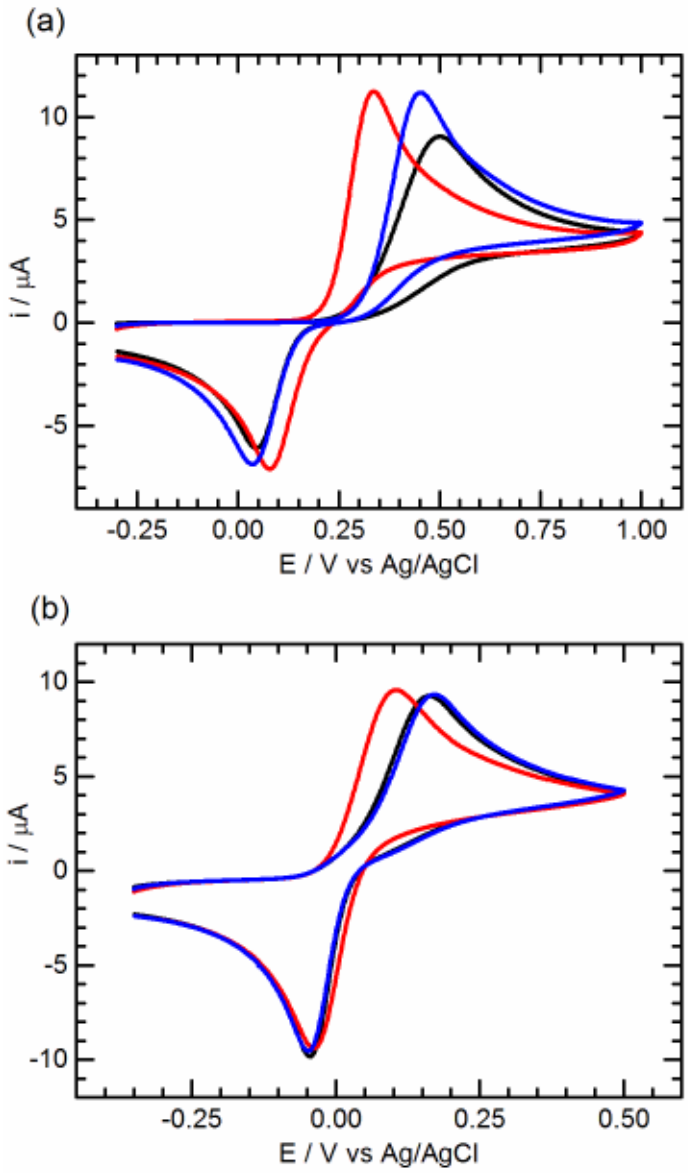

Figure 3.13 Cyclic voltammograms of 0.5 × 10^{-3} M hydroquinone in 0.1 M PBS: (a) at pH 5; (b) at pH 8.5. Working electrode: clean BDD (black), BDD modified with GNF-COOH (red) and BDD modified with GNF-amide (blue). Scan rate 50 mV s^{-1}. First scans shown. Adapted from [6].

The oxidation of hydroquinone (H_2Q) to benzoquinone (Q) was studied at clean BDD, GNF-COOH modified and GNF-amide modified electrodes over the pH range 5.0 to 8.5. **Figure 3.13** shows cyclic voltammograms recorded for hydroquinone in phosphate buffer solutions of pH 5 (a) and 8.5 (b). The voltammograms at a clean BDD are shown

in blue, scans at BDD modified with GNF-COOH are in red, and those at BDD modified with GNF-amide are in blue. At BDD the response was very irreversible, as has been reported previously [17] with ΔE_p being *ca.* 200 mV at pH 8 and >450 mV at pH 5. Modification of the BDD with a layer of GNF-COOH resulted in a decrease in peak separation (ΔE_p *ca*. 150 mV at pH 8.5, 250 mV at pH 5). A shift in both oxidation and reduction peaks towards reduced overpotential is observed at the GNF-COOH electrode; however the shift in oxidation peak potential is greater than that for the reduction peak. Indeed it was found that the anodic shift in the reduction peak position of ca. 40 mV compared to the peak at clean BDD was constant and independent of pH over the range tested. In contrast, the cathodic shift in the oxidation peak for GNF-COOH compared to BDD was pH-dependent and was greater at lower pH. A small improvement in electron transfer kinetics is observed for the GNF-amide modified electrode, with respect to the oxidation peak current, although little change to ΔE_p is observed on modifying the electrode.

3.3.8.1 pH-Dependence of the Q/H_2Q Reaction

Consider the reaction

$$O + mH^+ + ne^- \rightleftharpoons R \tag{3.5}$$

where O is the oxidised species, R is the reduced species, and *m* and *n* are the stoichiometric numbers of protons and electrons, respectively. The equilibrium potential, *E*, is given by the Nernst equation:

$$E = E^\circ - \frac{RT}{nF}\ln\frac{[R]}{[O][H^+]^m} \tag{3.6}$$

where E^0 is the standard potential, *R* the gas constant and *T* is the temperature in Kelvin. At equilibrium, [O] = [R] and

$$\mathrm{E} = \mathrm{E}^0 + \frac{mRT}{nF}\ln[\mathrm{H}^+] \tag{3.7}$$

For the benzoquinone reduction shown in Scheme 3.1, m = n = 2, and replacing the natural logarithm with base 10 logarithm gives the pH dependence:

$$E = E^0 - \frac{2.3RT}{F}\ \mathrm{pH} \tag{3.8}$$

At 25 °C the equilibrium potential changes by −59 mV per pH unit. The equilibrium potential is often estimated from CV data as the average of the oxidation and reduction peak potentials (E_{pa} + E_{pc}) / 2.

Due to the significant changes in peak position, especially at lower pH, depending on whether the BDD is clean or modified, further investigation of the ET kinetics was undertaken. The experiments were repeated in PBS solution of pH ranging from 5 to 8.5. E_{pa}, E_{pc} and ΔE_p are plotted in Figure 3.14. The error bars represent one standard deviation.

Figure 3.14(a) shows how E_{pa} and E_{pc} change with pH of the supporting electrolyte. A linear relationship is observed between peak position and pH for both oxidation and reduction at the BDD electrode, but the rate of change is very different. Analysis of the gradients gives a relationship of 96 and 28 mV per pH unit for E_{pa} and E_{pc}, respectively. The H_2Q/Q redox reaction is usually considered a $2e^-/2H^+$ process:

$$Q + 2e^- + 2H_3O^+ \rightleftharpoons H_2Q + 2H_2O \tag{3.9}$$

Or in alkaline solution:

$$Q + 2e^- + 2H_2O \rightleftharpoons H_2Q + 2OH^- \tag{3.10}$$

A 59 mV shift in peak position with pH is predicted for a Nernstian $2e^-/2H^+$ process.

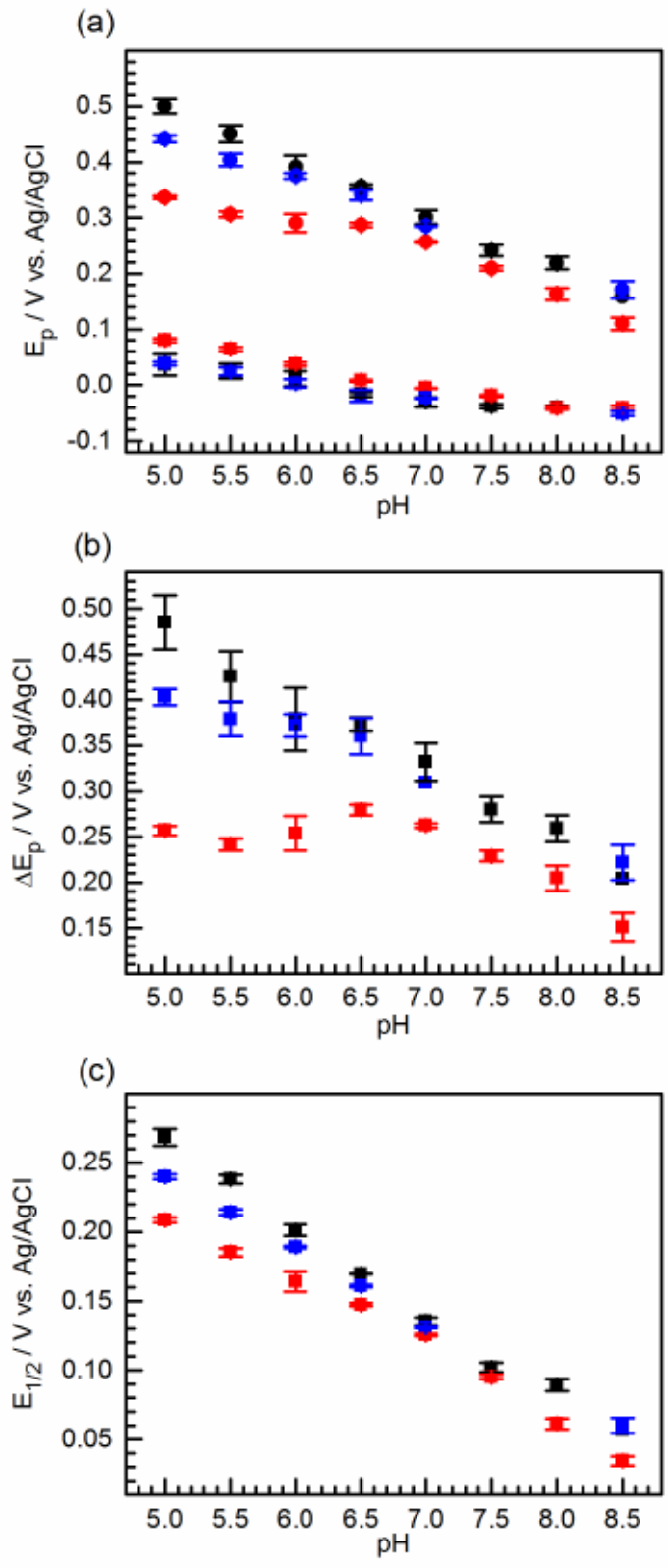

Figure 3.14 (a) Peak potential of hydroquinone oxidation (circles) and benzoquinone reduction (squares); (b) peak separation; (c) $E_{1/2}$ as a function of pH at clean BDD electrode (black), GNF-COOH modified BDD (red) and GNF-amide modified BDD (blue). Adapted from [6].

Figure 3.14(b) shows that ΔE_p at clean BDD is roughly linearly dependent on pH, although the reaction was found to be very surface sensitive and resulted in a large standard deviation. Because the kinetics of the reaction at BDD are so sluggish, it is not possible to estimate the equilibrium potential from experimental data. The Nernst equation describes reversible ET reactions with fast kinetics, which clearly isn't the case for the Q/H_2Q redox reaction at BDD. $E_{1/2}$ was calculated as $E_{pa} - E_{pc}$ and plotted in **Figure 3.14**(c). $E_{1/2}$ exhibits pH-dependent behaviour with a gradient of 61 mV per pH unit at the clean BDD electrode, suggesting that the reaction is a $2e^-$, $2H^+$ process.

At both GNF-COOH and GNF-amide modified BDD, E_{pc} has a similar gradient as E_{pc} at clean BDD. E_{pa} data points follow the linear response for clean BDD in neutral and alkaline conditions but begin to diverge from them in acidic solution, especially at GNF-COOH electrode and to a much lesser extent at GNF-amide electrode (**Figure 3.14**(a)). At both modified electrodes, ΔE_p follows the data for the clean BDD in neutral and slightly alkaline conditions, but at GNF-COOH electrode, ΔE_p becomes independent of pH below pH 6.5. At GNF-amide modified electrode, the pH dependence of ΔE_p follows that at the clean BDD electrode, but deviates from it slightly at more acidic solutions.

For the GNF-COOH modified electrode two distinct behaviours can be noted. At pH > 6.5 the relationship between $E_{1/2}$ and pH is similar to that seen at BDD (61 mV per pH unit). However at pH < 6.5 a different gradient of 40 mV per pH unit can be fitted to the data. Clearly a change in reaction mechanism takes place at ca. pH 6.5, or alternatively the manner in which the H_2Q reactant or Q product interacts with GNF-COOH changes in this pH range. The pH-independent behaviour of ΔE_p in acidic solution can be understood by considering the slopes of E_{pa} and E_{pc}, which are roughly equal below pH 6.5.

The change in the reaction mechanism occurs in the pH region where COOH groups are in a dynamic equilibrium with carboxylate groups as seen in the titration curve (**Figure 3.5**). At these lower pH values there would be protons readily available at the

flake edges to participate in proton transfer reactions and to provide hydrogen bonding sites, thereby creating conditions that differ substantially from those in the bulk solution.

A 40 mV shift with pH unit is close to the theoretical value of 29.5 mV per pH unit predicted for a $2e^-/1H^+$ process:

$$Q + 2e^- + H_3O^+ \rightleftharpoons HQ^- + H_2O \qquad (3.11)$$

Such a reaction mechanism is unlikely in acidic, buffered solution as it requires hydroquinone to be deprotonated, which is not possible given its pK_a is 9.9 [18]. A mechanism with a $2e^-/1H^+$ relationship would however be possible in the presence of an additional, non-solution, source of protons, such as the COOH-terminating groups offered by GNF-COOH:

$$Q + 2e^- + \text{GNF-COOH} + H_3O^+ \rightleftharpoons H_2Q + \text{GNF-COO}^- + H_2O \qquad (3.12)$$

In the case of the hydroquinone oxidation reaction it has been shown that modification of glassy carbon electrodes with phthalate bases (which contain two COOH groups) shifts the oxidation potential cathodically [19]. The proposed mechanism involves surface COO^- groups accepting the protons liberated in the oxidation of hydroquinone and thus stabilising the reaction products. In effect the shift in oxidation potential is a thermodynamic consequence of the change in reaction mechanism rather than an improvement in electron transfer kinetics.

A similar process may be taking place in our system. Some improvement in electron transfer kinetics is observed on modifying the BDD electrode with GNF, as can be seen in the increase in oxidation peak currents for both GNF-amide and GNF-COOH electrodes (**Figure 3.13**). The GNF-amide electrode also shows a small cathodic shift in oxidation potential as pH is lowered, indicating improved electron transfer kinetics. H_2Q/Q can interact with the GNF via hydrogen bonding or electrostatic interactions with the edge groups or by hydrophobic or π–π interactions with the GNF basal plane. Such

surface adsorption has been proposed to explain the improved electron transfer kinetics for this process (both oxidation and reduction) experienced at sp^2 carbon materials [20] in comparison to BDD, where limited surface adsorption is believed to take place [21]. It is also possible that some acid groups remain at the GNF, as discussed in section 3.3.3, and that there are enough of these acid groups to cause a noticeable difference in the reaction. The marked change in proton concentration dependence noted at pH < 7 is unique to the acid-terminated GNF and strongly suggests the COOH groups play a role in the reaction mechanism, as shown in Equation (3.12). At pH > 7 the solution is sufficiently basic to allow the deprotonation accompanying hydroquinone oxidation to proceed predominantly via a solution phase mechanism involving OH^- as the base (Equation (3.10)). However at pH < 7 there is a strong thermodynamic driving force for the COOH edge groups of the GNF to protonate, concomitant with conditions where there are fewer basic solution species. At this point a mechanism such as that shown in Equation (3.12) begins to dominate and is reflected by the change in proton concentration dependence of the oxidation peak position.

3.3.8.2 Exploring the Mechanism for Hydroquinone Oxidation

Proton-coupled electron transfer (PCET) reactions play a key role in essential biological processes. Quinone groups are often involved in PCET reactions [22], as is the case for photosynthesis, where the reduction of plastoquinone and oxidation of the phenol group of a tyrosine residue are central to the function of photosystem II [23]. PCET can occur stepwise, where either the proton or the electron is transferred first, or in a concerted fashion (CPET), where both the proton and the electron are transferred in a single step [24]. The concerted pathway avoids high-energy intermediates and therefore tends to exhibit a lower overpotential [25]. For a long time, significant effort has been made to elucidate the mechanism of various PCET reactions in order to understand and mimic the efficiency of enzymatic systems.

A sequential PCET mechanism can be confirmed if an intermediate can be isolated experimentally. This may not always be straightforward, and other techniques have been developed to distinguish the stepwise pathways from a concerted pathway. The extensive mechanistic studies of phenol oxidation undertaken by Savéant and co-workers [24, 26] show that cyclic voltammetry experiments in unbuffered media can confirm or rule out a concerted pathway. If CPET is operative, the oxidation wave is expected to shift to a higher potential with respect to a buffered electrolyte having the same pH, while its peak potential should be independent of the pH for pH values below the pK_a of the phenolic OH. The assignment of CPET can be further corroborated by a kinetic isotope effect which can be revealed by comparing CVs recorded in D_2O and H_2O.

In order to explore the mechanism of proton and electron transfer for the H_2Q/Q couple, experiments were carried out in unbuffered media in the pH range 5.5 to 8.2. Cyclic voltammograms recorded in 0.1 M KCl and the associated oxidation peak potentials are shown in **Figure 3.15**. The data show that in unbuffered media the E_{pa} is shifted to higher potentials compared to buffered solutions and, crucially, the E_{pa} values are independent of pH over this pH range. The behaviour of hydroquinone in D_2O was also studied. **Figure 3.15**(c) shows the cyclic voltammogram at clean BDD in D_2O. The pD of the D_2O solution, based on the smaller dissociation constant of D_2O, is estimated to be 0.4 units higher than the pH of a corresponding H_2O solution and therefore about 6.6. When D_2O is used as the solvent, the main oxidation peak potential shifts to higher values compared to H_2O of similar pH.

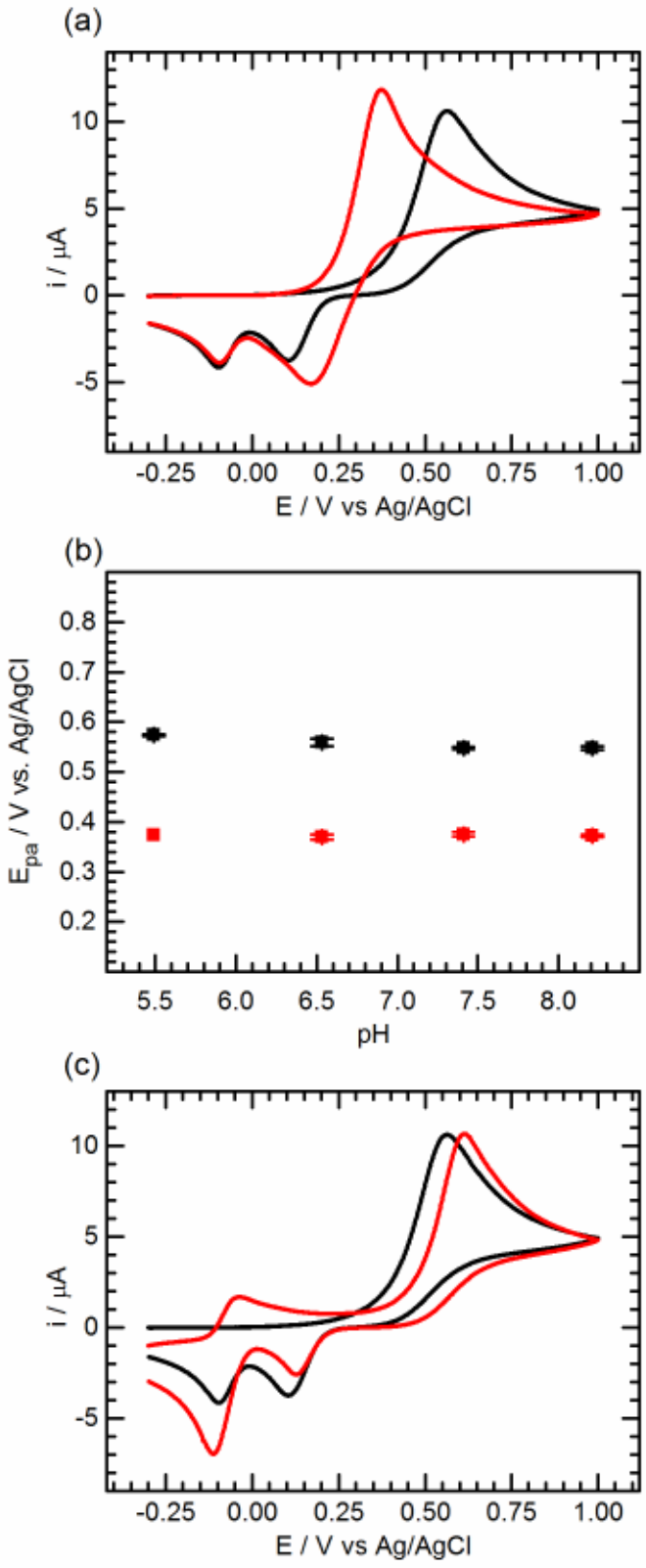

Figure 3.15 (a) CVs of 0.5 × 10^{-3} M hydroquinone at clean BDD electrode (black line) and GNF-COOH modified electrode (red line) in unbuffered H_2O pH 6.6. (b) Peak potential of hydroquinone oxidation in unbuffered KCl electrolyte as a function of pH at a clean BDD electrode (black) and GNF-COOH modified electrode (red). (c) CVs of 0.5 × 10^{-3} M hydroquinone at clean BDD electrode in unbuffered H_2O pH 6.5 (black line) and D_2O pD 6.6 (red line). Supporting electrolyte: 0.1 M KCl. Scan rate: 50 mV s^{-1}. First scans shown. Adapted from [27].

A second set of peaks at more negative potentials appear in unbuffered solutions after the initial oxidation wave. **Figure 3.16**(a) gives a comparison of the CVs at clean BDD and GNF-COOH modified BDD at pH 8.21. The ratio of peak heights is plotted in **Figure 3.16**(b) as a function of pH. The peak separation of ca. 60 mV is indicative of reversible kinetics, and the peak potentials are independent of pH over the pH range examined. The fact that the peak height of this reversible redox wave decreases with decreasing pH suggests it is due to a stepwise PET as described by Costentin et al [24]. The reversible kinetics support the assignment of this mechanism. Upon modification of the electrode with GNF-COOH, there is no shift in E_{pa}, but the height of peak II is smaller, and the ratio of peak currents at GNF-COOH modified electrode increases more rapidly under acidic conditions. These observations are in agreement with the conclusions made above regarding the role played by COOH groups in the reaction mechanism. When GNF-COOH are present on the electrode surface they can act as a proton source and sink, allowing the reaction to proceed to a greater extent via the concerted pathway. The results presented here are in agreement with those reported by Costentin et al. [24] in the above-mentioned paper and strongly suggest that the oxidation of hydroquinone at both BDD and GNF-COOH modified BDD follows the CPET mechanism in buffered media. In unbuffered media, two competing pathways are operative: CPET, which dominates in acidic solutions, and PET in basic conditions.

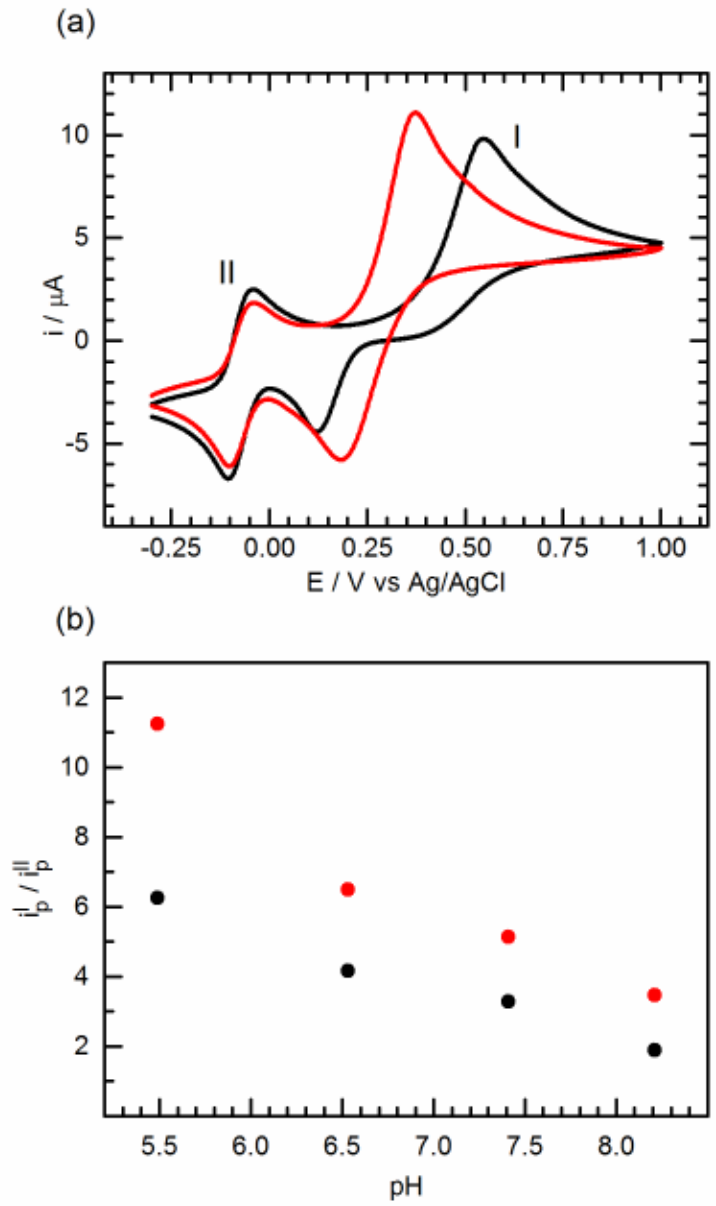

Figure 3.16 (a) CV of 0.5 × 10^{-3} M hydroquinone at clean BDD electrode (black line) and GNF-COOH modified electrode (red line) in unbuffered H2O. The pH of the H2O electrolyte solution was adjusted to 8.21 with KOH. Supporting electrolyte: 0.1 M KCl. Scan rate: 50 mV s^{-1}. Second scans shown. (b) Ratio of peak heights of hydroquinone oxidation as a function of pH at clean BDD electrode (black) and GNF-COOH modified electrode (red). Adapted from [27].

3.3.9 Electrochemistry of $[Ru(NH_3)_6]^{2+/3+}$ at GNF-Modified Electrode

$[Ru(NH_3)_6]^{3+/2+}$ is considered an outer-sphere redox couple that is often used as a standard probe as it undergoes a reversible one-electron redox reaction. However, both the reduced and especially the oxidised species carry a large positive charge and we can expect the GNF to be negatively charged at pH values above ca. 3. Therefore, we were interested to see if there was any interaction between the positively charged redox probe and the negative charge at the modified electrode.

Cyclic voltammograms were recorded in 0.1 M PBS at pH 7 at both clean BDD and BDD modified with GNF-COOH, and the results are shown in **Figure 3.17**. Reversible behaviour was seen in our experiments at a clean BDD electrode (**Figure 3.17**(a)) with peaks at −219 mV and −149 mV for reduction and oxidation, respectively. The peak potentials are independent of scan rate in the range 50–250 mV s^{-1} and the peak separation is 70 mV, which is close to the theoretical value of 59 mV. At GNF-COOH modified electrode, the current peaks occur at the same potentials as at the unmodified BDD. There is also a slight increase in the reduction current. However, what is noticeable especially at higher scan rates (**Figure 3.17**(b)) is the changed shape of the current response. The reaction clearly doesn't follow the usual mass transfer regime at the GNF-COOH modified electrode, but instead there is an additional set of peaks appearing at ca. −350 mV (reduction) and −300 mV (oxidation).

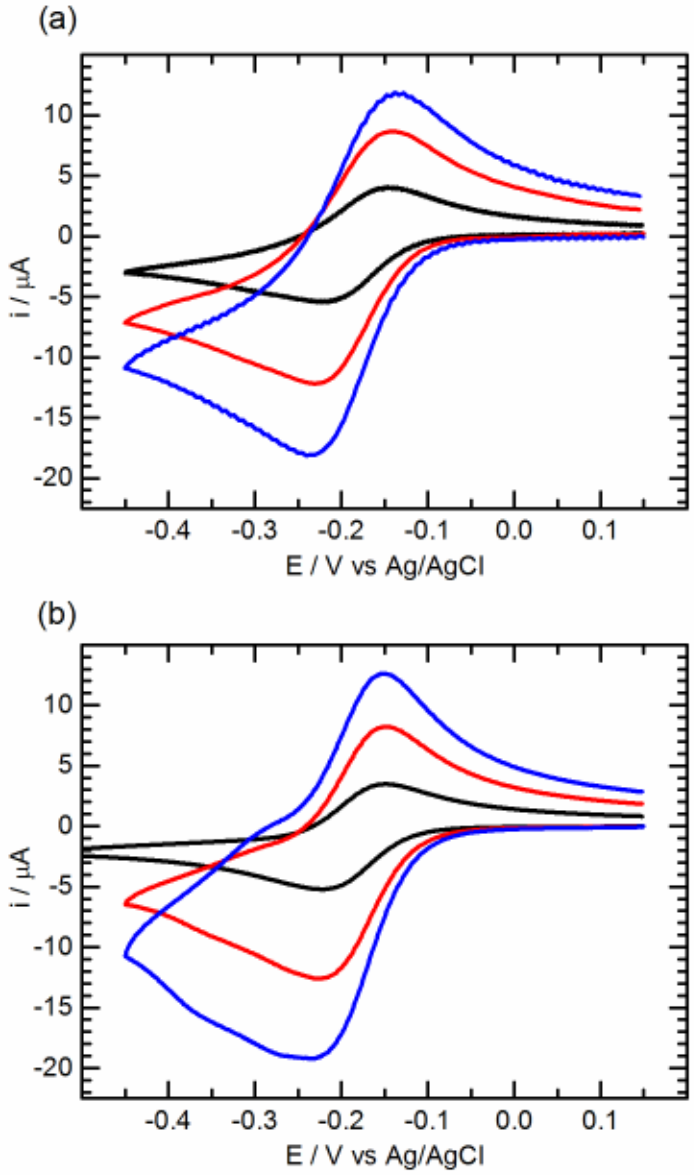

Figure 3.17 Cyclic voltammograms of 0.5×10^{-3} M $[Ru(NH_3)_6]Cl_3$ in 0.1 M PBS pH 7 at (a) clean BDD and (b) GNF-COOH modified BDD. Scan rates 50 mV s^{-1} (black), 250 mV s^{-1} (red) and 500 mV s^{-1} (blue).

The additional peaks in **Figure 3.17**(b) are poorly resolved, possibly because there is only a small amount of GNF-COOH present at the electrode surface and hence the surface area has not increased appreciably. To be able to analyse the CVs and determine the mechanism responsible for the redox peaks, a signal enhancement was needed. To achieve this, GNF complexed with Ca^{2+} were used. There will be an increase in the concentration of GNF material on the electrode surface due to the

insolubility of the Ca^{2+} complexed flakes that is expected to increase the intensity of the additional set of peaks compared to the acid-terminated GNF.

Using GNF-Ca modified BDD, cyclic voltammograms were recorded at scan rates ranging from 5 to 500 mV s^{-1} (**Figure 3.18**). Modifying the electrode with GNF-Ca has clearly enhanced the second set of peaks compared to **Figure 3.17**(b).

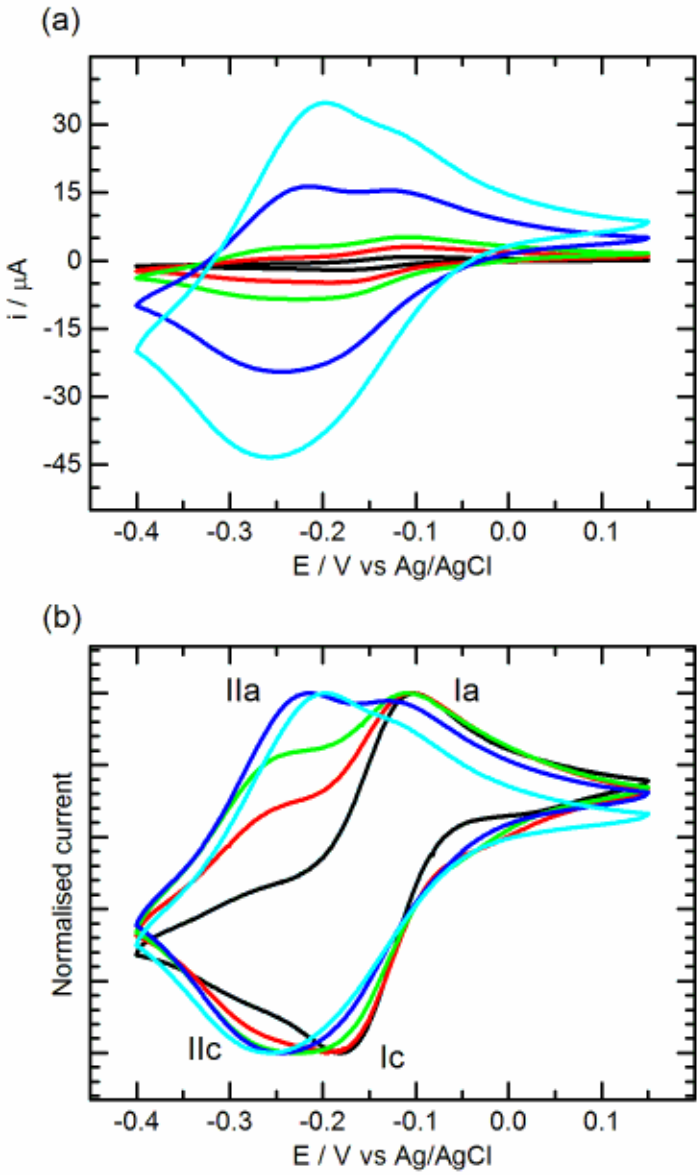

Figure 3.18 (a) Cyclic voltammograms of 0.5 × 10^{-3} M $[Ru(NH_3)_6]Cl_3$ in 0.1 M PBS pH 3 at GNF-Ca modified BDD. Scan rates 5 (black), 25 (red), 50 (green), 250 (blue) and 500 (light blue) mV s^{-1}. (b) Cyclic voltammograms from (a) with normalised current.

The appearance of additional peaks in a cyclic voltammogram may be due to chemical reactions leading to different species or adsorption onto the electrode surface. The potential at which the new set of peaks occurs relative to the solution phase process can reveal whether only the oxidised or the reduced species is adsorbed. Peaks at potentials more negative than the solution-phase redox peaks are due to the oxidised species being adsorbed onto the electrode surface. The stronger the adsorption of the oxidised species, the more the postpeak succeeds the diffusion peak. When adsorption is weak, the difference in energies for reduction of adsorbed and dissolved species is small, and a separate postpeak is not observed.

In this case we see a poorly resolved postpeak, especially for the cathodic process, that could arise from only the oxidised species being adsorbed. To investigate whether one or both redox states are adsorbed, the scan rate dependence of the peak current was studied. For a diffusion-controlled redox reaction of a solution species the peak current increases linearly as a function of the square root of the scan rate, whereas for an adsorbed species, there is a linear relationship between the peak current and the scan rate.

The oxidation peak heights, i_{pa}, from **Figure 3.18**(a) are plotted against either v or $v^{1/2}$ and shown in **Figure 3.19**. Only the oxidation peaks were chosen as peak IIa is more clearly resolved in the cyclic voltammograms than IIc. From **Figure 3.19**(a), the linear relationship of i_{pa} confirms that peaks Ia and Ic stem from the solution-phase redox process:

$$[Ru(NH_3)_6]^{3+} (aq) + e^- \rightleftharpoons [Ru(NH_3)_6]^{2+} (aq) \qquad (3.13)$$

As i_{pa} of peak IIa depends linearly on v and not $v^{1/2}$, it can be concluded that peaks IIa and IIc arise from adsorbed species:

$$[Ru(NH_3)_6]^{3+} (ads) + e^- \rightleftharpoons [Ru(NH_3)_6]^{2+} (ads) \qquad (3.14)$$

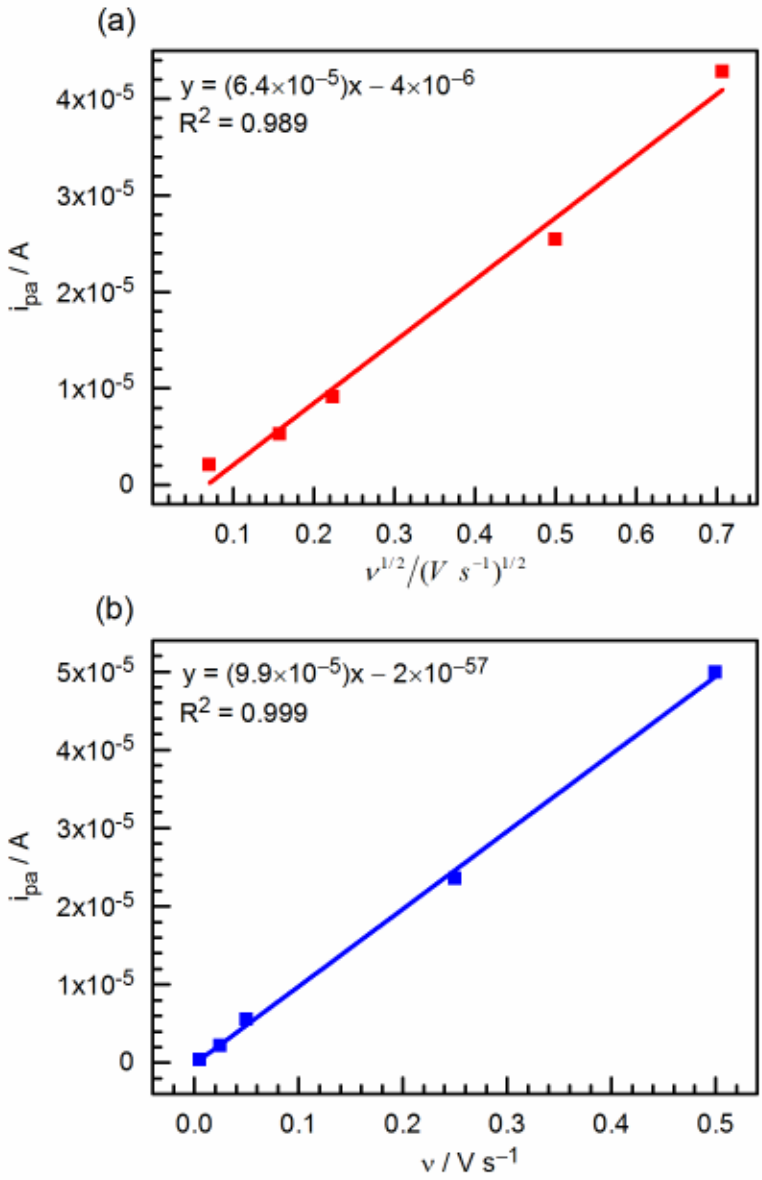

Figure 3.19 (a) Peak current i_{pa} of peak Ia determined from **Figure 3.18**(a) plotted against the square root of scan rate v. (d) i_{pa} of peak IIa determined from **Figure 3.18**(a) plotted against v.

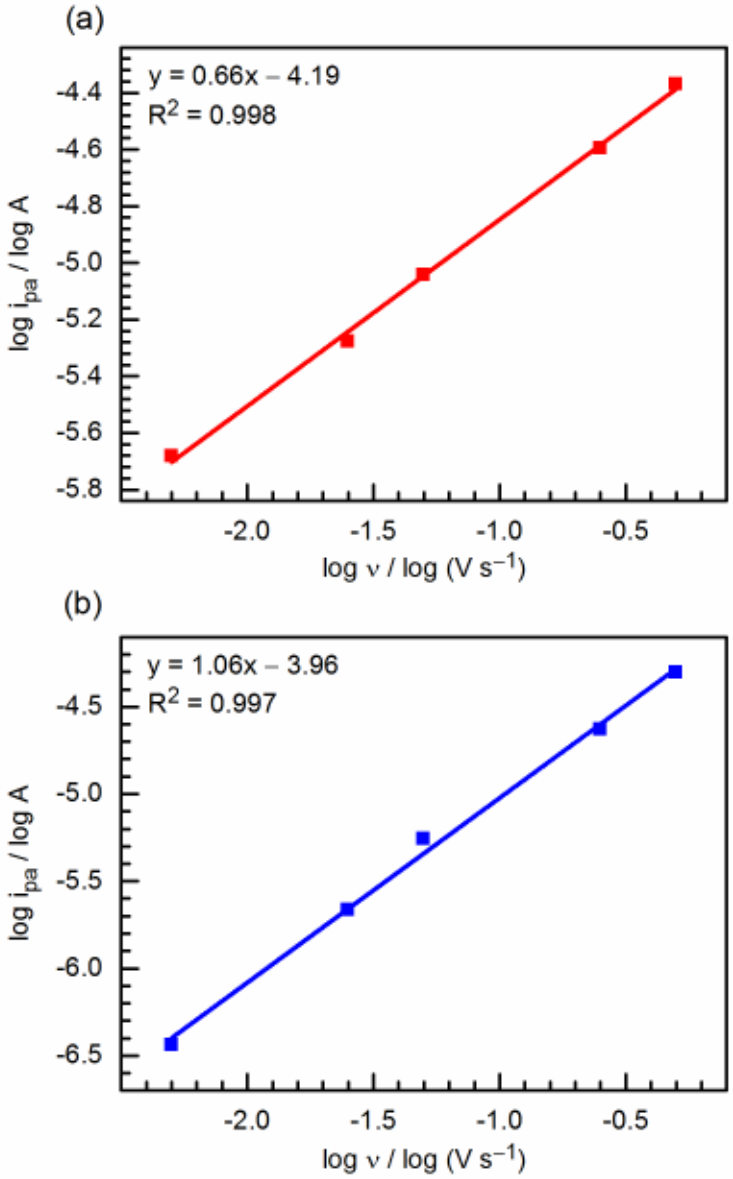

Figure 3.20 log i_{pa} of (a) peak Ia and (b) peak IIa determined from **Figure 3.19**(a) plotted against log v.

Logarithms were taken of the peak currents and these were plotted against the logarithm of scan rate in **Figure 3.20**. A linear relationship is expected and the gradient can be used to assess the extent of adsorption contributing to the redox process. A value of 0.5 is indicative of diffusion control, whereas values above that indicate adsorption alongside diffusion. **Figure 3.20**(a) shows that the gradient for peak Ia is significantly above 0.5, suggesting that adsorption contributes to the diffusion-

controlled redox reaction. In **Figure 3.20**(b) the gradient for peak IIa is close to 1, confirming that only adsorbed species are contributing to this peak.

We assume that a similar adsorption is taking place at the acid-terminated GNF, but due to the smaller amount of material adhering to the electrode surface the additional peaks are smaller in size, which restricts any analytical treatment of the peak currents. GNF-Ca on the other hand is insoluble and therefore will adhere more strongly to the BDD surface, allowing a greater amount of $[Ru(NH_3)_6]^{3+/2+}$ to adsorb onto the modified electrode surface, which leads to more intense redox peaks arising from the adsorbed species.

It is unclear whether the $[Ru(NH_3)_6]^{3+/2+}$ species is adsorbed onto the basal plane of the GNF or whether it is interacting electrostatically with the negatively charged carboxylate functionalities. The presence of carboxylic acids in GNF-Ca can be detected in the IR spectrum (**Figure 3.4**) and the ratio of free carboxylate groups to carboxylates complexed with Ca^{2+} was estimated from XPS data in Section 3.3.2. Considering that there is a significant number of non-complexed functionalities present, it is feasible that $[Ru(NH_3)_6]^{3+}$ forms an ion pair with the free COO^- groups. To see if the metal centre could be reduced and oxidised while the ligands are interacting electrostatically with carboxylate groups, acid-terminated GNF were complexed with $[Ru(NH_3)_6]^{3+}$. Cyclic voltammetry recorded with different scan rates (**Figure 3.21**(a)) revealed a poorly resolved reduction peak in the form of a shoulder at −326 mV and an oxidation peak at −184 mV when v = 100 mV s^{-1}. Although oxygen was removed from the electrolyte prior to recording the CVs, residual oxygen may be present that undergoes reduction at the modified electrode in the same potential range where $[Ru(NH_3)_6]^{3+}$ is reduced. Additionally, the onset of hydrogen evolution can also interfere with the current response at more negative potentials, making it difficult to determine the peak potential and the current arising from $[Ru(NH_3)_6]^{3+}$ reduction. Further analysis will therefore be confined to the oxidation peak only.

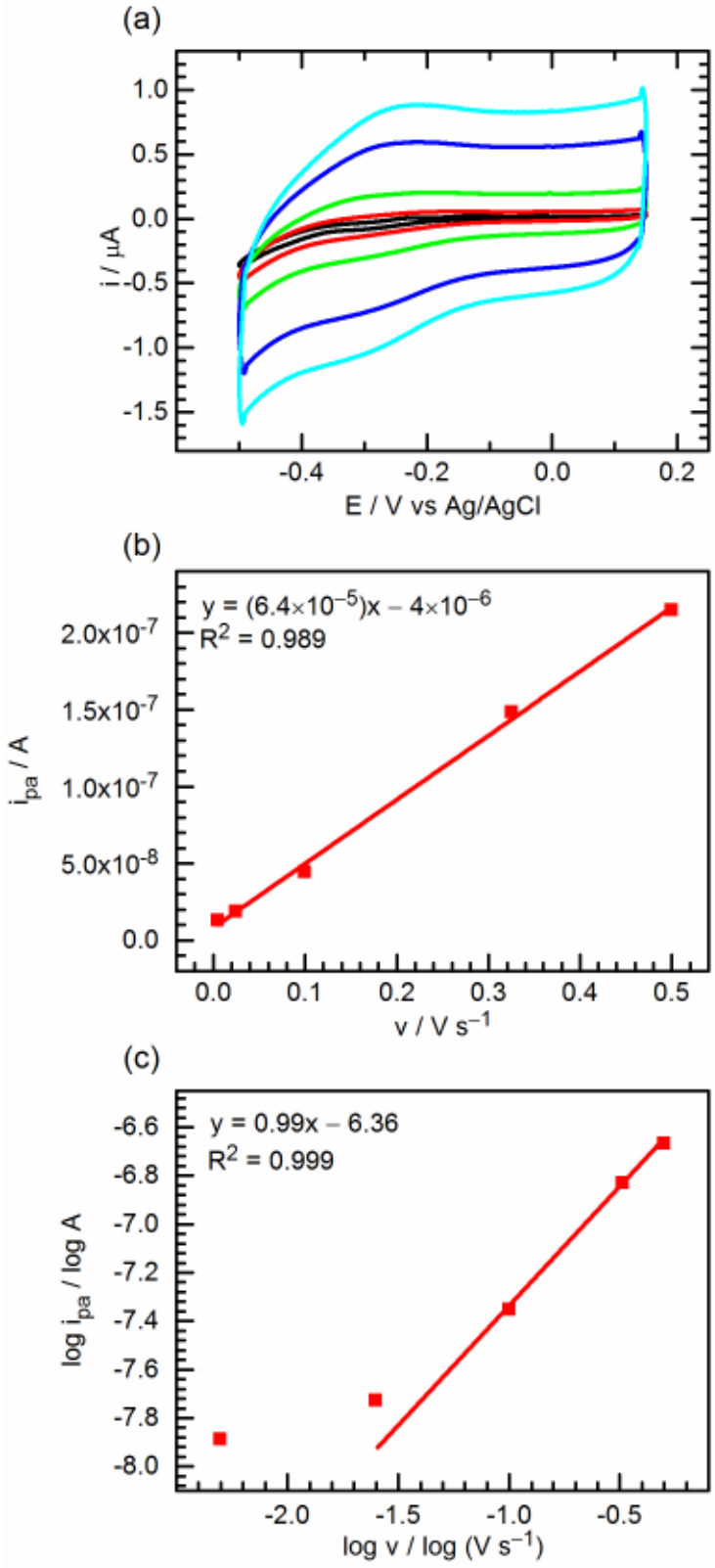

Figure 3.21 (a) Cyclic voltammograms recorded at a BDD modified with $[Ru(NH_3)_6]^{3+}$ complexed GNF. Scan rates 5 (black), 25 (red), 100 (green), 325 (blue) and 500 (light blue) mV s^{-1}. Electrolyte: 0.1 M K_2HPO_4. (b) A plot of oxidation peak current i_{pa} against scan rate v. (c) log i_{pa} plotted against log v.

Scan rate study (**Figure 3.21**(b)) shows that the oxidation peak current is linearly dependent on the scan rate, indicating that the redox reaction is not diffusion controlled and therefore the redox species is bound to the surface. When the scan rate is 5 mV s^{-1}, several oxidation peaks can be discerned in the current trace. This suggests that the $[Ru(NH_3)_6]^{3+}$ species exists in more than one environment, perhaps due to various coordination modes and numbers of the amine ligands to the carboxylate groups at the flake edges.

Table 3.3 shows the oxidation peak potential values at different scan rates together with peak currents. It can be seen that the main oxidation peak shifts with scan rate and varies from −145 mV at v = 25 mV s^{-1} to −225 mV at v = 500 mV s^{-1}. The cathodic peak potentials are relatively stable with a slight shift to more negative potentials, although as mentioned earlier it is difficult to determine the E_{pc} with certainty. The shift in E_{pa} and the asymmetric shape of the oxidation peak further suggests that the $[Ru(NH_3)_6]^{3+}$ species exists in various different environments when the precipitate is formed. Some of the $[Ru(NH_3)_6]^{3+}$ species may be so weakly complexed with the COO^- that the interaction between the charged species can be overcome by immersion in electrolyte or applying a potential. This results in a population of both surface-bound and solution-phase $[Ru(NH_3)_6]^{3+}$ that would undergo reduction and consequent oxidation at different potentials. The solution-phase $[Ru(NH_3)_6]^{3+}$ would give more prominent redox peaks at lower scan rates while at higher scan rates the adsorbed species would present more intense redox peaks.

The existence of both adsorbed and solution-phase species is evident when the plot of log i_{pa} against log v is examined (**Figure 3.21**(c)). The data points can't be fitted with a linear regression line, and although the regression coefficient is close to 1 at higher scan rates, at slow scan rates the relationship between log i_{pa} and log v deviates significantly from what is expected of a non-diffusion controlled process.

Table 3.3: Scan rates, oxidation peak currents and oxidation peak potentials extracted from **Figure 3.21**.

v / mV s^{-1}	I_{pa} / µA	E_{pa} / V
5	0.0129	−0.119
25	0.0187	−0.145
100	0.0445	−0.184
325	0.148	−0.213
500	0.215	−0.225

3.4 Conclusion

In this chapter, further characterisation of GNF materials is presented to complement existing data found in literature [7, 8], focusing on the acid/base properties of GNF-COOH, IR spectroscopy and electrochemical characterisation using cyclic voltammetry both with and without redox probes.

Modifying the BDD surface with GNF results in a clearly detectable difference in the voltammetric response compared to the unmodified surface across the whole pH range examined. Therefore, CV in the aqueous phase can be employed to study the various GNF samples by using a BDD electrode modified with a layer of adsorbed GNF.

Neither amide nor carboxylic acid –terminated GNF shows a detrimental effect on electron transfer rate with respect to the outer-sphere FcMeOH redox couple. This result is consistent with the observed fast electron transfer kinetics towards these species obtained using single layer graphene electrodes [12, 28]. The high density of carboxylic acid or amide functionalities does not appear to perturb the electrochemical response under these reaction conditions.

pH titration experiments reveal that in solution pH of ca. 4 to 8 the edge groups are present in a range of protonation states. The response towards hydroquinone reduction

shows deviation from the response at clean BDD at pH < 7 and in more acidic pH conditions the edge groups clearly play a role in the reaction mechanism.

At the present time it is unclear in what orientation the GNF are arranged on the electrode surface, as their small size and transparency makes the immobilised layer difficult to characterise. However as the coverage and flake orientation will clearly be important for fully understanding the electrochemical response, further studies into the determination and control of the electrode layer morphology are needed and these will be described in Chapter 6.

References for Chapter 3

1. McCreery, R. L., Advanced Carbon Electrode Materials for Molecular Electrochemistry. *Chem. Rev.* **2008,** *108* (7), 2646-2687.
2. Wildgoose, G. G.; Abiman, P.; Compton, R. G., Characterising Chemical Functionality on Carbon Surfaces. *J. Mater. Chem.* **2009,** *19* (28), 4875-4886.
3. McDermott, C. A.; Kneten, K. R.; McCreery, R. L., Electron Transfer Kinetics of Aquated $Fe^{+3/+2}$, $Eu^{+3/+2}$, and $V^{+3/+2}$ at Carbon Electrodes: Inner Sphere Catalysis by Surface Oxides. *J. Electrochem. Soc.* **1993,** *140* (9), 2593-2599.
4. Chen, P.; Fryling, M. A.; McCreery, R. L., Electron Transfer Kinetics at Modified Carbon Electrode Surfaces: The Role of Specific Surface Sites. *Analytical Chemistry* **1995,** *67* (18), 3115-3122.
5. Chen, P.; McCreery, R. L., Control of Electron Transfer Kinetics at Glassy Carbon Electrodes by Specific Surface Modification. *Analytical Chemistry* **1996,** *68* (22), 3958-3965.
6. Lounasvuori, M. M.; Rosillo-Lopez, M.; Salzmann, C. G., et al., Electrochemical Characterisation of Graphene Nanoflakes with Functionalised Edges. *Faraday Discussions* **2014,** *172* ( ), 293-310.
7. Salzmann, C. G.; Nicolosi, V.; Green, M. L. H., Edge-Carboxylated Graphene Nanoflakes from Nitric Acid Oxidised Arc-Discharge Material. *J. Mater. Chem.* **2010,** *20* (2), 314-319.
8. Rosillo-Lopez, M.; Lee, T. J.; Bella, M., et al., Formation and Chemistry of Carboxylic Anhydrides at the Graphene Edge. *RSC Advances* **2015,** *5* (126), 104198-104202.
9. Sutton, C. C. R.; Franks, G. V.; da Silva, G., Modeling the Antisymmetric and Symmetric Stretching Vibrational Modes of Aqueous Carboxylate Anions. *Spectrochimica Acta Part A: Molecular and Biomolecular Spectroscopy* **2015,** *134*, 535-542.
10. Szabó, T.; Berkesi, O.; Dékány, I., DRIFT Study of Deuterium-Exchanged Graphite Oxide. *Carbon* **2005,** *43* (15), 3186-3189.
11. Lounasvuori, M. M.; Rosillo-Lopez, M.; Salzmann, C. G., et al., The Influence of Acidic Edge Groups on the Electrochemical Performance of Graphene Nanoflakes. *J. Electroanal. Chem.* **2015,** *753*, 28-34.
12. Li, W.; Tan, C.; Lowe, M. A., et al., Electrochemistry of Individual Monolayer Graphene Sheets. *ACS Nano* **2011,** *5* (3), 2264-2270.
13. Bard, A. J.; Faulkner, L. R.; Leddy, J., *Electrochemical Methods : Fundamentals and Applications*. 2nd ed.; Wiley: New York ; Chichester, 2001; p xxi, 833 p.
14. Mukherjee, S.; Kumar, S.; Misra, A. K., et al., Removal of Phenols from Water Environment by Activated Carbon, Bagasse Ash and Wood Charcoal. *Chem. Eng. J.* **2007,** *129* (1–3), 133-142.
15. Nordlund, J. J.; Grimes, P. E.; Ortonne, J. P., The Safety of Hydroquinone. *Journal of the European Academy of Dermatology and Venereology* **2006,** *20* (7), 781-787.
16. Enguita, F. J.; Leitao, A. L., Hydroquinone: Environmental Pollution, Toxicity, and Microbial Answers. *Biomed Research International* **2013**.

17. Duo, I.; Levy-Clement, C.; Fujishima, A., et al., Electron Transfer Kinetics on Boron-Doped Diamond Part I: Influence of Anodic Treatment. *J. Appl. Electrochem.* **2004,** *34* (9), 935-943.
18. Baxendale, J. H.; Hardy, H. R., The Ionization Constants of Some Hydroquinones. *Transactions of the Faraday Society* **1953,** *49* (0), 1140-1144.
19. Medina-Ramos, J.; Alligrant, T. M.; Clingenpeel, A., et al., Comparing the Hydrogen-Bonding Effect of Brönsted Bases in Solution and When They Are Covalently Bound to the Surface of Glassy Carbon Electrodes in the Electrochemical Behavior of Hydroquinone. *The Journal of Physical Chemistry C* **2012,** *116* (38), 20447-20457.
20. DuVall, S. H.; McCreery, R. L., Control of Catechol and Hydroquinone Electron-Transfer Kinetics on Native and Modified Glassy Carbon Electrodes. *Analytical Chemistry* **1999,** *71* (20), 4594-4602.
21. Granger, M. C.; Witek, M.; Xu, J., et al., Standard Electrochemical Behavior of High-Quality, Boron-Doped Polycrystalline Diamond Thin-Film Electrodes. *Analytical Chemistry* **2000,** *72* (16), 3793-3804.
22. Quan, M.; Sanchez, D.; Wasylkiw, M. F., et al., Voltammetry of Quinones in Unbuffered Aqueous Solution: Reassessing the Roles of Proton Transfer and Hydrogen Bonding in the Aqueous Electrochemistry of Quinones. *J. Am. Chem. Soc.* **2007,** *129* (42), 12847-12856.
23. Kern, J.; Renger, G., Photosystem II: Structure and Mechanism of the Water:Plastoquinone Oxidoreductase. *Photosynth. Res.* **2007,** *94* (2), 183-202.
24. Costentin, C.; Louault, C.; Robert, M., et al., Evidence for Concerted Proton−Electron Transfer in the Electrochemical Oxidation of Phenols with Water as Proton Acceptor. Tri-Tert-Butylphenol. *J. Am. Chem. Soc.* **2008,** *130* (47), 15817-15819.
25. Hammes-Schiffer, S., Proton-Coupled Electron Transfer: Moving Together and Charging Forward. *J. Am. Chem. Soc.* **2015,** *137* (28), 8860-8871.
26. Costentin, C.; Louault, C.; Robert, M., et al., The Electrochemical Approach to Concerted Proton—Electron Transfers in the Oxidation of Phenols in Water. *Proceedings of the National Academy of Sciences* **2009,** *106* (43), 18143-18148.
27. McCreery, R.; Hu, C.-C.; Macpherson, J., et al., Role of Surface Contaminants, Functionalities, Defects and Electronic Structure: General Discussion. *Faraday Discussions* **2014,** *172* (0), 365-395.
28. Valota, A. T.; Kinloch, I. A.; Novoselov, K. S., et al., Electrochemical Behavior of Monolayer and Bilayer Graphene. *ACS Nano* **2011,** *5* (11), 8809-8815.

4 GNF-COOH and Ferri/Ferrocyanide

4.1 Introduction

The $[Fe(CN)_6]^{3-/4-}$ redox couple is often used as a standard probe to characterise electrode surface area and to study electrode kinetics, even though some complicating factors regarding the use of this probe are well documented. Several previous reports have found that, especially at metal electrodes, the standard heterogeneous electron transfer rate constant k^0 of $[Fe(CN)_6]^{3-/4-}$ depends on the identity and concentration of the supporting electrolyte [1, 2]. Noel and Anantharaman [3] have observed the cation dependence at glassy carbon electrodes, showing that the effect is not limited to metal electrodes. An increase in k^0 with increasing potassium ion concentration was attributed to a transition state complex involving K^+ [1], in agreement with previous reports from Sohr et al.[4, 5] who devised a model of the redox species forming a dimer via a bridging cation.

A systematic investigation into the influence of surface oxygen functionalities using glassy carbon electrodes showed that the $[Fe(CN)_6]^{3-/4-}$ CV response did not show a dependence on any specific surface oxygen groups, although it was sensitive to the presence of adsorbates [6]. However, other studies have shown pH dependence in the electron transfer kinetics of this couple at glassy carbon electrodes, the process becoming slower as pH is increased [7]. This effect was attributed to the presence of surface carboxylic acid functionalities that become deprotonated and hence negatively charged in more alkaline solutions; therefore electrostatic repulsion occurs between the electrode surface and the negatively charged redox species. At polycrystalline BDD electrode, the presence of COOH groups slows down the electron transfer kinetics of $[Fe(CN)_6]^{3-/4-}$ dramatically [8, 9], and due to the pH dependence of the reaction, electrostatic repulsion was inferred as the cause of the change in kinetics. Yagi et al. [10] also found that oxygen plasma treatment of BDD caused the HET for this couple to slow down, and although they weren't able to identify the oxygen functionalities on the surface, carboxyl groups were proposed to be present and to act as a repulsive site to negatively charged redox species.

In light of the considerable evidence summarised above showing that carboxylic acid groups at the surface of carbon electrodes slow down the HET for $[Fe(CN)_6]^{3-/4-}$, we chose to study this redox couple at GNF-modified BDD. The abundance of COOH groups present at the edge-carboxylated flakes is expected to magnify any effect the acidic groups may have on this redox couple. At the same time, the amide-terminated GNF can be used as control to confirm that any differences in the electrochemical behaviour are due to the COOH groups and not other factors such as carbonyl groups or increased sp^2 carbon present at the surface.

The work presented in this Chapter has been published in [11].

4.2 Experimental Methods

All aqueous solutions were prepared with doubly deionised water, taken from a Milli-Q water purification system, with a resistivity of not less than 18.2 MΩ cm at 25 °C.

4.2.1 Electrochemical Experiments

Potassium ferricyanide ($K_3[Fe(CN)_6]$) and potassium hexacyanoruthenate(II) ($K_4[Ru(CN)_6]$) were obtained from Sigma-Aldrich and used as received. GNF-COOH were drop-coated onto the working electrode surface or added to the solution along with the redox probe. Other experimental details are described in Section 3.2.5.

4.2.2 Infrared Spectroscopy Experiments

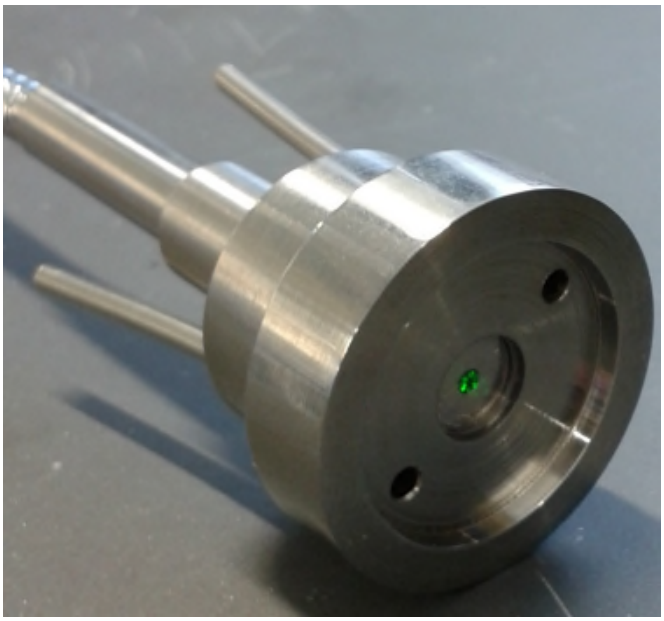

Figure 4.1 Spectroscopy cell used in this Chapter.

The stability of $[Fe(CN)_6]^{3-/4-}$ in solution was investigated by recording the IR absorption of the cyanide ligands over a 24-hour period. ATR-FTIR spectra were recorded with a Bruker ISF 66/S spectrometer (Bruker, UK) fitted with a liquid nitrogen-cooled MCT A detector and a silicon ATR prism at 4 cm^{-1} resolution. A stainless steel

cell (**Figure 4.1**) was placed on top of the IRE with two narrow steel tubes at the top of the cell that acted as the inlet and outlet for the sample. Plastic tubing was attached to the steel tubes and the sample was introduced at one end via a syringe. The sample was then pumped back and forth to remove any air bubbles. The length of the plastic tubing and the small surface area exposed to the atmosphere meant that contamination of samples in D_2O by atmospheric water was minimised. A single spectrum was computed by Fourier transformation of 250 averaged interferograms for background and sample and the software was programmed to record a spectrum every 60 minutes. The background spectrum was of pure water and air for experiments in H_2O and D_2O, respectively. Spectra recorded in H_2O were manipulated using the baseline and atmospheric correction functions in OPUS software. Spectra recorded in D_2O were manipulated by subtracting a spectrum of D_2O only, which was first scaled to match the absorbance at 2080–2740 cm^{-1} in sample spectra.

4.2.3 Spectroelectrochemical Experiments

To probe the effect of solution-phase GNF on the reversibility of the $[Fe(CN)_6]^{3-/4-}$ redox couple, the IR absorption of the cyanide ligands was monitored during oxidation and reduction using an in situ technique. ATR-FTIR spectra were recorded as detailed in Section 4.2.2. An electrochemical cell (**Figure 4.2**) with a volume of 20 µl was used with a Pt mesh working electrode situated 0.1–0.3 mm above the prism. A Pt sheet counter and Ag/AgCl reference electrode were placed in a chamber separated from the sample chamber by a Vycor frit. Working electrode potentials were set at 0 V for reduction of $[Fe(CN)_6]^{3-}$ to $[Fe(CN)_6]^{4-}$ and +350 mV for oxidation of $[Fe(CN)_6]^{4-}$ to $[Fe(CN)_6]^{3-}$. IR difference spectra were constructed by recording a background spectrum at one potential, then switching to the second potential and recording a sample spectrum at specific time intervals.

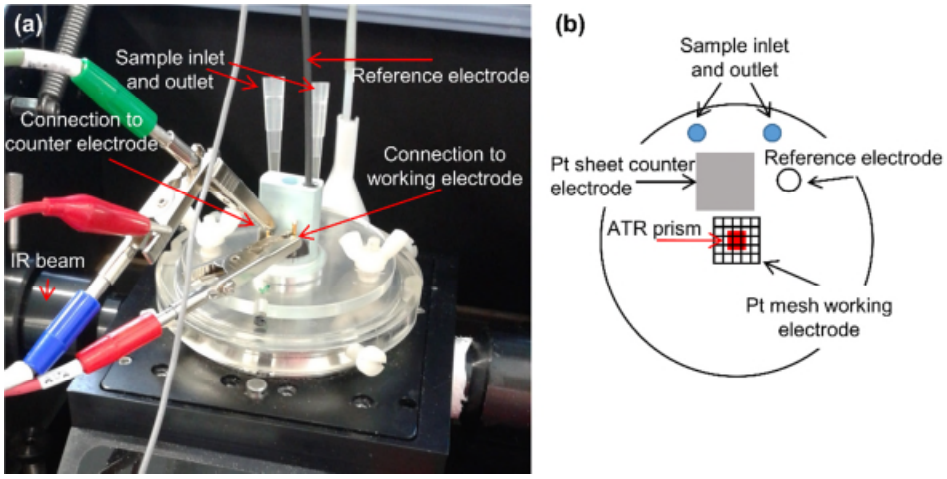

Figure 4.2 (a) Spectroelectrochemical setup used in this Chapter. (b) Schematic of the cell viewed from the top.

4.3 Results and Discussion

4.3.1 The Effect of Solution pH

Figure 4.3(a) shows CVs for 0.5 × 10^{-3} M $K_3[Fe(CN)_6]$ at a clean BDD electrode in background electrolyte of 0.1 M pH 4.6 and 9.2 PBS. At the BDD electrode the peak separation ΔE_p remains constant at (65 ± 2) mV over the whole pH range examined (pH 4.6–9.2) indicating close to reversible electron transfer kinetics. The $E^{0'}$ of the couple, taken as ½(E_{pa} + E_{pc}), shifts towards higher values with increasing pH, being found at ca. 50 mV higher at pH 9.2 than at pH 4.6. The peak currents for oxidation and reduction also decrease marginally over the same pH range. The $[Fe(CN)_6]^{3-/4-}$ electron transfer process has been shown to be inhibited at oxygen-terminated BDD surfaces when the oxygen termination is achieved by acid washing [12] or oxygen plasma treatment [9]; when oxygen termination is introduced by alumina polishing, as in this study, effectively reversible electron transfer kinetics are observed [9]. **Figure 4.3**(a) suggests a small degree of interaction of $[Fe(CN)_6]^{3-/4-}$ with the BDD surface, which is possibly due to the presence of non-diamond-like carbon impurities in the electrode. sp^2-hybridised carbon is a common impurity in BDD electrodes, and on sp^2-

hybridised carbon such as glassy carbon, the $[Fe(CN)_6]^{3-/4-}$ redox reaction is thought to proceed via an adsorbed intermediate [10] because the HET is affected by a physisorbed molecular layer [6].

Figure 4.3(b) shows the response of 0.5×10^{-3} M $K_3[Fe(CN)_6]$ at pH 4.6 and 9.2 at a GNF-COOH modified electrode. The response at this electrode is found to be very dependent on pH, particularly for pH < 8. Peak currents for both oxidation and reduction decrease and ΔE_p increases as the pH is lowered: at pH 7 ΔE_p = 109 mV; pH 6 ΔE_p = 120 mV; pH 5 ΔE_p = 213 mV and pH 4.6 ΔE_p = 250 mV. This indicates that electron transfer becomes slower under these experimental conditions, which could be attributed to a change in the nature of the redox molecule, an unfavourable interaction with the electrode surface (or loss of a favourable interaction) or formation of an adsorbed inhibiting layer on the electrode. The response doesn't show a dependence on time or potential, as it is observed immediately from the first CV scan and the response does not get worse with cycling (currents rather increase marginally with consecutive scans). This would indicate that the effect cannot be attributed to formation of a surface film that deposits as a function of time or applied potential. However it does not preclude the fast, spontaneous formation of an adsorbed layer, formed independently of applied potential.

As detailed in the Introduction to this Chapter, $[Fe(CN)_6]^{3-/4-}$ has been reported to be inhibited by deprotonated carboxylic acid moieties at carbon electrodes. Panzer and Elving [13] reported decreased reversibility on freshly cleaved pyrolytic graphite electrodes in more alkaline solution, but they also saw a shift to more negative potentials with increasing pH for both reduction and oxidation peaks, which was explained by the acid-anion equilibria involving ferrocyanic and ferricyanic acids. What is observed here is the opposite: the more protonated the GNF are, the more unfavourable the interaction is with the negatively charged redox species. No shift

attributable to the acid-anion equilibrium is observed here. In fact, $E^{0'}$ shifts positively with increasing pH, the opposite of what Panzer and Elving reported.

Figure 4.3(c) shows the response of the GNF-amide modified electrode towards 0.5×10^{-3} M $K_3[Fe(CN)_6]$ in 0.1 M pH 4.6 and pH 9.2 PBS. For this electrode there is no pH dependence on the voltammetric response and the electron transfer kinetics appear only slightly less reversible than at clean BDD (ΔE_p = (70 ± 1) mV at 50 mV s^{-1}) over pH range 4.6–9.2. In fact the response is less dependent on pH than at a clean BDD electrode. Thus it is apparent that carbonyl, amide or amine functionalities have little influence on the electrochemical response of $[Fe(CN)_6]^{3-/4-}$ at GNF-modified electrodes. The observed inhibition of current at the GNF-COOH electrode can therefore be attributed specifically to the presence of the acid functionalities.

We estimate from titration of the GNF-COOH (Section 3.3.4) that the COOH edge groups are fully deprotonated at pH higher than 8, hence we might expect the $[Fe(CN)_6]^{3-/4-}$ redox reaction to be inhibited at more alkaline pH. However we observe relatively reversible electrochemistry at pH 7 and above, and at pH 9.2 (where all of the COOH will be deprotonated and negatively charged) the response is identical to that at a clean BDD electrode. Therefore an electrostatic argument for the observed behaviour is clearly inappropriate in this case. Study of the $[Fe(CN)_6]^{3-/4-}$ redox couple is made still more difficult due to its complex solution chemistry, in particular its preference for ion-pairing with solution cations [1-3] and propensity to lose ligands and form aggregates that are intermediates to Prussian Blue film deposition [15-18]. Additionally acid/base equilibria involving protonation of the nitrogen of the cyanide ligands becomes important over some pH ranges (pK_a of $H[Fe(CN)_6]^{3-}$ is ca. 4.2 [19]).

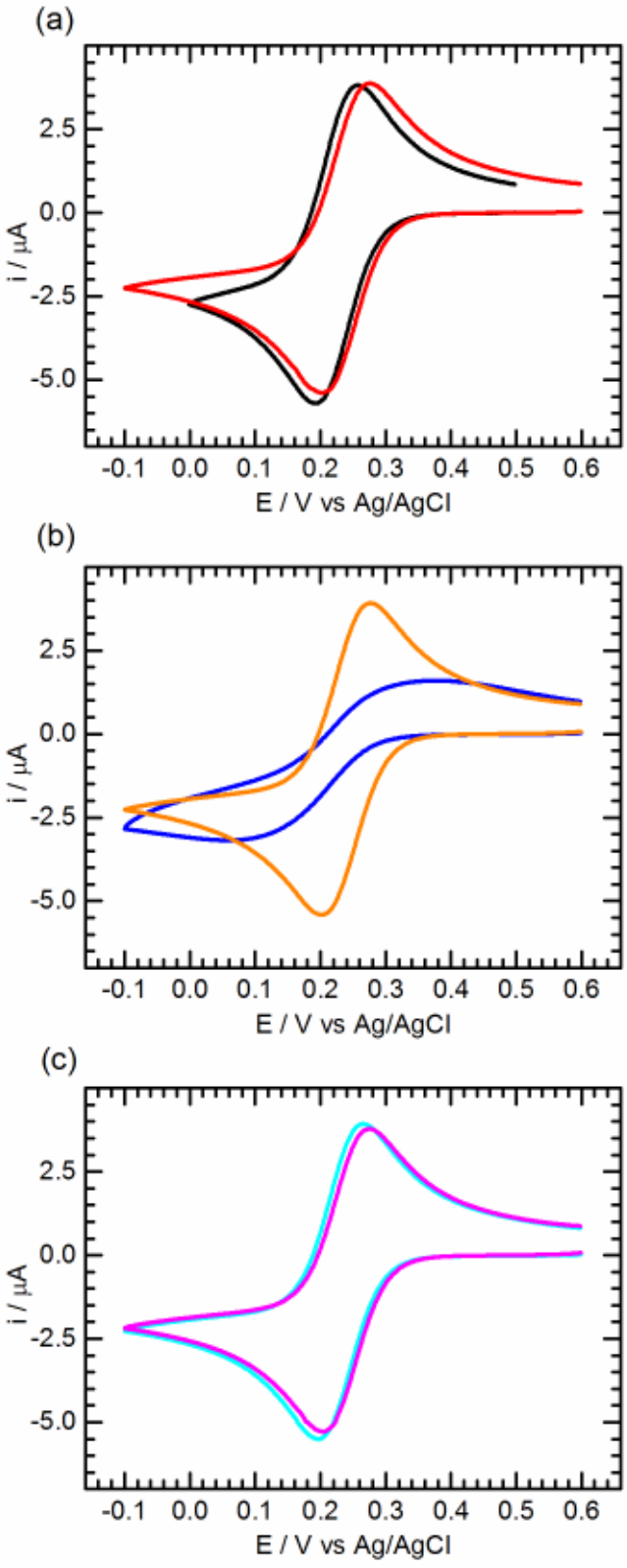

Figure 4.3 Cyclic voltammograms of 0.5×10^{-3} M $K_3[Fe(CN)_6]$ recorded in 0.1 M PBS. Working electrode: (a) BDD; (b) BDD modified with GNF-COOH; (c) BDD modified with GNF-amide. Solution pH 4.6 (black, blue, light blue); 9.2 (red, orange, pink). Scan rate 50 mV s^{-1}. First scans shown. Adapted from [14].

Due to the differing bonding environments of the COOH groups and electrostatic and hydrogen-bonding interactions between neighbouring groups, protonation/deprotonation takes place over a wide pH range, as shown by the titration curve in **Figure 3.5**. We see slower kinetics at the GNF-COOH modified electrode at pH < 8, coinciding with the pH range where GNF-COOH are involved in dynamic protonation equilibria. The instability of $[Fe(CN)_6]^{3-/4-}$ in these conditions may be due to the environment within the diffusion layer surrounding the GNF, where some of the carboxylic acid groups may be acidic enough to protonate the redox molecule, promoting cyanide ligand loss in the form of HCN and allowing deposition of films similar in nature to Prussian Blue [20]. Solutions of $[Fe(CN)_6]^{3-}$ at pH 3.6 have been reported to have different UV-Vis spectral features to those at higher pH (indicating protonation or ligand loss) and to develop blue precipitates on standing [21]. Although our solution pH values of ≥ 4.6 would not be considered acidic enough to cause decomposition of $[Fe(CN)_6]^{3-}$, a higher concentration of protons may be present close to the electrode surface due to the high density of carboxylic acid functionalities.

4.3.2 The Effect of Background Electrolyte Concentration

To determine whether a cation dependence is seen at clean BDD, and whether modifying the electrode with GNF changes the response, cyclic voltammograms of $[Fe(CN)_6]^{3-/4-}$ were recorded in electrolyte solutions of different concentrations. In these experiments the background electrolyte was KCl so the solutions are not buffered, but are all in the pH range 5-6. **Figure 4.4** shows CVs at clean BDD, GNF-COOH and GNF-amide with 0.5×10^{-3} M $K_3[Fe(CN)_6]$ in 1 M (a), 0.1 M (b) and 0.01 M KCl (c). Increasing the concentration of the supporting electrolyte causes a shift in $E^{0'}$ to more positive potentials for all electrodes studied here, confirming that the electrolyte plays a role in the redox equilibrium. At high ionic strength (1 M KCl) the CV response at all three electrodes is reversible, but at 0.1 M KCl currents at the GNF-COOH electrode are much reduced and ΔE_p is significantly increased. In 0.01 M supporting electrolyte

the responses at clean BDD and GNF-amide modified electrodes are still reversible but the CV at the GNF-COOH electrode shows significant inhibition. The response appears sigmoidal, resembling the CV expected at an array of microelectrodes, or response through pinholes of an electrode partially covered in insulating material. Calculated values of ΔE_p are listed in Table 4.1.

Table 4.1: Calculated values of peak potential separation ΔE_p in various concentrations of supporting electrolyte KCl.

Electrode	ΔE_p / mV		
	0.01 M KCl	**0.1 M KCl**	**1 M KCl**
BDD only	74 ± 6	69 ± 2	75 ± 1
GNF-COOH	Unable to calculate	137 ± 27	92 ± 6
GNF-amide	88 ± 3	69 ± 1	68 ± 1

The results are qualitatively the same in other supporting electrolytes of the same concentration (see Appendix 1). The pH of 0.01 M KCl is around 5, so the experiment was repeated in 0.01 M KCl solution, the pH of which was brought up to 8.5 with KOH (see Appendix 1). The rise in pH improved the kinetics of the redox reaction at GNF-COOH modified BDD, giving ΔE_p = (231 ± 21) mV.

At low ionic strength the electrostatic interaction between the electrode and the redox probe will be enhanced as screening by solution ions in the double layer is less effective. These conditions seem to amplify the inhibiting effect of the COOH groups on the $[Fe(CN)_6]^{3-/4-}$ electrochemistry, particularly at lower pH. Additionally the stability of the $[Fe(CN)_6]^{3-/4-}$ species may also be affected by the low ionic strength conditions as ion-pairing with K^+ will be less effective at lower cation concentration.

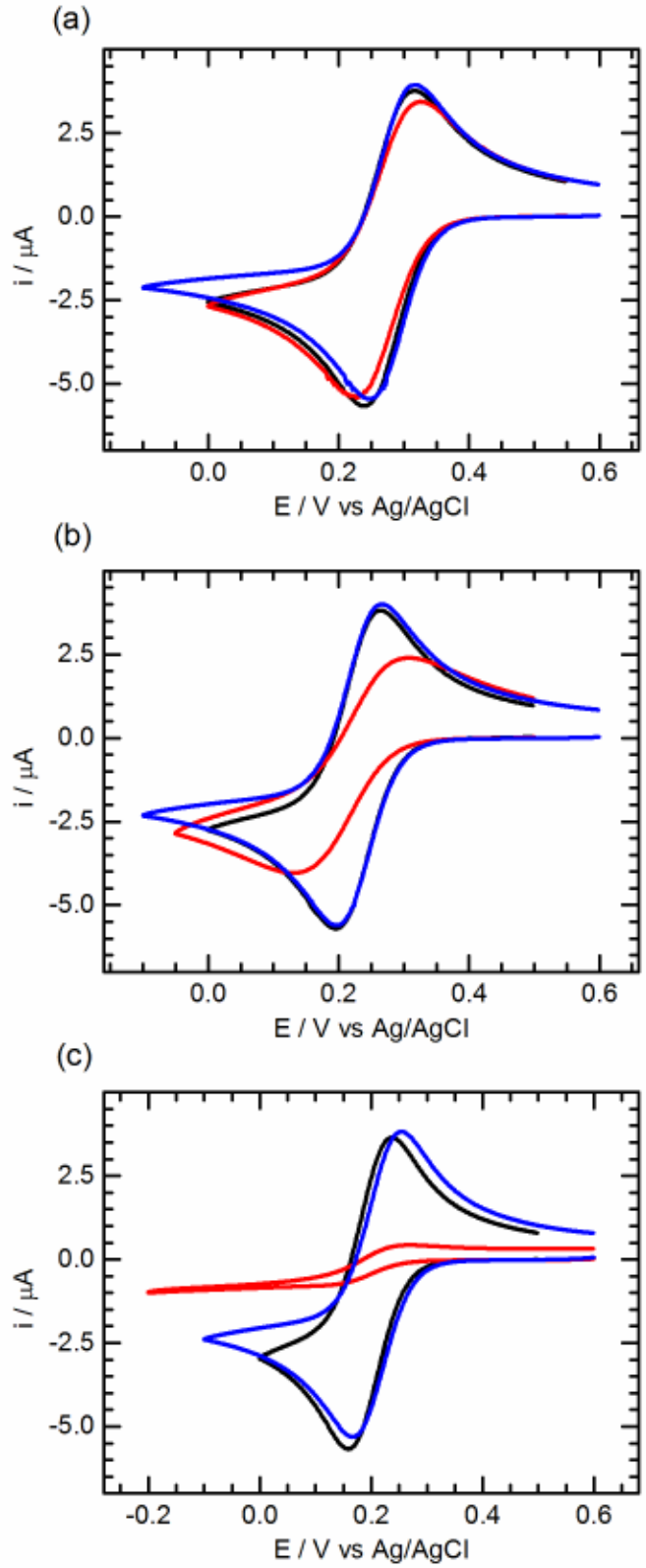

Figure 4.4 Cyclic voltammograms of 0.5×10^{-3} M $K_3[Fe(CN)_6]$ recorded in different concentrations of KCl: (a) 1 M; (b) 0.1 M; (c) 0.01 M. Working electrode: BDD (black); BDD modified with GNF-COOH (red); BDD modified with GNF-amide (blue). Scan rate 50 mV s^{-1}. First scans shown. Adapted from [14].

Beriet and Pletcher [2] suggested the decomposition of $[Fe(CN)_6]^{3-/4-}$ on a platinum electrode surface to form a blocking species. Other groups have found evidence of $[Fe(CN)_6]^{3-/4-}$ adsorption onto platinum electrodes as a Prussian Blue film that inhibits electron transfer [22], although Prussian Blue itself is electroactive [23]. Excess free CN^- in the electrolyte solution prevents $[Fe(CN)_6]^{3-/4-}$ from chemisorbing on Pt surface by occupying chemisorption sites and thus prevents $[Fe(CN)_6]^{3-/4-}$ decomposition [17, 18]. The inhibiting effect of adsorbed species on the electrode surface was observed to grow gradually stronger as the adsorption proceeded [22], whereas in the experiments conducted in this study the effect is seen immediately, and is at its strongest in the first cycle.

Although it is difficult to provide a definitive explanation, it is known that $[Fe(CN)_6]^{3-/4-}$ can be unstable in solution, particularly at low ionic strength and low pH. Cyanide ligand loss and subsequent adsorption/decomposition of ferrocyano-species onto metal and carbon electrodes are well documented [2, 15-17, 22-24]. The $[Fe(CN)_6]^{3-/4-}$ redox reaction is believed to take place via activated ion-paired complexes such as $K_2[Fe(CN)_6]^{2-/1-}$. If these ion-pair complexes cannot form, for example at low ionic strength, then the electron transfer rate is much slower [1]. The electrochemical response of $[Fe(CN)_6]^{3-/4-}$ in the presence of GNF-COOH at pH < 7 suggests a lack of stability of the ion-paired redox species and hence sluggish electron transfer kinetics. At low ionic strength the response is consistent with a spontaneous deposition of blocking species on the electrode surface, indicating the real lack of stability of the redox molecule in these solution conditions.

In the previous Section we discovered that the presence of COOH groups at the electrode greatly inhibits the $[Fe(CN)_6]^{3-/4-}$ redox reaction at lower pH. The effect is exacerbated in low ionic strength solutions, as $[Fe(CN)_6]^{3-}$ is considerably less stable in solution in the absence of ion-pairing to K^+. Interestingly, when experiments with the GNF-COOH are repeated with $[Ru(CN)_6]^{3-/4-}$ as the redox couple the CV response is

found to be independent of pH (see Appendix 1). The process appears reversible over the pH range 4.5–9.2 with no evidence of the inhibition and proposed surface film formation seen for $[Fe(CN)_6]^{3-/4-}$. This would suggest that a mechanism requiring specific interaction between the COOH groups and the cyanide ligands of the redox species can be ruled out and it is more likely the complex solution chemistry of $[Fe(CN)_6]^{3-/4-}$ that results in the observed response.

4.3.3 Cyclic Voltammetric Studies of $[Fe(CN)_6]^{3-/4-}$ Redox Couple in the Presence of GNF-COOH in Solution

To explore further our previous observations that the $[Fe(CN)_6]^{3-/4-}$ species are unstable in the solution environment surrounding the GNF, cyclic voltammetry was performed with both $[Fe(CN)_6]^{3-}$ and GNF present in solution. All CVs were recorded at a freshly polished, clean BDD electrode. The experiment was also carried out with the $[Ru(CN)_6]^{3-/4-}$ redox species in solution for comparison. It can be seen from **Figure 4.5** that presence of GNF in solution influences both redox reactions, but the extent to which this happens differs greatly. In the case of $[Ru(CN)_6]^{3-/4-}$, the presence of GNF in solution leads to a small increase in peak separation and a small decrease in peak height. In the case of $[Fe(CN)_6]^{3-/4-}$, on the other hand, the peak height is drastically reduced and the voltammogram has a sigmoidal shape, indicative of electrode blocking. This is the same response as we obtained when COOH-terminated GNF were immobilised directly on the electrode surface (**Figure 4.4**(b)). The decrease in current observed for the $[Ru(CN)_6]^{3-/4-}$ couple we attribute to a small lowering of the effective diffusion coefficient of the probe due to the large GNF particles dispersed in the solution. We would expect a similar inhibition for $[Fe(CN)_6]^{3-/4-}$; however these results indicate that GNF have a profound effect on the electron transfer process of this species, rather than simply blocking diffusion. As discovered in Sections 4.3.1 and 4.3.2 it is specifically the COOH edge groups which affect the $[Fe(CN)_6]^{3-/4-}$ in this way, suggesting a protonation process may be responsible for these observations.

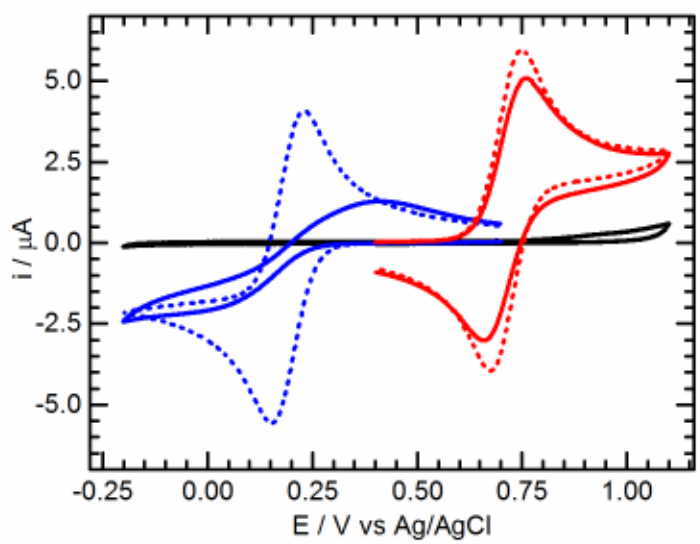

Figure 4.5 Cyclic voltammograms of 0.5×10^{-3} M $K_3[Fe(CN)_6]$ (dashed blue); 0.5×10^{-3} M $K_3[Fe(CN)_6]$ and 34 µg ml^{-1} GNF (solid blue); 0.5×10^{-3} M $K_4[Ru(CN)_6]$ (dashed red); 0.5×10^{-3} M $K_4[Ru(CN)_6]$ and 34 µg ml^{-1} GNF (solid red); 34 µg ml^{-1} GNF only (black). Working electrode: BDD. Supporting electrolyte: 10^{-3} M KCl. Scan rate: 50 mV s^{-1}. First scans shown. Reproduced from [11].

4.3.4 Isotope Effect of H_2O and D_2O on $[Fe(CN)_6]^{3-/4-}$ Redox Couple at GNF-COOH Modified Electrode

Having established the importance of the acidic functionalities in electron transfer process for $[Fe(CN)_6]^{3-/4-}$, CV experiments were carried out in low ionic strength (0.01 M KCl) solutions with GNF immobilised on the electrode surface and either H_2O or D_2O as the solvent. The results are presented in **Figure 4.6**. When H_2O is used as the solvent, the CV shows significant inhibition in the first cycle. The response improves slightly during repeated cycling, but the 10th cycle still shows significant irreversibility of the redox reaction. In D_2O, the first cycle shows inhibited electron transfer, but the response improves during repeated cycling with increase in peak heights and decrease in peak separation. By the tenth scan, the response in D_2O is essentially reversible.

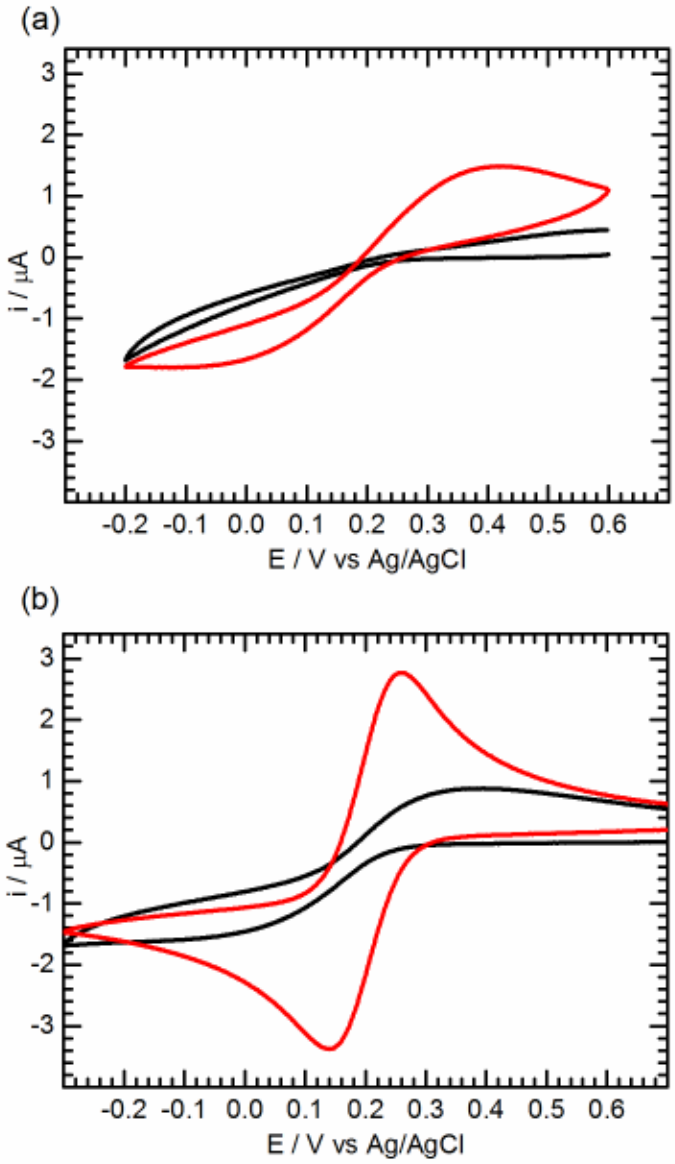

Figure 4.6 Cyclic voltammograms of 0.5 × 10^{-3} M $K_3[Fe(CN)_6]$ recorded at GNF-COOH modified BDD in (a) H_2O; (b) D_2O. First scans (black) and 10th scans (red) shown. Supporting electrolyte 0.01 M KCl. Scan rate 50 mV s^{-1}. Adapted from [11].

When the GNF are surrounded with H_2O molecules, the constant protonation and deprotonation of the carboxylic acid edge groups does not lead to a change in the chemical identity of the acid groups. However, if the H_2O molecules are replaced by D_2O, the dynamic acid/base equilibrium will gradually lead to predominantly COOD around the flake edges as the protons are exchanged and diffuse away from the electrode surface. Therefore we propose that during the first cycles in D_2O, the GNF edges are still mostly decorated with COOH groups and these inhibit the redox

reaction. However, as COOD groups begin to dominate, the redox reaction is allowed to proceed uninhibited, leading to a near reversible CV by the 10th scan. The results also suggest that if an electrode blocking species is responsible for the inhibited electron transfer, it forms reversibly and can dissolve or desorb from the electrode surface according to changes in the diffusion layer. Thus the redox reaction is able to become more reversible with cycling in D_2O as the concentration of protons at the GNF-modified electrode surface decreases.

4.3.5 Spectroelectrochemical Studies of $[Fe(CN)_6]^{3-/4-}$

The $[Fe(CN)_6]^{3-/4-}$ redox reaction can be conveniently monitored with ATR-FTIR because the cyanide stretch is sensitive to the oxidation state of the iron centre. $[Fe(CN)_6]^{3-}$ absorbs at 2116 cm^{-1}, whereas in $[Fe(CN)_6]^{4-}$ the absorption frequency is shifted to 2036 cm^{-1} and the extinction coefficient is four times larger.

ATR-FTIR coupled with in situ controlled potential experiments were performed for 1×10^{-3} M $K_3[Fe(CN)_6]$ in 0.01 M KCl. The sample was introduced to the in situ electrochemical cell and a potential of 0 V was applied to drive the reduction of $[Fe(CN)_6]^{3-}$ to $[Fe(CN)_6]^{4-}$. The resulting IR spectrum shows a negative $[Fe(CN)_6]^{3-}$ band and positive $[Fe(CN)_6]^{4-}$ band (solid line, **Figure 4.7**(a)). When the intensity of the $[Fe(CN)_6]^{4-}$ band did not increase anymore, all $[Fe(CN)_6]^{3-}$ present in the sample chamber was assumed to have been converted to $[Fe(CN)_6]^{4-}$. The reaction reached completion in about 2 minutes, as indicated by the intensity of the $[Fe(CN)_6]^{4-}$ band. The height of the $[Fe(CN)_6]^{4-}$ band as a function of time is plotted in **Figure 4.7**(b). The potential was then switched to +350 mV to oxidise $[Fe(CN)_6]^{4-}$back to $[Fe(CN)_6]^{3-}$. The resulting IR spectrum shows a positive $[Fe(CN)_6]^{3-}$ band and negative $[Fe(CN)_6]^{4-}$ band (dashed line, **Figure 4.7**(a)). As was the case for the reduction, the negative $[Fe(CN)_6]^{4-}$ band reached full height after about 2 minutes, indicating full conversion back to $[Fe(CN)_6]^{3-}$.

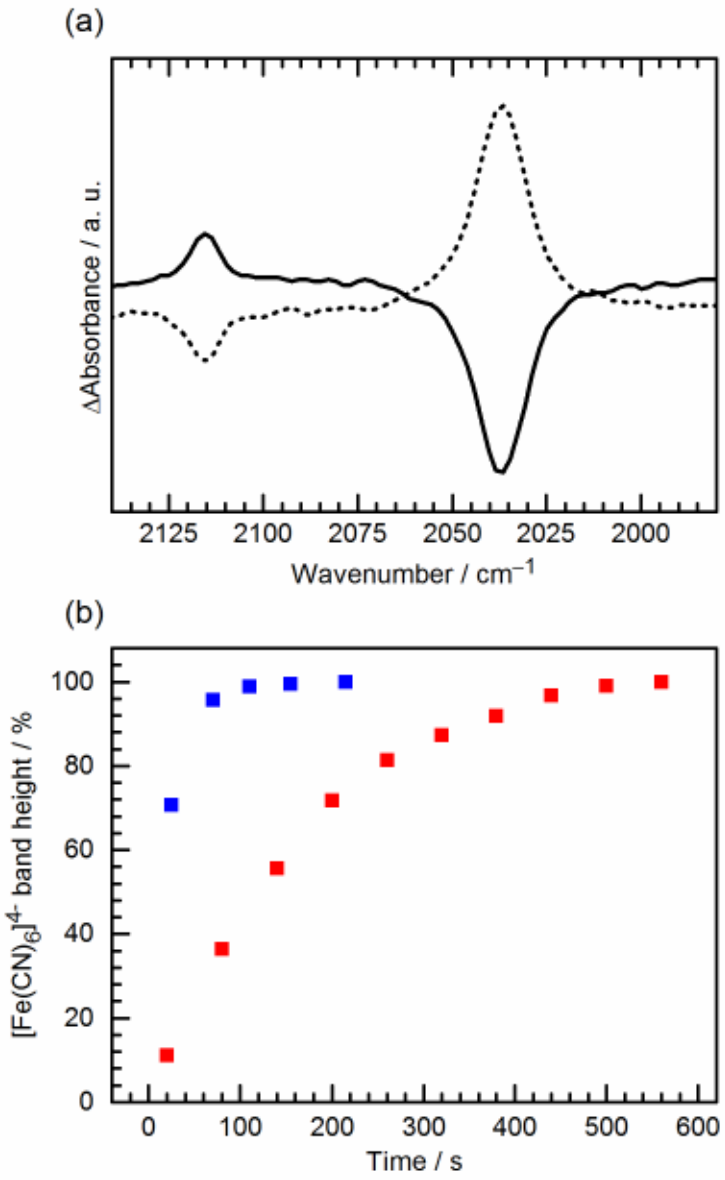

Figure 4.7 (a) Difference spectra of $[Fe(CN)_6]^{3-}$ and $[Fe(CN)_6]^{4-}$. After reduction of $[Fe(CN)_6]^{3-}$, the IR spectrum shows a negative $[Fe(CN)_6]^{3-}$ band and positive $[Fe(CN)_6]^{4-}$ band (solid line). Oxidation of $[Fe(CN)_6]^{4-}$ results in a positive $[Fe(CN)_6]^{3-}$ band and negative $[Fe(CN)_6]^{4-}$ band (dashed line). (b) Height of the $[Fe(CN)_6]^{4-}$ CN stretch band at 2036 cm^{-1} relative to the intensity of absorption at full conversion as a function of time. Blue squares: 1×10^{-3} M $K_3[Fe(CN)_6]$; red squares: 1×10^{-3} M $K_3[Fe(CN)_6]$ and 3.2 µg ml^{-1} of GNF. Electrolyte: 0.01 M KCl. Potentials: 0 V (reduction), +350 mV (oxidation). Reproduced from [11].

The $[Fe(CN)_6]^{3-}$ solution was then replaced by a solution containing 1×10^{-3} M $K_3[Fe(CN)_6]$ in 0.01 M KCl and 3.2 µg ml^{-1} of GNF. The concentration of acidic protons from the GNF is estimated to be 22 µM and only a small fraction would be dissociated. Therefore the GNF did not significantly alter the pH of the solution. The experiment was then repeated and a potential of 0 V applied. With the GNF present, the reaction

proceeded much more slowly. After 2 min, the $[Fe(CN)_6]^{4-}$ band was only 40% of the intensity expected for full conversion of $[Fe(CN)_6]^{3-}$ to $[Fe(CN)_6]^{4-}$. Full conversion took approximately 9 min, compared to 2 min for the same volume and concentration of the control solution. The influence of GNF on the oxidation reaction was essentially the same.

The observations reported here support the CV experiments described in above. The presence of GNF clearly inhibits the reversibility of the $[Fe(CN)_6]^{3-/4-}$ redox couple. Moreover, it was shown in **Figure 4.5** that the observed decrease in current could not be explained by diffusion effects alone. Therefore, the reason why the reaction takes longer to complete with GNF in solution is likely to lie in the solution stability of the redox species.

4.3.6 Stability of $[Fe(CN)_6]^{3-/4-}$ in the Presence of GNF-COOH

Beriet and Pletcher [2] made the observation that the poisoning of an electrode surface by the $[Fe(CN)_6]^{3-/4-}$ redox couple required the presence of both Fe(II) and Fe(III) species. We therefore used an equimolar solution of $K_3[Fe(CN)_6]$ and $K_4[Fe(CN)_6]$ in H_2O to probe their stability in solution in the absence of applied potential. To gauge the impact of GNF on the stability of $[Fe(CN)_6]^{3-/4-}$, a second solution was prepared, this one also containing 30 µg ml^{-1} GNF. The concentration of GNF was high enough to impart a brownish hue to the solution but low enough to not alter the pH significantly (pH of both solutions was 6.5 ± 0.1).

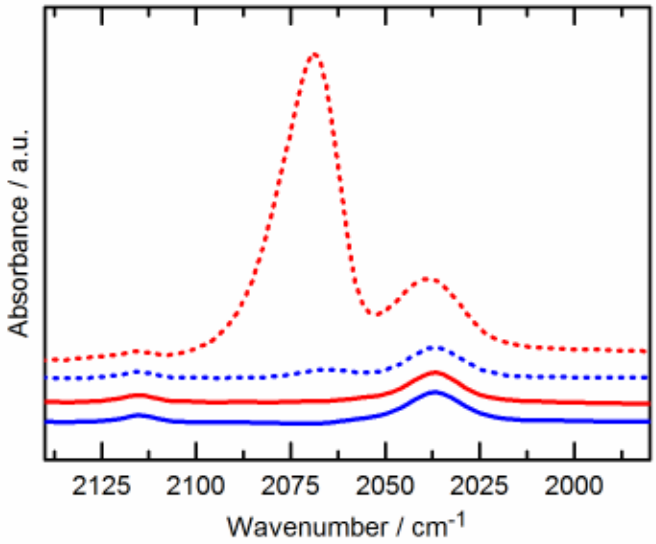

Figure 4.8 Infrared spectra of 2 × 10^{-3} M $K_3[Fe(CN)_6]$ and 2 × 10^{-3} M $K_4[Fe(CN)_6]$ in H_2O at *t* = 0 h (solid blue) and at *t* = 24 h (dashed blue); with 30 µg ml^{-1} GNF at *t* = 0 h (solid red) and at *t* = 24 h (dashed red). Spectra are offset for clarity. Reproduced from [11].

The IR spectrum of both samples initially shows two peaks; the $[Fe(CN)_6]^{4-}$ CN stretch at 2036 cm^{-1} and the $[Fe(CN)_6]^{3-}$ CN stretch at 2116 cm^{-1} (**Figure 4.8**). No peaks are detected in the 1700–1200 cm^{-1} region that could be associated with GNF, although the concentration of flakes is too low for this purpose. Over time, a third peak begins to emerge in both samples. In the control solution, this peak at 2069 cm^{-1} is detectable above the noise after about 13 h, whereas with GNF in solution, the intensity of this third peak surpasses that of the $[Fe(CN)_6]^{3-}$ peak after 3 h. Mixing the GNF sample by pumping gently with a syringe back and forth caused a decrease in the intensity of the peak at 2069 cm^{-1}.

As described in Section 4.3.4, the identity of solvent has a marked influence on the reversibility of the $[Fe(CN)_6]^{3-/4-}$ redox couple. To further explore this, stability experiments were repeated in D_2O as shown in **Figure 4.9**. In H_2O, a new band appeared in between the two cyanide stretch bands after a couple of hours. In D_2O, no new band is seen after four hours whereas in H_2O, the new band at that point was already comparable in size to the $[Fe(CN)_6]^{4-}$ stretch. After 24 hours in D_2O the new

band did become evident, but its appearance is accompanied with a H_2O band due to H_2O contamination from atmospheric moisture, leading to the conclusion that the presence of appreciable concentration of protons is necessary for the decomposition/precipitation reaction to proceed.

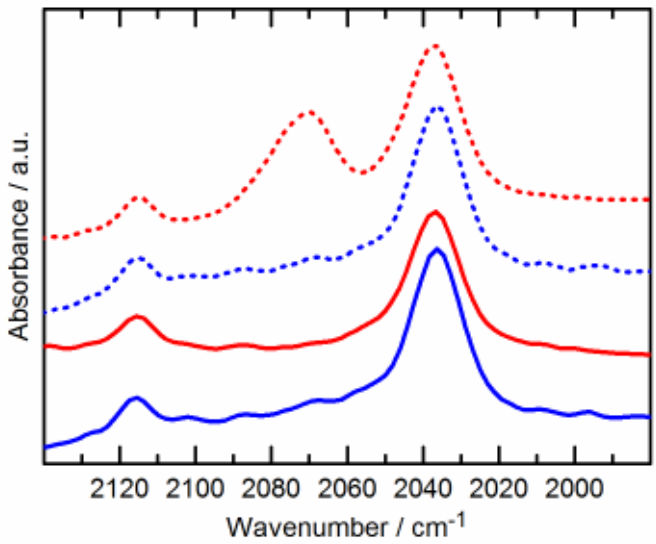

Figure 4.9 ATR-FTIR spectra of 2×10^{-3} M $K_3[Fe(CN)_6]$ and 2×10^{-3} M $K_4[Fe(CN)_6]$ with 30 µg ml^{-1} GNF In H_2O at t = 0 h (solid red) and t = 4 h (dashed red), in D_2O at t = 0 h (solid blue) and t = 4 h (dashed blue). Spectra are offset for clarity. Reproduced from [11].

The substitution of deuterium for hydrogen in a water molecule has little effect on the molecular dimensions defined by bond length and bond angle, but the O–D bond is slightly stronger than the O–H bond. The difference in bond strength leads to a smaller dissociation constant for D_2O than H_2O, making H_2O a fivefold stronger acid [25]. Liquid D_2O is more viscous than liquid H_2O and has a slower rate of molecular reorientations and translations [26], leading to the conclusion that there is more structural order in D_2O due to a higher degree of hydrogen bonding [27]. This can be attributed to lower intermolecular vibrational frequencies caused by isotopic substitution but also the greater strength of hydrogen bonding in D_2O than in H_2O [27]. Additionally, protons are able to diffuse rapidly in water *via* the Grotthuss mechanism [28]. It has recently been demonstrated that the mechanism is strongly influenced by the local hydration structure of the proton and involves the concerted motion of several protons [29]. The

reorganisation and rotation of molecules involved in the Grotthuss mechanism are slower in D_2O than in H_2O, making D^+ transport in heavy water less efficient than proton transport in H_2O. Thus the instability of $[Fe(CN)_6]^{3-/4-}$ in the presence of GNF appears to be exacerbated by the readily available H^+ in the localised acidic conditions in the region of the carboxylic acid edge groups. Increased stability in D_2O can be attributed either to the increased strength of the O–D bond (making D^+ less available) or slower diffusion of D^+ from the GNF to $[Fe(CN)_6]^{3-/4-}$.

4.3.6.1 Identity of decomposition product

The new IR absorption band observed in **Figure 4.8** is very high in intensity compared to the other two CN stretch bands. Given that the $[Fe(CN)_6]^{4-}$ and $[Fe(CN)_6]^{3-}$ bands are not greatly diminished, it is clear that the new cyano species cannot be present in high concentration. The intensity of the new band may then be due to either a species present in low concentration with a high extinction coefficient, or the accumulation of a species in the region near the ATR prism. A new species with a high extinction coefficient is unlikely, as the most plausible solution species candidate that absorbs in this region is free cyanide, the absorption coefficient of which is very small compared to the bound form [30]. The most likely explanation is the accumulation of a non-soluble species at the surface of the internal reflection element, which in the cell geometry is at the bottom of the cell. This would also explain why the intensity of the other CN stretch bands does not change significantly, since the amount of precipitate does not need to be large in order to give an appreciable signal. UV–Vis spectra taken in situ with the same solution (see Appendix 1) do not offer evidence of the formation of a coloured species, but it is important to bear in mind that the UV–Vis probes the bulk solution (where the overall concentration of this new species is low) whereas ATR-FTIR only reaches a few microns at the bottom of the cell (where the species accumulates).

The best-known hexacyanoferrate complex is Prussian Blue, which absorbs in the region of 2070–2100 cm^{-1} depending on the whether the Fe^{3+} is hydrolysed (lower

cm^{-1}) or not (higher cm^{-1}) [31] and it could be envisaged to accumulate at the bottom of the cell by precipitation, although the UV–Vis data does not offer direct evidence of Prussian Blue. Other well-known related compounds are Prussian White (all ferrous), which absorbs between 2080–2060 cm^{-1} and Prussian Yellow/Everitt's Salt (all ferric), absorbing near 2175 cm^{-1}. During the reduction of $[Fe(CN)_6]^{3-}$ to $[Fe(CN)_6]^{4-}$ an adsorbed intermediate has been reported that absorbs between 2070–2080 cm^{-1} [32]. Similarly, an adsorbed species on Pt has been observed during potential cycling that gives an IR band 2090–2070 cm^{-1} and inhibits ET, concluded to be a (unnamed) colourless soluble (i.e. containing K^+) mixed-valency compound [22]. Hence although we have clearly detected a decomposition product formed in the presence of COOH-terminated GNF, we cannot be absolutely certain of its identity.

4.4 Conclusion

Above, we have described how the presence of GNF influences the $[Fe(CN)_6]^{3-/4-}$ redox system. It was determined that it is specifically the acidic groups around the edges of GNF that are responsible for the irreversible behaviour of the $[Fe(CN)_6]^{3-/4-}$ redox couple and therefore we have explored further the influence of protons on this redox reaction. We showed that the acid groups at GNF-COOH severely inhibit the redox reaction of $[Fe(CN)_6]^{3-/4-}$ in acidic solution when more acid groups are expected to be protonated; therefore, electrostatic repulsion cannot be used to explain the effect of GNF-COOH on this redox couple.

Although the solutions used in this study at pH ≥ 4.6 would not be considered acidic enough to cause decomposition of $[Fe(CN)_6]^{3-}$, the high density of COOH groups on the GNF may lead to localised acidic conditions, promoted by the ready availability of protons at the edges of the flakes. Thus there are several mechanisms by which the very acidic local environment of the COOH-GNF could inhibit electron transfer, including disruption to the ion paired activated species required for fast electron

transfer, protonation of CN ligands, ligand loss or formation of insoluble decomposition products.

When deuterated water is substituted for H_2O, the presence of GNF has much less influence on the $[Fe(CN)_6]^{3-/4-}$ redox reaction. Consecutive cycles in D_2O saw the voltammetric response of $[Fe(CN)_6]^{3-/4-}$ quickly return to near reversible. IR spectroscopic studies also showed the $[Fe(CN)_6]^{3-/4-}$ species to be more stable in the presence of GNF when dissolved in D_2O rather than H_2O.

The results described in this Chapter lead to the interpretation that the presence of GNF in an aqueous solution of $K_3[Fe(CN)_6]$ and $K_4[Fe(CN)_6]$ promotes the decomposition of $[Fe(CN)_6]^{3-}$ and/or $[Fe(CN)_6]^{4-}$. The intense new IR absorption band that emerges after only some hours indicates the formation of a non-soluble species. However, it was not possible to determine the identity of the decomposition product from the experimental results and further work would be needed to identify the new species observed in this study.

References for Chapter 4

1. Peter, L. M.; Dürr, W.; Bindra, P., et al., The Influence of Alkali Metal Cations on the Rate of the $Fe(CN)_6^{4-}/Fe(CN)_6^{3-}$ Electrode Process. *J. Electroanal. Chem.* **1976,** *71* (1), 31-50.
2. Beriet, C.; Pletcher, D., A Microelectrode Study of the Mechanism and Kinetics of the Ferro/Ferricyanide Couple in Aqueous Media: The Influence of the Electrolyte and Its Concentration. *J. Electroanal. Chem.* **1993,** *361* (1-2), 93-101.
3. Noel, M.; Anantharaman, P. N., Voltammetric Studies on a Glassy Carbon Electrode. Part II. Factors Influencing the Simple Electron-Transfer Reactions-the $K_3[Fe(CN)_6]$-$K_4[Fe(CN)_6]$ System. *Analyst* **1985,** *110* (9), 1095-1103.
4. Sohr, R.; Müller, L.; Landsberg, R., Elektrochemische Untersuchungen Am Redoxsystem Hexacyanoferrat(II)/Hexacyanoferrat(III) an Graphitelektroden. *J. Electroanal. Chem.* **1974,** *50* (1), 55-63.
5. Sohr, R.; Müller, L., Der Einfluss Des Leitsalzes Auf Die Geschwindigkeit Des Elektronenaustausches Im Redoxsystem $[Fe(CN)_6]^{3-}/[Fe(CN)_6]^{4-}$. *Electrochim. Acta* **1975,** *20* (6), 451-455.
6. Chen, P.; McCreery, R. L., Control of Electron Transfer Kinetics at Glassy Carbon Electrodes by Specific Surface Modification. *Analytical Chemistry* **1996,** *68* (22), 3958-3965.
7. Deakin, M. R.; Stutts, K. J.; Wightman, R. M., The Effect of pH on Some Outer-Sphere Electrode Reactions at Carbon Electrodes. *J. Electroanal. Chem.* **1985,** *182* (1), 113-122.
8. Granger, M. C.; Swain, G. M., The Influence of Surface Interactions on the Reversibility of Ferri/Ferrocyanide at Boron-Doped Diamond Thin-Film Electrodes. *J. Electrochem. Soc.* **1999,** *146* (12), 4551-4558.
9. Hutton, L. A.; Iacobini, J. G.; Bitziou, E., et al., Examination of the Factors Affecting the Electrochemical Performance of Oxygen-Terminated Polycrystalline Boron-Doped Diamond Electrodes. *Analytical Chemistry* **2013,** *85* (15), 7230-7240.
10. Yagi, I.; Notsu, H.; Kondo, T., et al., Electrochemical Selectivity for Redox Systems at Oxygen-Terminated Diamond Electrodes. *J. Electroanal. Chem.* **1999,** *473* (1–2), 173-178.
11. Lounasvuori, M. M.; Rosillo-Lopez, M.; Salzmann, C. G., et al., The Influence of Acidic Edge Groups on the Electrochemical Performance of Graphene Nanoflakes. *J. Electroanal. Chem.* **2015,** *753*, 28-34.
12. Granger, M. C.; Witek, M.; Xu, J., et al., Standard Electrochemical Behavior of High-Quality, Boron-Doped Polycrystalline Diamond Thin-Film Electrodes. *Analytical Chemistry* **2000,** *72* (16), 3793-3804.
13. Panzer, R. E.; Elving, P. J., Behavior of Carbon Electrodes in Aqueous and Nonaqueous Systems. *J. Electrochem. Soc.* **1972,** *119* (7), 864-874.
14. Lounasvuori, M. M.; Rosillo-Lopez, M.; Salzmann, C. G., et al., Electrochemical Characterisation of Graphene Nanoflakes with Functionalised Edges. *Faraday Discussions* **2014,** *172* ( ), 293-310.

15. Więckowski, A.; Szklarzyk, M., The State of the Polycrystalline Platinum Electrode During the Heterogeneous Electron-Transfer Reaction: $Fe(CN)_6^{3-}+e^-$ $Fe(CN)_6^{4-}$. *J. Electroanal. Chem.* **1982,** *142* (1–2), 157-170.
16. Pons, S.; Datta, M.; McAleer, J. F., et al., Infrared Spectroelectrochemistry of the $Fe(CN)_6^{4-}/Fe(CN)_6^{3-}$ Redox System. *J. Electroanal. Chem.* **1984,** *160* (1–2), 369-376.
17. Kawiak, J.; Kulesza, P. J.; Galus, Z., A Search for Conditions Permitting Model Behavior of the $Fe(CN)^{3-/4-}{}_6$ System. *J. Electroanal. Chem.* **1987,** *226* (1–2), 305-314.
18. Huang, W.; McCreery, R., Electron Transfer Kinetics of $Fe(CN)_6^{3-4-}$ on Laser-Activated and CN−-Modified Pt Electrodes. *J. Electroanal. Chem.* **1992,** *326* (1–2), 1-12.
19. Domingo, P. L.; Garcia, B.; Leal, J. M., Acid–Base Behaviour of the Ferrocyanide Ion in Perchloric Acid Media Potentiometric and Spectrophotometric Study. *Can. J. Chem.* **1987,** *65* (3), 583-589.
20. Domingo, P. L.; García, B.; Leal, J. M., Acid–Base Behaviour of the Ferricyanide Ion in Perchloric Acid Media. Spectrophotometric and Kinetic Study. *Can. J. Chem.* **1990,** *68* (2), 228-235.
21. Yang, R.; Qian, Z.; Deng, J., Electrochemical Deposition of Prussian Blue from a Single Ferricyanide Solution. *J. Electrochem. Soc.* **1998,** *145* (7), 2231-2236.
22. Pharr, C. M.; Griffiths, P. R., Infrared Spectroelectrochemical Analysis of Adsorbed Hexacyanoferrate Species Formed During Potential Cycling in the Ferrocyanide/Ferricyanide Redox Couple. *Analytical Chemistry* **1997,** *69* (22), 4673-4679.
23. Karyakin, A. A., Prussian Blue and Its Analogues: Electrochemistry and Analytical Applications. *Electroanalysis* **2001,** *13* (10), 813-819.
24. Lee, C.; Anson, F. C., Inhibition of the Electroreduction of $Fe(CN)_6^{3-}$ at Microelectrodes in the Absence of Supporting Electrolyte: Mediation of the Inhibited Reduction by Methyl Viologen. *J. Electroanal. Chem.* **1992,** *323* (1–2), 381-389.
25. Riley, T.; Long, F. A., Deuterium Isotope and Solvent Effects on the Kinetics of the Keto-Enol Interconversion of 2-Acetylcyclohexanone. *J. Am. Chem. Soc.* **1962,** *84* (4), 522-526.
26. Vinogradov, S. N.; Linnell, R. H., *Hydrogen Bonding*. Van Nostrand Reinhold: New York; London, 1971.
27. Némethy, G.; Scheraga, H. A., Structure of Water and Hydrophobic Bonding in Proteins. IV. The Thermodynamic Properties of Liquid Deuterium Oxide. *The Journal of Chemical Physics* **1964,** *41* (3), 680-689.
28. de Grotthuss, C. J. T., Memoir on the Decomposition of Water and of the Bodies That It Holds in Solution by Means of Galvanic Electricity. *Biochimica et Biophysica Acta (BBA) - Bioenergetics* **2006,** *1757* (8), 871-875.
29. Hassanali, A.; Giberti, F.; Cuny, J., et al., Proton Transfer through the Water Gossamer. *Proceedings of the National Academy of Sciences* **2013,** *110* (34), 13723-13728.
30. Le Caër, S.; Vigneron, G.; Renault, J. P., et al., First Coupling between a LINAC and FT-IR Spectroscopy: The Aqueous Ferrocyanide System. *Chemical Physics Letters* **2006,** *426* (1–3), 71-76.
31. Christensen, P. A.; Hamnett, A.; Higgins, S. J., A Study of Electrochemically Grown Prussian Blue Films Using Fourier-Transform Infra-Red Spectroscopy. *Journal of the Chemical Society, Dalton Transactions* **1990,** (7), 2233-2238.
32. Kunimatsu, K.; Shigematsu, Y.; Uosaki, K., et al., Study of the $Fe(CN)^{3-}{}_6/Fe(CN)^{4-}{}_6$ Redox System on Pt by EMIRS: Part I. Infrared Spectra of the Intermediates in the Charge Transfer. *J. Electroanal. Chem.* **1989,** *262* (1–2), 195-209.

5 Potential-Induced Dissociation of Acid Groups

5.1 Introduction

It is well-known that the pK_a of an acid depends on the local environment. An obvious example of this are enzymes where functional groups comprising the active site often have very different pK_a values due to charge interactions, such as ion pairing with charged groups or ions and hydrogen bonding with other functional groups or water molecules, and different polarity of the surrounding medium, such as being buried in hydrophobic pockets of the enzyme. The pK_a of the metal-bound water molecule in the active site of histone deacetylase (HDAC) depends on the identity of the metal centre and shifts from 10.0 in Co(II)-HDAC to 9.1 in Zn(II)-HDAC [1]. The imidazole group of a histidine side chain is present in the active site of several enzymes and usually hydrogen bonds with a negatively charged carboxylate, as is the case in myoglobin,

where the pK_a of the imidazole group is ca. 8 [2]. If the imidazole-carboxylate pair is buried in a hydrophobic region, the pK_a will be significantly higher, and hydrogen bonding to an uncharged carbonyl lowers the pK_a of histidine residues [1].

Due to the importance of self-assembled monolayers (SAMs) and functionalised surfaces, the effect of surface-immobilisation on the pK_a of a molecule has been studied widely. Many different techniques have been employed, such as contact angle titration [3], quartz crystal microbalance [4], and surface plasmon resonance spectroscopy [5]. Sukenik's group have used in situ infrared spectroscopy to study siloxane-anchored carboxylic acid –terminated SAMs and reported an increase of ca. 2 units in the pK_a of a surface-immobilised acid compared to that in solution (7.5 compared to 5.4) [6]. A later, more detailed analysis undertaken by the same group [7] was able to distinguish between monomeric and oligomeric/dimeric groups in a SAM and the pK_a values were reported as 4.9 and 9.3, respectively.

In addition to interaction with the solvent and neighbouring molecules in the SAM itself, the identity and concentration of solution species will also influence the association constant. A Langmuir monolayer of NH_2-terminated lipid at the air-water interface was observed to have a pK strongly dependent on the ionic strength of the subphase, the pK ranging from 5.1 to 10.5 as the ionic strength increased from 0 to 0.1 [8].

Carboxylic acid groups are present at many carbon materials, but they form only a fraction of the functional groups, the identities of which are various and ill-defined, especially in graphene oxide. Here we take advantage of the well-characterised nature of the GNF, where carboxylic acid groups are the predominant oxygen-containing moiety present and hence we are able to interrogate the behaviour of the carboxylic acid groups in isolation.

The acid-terminated GNF were used to study the effect of applied potential on protonation state of acid functionalities confined to an electrode surface. The GNF were

immobilised onto an electrode surface and ATR-FTIR spectroscopy was used to monitor how the population of carboxylic acid and carboxylate groups change in response to an applied potential.

The presence of the COOH edge groups renders the GNF highly water-soluble, although a few monolayers physisorb sufficiently strongly to an electrode surface to allow CV investigations to be carried out. In this study an increased coverage of the electrode surface was required, hence the GNF were complexed by the addition of Ca^{2+} cations. This results in crosslinking of the GNF, forming an insoluble, disordered, three-dimensional structure that can be immobilised onto an electrode surface and remains intact during electrochemical cycling. The porous nature of this Ca^{2+}-complexed GNF results in a large surface area and hence increases the sensitivity of the spectroelectrochemical measurements. As not all of the edge groups are complexed to Ca^{2+}, a number are free to undergo protonation and deprotonation in response to applied potential, as described in this study. The work presented in this Chapter has been published in [9].

5.2 Experimental Methods

All aqueous solutions were prepared with doubly deionised water, taken from a Milli-Q water purification system, with a resistivity of not less than 18.2 MΩ cm at 25 °C.

In situ spectroelectrochemical experiments were performed using a Bruker Tensor 27 spectrometer (Bruker, UK) fitted with a room temperature DLaTGS detector at 4 cm^{-1} resolution and a diamond crystal as the internal reflection element. The potential was controlled with a Palmsens Emstat2 potentiostat (Palmsens, NL) running PSTrace (v3.0) software. An electrochemical cell with a volume of 2 ml was positioned over the ATR element. The electrodes were as detailed in Section 3.2.5.

3.3×10^{-3} g of dry acid-terminated GNF was used to prepare GNF-Ca precipitate. Further details of the method can be found in Section 3.2.1. In Section 3.3.4, the number of acidic protons was estimated to be 7×10^{-3} mol per gram of GNF. After washing, the GNF-Ca precipitate was suspended in 8.3×10^{-4} l of water and 4×10^{-6} l of the aqueous precipitate suspension was drop-coated onto the electrode in all spectroelectrochemical experiments. The amount of GNF-Ca on the electrode is estimated at $(1.8 \pm 0.4) \times 10^{-5}$ g, assuming full complexation and one Ca^{2+} per two carboxylate groups.

Spectroelectrochemical experiments were carried out in background electrolyte solutions of different pH in the range 3.0 to 9.2. The solutions were prepared by mixing different proportions of KH_2PO_4, K_2HPO_4, H_3PO_4, Na_2SO_4, H_2SO_4, HCl, KCl, KOH and NaOH. The pH of the electrolyte was checked with a pH meter.

IR difference spectra were constructed by recording a background spectrum at one potential, then switching to the second potential and recording a sample spectrum at specific time intervals. The potentials used throughout were −0.5 V and +1.0 V. Three full potential cycles (+1 V followed by −0.5 V) were recorded to assess the reproducibility of the response. A single spectrum was computed by Fourier transformation of 100 averaged interferograms for background and sample and the software was programmed to record a spectrum every 170 seconds. One potential step was 720 seconds in duration, during which time four sample spectra and one background spectrum were recorded. After the initial sample spectrum, the subsequent three spectra were consistently of similar intensity, indicating that the changes upon polarisation stabilised after about three minutes and remained stable for at least another 10. These three spectra from each potential step were processed using the atmospheric compensation function of OPUS software and averaged.

The GNF-Ca modified electrode was located above the diamond internal reflectance element prism of an ATR-FTIR spectrometer as shown in **Figure 5.1**. The thickness of

the GNF-Ca layer was not determined but the insertion of the electrode into the electrochemical cell resulted in a fairly rapid swelling of the layer as water penetrated the pores, resulting in good contact of the GNF-Ca with the internal reflection element (see Section 5.6).

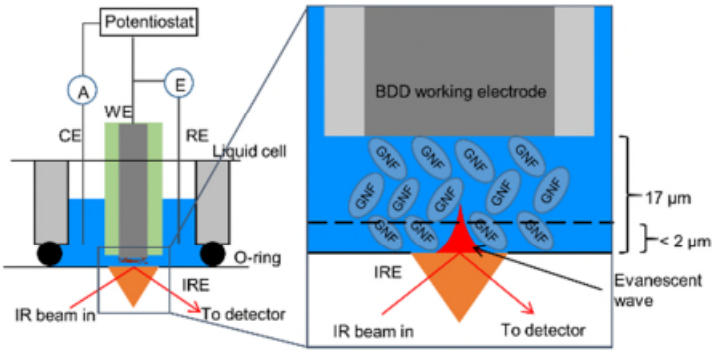

Figure 5.1 Experimental setup in in situ spectroelectrochemical experiments. Adapted from [9]

5.2.1 Construction of Calibration Curves

For the sulphate calibration curve, 2 ml of aqueous K_2SO_4 at different concentrations was placed in the electrochemical cell positioned over the internal reflection element. IR spectra were recorded with the clean ATR element as background. For the carboxylate group calibration curve, acetic acid solutions of different concentrations were prepared and the pH was adjusted with potassium hydroxide to deprotonate all acid groups. A background of the clean ATR prism was collected and 1 µl of each solution was then pipetted onto the prism and allowed to dry before recording a sample spectrum. The sulphate bands and carboxylate stretches were fitted with Gaussian peak shapes and the peak areas were plotted against either the molarity of the solution or the number of moles in each sample. Each measurement was repeated three times and the results were plotted with error bars representing one standard deviation. The data points were fitted with a linear equation, the intercept of which was fixed to zero to

ensure physically meaningful estimations of small numbers of moles from the calibration curve.

5.3 Estimating the Distance between the Electrode Surface and the ATR Internal Reflection Element

In the experimental setup, the working electrode surface is located close above the ATR prism, trapping a small amount of solution. The setup can therefore be considered as a thin-layer cell and the special conditions of diffusion can be exploited in estimating the distance between the electrode surface and the internal reflection element [10]. When the thickness of solution is less than about 50 µm, diffusion can homogenise the solution continuously so that concentration gradients do not exist. Provided that the potential scan rates are slow enough to maintain a homogeneous solution, mass transfer effects can be ignored. Theoretical cyclic voltammetric responses in a thin-layer cell will therefore show identical peak potentials for the forward and reverse scans, and peak currents that depend linearly on the scan rate. The peak current is

$$i_p = n^2F^2\nu VC_O^*/4RT \tag{5.1}$$

where n is the number of electrons transferred, F the Faraday constant, ν the scan rate, V the volume of the thin layer, C_O^* the initial concentration of species O, R the gas constant and T the temperature. Ferrocenemethanol (FcMeOH) was chosen as the redox probe as it is well known to undergo a reversible, one-electron, outer-sphere redox reaction. The volume of the thin-layer cell is modelled as a cylinder with dimensions $A \times h$, where A is the area of the BDD with radius 1.5 mm and h is the distance to be determined. To eliminate height differences resulting from the ATR prism not being exactly flush with the base plate, a glass cover slip (diameter 15 mm) was placed at the bottom of the cell. From six CVs, with scan rates between 5 and 17 mV s^{-1}, the volume was calculated to be (122 ± 4) × 10^{-9} l, giving h ca. 17 µm. The

GNF-Ca layer thickness is assumed to be equal to *h* (for evidence see Section 5.6). The peak currents for oxidation and reduction at each scan rate are listed in **Table 5.1** along with the thin layer cell volumes calculated from Equation (5.1) and the corresponding distance *h* between the IRE and the electrode surface.

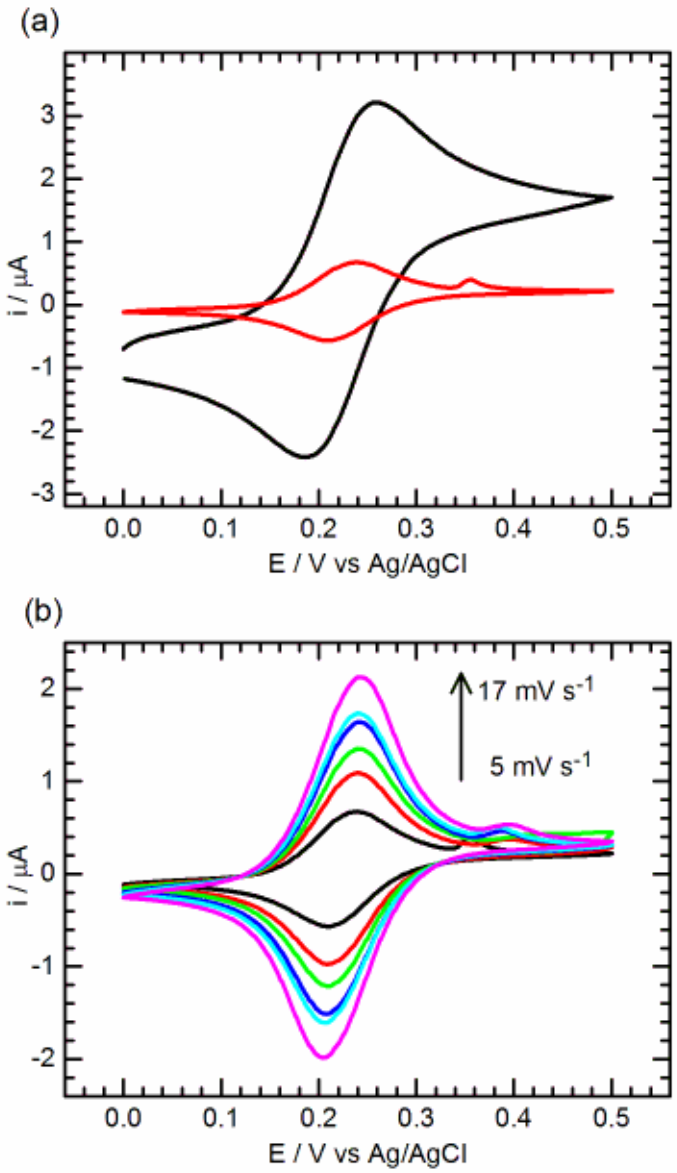

Figure 5.2 Cyclic voltammograms of 1.13×10^{-3} M FcMeOH in 0.1 M NaCl in IR setup. (a) Black line: BDD positioned 5 mm above ATR prism. Red line: BDD positioned against ATR prism, creating thin-layer conditions. Scan rate 5 mV s^{-1}. (b) CVs recorded in the thin-layer geometry with scan rates 5, 8 10, 12, 14 and 17 mV s^{-1}. Reproduced from [9].

Table 5.1: Scan rates, peak currents for forward and backward scans, calculated volumes of the thin-layer cell and distance *h* between electrode and IRE. Adapted from [9].

v / mV s^{-1}	i_p / µA	V / 10^{-9} l	h / µm
5	0.65	120	17.0
5	−0.67	123	17.4
8	1.06	123	17.4
8	−1.08	125	17.7
10	1.33	123	17.4
10	−1.37	127	17.9
12	1.58	122	17.2
12	−1.64	126	17.9
14	1.73	114	16.2
14	−1.77	117	16.5
17	2.15	117	16.6
17	−2.18	119	16.8

5.4 Penetration Depth of IR Evanescent Wave

In the attenuated total reflection mode, the infrared beam is incident at a crystal made of a material with a high refractive index such as diamond. The sample is placed in contact with the crystal on the other side of the infrared beam. At angles above the so-called critical angle, total reflection of the light occurs, and an evanescent wave forms that extends into the sample. The penetration depth is the distance where the amplitude of the electric field falls to 1/e of its value at the surface and is given by

$$d_p = \frac{\lambda}{2\pi\,(n_1^2 \sin^2\theta - n_2^2)^{1/2}} \tag{5.2}$$

where λ is wavelength, θ is the angle of incidence of the IR beam and n_1 and n_2 are the refractive indices of the crystal and the sample, respectively. The volume of the evanescent wave can be used to compare sample absorbance in ATR mode to that in transmission mode and hence gain quantitative information about the sample [11]. This volume, known as the effective penetration, d_e, is unique for parallel and perpendicular polarisation and they are given by:

$$d_{e\perp} = \frac{n_1^2 n_2 cos\theta}{(n_1^2 - n_2^2)} \cdot \frac{\lambda}{\pi\sqrt{n_1^2 \sin^2\theta - n_2^2}} \tag{5.3}$$

$$d_{e\parallel} = \frac{n_1^2 n_2 \cos\theta}{(n_1^2 - n_2^2)} \cdot \frac{2n_1^2 \sin^2\theta - n_2^2}{(n_1^2 - n_2^2)\sin^2\theta - n_2^2} \cdot \frac{\lambda}{\pi\sqrt{n_1^2 \sin^2\theta - n_2^2}} \tag{5.4}$$

d_e for an unpolarised beam is given by

$$d_e = \frac{d_{e\perp} + d_{e\parallel}}{2} \tag{5.5}$$

Taking diamond as the crystal, pure water as the sample and θ = 45°, values of d_p and d_e were calculated at different wavenumbers and listed in **Table 5.2**.

Table 5.2: Penetration depth d_p and the effective penetration d_e calculated at different wavenumbers. Values of n_1 were found in ref [12] and values of n_2 in ref [13]. Reproduced from [9].

n_1	n_2	$\tilde{\nu}$ / cm^{-1}	d_p / µm	d_e / µm
2.38	1.22	1000	1.37	2.03
2.38	1.33	1400	1.10	1.91
2.38	1.33	1670	0.92	1.59
2.38	1.33	2000	0.77	1.34
2.38	1.35	2500	0.63	1.13
2.38	1.43	3000	0.60	1.20

The penetration depths were calculated above using pure water as the sample. The refractive index of water will depend on the amount of dissolved ions and n_2 will therefore be slightly different for an electrolyte solution. Berlind's group have measured the effect of ion concentration on refractive indices of fluids [14] at wavelengths in the range 0.93-5.93 eV, and their results can be used to estimate the change in d_p at wavelengths relevant to this study. They found that at 0.93 eV (7500 cm^{-1}) n changed by 0.01 units for every 1 M change in ion concentration, which translates to a maximum increase in d_p of 2% when the ionic strength changes from 0 to 1 M. Similar estimates can be made based on data reported in [15] and [16].

5.5 Proposed Mechanism for Potential-Induced Deprotonation of Acid Edge Groups

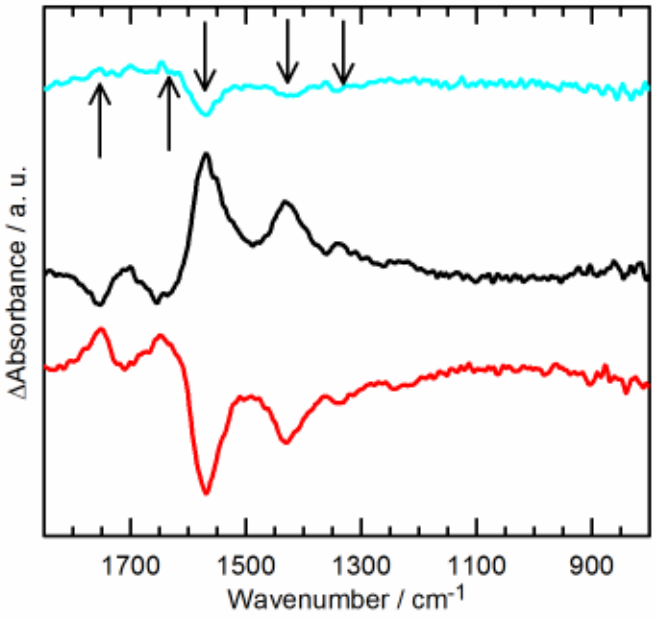

Figure 5.3 Difference spectra of BDD modified with GNF-Ca in 0.1 M NaCl electrolyte at pH 7. Initial application of +1 V, background spectrum recorded without applied potential (light blue); spectrum after subsequent application of −0.5 V (black); spectrum after subsequent application of +1 V (red). Arrows on top spectrum indicate direction of spectral features relative to baseline as a guide to the eye. Reproduced from [9].

Using the in situ ATR-FTIR cell shown in **Figure 5.1**, the effect of applied potential on the acid GNF-Ca edge groups was investigated in 0.1 M NaCl electrolyte at pH 7. A positive potential of 1.0 V was first applied and changes to the IR spectrum relative to a background spectrum measured, as shown by the difference spectrum in **Figure 5.3** (light blue). The background was a spectrum of the modified electrode equilibrated in the same electrolyte for 50 min with no applied potential. It can be seen that the initial application of positive potential results in very weak features in the spectrum, indicating that only a small change is taking place in the setup. The spectrum recorded at 1.0 V acted as the background for the subsequent spectrum recorded with applied potential

of −0.5 V (**Figure 5.3**, black). The spectrum now shows decreases in absorbance (losses) of peaks at 1760 cm^{-1} and 1635 cm^{-1} attributed to weakly hydrogen-bonded monomeric C=O of the carboxylic acid and a water bending mode respectively. Increases in absorbance (gains) are observed at 1580 cm^{-1}, 1430 cm^{-1} and 1340 cm^{-1} attributed to carboxylate stretches. We attribute the changes to deprotonation of carboxylic acid functionalities on application of a negative potential. Subsequent application of 1.0 V (with the −0.5 V spectrum acting as the background) gave a mirror-image response (**Figure 5.3**, red) with gains of C=O and water modes and losses in carboxylates.

This set of spectra show that the initial application of a positive potential does not result in much change in the protonation state of the GNF-Ca edge groups and that application of −0.5 V is required to induce the first deprotonation step.

Previous studies of the protonation state of carboxylic acid groups as a function of applied potential can be divided into two categories: those who observe (as we do) that a negative potential results in deprotonation [17-20] and studies who observe the opposite, that protonation takes place at negative potentials [21-25]. The latter studies describe an electric-field mechanism, where the acid head-groups are within close enough proximity to the electrode surface to respond to changes to the electrode potential and the negative applied potential drives protonation. This was explained by the relationship between pK_a(app) and surface potential φ given in Equation (5.6):

$$\mathrm{p}K_a(\mathrm{app}) = \mathrm{p}K_a - \frac{F\phi}{2.3RT} \qquad (5.6)$$

Equation (5.6) therefore predicts that when a negative electrode potential is applied (φ is negative), a positive shift in pK_a(app) will take place. This will result in protonation of any deprotonated acids.

As the opposite trend is observed here, another mechanism must be operational in this case. We rationalise our observations using a mechanism that considers deprotonation to be driven by electrolyte ion migration [17-20]. In NaCl electrolyte at negative applied potential Na^+ ions will migrate towards the electrode, while Cl^- ions will be repelled. While the pK_a of the GNF-COOH groups is defined by the position of equilibrium in Equation (5.7), it has been shown that the apparent pK_a, pK_a(app), of an acid in an electrolyte solution is additionally dependent on the local activity of cations (a_{M^+}) and the equilibrium constant (K_{as}) for cation association with the deprotonated acid shown in Equation (5.7) [17].

$$\text{GNF-COOH} + H_2O \rightleftharpoons \text{GNF-COO}^- + H_3O^+ \tag{5.7}$$

$$\text{GNF-COO}^- + M^+ \rightleftharpoons \text{GNF-COO}^-M^+ \tag{5.8}$$

Hence the observed pK_a(app) is given by Equation (5.9)[2]:

$$pK_a(\text{app}) = pK_a + pK_{as} - \log(a_{M^+}) \tag{5.9}$$

where K_{as} is the equilibrium constant for the association between conjugate base and solution cations, M^+, and a_M+ is the cation activity. Thus when a negative electrode potential is applied, the local Na^+ activity increases, resulting in a negative shift in pK_a(app) of the acid. pK_a(app) can then be substituted into Equation (3.3):

$$pH = pK_a(\text{app}) + \log_{10}\left(\frac{[A^-]}{[HA]}\right) \tag{5.10}$$

If pK_a(app) is lowered sufficiently relative to the pH of the solution, then deprotonation of the acid groups will take place, as is observe here. pH titration studies described in Section 3.3.4 showed that between pH 3 and pH 8 the GNF acid groups are found in a range of protonation states with no single defined pK_a. Therefore, as the experiments in

[2] For derivation of Equation (5.9) see Appendix 2.

.

0.1 M NaCl are within this intermediate pH range (pH 7), a small perturbation in a_{M^+} could result in a sufficiently negative shift in pK_a(app) of some of the acid groups to induce deprotonation, as indicated by the spectral changes in Figure 5.3. Figure 5.4 illustrates the proposed mechanism graphically.

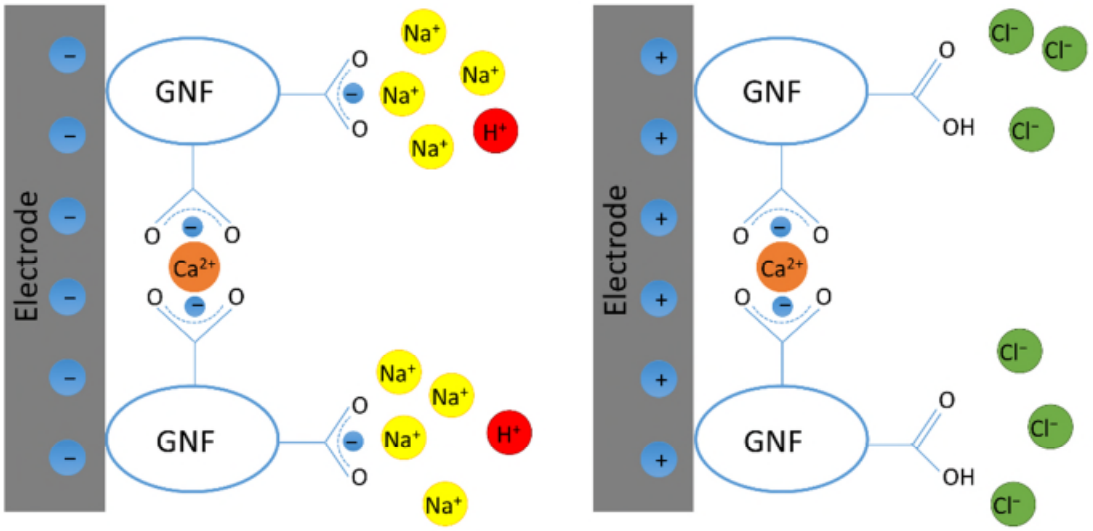

Figure 5.4 Potential-induced changes in cation activity in the electrode-electrolyte interfacial region drive protonation and deprotonation of acidic surface groups.

The reason for different reported behaviour of electrode-immobilised acids seems to be related to the distance between the acid groups and the underlying electrode. Acids located closer to the electrode (e.g. on short chain SAMs) are under a greater influence of the electric field and therefore respond as predicted by Equation (5.6). A mixture of behaviours is reported for longer chain SAMs and more disordered systems. The acids respond either to the change in surface potential of the electrode, or to the change in cation activity (as we describe) depending on how closely they are bound to the electrode and on the local environment. For example, acid groups buried within hydrophobic alkyl chains of SAMs respond to the electrode field, while acids further from the electrode and in contact with solution are more likely to respond to changes in solution conditions than changes to surface potential.

5.6 Evidence of Electrolyte Ion Migration

To test the above hypothesis and gain evidence of electric field driven ion migration, experiments were repeated using Na_2SO_4 and K_2SO_4 electrolytes. The sulphate anion is strongly IR active, thus allowing us to monitor both the protonation/deprotonation of the surface acid groups and the sulphate anion concentration at the electrode/electrolyte interface simultaneously.

IR spectra were first recorded during equilibration of the modified electrode in a sulphate electrolyte. This is shown in **Figure 5.5** where the black line represents the IR spectrum of the modified electrode in 0.1 M K_2SO_4 immediately after insertion, the red line after 5 minutes' equilibration and blue line after 35 minutes' equilibration. The absorbance bands arising from the carboxylate are seen at 1575 cm^{-1} ($\nu_{as}(COO^-)$) and 1420 and 1350 cm^{-1} ($\nu_s(COO^-)$), and the ν(C=O) of the protonated carboxylic acid is clearly visible at 1720 cm^{-1}. The increase in the intensity of these bands suggests that the GNF layer is swelling as water penetrates the structure, resulting in good contact of the GNF with the IRE as mentioned in Section 5.2. The water bending mode at 1640 cm^{-1} increases with time, indicating an interaction between water molecules and GNF-Ca. A small SO_4^{2-} absorbance band at 1100 cm^{-1} suggests that the sulphate concentration is slightly higher at the surface than in the bulk solution. Because the absorption band appears at the same wavenumber as the solution species and does not split into several bands, it can be concluded that there is no change in the symmetry of the anion and the hydration shell of SO_4^{2-} is retained.

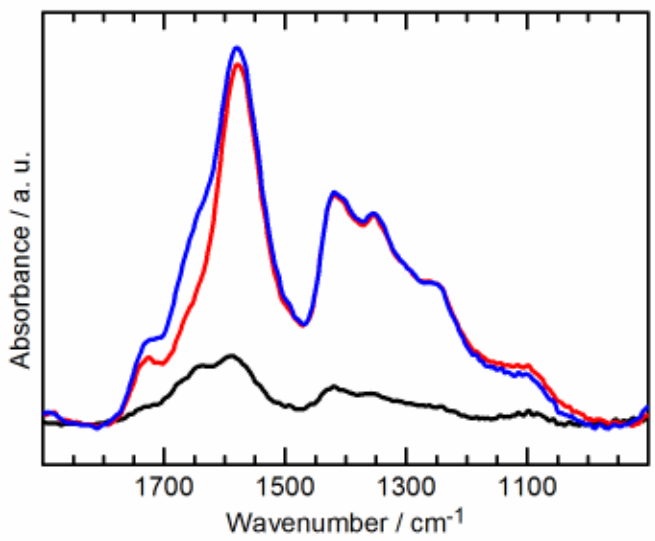

Figure 5.5 GNF-Ca modified electrode immersed in 2 ml of 0.1 M K_2SO_4 electrolyte in spectroelectrochemical setup after 0 minutes (black line), 5 minutes (red line) and 35 minutes (blue line). Background: electrolyte only. Reproduced from [9].

This supports the hypothesis that application of electrode potential induces electrolyte ion migration and hence changes in anion concentration are seen in the interfacial region above the ATR crystal. Although the Na^+ cation is IR inactive, it can be assumed that it also migrates in response to the electrode field in the opposite direction to the sulphate and hence local changes in the cation activity could lead to deprotonation as described above.

Difference spectra were also recorded relative to electrode equilibrated for 50 min without applied potential. The background spectrum was collected before any application of potential, and all subsequent spectra were recorded relative to that background. The potential step duration was kept at 720 seconds and four sample spectra were recorded during the initial 600 seconds in order to keep all other experimental parameters as similar as possible to all other experiments reported.

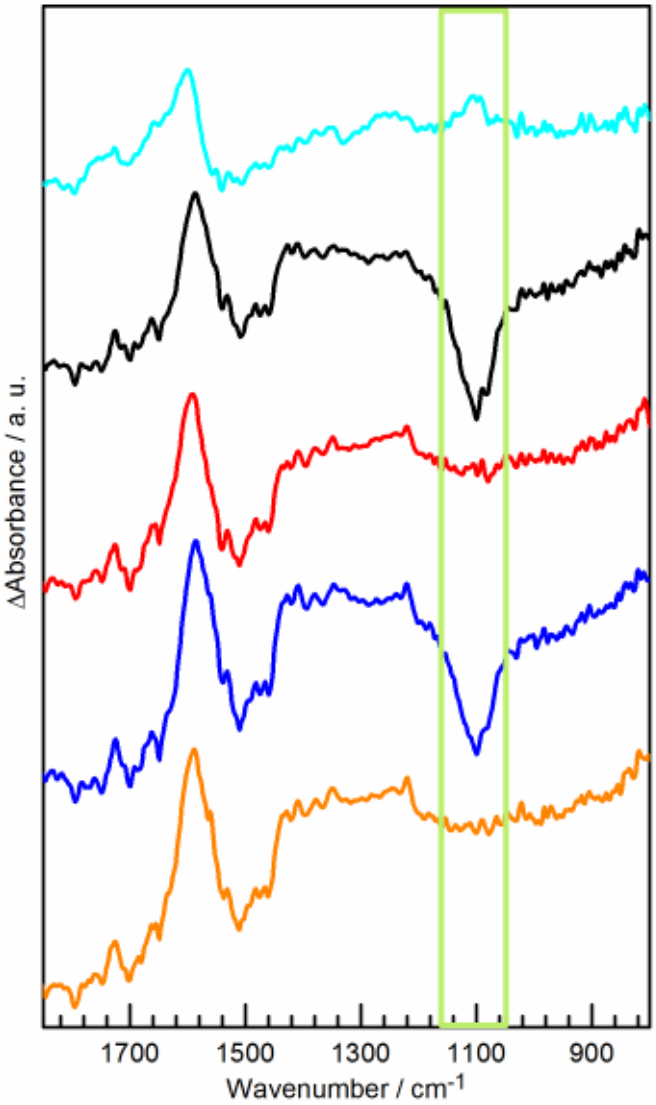

Figure 5.6 Difference spectra of BDD modified with GNF-Ca in 0.1 M Na_2SO_4 pH 7. Background recorded at the beginning of experiment before the application of potential. Potentials: +1 V (light blue); −0.5 V (black); +1 V (red); −0.5 V (blue); +1 V (orange). The sulphate band at 1100 cm^{-1} is highlighted in green. Reproduced from [9].

The initial application of +1 V (**Figure 5.6**, light blue) causes only a small increase in the sulphate band compared to the equilibrium absorbance, whereas applications of −0.5 V (black, blue) result in a large negative-going band, indicating a loss of SO_4^{2-} from the electrode surface at negative potentials. Further applications of +1 V (red, orange) cause the sulphate band region to return to zero absorbance relative to the background.

Figure 5.6 shows that a measureable change in the local activity of the electrolyte ions takes place in response to the electric field at the electrode. This supports the hypothesis that application of electrode potential induces electrolyte ion migration and hence changes in anion concentration are seen in the interfacial region above the ATR crystal.

It is evident from **Figure 5.6** that only −0.5 V and not +1.0 V results in a change in the sulphate band. It was determined from **Figure 5.3** that a negative potential was necessary for deprotonation of acid groups to occur and that the initial spectrum recorded at +1.0 V was nearly featureless. The experimental results presented in **Figure 5.6** and **Figure 5.3** can be rationalised by considering the increase in concentration of sulphate at the electrode surface compared to bulk solution during equilibration as shown in **Figure 5.5**. Because the concentration of SO_4^{2-} is already higher than in the bulk solution prior to applying a potential, a positive potential of +1 V forces the anions to migrate against a concentration gradient and hence only a minor increase is observed (**Figure 5.6**, light blue). When a negative potential is applied, SO_4^{2-} ions are repelled away from the electrode towards a region of lower concentration, resulting in a large negative sulphate band in the IR difference spectrum (**Figure 5.6**, black).

Similarly, we can assume that cations have been depleted from the electrode surface during equilibration, so upon application of a positive potential the cations migrate against a concentration gradient, resulting in little change in concentration at the electrode and therefore only a small number of carboxylate groups can be observed to undergo protonation as seen in **Figure 5.3** (light blue). Upon application of a negative potential, a larger change in the cation concentration occurs that in turn leads to a larger number of carboxylic acids to deprotonate.

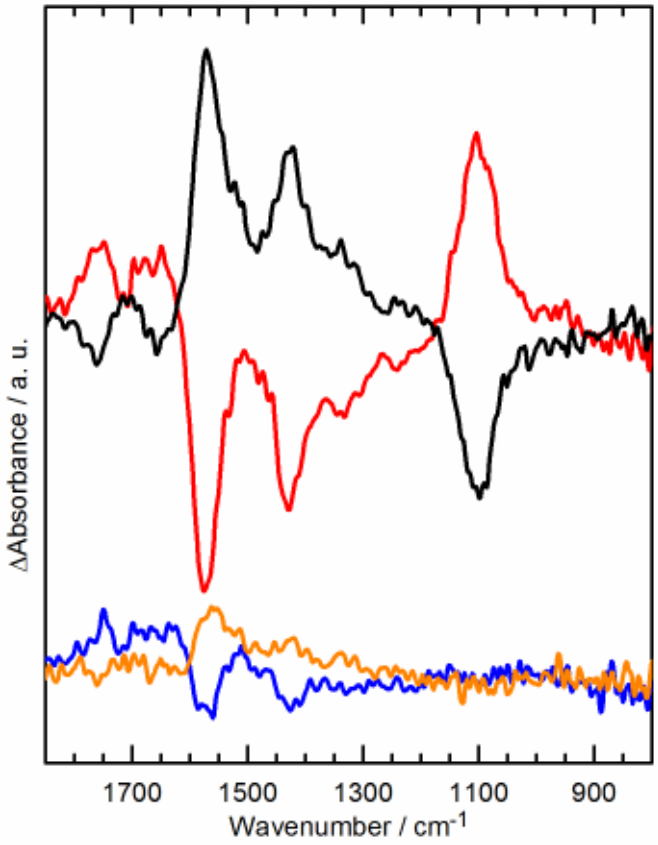

Figure 5.7 Difference spectra in different concentrations of supporting electrolyte Na_2SO_4 at pH 7. BDD modified with GNF-Ca in 0.1 M: application of −0.5 V (black); application of +1 V (red). BDD modified with GNF-Ca in 1×10^{-3} M: application of −0.5 V (orange); application of +1 V (blue). A background spectrum was collected at each potential immediately prior to switching the applied potential. Reproduced from [9].

It was then hypothesised that lowering the concentration of the supporting electrolyte, the activity change would be smaller and consequently the protonation of carboxylate groups would be suppressed. The experiment was therefore repeated in different concentrations of Na_2SO_4 electrolyte, and the results are presented in **Figure 5.7**.

In 0.1 M Na_2SO_4 (black and red) identical spectral changes to those seen in NaCl were observed on application of potential: negative potential resulted in increase in carboxylate and decrease in C=O (deprotonation) and positive potential resulted in decrease in carboxylate and increase in C=O (protonation). The feature at 1100 cm^{-1} arises from $\nu_{as}(SO_4^{2-})$ of the solution-phase sulphate anion and can be seen to decrease when a negative potential is applied.

When the concentration of Na_2SO_4 was lowered to 1×10^{-3} M, the potential-induced changes in the sulphate band become too small to detect, as shown in the orange and blue curves in **Figure 5.7**. Some protonation/deprotonation of the GNF-Ca acid groups is still observed; however, the spectral response is significantly less intense than observed in 0.1 M electrolyte. As was shown in Section 5.4, some of the intensity decrease can be attributed to a change in solution reflective index at lower ionic strength; however it is unlikely that a decrease in IR penetration depth of less than 2% would lead to the extent of signal suppression seen in **Figure 5.7**. The ionic strength dependence of the spectral response therefore supports the hypothesis that the deprotonation is driven by changes to the local cation activity on the application of potential. As described by Equation (5.9), for deprotonation to be observed, the local activity of M^+ must increase enough to lower pK_a(app) of acid groups enough to drive proton loss at the pH of the solution [18]. At lower electrolyte concentration, only a small local increase in cation activity can occur; so fewer acid groups will have their pK_a(app) lowered enough to induce dissociation. Therefore, the spectral features observed in 1×10^{-3} M Na_2SO_4 (orange and blue curves) are considerably weaker than in 0.1 M Na_2SO_4 (black and red curves), as fewer acid groups have a sufficiently low pK_a to deprotonate under these conditions.

5.7 Quantifying Changes in Ion Activity

In the previous Section, we showed that electric field driven changes in the sulphate IR band allows the indirect monitoring of cation activity at the electrode. In order to quantify the cation activity, the same indirect approach is adopted. Peak areas of sulphate bands in the difference spectra are determined by peak fitting and the activity change of SO_4^{2-} at the electrode surface is found using a calibration curve. The activity change of the monovalent cation is then estimated from stoichiometry as $2\times\Delta a_{SO_4^{2-}}$.

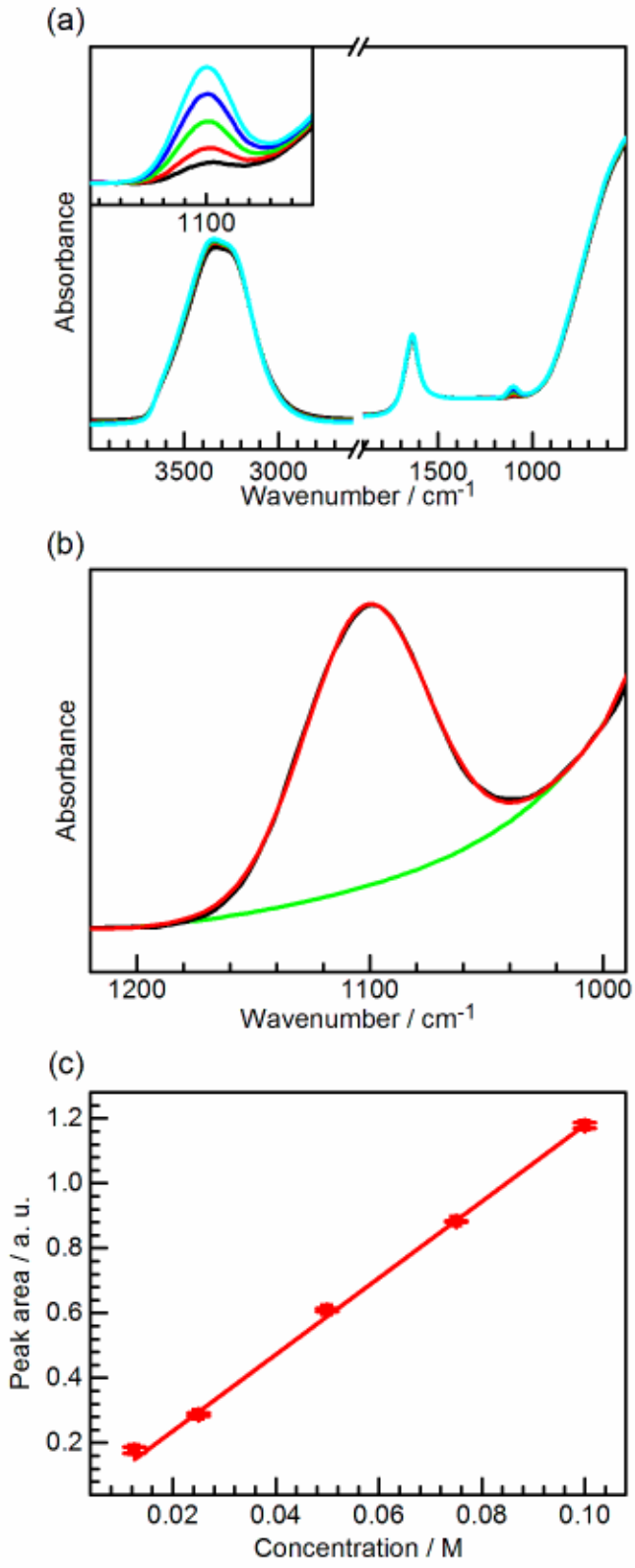

Figure 5.8 (a) Infrared spectra of aqueous solutions of K_2SO_4 at different concentrations. The pH of all solutions was ca. 7. Inset: Magnification of the SO_4^{2-} absorption bands. (b) Peak fit of the sulphate absorption band from 0.075 M K_2SO_4 spectrum. (c) Peak areas from Fig 1.1 plotted against concentration of K_2SO_4 and a linear fit of data points. Error bars represent one standard deviation. Reproduced from [9].

Figure 5.8(a) shows IR spectra of different concentrations of aqueous K_2SO_4 and the inset shows the sulphate absorption band at 1100 cm^{-1}. In **Figure 5.8**(b) the peak fitting is illustrated for 0.075 M solution. The peak areas were then plotted against concentration and the data points were fitted with a linear regression line (**Figure 5.8**(c)). The intercept was fixed to zero to ensure physically meaningful estimations of small numbers of moles from the calibration curve.

Difference spectra recorded at equilibrated state and under potential control in 0.1 M K_2SO_4 electrolyte (pH 7) were fitted with Gaussian peaks and the linear fit equation was used to calculate the change in sulphate ion concentration at the electrode from the sulphate peak area. From **Figure 5.5** the activity increase at the electrode surface at equilibrated state was found to be 7.6×10^{-3} M and from three different experiments it was determined that $\Delta a_{SO_4^{2-}}$ changes by $(3.5 \pm 0.4) \times 10^{-3}$ M when the potential is changed from +1 V to −0.5 V. Δa_{M^+} was therefore estimated to be 1.53×10^{-2} M at equilibrated state and $(7.0 \pm 0.6) \times 10^{-3}$ M on application of −0.5 V. **Table 5.3** lists the peak areas and corresponding activity changes.

Table 5.3: Peak areas from difference spectra obtained at different potentials and the calculated activity change in sulphate ion at the electrode surface. Reproduced from [9].

E / V	Conditions	Peak area	$\Delta a_{SO_4^{2-}}$ / M	Δa_{M^+} / M
Equilibration	0.1 M K_2SO_4 with O_2	0.090	0.0076	0.0153
1	0.1 M K_2SO_4 with O_2	0.041	0.0035	0.0069
−0.5	0.1 M K_2SO_4 with O_2	−0.041	0.0035	0.0069
1	0.1 M K_2SO_4 with O_2	0.046	0.0039	0.0078
−0.5	0.1 M K_2SO_4 with O_2	−0.043	0.0036	0.0073
1	0.1 M K_2SO_4 no O_2	0.034	0.0029	0.0058
−0.5	0.1 M K_2SO_4 no O_2	−0.044	0.0037	0.0074

As was discussed in Section 5.5, the initial application of +1 V leads to very weak changes in the IR spectra. The reason behind this observation was presented in Section 5.6, where it was shown that a preconcentration of sulphate occurs at the

electrode surface during equilibration. We have successfully quantified that preconcentration and found it to be larger than the subsequent electric field driven migratory loss of sulphate on application of −0.5 V. Our calculations are therefore consistent with our observation that the initial application of a positive potential does not induce large changes in IR bands arising from the protonation of carboxylates.

5.8 Ruling Out pH Change at Interface

Seeing protonation and deprotonation of the acid groups suggests that there might be a pH change occurring at the interface that drives the acid association. Especially at negative potential there are several reactions that can lead to an increase in the pH, such as oxygen reduction and hydrogen evolution. Experiments were therefore conducted to investigate the possibility of such reactions.

Cyclic voltammetry was performed in oxygenated and deoxygenated background electrolyte as shown in **Figure 5.9**(a), and IR difference spectra under potential control were recorded in the same electrolyte conditions (**Figure 5.10**). The presence of oxygen leads to a small increase in cathodic current attributed to oxygen reduction at the modified electrode compared to deoxygenated solution **Figure 5.9**. However, the effect of deoxygenating the electrolyte has no significant impact on the difference spectra recorded while applying potentials (**Figure 5.10**). This suggests that a pH change at the electrode surface due to oxygen reduction can be discounted as the cause of the spectral features.

We observed in **Figure 5.7** that the spectral changes were almost completely suppressed when the background electrolyte concentration was lowered while the pH was held constant. Significant changes in the protonation state of the acid groups are seen when the electrolyte concentration is 0.1 M, but as the concentration is lowered to 10^{-3} M, the changes become barely detectable. **Figure 5.9**(b) shows cyclic voltammetry in the same background electrolyte concentrations 0.1 M and 10^{-3} M. CV

response in these different ionic strength solutions is within variation of repeated experiments under the same conditions, indicating that additional redox chemistry that could result in pH change (O_2, H^+ or water reduction) does not proceed at a significantly different rate at lower ionic strength. As the spectral response (**Figure 5.7**) is very different in lower ionic strength solution, we can conclude that ion activity rather than pH change or redox chemistry must be responsible for the observed changes.

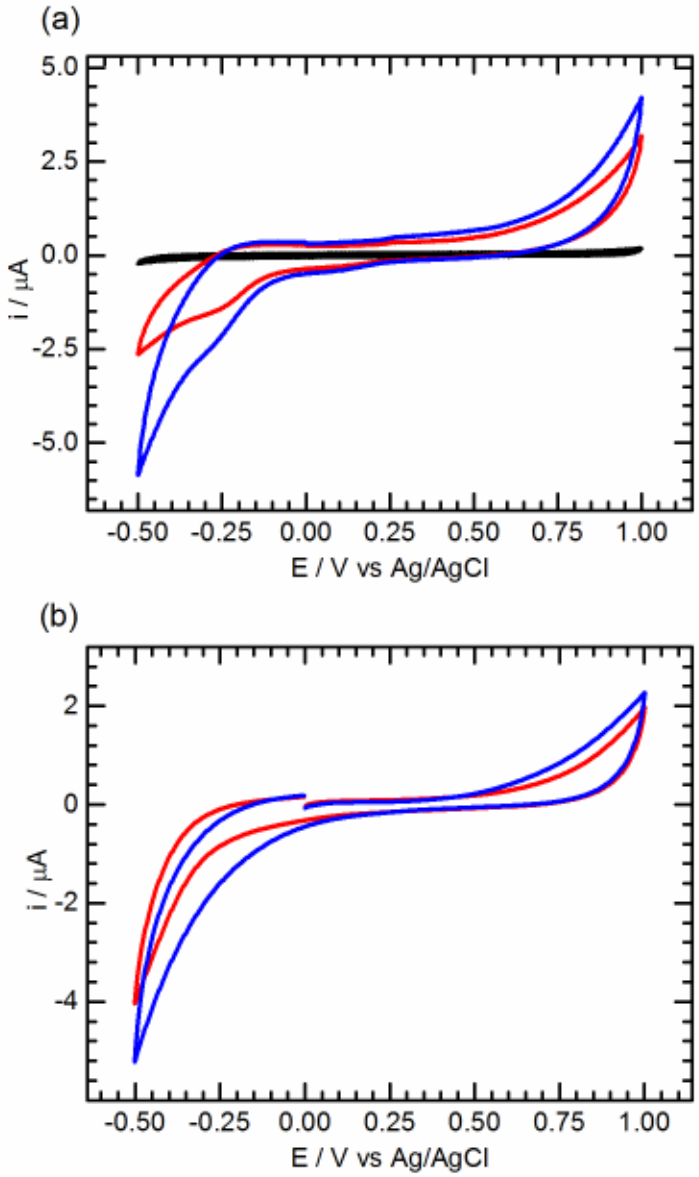

Figure 5.9 (a) Cyclic voltammograms in 0.1 M PBS at pH 7 with and without oxygen present in solution. Clean BDD with O_2 (black); BDD modified with GNF-Ca with O_2 (blue); BDD modified with GNF-Ca without O_2 (red). (b) Cyclic voltammograms in different ionic strength solutions. BDD modified with GNF-Ca in 1×10^{-3} M PBS at pH 7 (red); in 0.1 M PBS at pH 7 (blue). Reproduced from [9].

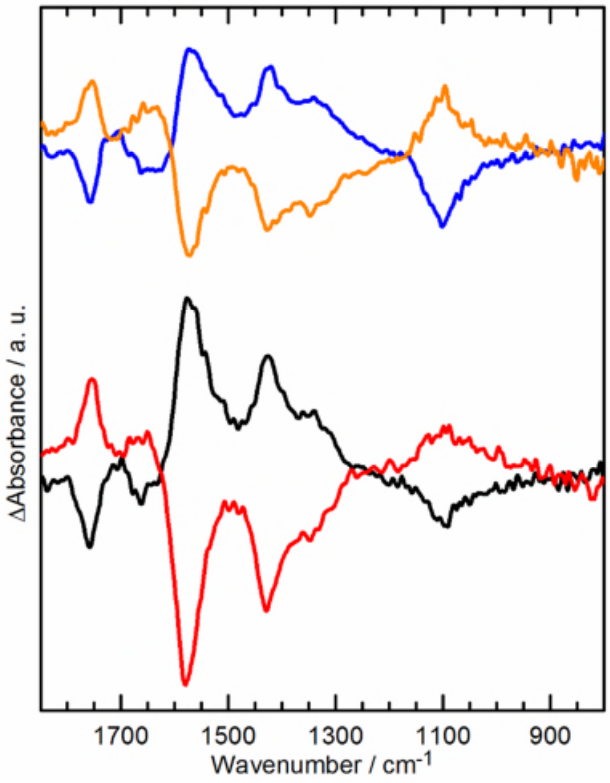

Figure 5.10 Difference spectra of BDD modified with GNF-Ca in 0.1 M K_2SO_4 pH 3.5. Application of −0.5 V (black); application of +1 V (red). Difference spectra under same conditions but electrolyte deoxygenated with argon for 20 minutes. Application of −0.5 V (blue); application of +1 V (orange). Reproduced from [9].

5.9 Investigating the Effect of Electrolyte Cation

Different supporting electrolytes were also compared to see whether the identity of the cation would have an effect on the potential-dependent acid ionisation. Difference spectra recorded in both 0.1 M Na_2SO_4 and 0.1 M K_2SO_4 at pH 7 (**Figure 5.11**) show that both K^+ and Na^+ cause nearly identical changes to the protonation state of the electrode-immobilised acid groups. The sulphate bands are of equal size, suggesting that the local increase in cation activity is very similar for both K^+ and Na^+.

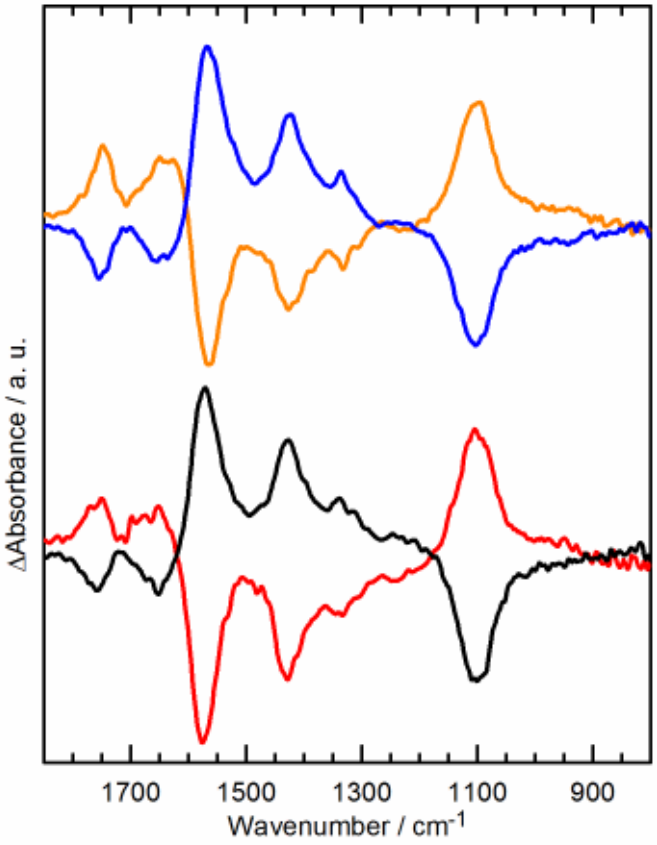

Figure 5.11 Difference spectra of BDD modified with GNF-Ca in 0.1 M K_2SO_4 pH 7; application of −0.5 V (black); subsequent application of +1 V (red). Difference spectra of BDD modified with GNF-Ca in 0.1 M Na_2SO_4 pH 6.8; application of −0.5 V (blue); subsequent application of +1 V (orange). Reproduced from [9].

Experiments were then repeated in an electrolyte solution of 0.1 M $CaCl_2$ at pH 3.5 (**Figure 5.12**, blue and orange), where the presence of Ca^{2+} results in essentially featureless difference spectra at both positive and negative potential. Ca^{2+} in excess will bind strongly to any previously non-complexed carboxylate groups in the GNF-Ca structure and hence suppresses the reversible potential-dependent protonation observed in NaCl electrolyte. This suggests that the spectral changes observed in NaCl must be attributed to protonation and deprotonation of non-complexed edge groups within the GNF-Ca assembly. This assignment is supported by the observation that the electrode-immobilised precipitate appears intact at the end of the experiment, so it is clear most of the interlinking Ca^{2+} complexation in unaffected by the application of potential. As GNF becomes water-soluble when not complexed, the precipitate would

not be present at the end of the experiment if application of potential removed the bound Ca^{2+}.

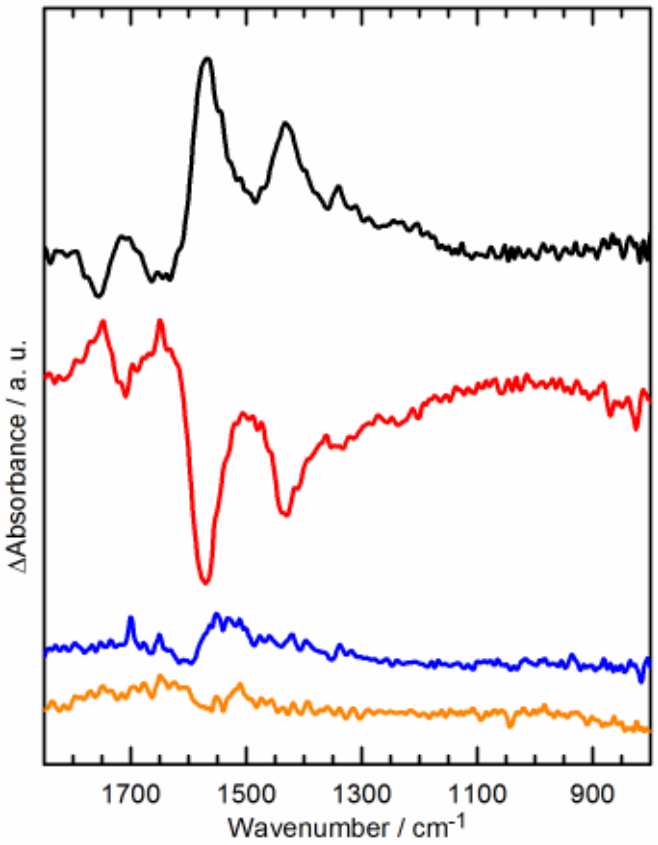

Figure 5.12 Difference spectra of BDD modified with GNF-Ca in 0.1 M NaCl electrolyte at pH 3.5. Application of −0.5 V (black); subsequent application of +1 V (red).Difference spectra of BDD modified with GNF-Ca in 0.1 M $CaCl_2$ pH 3.5. Application of −0.5 V (blue); subsequent application of +1 V (orange).

5.10 Estimating the Number of Acid Groups Undergoing Potential-Induced Changes

The amount of GNF-Ca on the electrode surface is estimated to be 1.8×10^{-5} g and the number of COOH groups 7×10^{-3} mol per gram of GNF. From this we can estimate the total number of both protonated and deprotonated COOH groups present on the electrode as 1.8×10^{-5} g $\times$ 7×10^{-3} mol g^{-1} = 1.26×10^{-7} mol, and XPS measurements have allowed us to quantify the fraction of carboxylate groups in GNF-Ca that remain

non-complexed and therefore available to contribute to the potential-dependent spectral features. It is likely that only a fraction of the non-complexed acid groups will undergo deprotonation due to the modest potential applied in this study. To estimate the number of non-complexed COO^-/COOH groups at the electrode surface undergoing potential-induced changes, the peak areas in potential difference spectra were compared with those of a simple carboxylic acid (acetic acid). Because the acid groups are bound to the surface, a calibration curve of an aqueous acid at different concentrations was deemed inapplicable and hence a calibration curve was constructed using varying amounts of a dried deprotonated acetic acid (acetate) deposited on the ATR prism to mimic a surface layer. A representative peak fit is shown in **Figure 5.13**(a) and the resulting calibration curves in **Figure 5.13**(b)-(c) for the asymmetric and symmetric stretches, respectively.

Because the number of groups undergoing changes is estimated based on peak areas in IR spectra, the result is dependent on the distance to the IRE. The dry potassium acetate film is very thin (thinner than the penetration depth calculated in Section 5.4) and it can therefore be assumed that the signal represents the total sample amount. However, when IR spectra are recorded of the thick GNF-Ca layer at the electrode surface, the signal isn't a straightforward reflection of the total number of acidic groups due to the exponential decay of the evanescent wave's electric field.

We can estimate the number of groups dissociating under applied potential by adjusting the peak areas in the difference spectra by the ratio of the effective penetration depth, d_e (Section 5.4), and the thickness of the GNF-Ca film, *h*, which is taken to be 17 µm as calculated in Section 5.3 [11]. The adjusted peak areas were then compared to the calibration curve to estimate the number of carboxylate groups lost and gained due to potential-induced protonation and deprotonation.

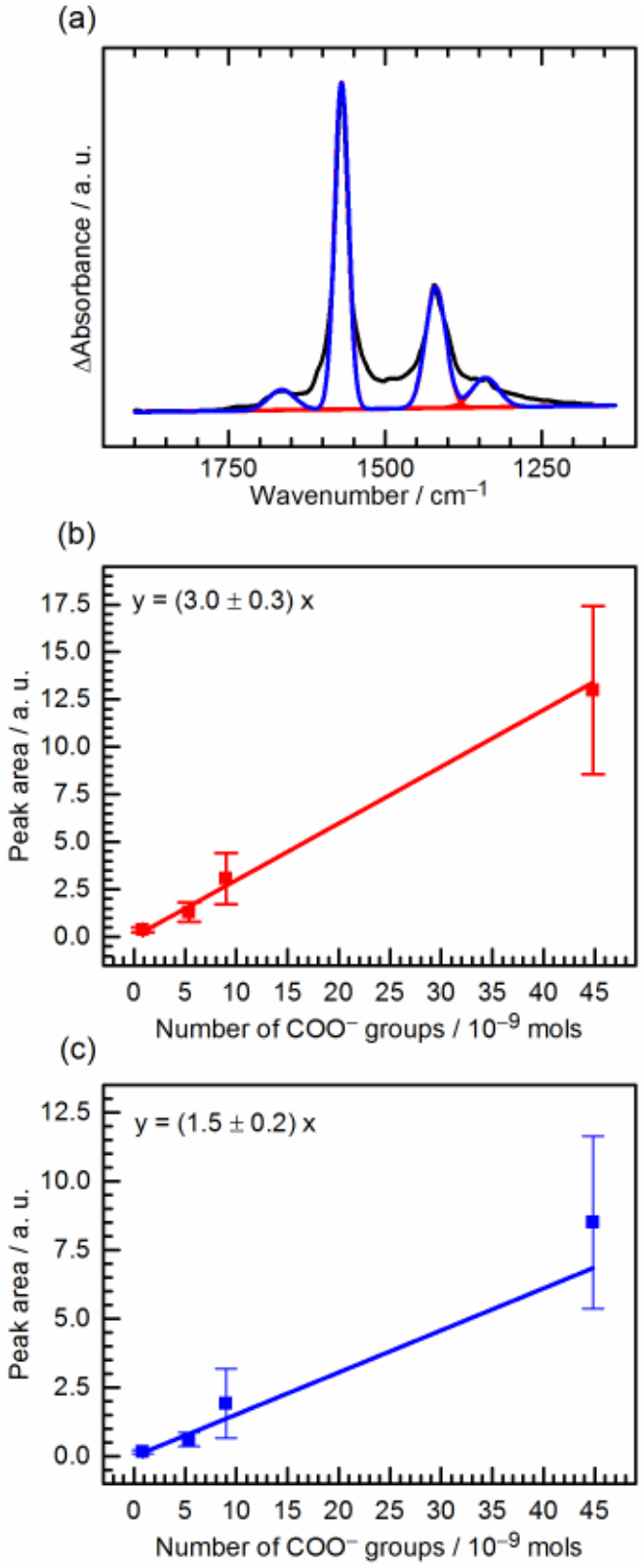

Figure 5.13 (a) Peak fit of drop-coated potassium acetate film containing 5.38 × 10^{-9} moles of acetate groups. Experimental data (black), baseline (green), peak fits (red), cumulative peak fit (blue). (b) Asymmetric stretch peak areas at 1565 cm^{-1} plotted against number of acetate groups and a linear fit of data points. (c) Symmetric stretch peak areas at 1415 cm^{-1} plotted against number of acetate groups and a linear fit of data points. Error bars represent one standard deviation. Reproduced from [9].

Figure 5.14 shows an example of peak fitted difference spectrum in 0.1 M K_2SO_4 pH 7. Peaks used in estimating the number of carboxylate groups were the asymmetric peak at 1570 cm^{-1} and the symmetric peak at 1430 cm^{-1}, and spectra from three separate experiments in 0.1 M K_2SO_4 pH 7 were evaluated, both with and without oxygen present in solution. The average areas found from the difference spectra were 0.034 and 0.023 for the asymmetric and symmetric peaks, respectively. These were adjusted by the ratio d_e/h, at each wavelength, giving adjusted peak areas of 0.241 and 0.215 for the asymmetric and symmetric peaks, respectively.

From the adjusted peak areas, the number of carboxylate groups changing protonation state has been evaluated as (4 ± 2) × 10^{-8} mol using the linear regression lines in Figure 5.13(b)–(c). The peak areas are listed in Table 5.4.

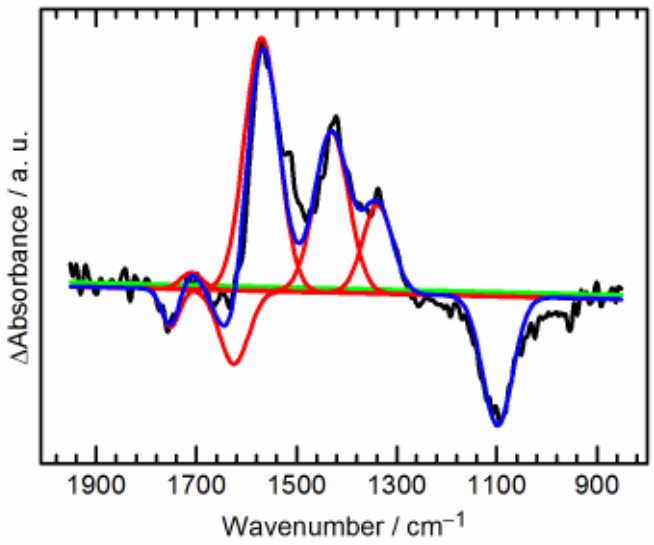

Figure 5.14 Peak fitted difference spectrum in 0.1 M K_2SO_4 pH 7 when applying −0.5 V to GNF-Ca modified BDD. Experimental data (black), baseline (green), peak fits (red), cumulative peak fit (blue). Reproduced from [9].

Table 5.4: Carboxylate asymmetric and symmetric stretch peak areas from difference spectra obtained at different potentials. Reproduced from [9].

E / V	Conditions	$\nu_{as}(COO^-)$ peak area	$\nu_{s}(COO^-)$ peak area
1	0.1 M K_2SO_4 with O_2	0.0326	0.0202
−0.5	0.1 M K_2SO_4 with O_2	−0.0453	−0.0261
1	0.1 M K_2SO_4 with O_2	0.00965	0.00882
−0.5	0.1 M K_2SO_4 with O_2	−0.0231	−0.0149
1	0.1 M K_2SO_4 no O_2	0.0582	0.0443
−0.5	0.1 M K_2SO_4 no O_2	−0.0987	−0.0568

Using Equation (5.9) and the modified Henderson-Hasselbalch equation (Equation (5.10), we can calculate what percentage of the total number of GNF-COOH groups this value of (1.5 ± 0.6) × 10^{-9} mol corresponds to. In our estimate of pK_a(app) we assume that the pK_a of carboxylic acid groups is 3 and that the pK_{as} of COOK is 0.5. These values are estimates but the actual values do not affect the relative resulting pK_a(app) in switching to −0.5 V. As for the calculations in Section 5.7, it was assumed that a_{M^+} changes from 0.2 M at equilibrium to 0.207 M when a negative potential is applied. Although Equation (5.10) applies to concentrations (or activities) rather than numbers of molecules we will still use it as an estimate of the ratio of deprotonated to protonated groups. Using these values, the change in the number of COO^- at −0.5 V compared to equilibrium is found to be +3.5%. **Table 5.5** lists the values used in the calculation.

Table 5.5: Values used to calculate change in the number of carboxylate groups at the electrode surface when a potential is applied. Reproduced from [9].

E / V	a_{M^+}	pK_a(app) = pK_a + pK_{as} − log(a_{M^+})	$[COO^-]/[COOH] = 10^{(pH - pK_a(app))}$
Equilibrium	0.2	4.20	399
−0.5	0.207	4.18	413

This calculated 3.5% increase in $[COO^-]$ at −0.5 V corresponds to (1.5 ± 0.6) × 10^{-9} mol of carboxylate, as determined from IR peak area. Because this number represents

3.5% of non-complexed groups and the total number of COO^-/COOH groups is estimated to be 1.26×10^{-7} mol, (35 ± 13)% of all COO^-/COOH groups remain non-complexed. Clearly the error associated with this value is very large and cannot be used to draw definitive conclusions about the degree of association of the acid groups. In comparison, the percentage of carboxylic acid groups remaining non-complexed was also calculated from XPS measurements in Section 3.3.2 and found to be (24 ± 6)%. Considering that the spectroelectrochemical method included many steps of calculations with a great number of assumptions and large uncertainties unavoidably associated with many of the variables, the value is in reasonable agreement with the value obtained by XPS measurements.

5.11 Predicting Potential-Dependent Changes in Solution Species

Although this study was initially concerned with the surface-bound carboxylic acids of the GNF electrode layer, electric field driven changes were observed in solution species too. As demonstrated in Section 5.7, we were able to quantify changes in ion activity as a consequence of applied potential. The quantification was performed from experimental data at pH 7 where no protonation of sulphate was expected. The intensity and shape of the sulphate bands in IR difference spectra changed when the solution pH was lowered to 3.5. This led us to consider the pK_a of the solution species as a factor in the appearance of potential-dependent IR features as well as the electrostatic migration of ions. Calculations were performed to predict the extent of change in solution speciation coupled with activity change and the results were compared with experimental difference spectra.

5.11.1 Sulphate

IR spectroscopy of sulphate in aqueous solution has been carried out by Hug [26], who lists the expected absorption frequencies of SO_4^{2-} and HSO_4^- species. Aqueous SO_4^{2-} is tetragonal with an IR inactive ν_s(S–O) at 980 cm^{-1} and triply degenerate IR active ν_{as}(S–O) at around 1100 cm^{-1}. Protonation to HSO_4^- lowers the symmetry of the anion, causing the symmetric stretch to become IR active around 900 cm^{-1}. At the same time the asymmetric stretch splits into two bands at around 1050 and 1200 cm^{-1}. Hence IR spectroscopy is an excellent technique to observe protonation of SO_4^{2-} in situ.

The spectral response of the sulphate bands at different pH is compared in **Figure 5.15**. At pH 7, an intense sulphate band is seen corresponding to loss of SO_4^{2-} from the electrode surface at negative potential (pink line). On application of +1 V, the loss seen at negative potential is reversed and the concentration of SO_4^{2-} is restored to equilibrium values (light blue). When the solution pH is lowered to 3.5, the sulphate band shows the same trend in response to applied potential as at pH 7, although the absorbance changes are much weaker and broader (blue, orange lines). At pH 3 (black, red lines) spectral changes for both GNF acid groups and solution sulphate are much lower in intensity. For the acid groups this is unsurprising, as only a small number of the most acidic groups can undergo deprotonation at this pH as very few have a pK_a of 3 or below.

Spectral changes in the sulphate region can be rationalised by considering predicted trends in interfacial activities of solution species in response to changes in a_{M^+} at the electrode. Sulphuric acid is diprotic and undergoes two dissociations as shown in Equations (5.11)-(5.12):

$$H_2SO_4 + H_2O \rightleftharpoons HSO_4^- + H_3O^+,\ pK_{a1} < 0 \quad (5.11)$$

$$HSO_4^- + H_2O \rightleftharpoons SO_4^{2-} + H_3O^+,\ pK_{a2} = 1.92 \quad (5.12)$$

pK_{a1} in Equation (5.11) is so low that HSO_4^- cannot be protonated by any realistic increase in a_{K^+}. We will therefore limit our calculations to the dissociation shown in Equation (5.12).

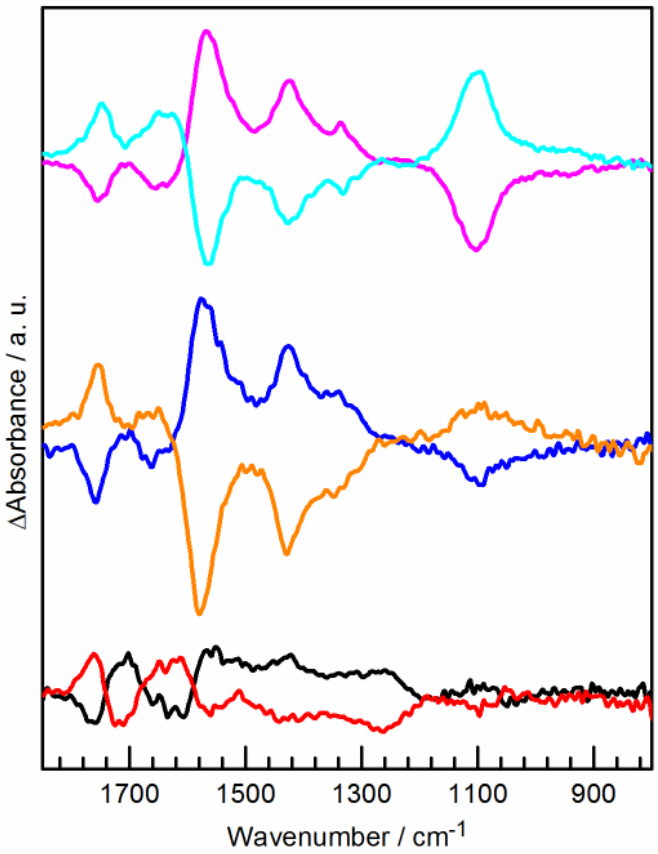

Figure 5.15 IR difference spectra of the GNF-Ca modified electrode interface in: 0.1 M pH 7 K_2SO_4, −0.5 V (pink), +1.0 V (light blue); 0.1 M pH 3.5 K_2SO_4, −0.5 V (blue), +1.0 V (orange); 0.1 M pH 3 K_2SO_4, −0.5 V (black), +1.0 V (red). Reproduced from [9].

Table 5.6: Predicted changes in activity of HSO_4^- and SO_4^{2-} on application of −0.5 V calculated from Equation (5.9). Reproduced from [9].

pH	*E* / V	a_{K^+} / M	pK_a(app) HSO_4^-	$\Delta a_{HSO_4^-}$ / 10^{-3} M	$\Delta a_{SO_4^{2-}}$ / 10^{-3} M
7	−	0.200	2.62	0	0
7	−0.5	0.207	2.60	0	0
3.5	−	0.198	2.62	0	0
3.5	−0.5	0.205	2.61	−0.35	+0.35
3	−	0.192	2.64	0	0
3	−0.5	0.199	2.62	−0.75	+0.75

Using the value for Δa_{K^+} of 7 × 10^{-3} M at −0.5 V, determined in section 5.7, Equation (5.9) can be used to calculate pK_a(app) for HSO_4^- with no applied potential and at –0.5 V. Changes in sulphate and HSO_4^- activity (approximating to concentration), resulting from the change in pK_a(app), have been calculated at different pH using the modified Henderson-Hasselbalch equation (Equation (5.10)). The predicted changes are presented in **Table 5.6**, and detailed calculations can be found in Appendix 3.

At pH 7, SO_4^{2-} activity is unperturbed by any change in pK_a(app), hence the spectral changes to the sulphate band result only from migration of the anion away from the electrode at −0.5 V. At pH 3.5, as the solution pH is closer to pK_a(app) values, deprotonation of 0.4 × 10^{-3} M of HSO_4^- is predicted at −0.5 V. Upon deprotonation of HSO_4^-, a decrease in intensity is predicted over the spectral range spanning ca. 1200 to 900 cm^{-1}; however, this will be concomitant with an increase in intensity centred at 1100 cm^{-1} as the sulphate activity is increased. Overall spectral changes in the sulphate region are therefore predicted to be very weak at pH 3.5, due to this cancelling effect, and broader than at pH 7 due to the contribution from HSO_4^- which exhibits bands over a wider wavenumber range than SO_4^{2-}. This analysis broadly fits with experimental results (**Figure 5.15**, blue), where a weaker and broader band is observed in the sulphate region compared to pH 7 (**Figure 5.15**, pink). An overall loss in intensity is still observed, as the above analysis ignores the electrostatic migration of

both anionic species away from the electrode. This results in a larger observed loss in spectral intensity for both species than predicted. The apparently smaller migratory loss of sulphate compared to pH 7 can be explained by rapid replenishment of any expelled SO_4^{2-} by deprotonation of HSO_4^- as equilibrium is restored.

The effect of the shift in pK_a(app) for HSO_4^- at −0.5 V is expected to be even more pronounced at pH 3, where the gain in SO_4^{2-} and loss of HSO_4^- is predicted to be greater (**Table 5.6**). However, the experimental results show almost non-existent spectral bands in the sulphate region (**Figure 5.15**, black), although a small gain of sulphate can be observed at 1100 cm^{-1} along with small losses of HSO_4^- at 1050 and 1200 cm^{-1}. Again, we must also consider the electrostatic migration of anionic species away from the electrode as well as deprotonation of HSO_4^-. Overall, compared to pH 7 and 3.5, the greater gain in SO_4^{2-} by deprotonation of HSO_4^- predicted by calculations is evident in the experimental spectra, as at higher pH the sulphate ν_{as}(S–O) decreases at −0.5 V but at pH 3 we can see it increasing at negative potential (**Figure 5.15**, black).

5.11.2 Phosphate

The analysis that was carried out with sulphate was also used to predict spectral changes in 0.1 M phosphate solutions at −0.5 V. Phosphoric acid has three dissociation constants as shown in Equations (5.13)-(5.15):

$$H_3PO_4^0 + H_2O \rightleftharpoons H_2PO_4^- + H_3O^+,\ pK_{a1} = 2.15 \quad (5.13)$$

$$H_2PO_4^- + H_2O \rightleftharpoons HPO_4^{2-} + H_3O^+,\ pK_{a2} = 7.2 \quad (5.14)$$

$$HPO_4^{2-} + H_2O \rightleftharpoons PO_4^{3-},\ pK_{a3} = 12.6 \quad (5.15)$$

Both pK_{a1} and pK_{a2} values are in the range where we can expect to observe deprotonation under our experimental conditions.

The number and intensity of infrared absorption bands associated with each species depends on the symmetry of the ion. Aqueous HPO_4^{2-} presents an IR active v_s(P–O) at ca. 850 cm^{-1} and the v_{as}(P–O) vibration is split into two bands at 1080 cm^{-1} and 990 cm^{-1}. Protonation to $H_2PO_4^-$ reduces the symmetry of the anion and leads to further splitting of v_{as}(P–O) into three bands located at around 1160, 1075 and 940 cm^{-1}, with v_s(P–O) appearing at ca. 870 cm^{-1}. The fully protonated $H_3PO_4^0$ species shows two v_{as}(P–O) bands at 1180 and 1005 cm^{-1} together with v_s(P–O) vibration present at 890 cm^{-1}. IR spectra of phosphate solutions at different pH are presented by Tejedor-Tejedor and Anderson [27] and Arai and Sparks [28].

The effect of potential on both GNF acid groups and solution phosphate species was studied at pH 3, 7 and 9. The experimental spectra obtained under these conditions are shown in **Figure 5.16**. At pH 3, losses are observed at 1005 and 1180 cm^{-1} on application of −0.5 V (black line) and these are assigned to v_{as}(P–O) and v(P=O), respectively, of $H_3PO_4^0$. Concurrently, gains corresponding to $H_2PO_4^-$ species are seen at 940 and 1155 cm^{-1} arising from the v_{as}(P–O) vibrations and 1077 cm^{-1} arising from v_s(P–O). At pH 9 and −0.5 V, the stretching modes of $H_2PO_4^-$ decrease while gains are seen at 1078 and 990 cm^{-1} that are assigned to v_{as}(P–O) and v_s(P–O), respectively, of HPO_4^{2-}. The spectral response at pH 7 is very similar to that obtained at pH 9.

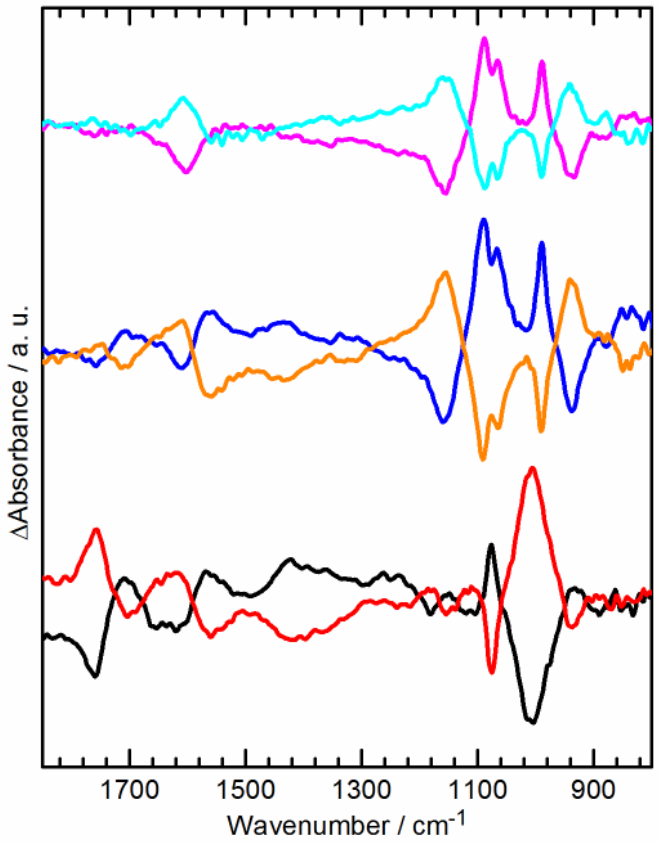

Figure 5.16 Difference spectra of BDD modified with GNF-Ca in 0.1 M KH_2PO_4/K_2HPO_4 electrolytes of different pH: pH 3 at +1 V (red) and −0.5 V (black); pH 7 at +1 V (orange) and −0.5 V (blue); pH 9 at +1 V (light blue) and −0 5 V (pink). Reproduced from [9].

Table 5.7: Changes in activity of H_3PO_4, $H_2PO_4^-$ and HPO_4^{2-} on application of −0.5 V calculated from Equation (5.9). Reproduced from [9].

pH	a_{K^+} / M	*E* / V	pK_a(app)	$\Delta a_{H_3PO_4}$ / 10^{-3} M	$\Delta a_{H_2PO_4^-}$ / 10^{-3} M	$\Delta a_{HPO_4^{2-}}$ / 10^{-3} M
3	0.080	−	3.22	0	0	0
3	0.087	−0.5	3.18	−2.0	+2.0	0
7	0.139	−	8.07	0	0	0
7	0.146	−0.5	8.05	0	−0.36	+0.36
9	0.200	−	7.91	0	0	0
9	0.207	−0.5	7.89	0	−0.23	+0.23

Table 5.7 shows the calculated changes in activities for H_3PO_4, $H_2PO_4^-$ and HPO_4^{2-} at pH 3, 7 and 9. Detailed calculations can be found in Appendix 4. At pH 3, our calculations predict that 2×10^{-3} M of phosphoric acid deprotonates to form $H_2PO_4^-$ at −0.5 V. We therefore expect to see significant losses in spectral intensity for H_3PO_4 species at 1172, 1005 and 889 cm^{-1}, with gains at 1159, 1077, 940 and 875 cm^{-1} for

$H_2PO_4^-$. This is broadly observed in the experimental spectrum (**Figure 5.16**, black), although as some gain bands are in similar positions to losses, they cancel each other out. However, a particularly strong absorption loss is seen at 1005 cm^{-1} for H_3PO_4, along with a gain at 1077 cm^{-1} for $H_2PO_4^-$ as predicted. At both pH 7 and 9, $H_2PO_4^-$ is predicted to undergo deprotonation to give HPO_4^{2-}. Experimentally, at pH 7 and 9 clear gains are observed at 1078 and 990 cm^{-1} corresponding to increased HPO_4^{2-}. The apparent splitting of the 1078 cm^{-1} band is due to simultaneous decrease in absorbance at 1077 cm^{-1}, which along with losses at 940 and 1155 cm^{-1} indicates concomitant loss of $H_2PO_4^-$, exactly as predicted.

The consequential generation of excess protons in this process explains why the intensity changes for the carbonyl and carboxylate bands in phosphate electrolyte are anomalously weak at pH 7. The acid edge groups of the GNF span a range of pK_a values from 3 to 8, and in pH 7 solution a decrease in the pK_a(app) should lead to deprotonation of a substantial number of these, as observed in chloride and sulphate electrolytes. However, in phosphate the local concentration of protons is much higher than in KCl and K_2SO_4 under the same conditions, due to the simultaneous potential-induced deprotonation of $H_2PO_4^-$. Hence the GNF acid dissociation equilibrium will strongly favour the protonated species under these conditions and the reversible deprotonation is subsequently suppressed with resulting low intensity changes in absorbance observed.

Figure 5.16 illustrates the effect of solution pH on the spectral features arising from the GNF acid groups with applied negative potential. At pH 3.5 (**Figure 5.16**, blue and orange) the trend of deprotonation at negative potential and protonation at positive potential is the same as that found at pH 7, as shown in **Figure 5.3**. Similar spectral changes are observed over a wide pH range from 3.5 to ca. 8; however, the ratio of the carbonyl bands to the carboxylate bands is pH-dependent, as is the spectral intensity. Different spectral behaviour is observed below pH 3.5 and above pH 8. At pH 9.2

(**Figure 5.16**, light blue and pink) the spectral features corresponding to carboxylic acid and carboxylates are very weak, although the trend is the same as observed at lower pH. At pH 3 (black and red) the carboxylate bands at ca. 1585, 1420 and 1360 cm^{-1} are weaker than observed at pH 3.5 and above, while the carbonyl band at ca. 1750 cm^{-1} is of similar intensity. Although there is still a loss of the carbonyl band at 1750 cm^{-1} on applying a negative potential, instead of a large increase in the carboxylate features it is instead accompanied with a gain in absorption at 1720 cm^{-1}.

The pH dependence of the response can be understood by considering the pK_a of the GNF edge groups. In Section 3.3.4 we found that these acid groups to undergo protonation over a wide range of pH from 3.5 to 8, indicating a range of pK_a values due to the different local environments of the COOH functionalities. The spectral data therefore confirms that over this pH range the GNF readily undergoes deprotonation on application of a negative potential, as the increase in cation activity under these conditions lowers the apparent pK_a of the acid functionalities enough to induce detectable loss of protons. At pH 9.2 very little deprotonation is observed, as the majority of the acid groups have a pK_a of < 8 and are therefore already deprotonated before the potential is applied. Likewise, at pH 3 little deprotonation of the acid groups is seen on application of negative potential, in this case because the pK_a of the COOH groups is > 3 so deprotonation is thermodynamically disfavoured. However, there is a very clear shift in the wavenumber for the C=O stretch of the acid groups on application of negative potential. There is a loss of absorbance at 1750 cm^{-1} assigned to monomeric weakly hydrogen bonded carbonyl and a gain at 1720 cm^{-1}, at a wavenumber consistent with increased hydrogen-bonding to the C=O moiety.

5.12 Conclusion

In this Chapter we have shown, using in situ IR spectroelectrochemistry, that a negative electrode potential results in deprotonation of electrode-immobilised

carboxylic acid GNF edge groups. We also observe deprotonation of solution H_3PO_4, $H_2PO_4^-$ and HSO_4^- close to the electrode on application of −0.5 V. We attribute both findings to a decrease in the apparent pK_a of the acids in response to a local increase in cation activity at the electrode at negative potential. This observation implies that speciation of acids near a biased electrode surface can differ significantly from that in bulk solution and this can be driven purely by cation migration in the absence of adsorption, redox chemistry or pH change. Although pK_a shifts for electrode-adsorbed species have been reported previously, here we show these cannot entirely be attributed to thermodynamic effects of surface immobilisation, as they are also observed for solution electrolyte ions.

The change in ion activity at the surface of the electrode was shown for the IR active, negatively charged SO_4^{2-}. Although monoatomic cations such as K^+ and Na^+ are IR inactive and therefore cannot be observed in the difference spectra, it can be assumed that positively charged particles migrate in the electric field in the opposite direction to the negatively charged SO_4^{2-}.

It was shown in Section 3.3.4 that the COOH edge groups of non-complexed GNF exhibit a wide range of pK_a values. Despite all of the edge groups being chemically identical, they occupy a range of different sites and their high density means that pK_a is strongly influenced by neighbouring groups. In spectroelectrochemical experiments at solution pH values ranging from 3.5 to 8, significant deprotonation of GNF acid groups can be observed, consistent with pK_a values of the GNF acid edge groups determined from titration studies.

For solution-phase species with well-defined pK_a values, changes in interfacial speciation on application of negative potential could be predicted. This result supports the proposed mechanism and shows that deprotonation in the interfacial region is driven by the lowering of effective pK_a by the increased cation activity.

Increases and decreases in the water bending mode at 1635 cm^{-1} are observed in all difference spectra, but currently it is unclear what induces these changes. Potential-induced change in the hydrogen-bonding environment of the carbonyl group is also apparent under various experimental conditions. The mechanism is currently unknown but may be related to the ion concentration or the applied electric field at the electrode. These aspects of the work require further investigation.

References for Chapter 5

1. Gantt, S. M. L.; Decroos, C.; Lee, M. S., et al., General Base–General Acid Catalysis in Human Histone Deacetylase 8. *Biochemistry* **2016,** *55* (5), 820-832.
2. Bradbury, J. H.; Carver, J. A., Conformational Differences between Various Myoglobin Ligated States as Monitored by Proton NMR Spectroscopy. *Biochemistry* **1984,** *23* (21), 4905-4913.
3. Wasserman, S. R.; Tao, Y. T.; Whitesides, G. M., Structure and Reactivity of Alkylsiloxane Monolayers Formed by Reaction of Alkyltrichlorosilanes on Silicon Substrates. *Langmuir* **1989,** *5* (4), 1074-1087.
4. Wang, J.; Frostman, L. M.; Ward, M. D., Self-Assembled Thiol Monolayers with Carboxylic Acid Functionality: Measuring pH-Dependent Phase Transitions with the Quartz Crystal Microbalance. *The Journal of Physical Chemistry* **1992,** *96* (13), 5224-5228.
5. Fears, K. P.; Creager, S. E.; Latour, R. A., Determination of the Surface pK of Carboxylic- and Amine-Terminated Alkanethiols Using Surface Plasmon Resonance Spectroscopy. *Langmuir* **2008,** *24* (3), 837-843.
6. Cheng, S. S.; Scherson, D. A.; Sukenik, C. N., In Situ Attenuated Total Reflectance Fourier Transform Infrared Spectroscopy Study of Carboxylate-Bearing, Siloxane-Anchored, Self-Assembled Monolayers: A Study of Carboxylate Reactivity and Acid-Base Properties. *Langmuir* **1995,** *11* (4), 1190-1195.
7. Gershevitz, O.; Sukenik, C. N., In Situ FTIR-ATR Analysis and Titration of Carboxylic Acid-Terminated SAMs. *J. Am. Chem. Soc.* **2004,** *126* (2), 482-483.
8. Ariga, K.; Nakanishi, T.; Hill, J. P., et al., Tunable pK of Amino Acid Residues at the Air−Water Interface Gives an L-Zyme (Langmuir Enzyme). *J. Am. Chem. Soc.* **2005,** *127* (34), 12074-12080.
9. Lounasvuori, M. M.; Holt, K. B., Acid Deprotonation Driven by Cation Migration at Biased Graphene Nanoflake Electrodes. *Chem. Commun.* **2017**.
10. Faulkner, L. R., Electrochemical Characterization of Chemical Systems. In *Physical Methods in Modern Chemical Analysis*, Kuwana, T., Ed. Academic Press: New York, 1983; Vol. 3, pp 137-248.
11. Pike Technologies, Depth of Penetration and Effective Penetration in ATR Sampling. http://www.azom.com/materials-video-details.aspx?VidID=2545 (accessed 14th October 2016).
12. Phillip, H. R.; Taft, E. A., Kramers-Kronig Analysis of Reflectance Data for Diamond. *Physical Review* **1964,** *136* (5A), A1445-A1448.
13. Hale, G. M.; Querry, M. R., Optical Constants of Water in the 200-nm to 200-µm Wavelength Region. *Appl. Opt.* **1973,** *12* (3), 555-563.
14. Berlind, T.; Pribil, G. K.; Thompson, D., et al., Effects of Ion Concentration on Refractive Indices of Fluids Measured by the Minimum Deviation Technique. *physica status solidi (c)* **2008,** *5* (5), 1249-1252.
15. Shippy, B. A.; Burrows, G. H., The Determination of Potassium and Sodium as Chlorides through Use of the Refractometer. *J. Am. Chem. Soc.* **1918,** *40* (1), 185-187.

16. West, C. J.; Hull, C., *International Critical Tables of Numerical Data, Physics, Chemistry and Technology, 1933*. 1st electronic ed.; Knovel: Norwich, NY, 2003.
17. Sugihara, K.; Shimazu, K.; Uosaki, K., Electrode Potential Effect on the Surface pK_a of a Self-Assembled 15-Mercaptohexadecanoic Acid Monolayer on a Gold/Quartz Crystal Microbalance Electrode. *Langmuir* **2000,** *16* (18), 7101-7105.
18. Futamata, M., Characterization of the First Layer and Second Layer Adsorbates on Au Electrodes Using ATR-IR Spectroscopy. *J. Electroanal. Chem.* **2003,** *550–551*, 93-103.
19. Goutev, N.; Futamata, M., Attenuated Total Reflection Surface-Enhanced Infrared Absorption Spectroscopy of Carboxyl Terminated Self-Assembled Monolayers on Gold. *Appl. Spectrosc.* **2003,** *57* (5), 506-513.
20. Luque, A. M.; Cuesta, A.; Calvente, J. J., et al., Potentiostatic Infrared Titration of 11-Mercaptoundecanoic Acid Monolayers. *Electrochem. Commun.* **2014,** *45*, 13-16.
21. White, H. S.; Peterson, J. D.; Cui, Q., et al., Voltammetric Measurement of Interfacial Acid/Base Reactions. *The Journal of Physical Chemistry B* **1998,** *102* (16), 2930-2934.
22. Burgess, I.; Seivewright, B.; Lennox, R. B., Electric Field Driven Protonation/Deprotonation of Self-Assembled Monolayers of Acid-Terminated Thiols. *Langmuir* **2006,** *22* (9), 4420-4428.
23. Rosendahl, S. M.; Burgess, I. J., Electrochemical and Infrared Spectroscopy Studies of 4-Mercaptobenzoic Acid SAMs on Gold Surfaces. *Electrochim. Acta* **2008,** *53* (23), 6759-6767.
24. Ma, C.; Harris, J. M., Surface-Enhanced Raman Spectroscopy Investigation of the Potential-Dependent Acid−Base Chemistry of Silver-Immobilized 2-Mercaptobenzoic Acid. *Langmuir* **2011,** *27* (7), 3527-3533.
25. Luque, A. M.; Mulder, W. H.; Calvente, J. J., et al., Proton Transfer Voltammetry at Electrodes Modified with Acid Thiol Monolayers. *Analytical Chemistry* **2012,** *84* (13), 5778-5786.
26. Hug, S. J., In Situ Fourier Transform Infrared Measurements of Sulfate Adsorption on Hematite in Aqueous Solutions. *J. Colloid Interface Sci.* **1997,** *188* (2), 415-422.
27. Tejedor-Tejedor, M. I.; Anderson, M. A., The Protonation of Phosphate on the Surface of Goethite as Studied by CIR-FTIR and Electrophoretic Mobility. *Langmuir* **1990,** *6* (3), 602-611.
28. Arai, Y.; Sparks, D. L., ATR–FTIR Spectroscopic Investigation on Phosphate Adsorption Mechanisms at the Ferrihydrite–Water Interface. *J. Colloid Interface Sci.* **2001,** *241* (2), 317-326.

6 Immobilisation of GNF on Electrode Surface

6.1 Introduction

In Chapters 3–5 GNF were immobilised on BDD electrodes by drop-coating from an aqueous suspension. This method, widely used in research to achieve electrode modification and surface immobilisation, is quick and facile but offers little control over the order and orientation of the immobilised layer. Additionally, when acid-terminated GNF are used, the high solubility of the flakes in water means that most of the drop-coated material is removed in the rinsing step. Therefore we estimate that only a few monolayers remain on the electrode, although it has not been possible to ascertain the degree of coverage. It is unlikely that drop-coating results in an ordered layer uniformly covering the area onto which the drop is deposited. Rather, the GNF are randomly oriented in a disordered layer on the electrode surface, leaving areas of the underlying electrode uncovered.

GNF-Ca was also drop-coated onto the electrode surface from an aqueous suspension. The insoluble nature of the GNF complexed with divalent cations means

that a thicker layer of immobilised material was achieved on the electrode surface compared to non-complexed GNF-COOH and GNF-amide.

In this Chapter, we explore two different ways of immobilising GNF onto a surface. The first method is direct attachment of GNF decorated with thiol groups (GNF-thiol) onto a gold substrate. STM is employed to image the surfaces after modification. For STM imaging it was desirable to deposit isolated GNF on the substrate. In order to achieve a good separation of GNF and to reduce the probability of GNF stacking, either very dilute solutions were drop-coated onto the substrate or more concentrated suspensions were spin-coated to achieve a sub-monolayer coverage.

The second approach utilises a small thiol linker molecule that forms a SAM on a gold substrate and to which GNF can then be attached. Amide bond formation by carboxylate groups and amines is a widely used reaction that is catalysed by carbodiimides. We have GNF terminated with carboxylic functionalities (GNF-COOH) that can be reacted with amine-terminated cysteamine SAMs to graft GNFs onto the surface. We also have GNF-amide with $–(C=O)NH(CH_2)_2NH_2$ moieties that can react with carboxylic acid end groups in a cysteine SAM. Both routes were explored in an attempt to immobilise GNF onto the substrate via covalent attachment. Similar methodology has been reported previously by Rahman [1], who attached carbon nanotubes decorated with carboxylic acid groups onto a 1-aminoundecanethiol SAM on gold.

A ferrocene derivative is used as an electrochemically active tag to confirm successful modification of the surface by CV and DPV. GNFs are tagged with ferrocene derivatives by two different methods: (a) Amine-terminated GNF are reacted with ferrocene carboxaldehyde via the formation of an imine, which is subsequently reduced to a secondary amine bond. The result is a covalent bond between GNF and ferrocene. (b) Deprotonated GNF-COOH and ferrocene carboxylic acid are incubated with $CaCl_2$,

resulting in an electrostatic interaction. **Scheme 6.1** and **Scheme 6.2** depict the molecular structures of the target materials.

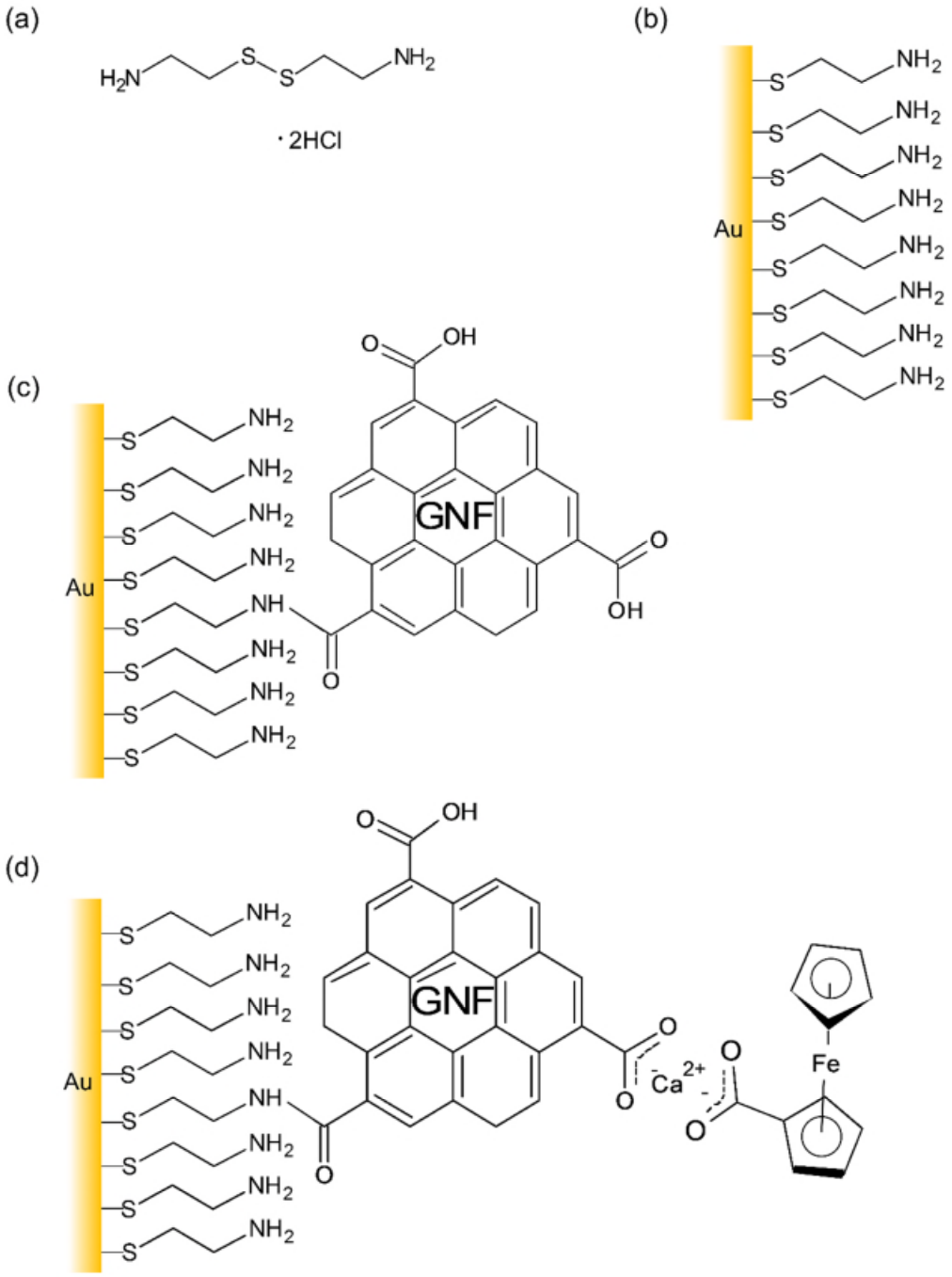

Scheme 6.1 (a) Cystamine dihydrochloride; (b) cysteamine SAM formed by cystamine on gold; (c) GNF-COOH attached onto cysteamine SAM on gold; ((d) ferrocene carboxylic acid attached onto Au-cysteamine-GNF-COOH.

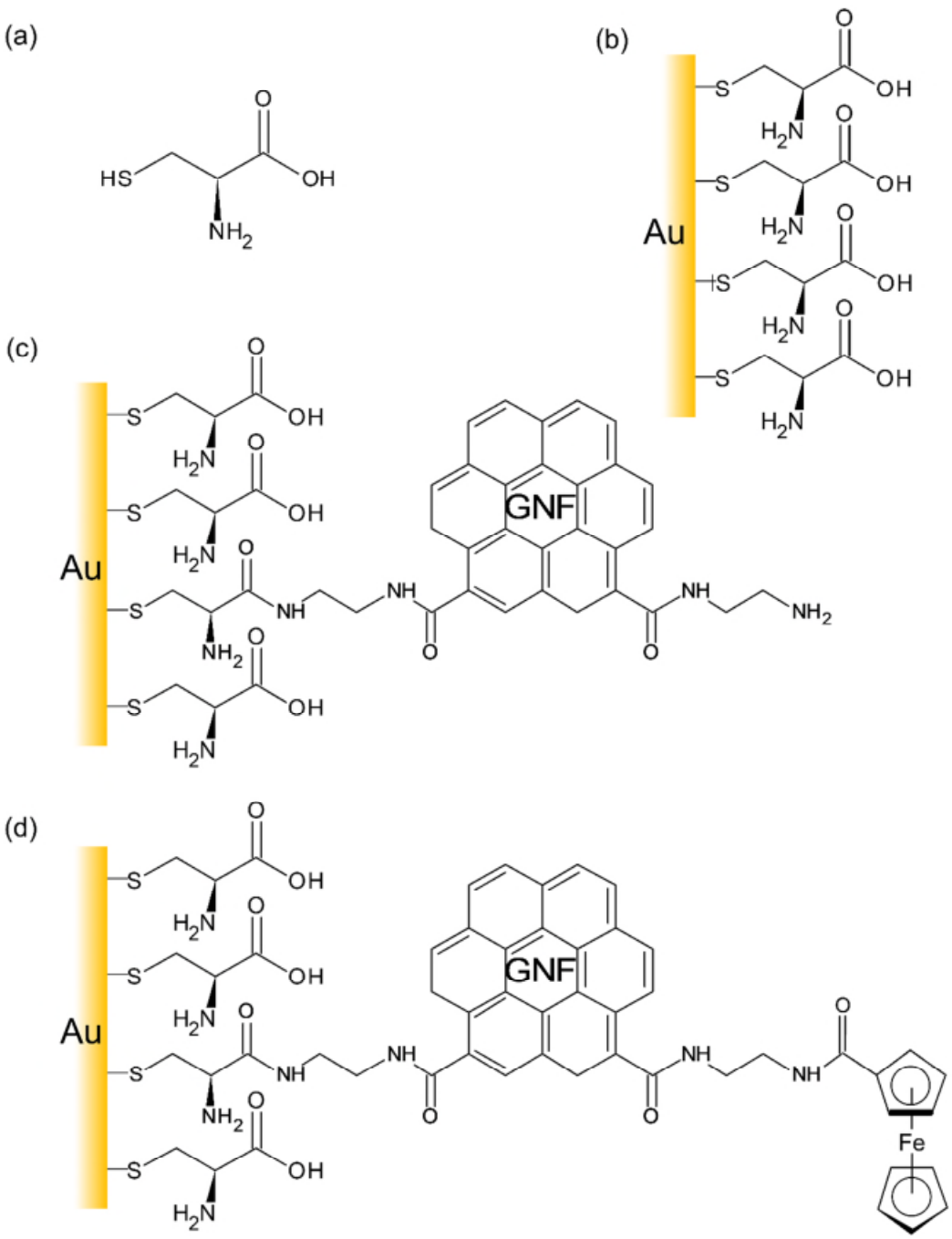

Scheme 6.2 (a) Cysteine molecule; (b) cysteine SAM on gold; (c) GNF-amide attached onto cysteine SAM on gold; (d) ferrocene carboxaldehyde attached onto Au-cysteine-GNF-amide.

XPS analysis is carried out on the surfaces to assess the outcome of the attachment. Survey spectra are acquired to determine the elements present in the sample, and high-resolution spectra are then acquired of the relevant regions. The N1s region can be used to ascertain the presence of nitrogen in the samples and will therefore confirm, alongside a peak in the S2p region, the successful formation of a self-assembled

monolayer. The C1s region will be used to compare the different sample preparations and the number of components in each peak fit is determined by our knowledge of the sample composition. In cysteamine SAM (**Scheme 6.1**(b)), carbon exists in two distinct chemical environments, –C–C–N and –C–C–S, with very similar C1s binding energies and therefore they will be fitted with one peak. When GNF-COOH is attached to the SAM as shown in **Scheme 6.1**(c) three new carbons in different chemical environments are introduced: sp^2-hybridised carbon, N–C=O and –C–COOH. In cysteine SAM (**Scheme 6.2**(b)) we find carbon in three different environments: –C–C–N, –C–C–S and –C–COOH. The first two will again be fitted with one peak. Upon attachment of GNF-amide (**Scheme 6.2**(c)) sp^2-hybridised carbon and N–C=O are introduced. The peak ratios are also expected to change when GNF are grafted onto the surface as the number of –C–C–N bonds increases and the number of –C–COOH decreases. The exact ratios will depend on several factors: the number of GNF particles successfully attached; the size of the particles; the number of edge groups present in a single particle; and the number of bonds formed per particle. Relevant C1s photoelectron binding energies are listed in **Table 6.1**.

Table 6.1: XPS binding energies of some carbon species.

Bonding type	***BE* / eV**	**References**
sp^2	284.3-284.8	[2-4]
sp^3	284.4-285.2	[4-6]
C–S, C–C–N	286.1-286.6	[7-9]
N–C=O	287.8-288.2	[7, 9, 10]
COOH	288.3-289.9	[8, 11, 12]

The high-resolution N1s region can in some cases aid in determining sample composition. However, although XPS spectra of GNF-amide ([13], supporting information) shows two distinct peak components for nitrogen corresponding to amine and amide, some reports have found amine and amide functionalities at such similar binding energies that they can't be resolved [7, 14]. Generally both amine and amide

peaks have binding energies in the range of 399.5 to 400.5 eV ([15] and references therein).

6.1.1 Thiol-Functionalised GNF

GNF functionalised with a thiol group have been synthesised from GNF-COOH [13] that can be directly attached onto a gold surface utilising the strong gold–sulphur bond. A cartoon of GNF-thiol is presented in **Scheme 6.3**. The basal plane is significantly larger than depicted here.

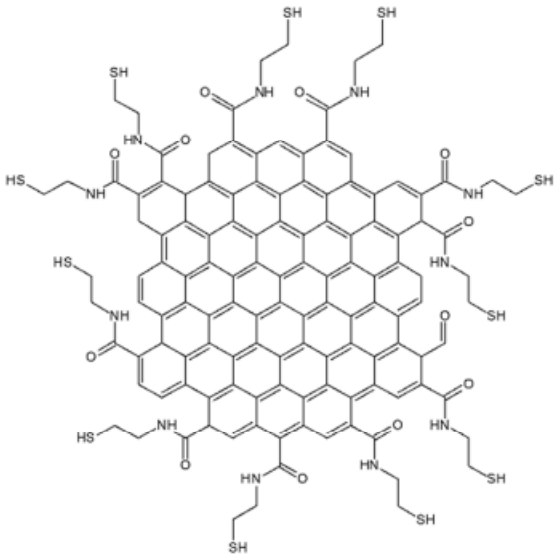

Scheme 6.3 Schematic depiction of edge-thiolated GNF. The image is not to scale; the aromatic region at the core of the flakes is significantly larger than is depicted here.

Infrared spectroscopy of GNF-thiol (**Figure 6.1**) shows an amide band at ca. 1660 cm^{-1}; N-H stretches at 3350 and 3450 cm^{-1} arising from the amine and amide functionalities; and C-H stretches at 2850 and 2920 cm^{-1}. These bands show that the majority of COOH groups have been converted to amides in the reaction with ethylene diamine, but some acid groups remain as evidenced by a small feature at 1715 cm^{-1}.

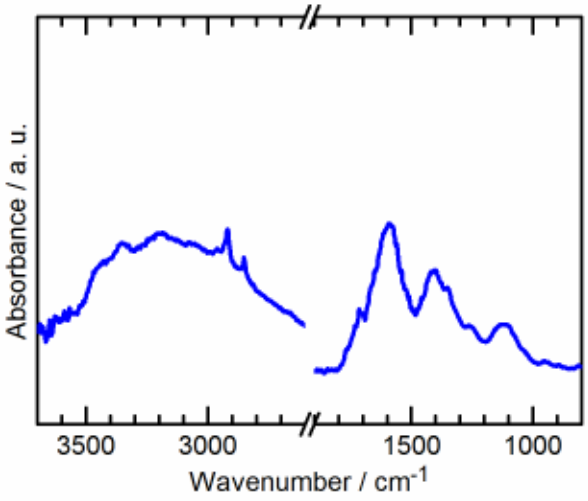

Figure 6.1 Infrared spectrum of GNF-thiol.

Liu et al. have reported immobilisation of single-walled carbon nanotubes (SWCNTs) onto Au(111) [16] via adsorption through thiol functionalities located at the open ends of the CNTs. Atomic force microscopy (AFM) imaging showed needle-like protrusions compatible with carbon nanotubes on the substrate and the density of the features increased with prolonged adsorption times. The substrates were stable to ultrasonication, strongly indicating chemisorption had taken place. By this method ordered, perpendicularly oriented CNT structures were achieved.

A similar approach was adopted by Minati et a. [17] who studied the chemisorption of thiol-functionalised multi-walled CNTs (MWCNTs) on gold. They commented on the issue of CNT aggregation in suspension that impeded the growth of an order SAM on the gold substrate. The dimensions of the CNTs were established by AFM as 40–160 nm (length) and 40–80 nm (diameter). The length dimension was found to be shorter than expected and it was hypothesised that shorter CNTs are preferentially adsorbed.

In this work, STM will be used to image GNF-thiol chemisorbed onto Au(111) substrates. GNF can bond with the Au surface atoms through one or more thiol groups and thus the orientation can range from vertical to horizontal. If the flakes bond through several thiol groups located around the edge and arrange horizontally on the substrate,

we would expect the height of features in STM images to be close to the theoretical thickness of the sp^2-hybridised carbon network of 0.34 nm [18]. Although most STM studies focus on pristine graphene grown directly on the substrate [19-21], Huang et al. have reported STM images of nanographene platelets deposited onto HOPG of 0.4 nm thickness [22]. If the GNF only form one bond with the substrate and arrange vertically, STM images would show a height in the region of 30 nm.

6.1.2 Electrochemistry of Ferrocene Derivatives

Ferrocene is a commonly used redox probe in non-aqueous systems. It is a neutral molecule consisting of an iron centre in the 2+ oxidation state sandwiched between two cyclopentadienyl ligands. Ferrocene undergoes a reversible one-electron oxidation to form the positively charged ferrocenium ion. Due to its reversibility and low oxidation potential, ferrocene is used as a standard in electrochemistry as Fc^+/Fc = 0.64 V vs. SHE. Electron-withdrawing substitutes, such as carboxylic acid and aldehyde, on the cyclopentadienyl rings shift $E^{0\prime}$ for the couple in the positive direction.

Ferrocene carboxaldehyde (FcCHO) is sparingly water-soluble and has therefore been mostly studied in non-aqueous systems. Abeed's group have reported reversible ET kinetics for FcCHO in DMSO and acetonitrile, with half-wave potential 0.75 V vs. Ag/AgCl [23]. Sharp et al. modified a Pt electrode with amine groups and anchored FcCHO molecules onto the surface [24]. The modified electrode exhibited reversible kinetics typical of surface-bound redox species.

Ferrocene carboxylic acid (FcCOOH) is more water-soluble than ferrocene and has been studied in aqueous systems. McCormack et al. [25] reported E_p values for the deprotonated form in pH 9.2 PBS as 0.39 and 0.29 V vs. Ag/AgCl for oxidation and reduction, respectively. Raoof's group [26] constructed a FcCOOH-modified carbon paste electrode that presented redox peaks at 0.38 and 0.27 V vs. Ag/AgCl in pH 7 PBS.

6.2 Experimental Methods

All aqueous solutions were prepared with doubly deionised water, taken from a Milli-Q water purification system, with a resistivity of not less than 18.2 MΩ cm at 25 °C.

6.2.1 Substrate Preparation

To study the self-assembled monolayers with XPS, fluorine-doped tin oxide (FTO) glass (Sigma-Aldrich, US) was used as the substrate. The glass was cut into 7×7 mm squares, cleaned with a mild detergent and then rinsed thoroughly with deionised water and ethanol. After cleaning, Au was deposited onto the substrate with a sputter coater (Emscope UK). For the deposition, argon pressure was 0.1 Torr, deposition current 40 mA and coating time 90 seconds.

In order to characterise the SAMs electrochemically, they were deposited onto commercial Au electrodes (BASi, US) according to the protocol described by Long et al. [27] with some modifications to the method. The electrodes were first polished using successively finer grades of alumina suspension down to 0.05 μm, rinsed thoroughly with ultrapure water after each step and dried using an ambient air flow. After mechanical polishing, electrochemical cleaning step was performed in 0.5 M H_2SO_4 by first holding the electrode at 2 V for 5 seconds and then switching to −0.32 V for 10 seconds. Then, 20 CV scans were run in 0.5 M H_2SO_4 between −0.26 V and 1.55 V at scan rate 4 V s^{-1}. In a fresh electrolyte solution, another 4 scans were run in the same potential range at scan rate 0.1 V s^{-1}. The electrodes were rinsed thoroughly with water and ethanol.

For STM studies, an atomically smooth substrate was needed. For this purpose, evaporated Au on Mica (Georg Albert PVD, Germany) was used. To further improve the flatness of the gold surface, flame annealing was performed by placing the

substrate onto a quartz plate and systematically sweeping back and forth with a propane flame for ca. 1 minute.

6.2.2 SAM Deposition

Three different types of SAM were deposited: two different thiols, L-cysteine and cystamine, were purchased from Sigma-Aldrich and used as received. Solution concentrations of 5×10^{-3} M (L-cysteine) and 2.5×10^{-3} M (cystamine) in degassed ethanol and deposition times of ca. 20 hours were employed. GNF-thiol were dispersed in water and deposited onto flame annealed Au substrates by either drop-coating or spin-coating. The drop-coating technique involved placing 15 µl of GNF-thiol solution onto the substrate for ca. 1 hour and then rinsing the substrate thoroughly with copious amounts of deionised water. Spin-coating was performed with a Laurell Technologies WS-650 spin-coater (US) from suspensions of concentrations varying from 8 to 124 µg ml^{-1}. The suspension was dispensed using a glass pipette in droplets of ca. 1 ml. The solution concentration, rotating speed and number of drops were varied in search of optimal deposition conditions.

6.2.3 Attaching GNF onto SAM

The reaction between a carboxylic acid and an amine to form an amide was exploited to covalently attach GNF onto a SAM. The reaction is catalysed by carbodiimides [28, 29] and coupling efficiency can be enhanced by using N-hydroxysulfosuccinimide (sulfo-NHS) [30]. The reaction mechanism is depicted in **Scheme 6.4**.

The general procedure was adapted from [31]. To activate the GNF acid groups, 0.4 mg of 1-ethyl-3-[3-dimethylaminopropyl]carbodiimide (EDC, Sigma-Aldrich, US) and 1.1 mg sulfo-NHS (Santa Cruz Biotechnology, US) were added to 1 ml of 0.1 mg ml^{-1} GNF-COOH, mixed well and left to react for 15 minutes. The cystamine-modified electrode was then immersed in the activated GNF-COOH solution for at least two

hours, after which the electrode was removed from solution and rinsed thoroughly. Alternatively, to modify the cysteine acid end groups, the cysteine-modified electrode was immersed in 1 ml of 0.01 M pH 6 PBS containing EDC and sulfo-NHS for 15 minutes. The activated electrode was then removed and immersed in a suspension of GNF-amide in H_2O or GNF-amide-FcCHO in ethanol for two hours before rinsing thoroughly.

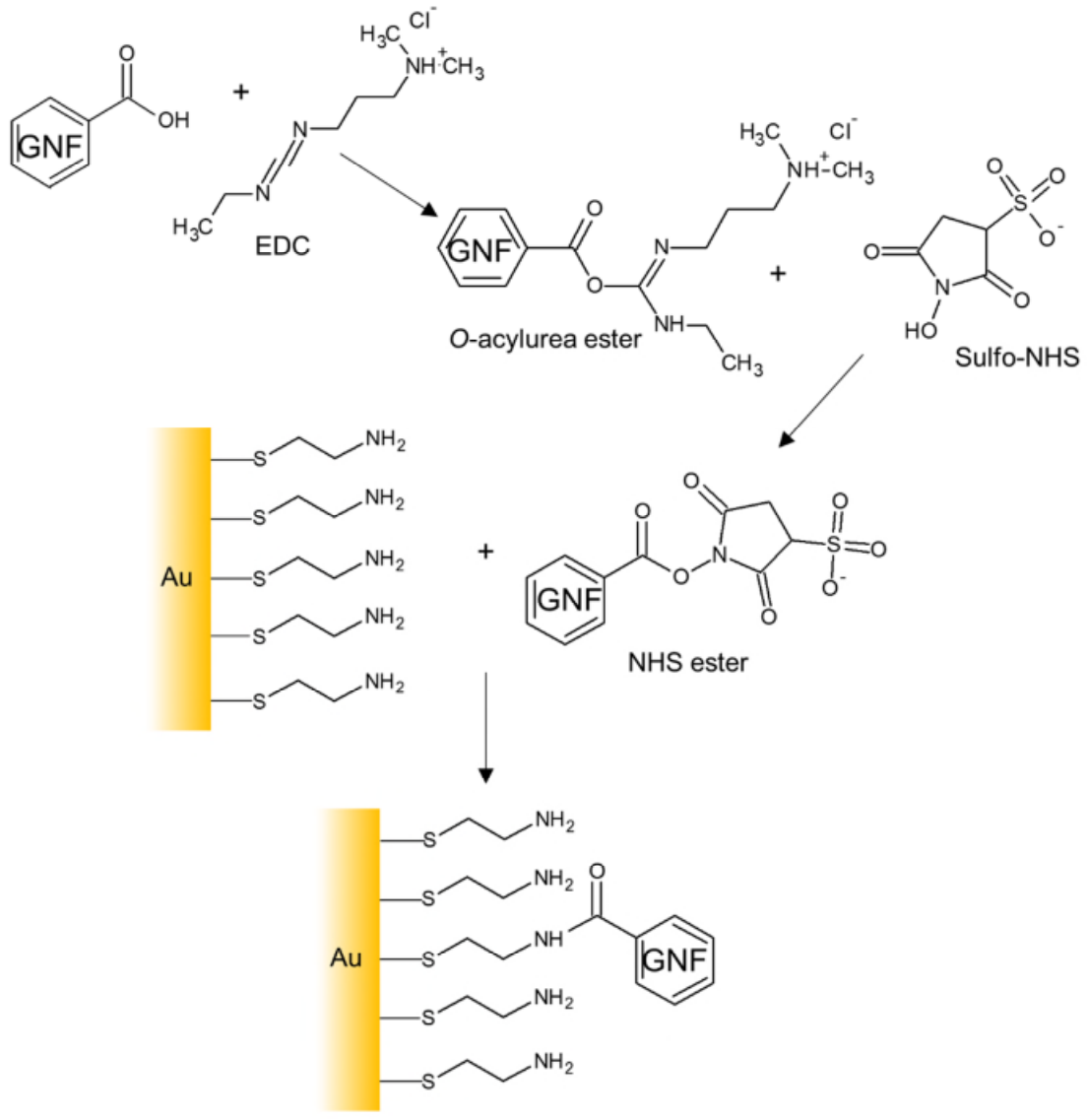

Scheme 6.4 Reaction scheme illustrating activation of carboxylate with EDC and formation of reaction intermediate after addition of sulfo-NHS. Adapted from [32].

6.2.4 Labelling GNFs with Ferrocene Derivatives

To label GNF-amide with ferrocene carboxaldehyde (FcCHO), GNF-amide were suspended in 10×10^{-3} M pH 7 PBS at an approximate concentration of 100 µg ml^{-1}, and the pH was adjusted to ca. 9.3 with 5 weight% K_2CO_3 solution. In a separate vial, 0.0185 g ferrocene carboxaldehyde (FcCHO) was dissolved in 0.5 ml dimethylformamide (DMF). The FcCHO solution was added to the GNF suspension and incubated for 30 minutes. 0.0011 g sodium borohydride ($NaBH_4$) was then added and the solution incubated for a further 10 minutes, after which the pH was adjusted to 7.3 by adding 0.1 M HCl. The precipitate was centrifuged, washed 4 times and re-suspended in 500 µl ethanol.

To label GNF-COOH with ferrocene carboxylic acid (FcCOOH), 10×10^{-3} M FcCOOH was prepared and the acid groups were deprotonated with dilute KOH. 20 µl of dilute KOH solution (pH 9) was pipetted onto the modified electrode surface to deprotonate all GNF-COOH. 30 µl of $FcCOO^-$ was then added and the solutions were allowed to mix for 5 minutes before adding 30 µl of 0.02 M $CaCl_2$. The electrode was incubated for approximately 7 hours and then rinsed thoroughly.

6.2.5 X-ray Photoelectron Spectroscopy

XPS was carried out on a Thermo Scientific K-Alpha spectrometer equipped with a monochromated Al K_α (hv = 1486.6 eV) X-ray source. All survey scans were scanned 3 times with a resolution of 1 eV, 400 µm spot size and 50 ms dwell time. All elemental regions were scanned 10 times with a resolution of 0.1 eV, 400 µm spot size and 50 ms dwell time. Elemental composition ratios were calculated from survey spectra using the element library function and the deconvolution of peaks was conducted using the quantification function in CasaXPS software. For background subtraction a Shirley background was used. The C1s region is best fitted with GL(30) line shape due to the wide natural line widths of the peaks [33]. The full width at half maximum (FWHM) of

the main C–C peak was constrained to between 1 and 1.6 eV and all other peaks were constrained to have the same shape and FWHM as the main C–C peak. All peaks were then optimised using a Gaussian-Lorentzian sum function and an iterative least-squares optimisation algorithm.

6.2.6 Scanning Tunnelling Microscopy

STM imaging was carried out using an Agilent 5500 scanning probe microscope (Agilent Technologies, US) in constant current mode. Lengths of platinum-iridium wire (Goodfellow, UK) were used as the probe and manually cut at one end to make sharp tips. The bias voltage and tunnelling current were varied to achieve the best possible resolution.

6.2.7 Electrochemical Experiments

A 1.6 mm diameter polycrystalline gold disk sealed in polychlorotrifluoroethylene (PCTFE) (BASi, US) was used as the working electrode. For DPV the following parameters were used: equilibration time 3 s; modulation time 0.05 s; interval time 0.5 s; step potential 0.0051 V; modulation amplitude 0.02502 V. All other experimental details are described in Section 3.2.5.

6.3 Results and Discussion

6.3.1 Thiol-Functionalised GNF

The survey spectra of unmodified Au and Au+GNF-thiol are presented in **Figure 6.2**(a), and the elemental composition detected from the survey spectra are collated in **Table 6.2**. In unmodified Au, only gold and carbon are detected in the survey spectra, whereas in Au+GNF-thiol the overall ratio of gold has decreased and oxygen and sulphur are present in high enough concentrations to be detected. Nitrogen was not

detected in the survey spectra of either sample, but the high resolution spectrum of the N1s region of Au+GNF-thiol (**Figure 6.2**(b), red) showed clear, albeit small peaks at 399.7 and 401.7 eV assigned to nitrogen in amine and amide, in agreement with the expected functional groups present in the sample. No nitrogen peaks were present in unmodified Au (**Figure 6.2**(b), black).

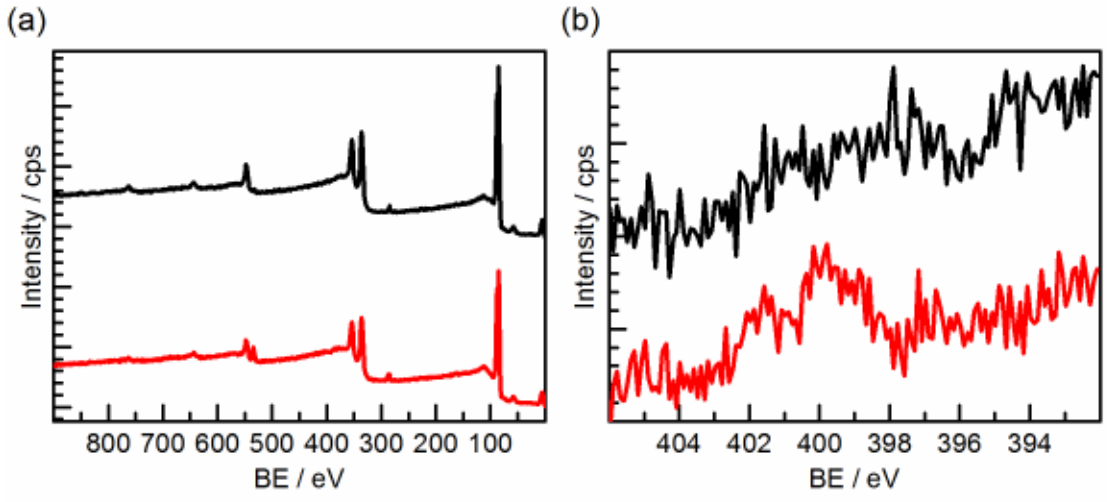

Figure 6.2 (a) Survey spectra of unmodified Au (black) and Au+GNF-thiol (red). (b) High-resolution spectrum of the N1s region of unmodified Au (black) and Au+GNF-thiol (red). Spectra are offset for clarity.

Table 6.2: Elemental composition calculated from peak areas in survey spectra in **Figure 6.2**.

Sample	Name	Position / eV	Atomic%
Unmodified Au	Au4d	336.1	55.5
	C1s	285.1	44.5
Au+GNF-thiol	C1s	286.1	48.7
	O1s	534.1	25.8
	Au4d	336.1	21.8
	S2p	162.1	3.7

The high resolution spectra of the C1s regions are compared in **Figure 6.3**. The spectrum of unmodified Au in **Figure 6.3**(a) can be fitted with three peaks at 284.3, 286.2 and 288.4 eV. These binding energies are typical of adventitious carbon, which is found on the surface of most samples that have been exposed to air [34]. The high

resolution spectrum of the Au+GNF-thiol C1s region is shown in **Figure 6.3**(b) and shows that there is a distinct difference in the composition of surface carbon in the two samples. The spectrum of Au+GNF-thiol has been fitted with four peaks at 284.7, 286.6, 287.8 and 289.3 eV. The binding energies of these peaks are very similar to those found in unmodified Au, but the ratios of peak areas are different, indicating that the surface has been modified. In addition to aromatic carbon on the GNF basal plane, we expect to see carbon in three other environments in a 1:1:1 ratio: C-S, C-N and N-C=O. The peak at 284.7 eV is assigned to C-C carbon and contains contributions of both sp^2 and sp^3-hybridised carbon found in GNF and adventitious carbon. The peak at 286.6 eV is attributed to both C-S and C-N carbon, and 287.8 eV is assigned to N-C=O. There is a small peak at 289.3 eV attributed to COOH functionalities remaining at the GNF-thiol edge after incomplete functionalisation of GNF-COOH. The ratio of peak areas at 286.6 eV and 287.8 eV is approximately 2:1, in agreement with our predicted composition and peak assignment, indicating successful deposition of GNF-thiol on the substrate. The peak parameters are summarised in **Table 6.3**.

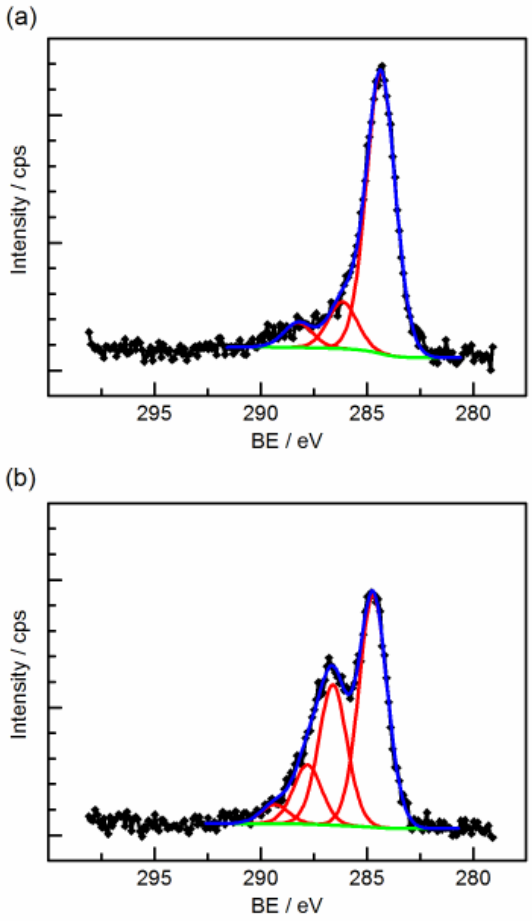

Figure 6.3 High-resolution XPS spectra of the C1s region of (a) Au and (b) Au+GNF-thiol. Experimental data is shown in black, background in green, peak fits in red and the cumulative peak fit in blue.

Table 6.3: Peak parameters from peak fit of C1s spectra in **Figure 6.3**.

Sample	Name	Position / eV	FWHM / eV	Line shape	%area
Unmodified Au	C–C	284.4	1.600	GL(30)	79.8
	C–O	286.2	1.600	GL(30)	7.0
	COOH	288.2	1.600	GL(30)	13.2
Au+GNF-thiol	C–C	284.7	1.560	GL(30)	51.6
	C–N, C–S	286.6	1.560	GL(30)	31.1
	N–C=O	287.8	1.560	GL(30)	13.1
	COOH	289.3	1.560	GL(30)	4.2

6.3.1.1 STM

Having established that GNF-thiol can be successfully deposited onto a gold substrate, the next step was to image them to see how they are oriented on the surface. For this purpose, STM was used. Gold evaporated on mica was chosen as substrate for these experiments because STM provides an extremely high resolution in the z direction and therefore it is important to use a flat substrate with small height differences. Two different deposition methods were attempted: spin-coating and drop-coating. It was hypothesised that spin-coating would reduce the chance of contamination due to shorter deposition time and because it is a one-step process with no need for a rinsing step. On the other hand it has been reported that adsorption kinetics of thiol-functionalised CNTs chemisorbing onto a gold substrate are very slow [16] and it is reasonable to assume that the same would apply to GNFs. Drop-coating would provide more time for sulphur-gold bonds to form, thereby allowing the use of a more dilute suspension that would reduce the possibility of particle agglomeration.

Spin-coated samples

Figure 6.4 shows STM images of a clean Au(111) surface (a) and GNF-thiol spin-coated onto Au(111) (b). The suspension concentration was 72 µg ml^{-1} and 10 drops were applied onto a surface rotating at 5000 rpm. The clean Au(111) surface is smooth, with terraces spanning over 100 nm. The herringbone reconstruction [35] can be discerned, indicating a well-prepared substrate. After spin-coating the GNF-thiol suspension onto the substrate, GNF are observed in the STM image as bright spots. To determine whether the flakes adsorb preferentially on edge sites, dislocations in the reconstruction or other defect sites, a lower coverage of the surface is necessary. This can be achieved by lowering the concentration of the GNF suspension or by reducing the number of drops applied onto the substrate.

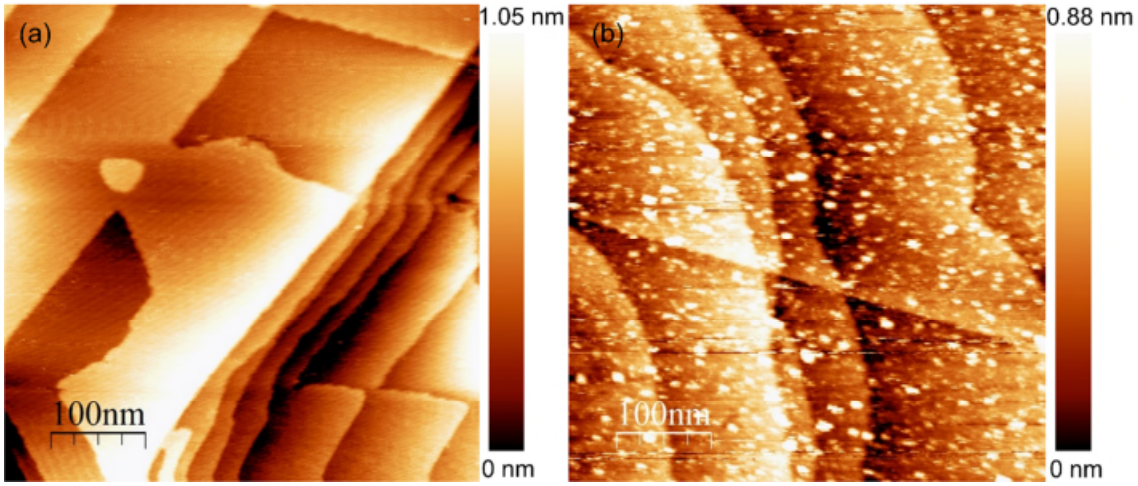

Figure 6.4 STM images of (a) clean Au(111); (b) GNF-thiol spin-coated onto Au(111). Suspension concentration 72 µg ml^{-1}.

In **Figure 6.5**(a)–(b), different concentrations of suspension are compared. Both suspensions were spin-coated by applying one drop onto a substrate rotating at 2000 rpm. **Figure 6.5**(a) shows an image of 8 µg ml^{-1} GNF-thiol spin-coated onto Au(111) substrate. Only a few features are visible in the image. In **Figure 6.5**(b) a high concentration of 124 µg ml^{-1} GNF-thiol was used to spin-coat onto the substrate. In this image many more bright spots are observed. A clear correlation between the concentration of spin-coated suspension and the number of bright spots in the image confirms that it is GNF-thiol that is detected on the Au(111) substrate.

When low concentrations of GNF-thiol are used, the flakes are seen to preferentially adsorb on or near the edge sites. We were not able to achieve high enough resolution to see whether the adsorption sites coincided with dislocations in the surface reconstruction.

Figure 6.5(c) and (d) show line profiles across a flake extracted from **Figure 6.5**(a) and (b) as indicated with green lines. The profiles from both dilute and concentrated suspension are similar, showing a rounded shape 15–20 nm in diameter and reaching a height of 1–1.7 nm. The lateral size was consistently found to be less than 30 nm which has been reported previously for acid-terminated flakes [13, 36]. This is

surprising as the tip convolution effect usually causes features to seem larger in the xy direction [37]. The height along z axis, although not a straightforward measurement of the physical height, was also found to be greater than that observed in previous STM studies of nanographene platelets (ca. 0.4 nm) [22].

The reason why the average particle size observed in STM images is smaller than expected may be that smaller GNF particles are preferentially adsorbed onto Au(111). Minati et al. reported of a discrepancy in the length distribution of thiol-CNTs after preparation and after adsorption on a gold substrate [17]. AFM experiments showed that on average CNTs adsorbed onto gold were shorter than the suspension they were adsorbed from, suggesting preferential adsorption of shorter CNTs. A similar result was arrived at by Wei et al. [38]. On the other hand, if the flakes are curved up in the middle rather than lying flat on the substrate, the lateral dimension would be reduced and the height would increase, as observed here. Being composed of a single-layer of carbon atoms, GNF are expected to be very flexible and able to bend in order to optimise the bond angle between the sulphur atom in the thiol group and the gold substrate. Such bending has been reported in single-walled CNTs bound on gold [39] due to the flexibility of the CNT and the preference to form Au-S bonds through multiple thiol groups located at both ends of the CNT.

It is also possible that due to the fairly high concentration of the suspension and the reduced water solubility of GNF-thiol compared to GNF-COOH, we might be seeing particles stacking together, causing the increased height observed. The height profiles in **Figure 6.5**(c)–(d) indicate that the particle height is greater when deposition is performed from a solution of higher concentration.

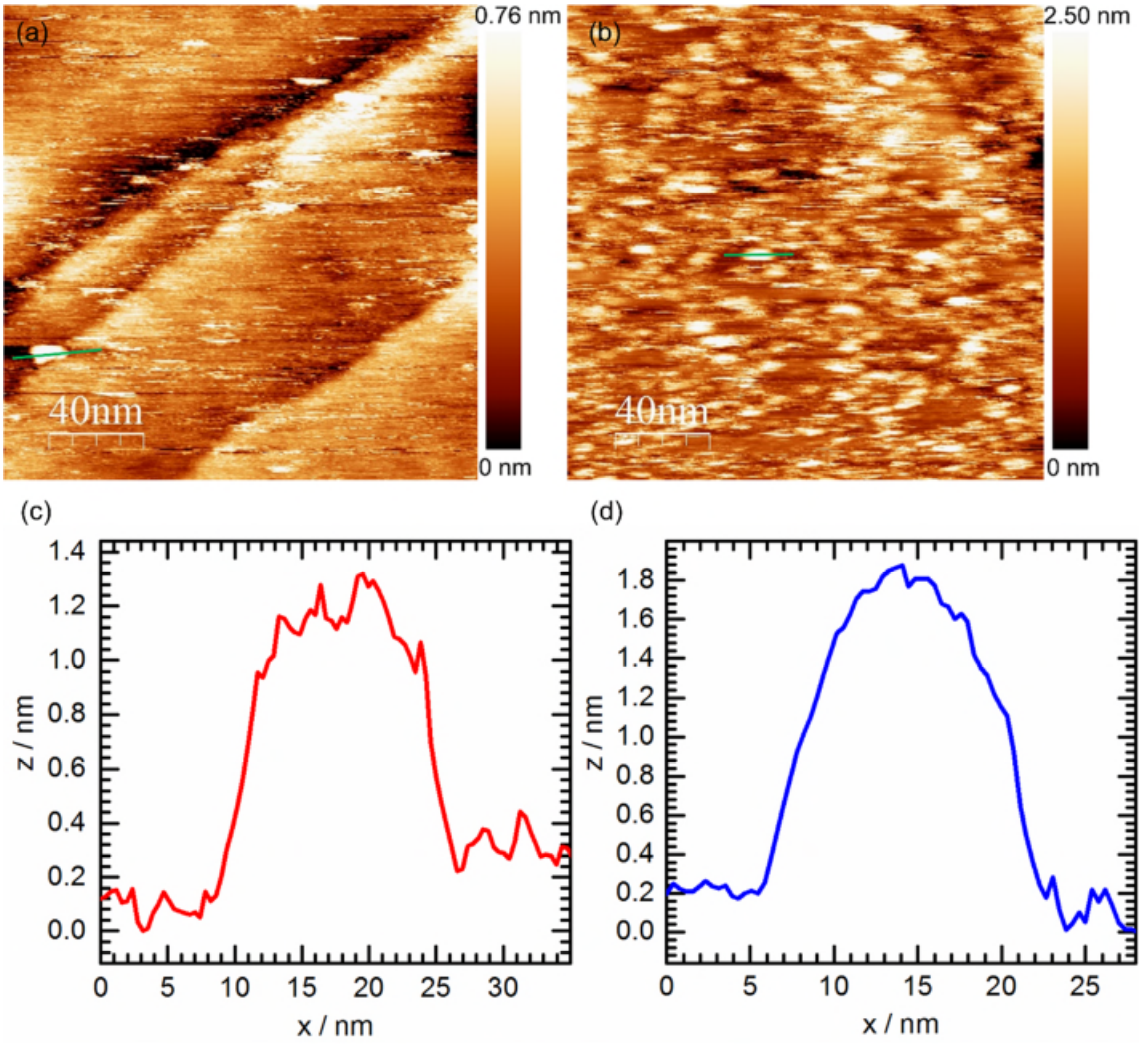

Figure 6.5 STM images of GNF-thiol spin-coated onto Au(111). Suspension concentration (a) 8 µg ml^{-1}; (b) 124 µg ml^{-1}. (c) Height profile from (a) along green line. (d) Height profile from (b) along green line.

Drop-coated samples

Drop-coating was also investigated as a method of depositing GNF onto Au substrate. A control deposition was performed using only doubly ionised water and this is shown in **Figure 6.6**. The Au(111) substrate has been well prepared, as indicated by the herringbone reconstruction and terraces spanning several hundred nanometres, but the appearance of brighter coloured areas suggests that at some point during the deposition, the substrate has been contaminated.

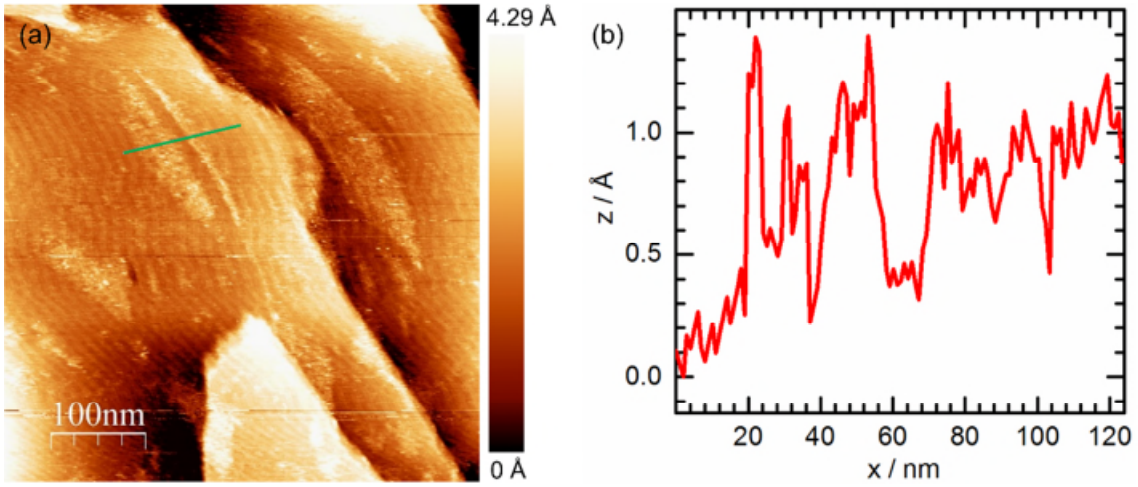

Figure 6.6 (a) STM image of Au(111) substrate after drop-coating distilled water. (b) Height profile from (a) along green line.

GNF-thiol were then drop-coated from a suspension at concentration 2 µg ml^{-1} and imaged with STM (**Figure 6.7**). Again the Au(111) substrate is well prepared as we can see the herringbone reconstruction of the surface. Bright features on the substrate that are assigned to GNF-thiol particles can be discerned on the surface. A height profile was taken across a flake along the green line in **Figure 6.7**(a) and is shown in **Figure 6.7**(b). The height of the flake is ca. 5 Å, which is very close to what was observed by Huang et al. [22] and indicates that the particles are oriented horizontally on the substrate and lying flat rather than bending. Therefore it seems likely that the particles observed in **Figure 6.5** were stacking together due to high concentration, forming few-layer graphene flakes.

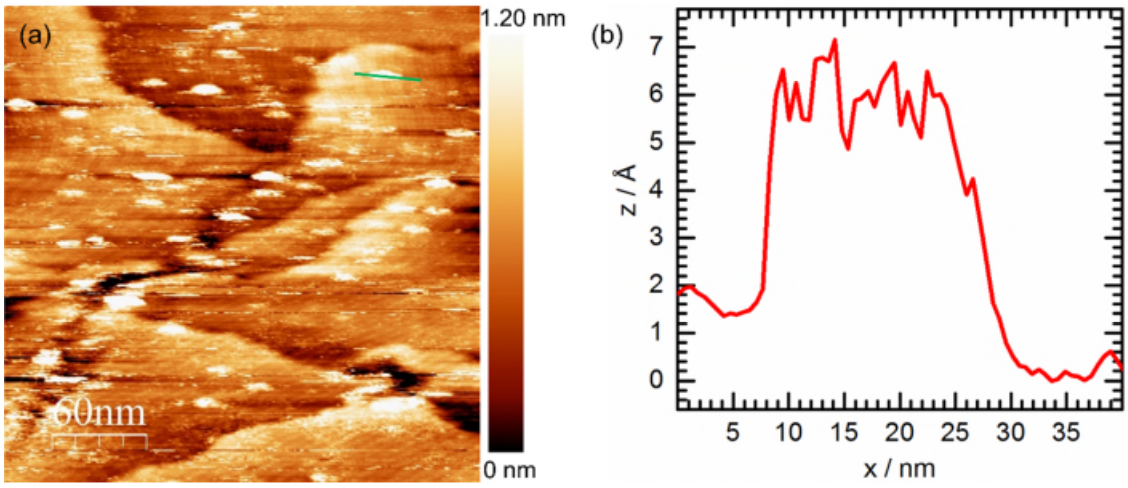

Figure 6.7 (a) STM image of 2 µg ml−1 GNF-thiol drop-coated on Au(111). (b) Height profile from (a) along green line.

High resolution imaging of GNF

Attempts were made to image the honeycomb structure of the graphene basal plane but these were unsuccessful. A few possible reasons for our inability to achieve a high resolution image of a GNF are discussed next.

It is difficult to remove all water from GNF samples Therefore it is possible that, despite the use of desiccant in the STM chamber, the GNF retain a layer of adsorbed water. Water molecules can get dragged around by the tip and interfere with the imaging process. The flakes themselves are mobile and may be easily moved around by the tip. Lateral manipulation is widely used as a tool to relocate molecules and it was first demonstrated by IBM researchers [40]. More recently, C_{60} molecules adsorbed on Si(100)−2 × 1 have been observed to move around by the influence of the tip even under UHV conditions [37]. If we are experiencing the flakes being dragged around then this would completely hinder any attempts to achieve good quality images.

Evidence of water molecules or graphene flakes being picked up by the tip was seen in some STM images. When the image sharpness suddenly goes from good to poor in

the middle of a raster line, it is indicative of the tip picking up something and dragging it along as it moves over the sample.

The sharpness of the tip is a variable that will to a great extent determine the resolution that is achieved. It is possible to cut tips by hand to a standard that allows atomic resolution on for example HOPG. Although it is possible, it seems unlikely that we never managed to get a good enough tip to see the honeycomb structure of graphene.

Evidence of contamination in the drop-coated sample was shown in **Figure 6.6**. Contamination is another variable that will have a detrimental effect on the quality of STM images.

6.3.2 GNF Attached onto SAM-functionalised Gold

GNF were covalently attached onto a SAM-functionalised Au substrate either with or without an electrochemically active tag. First, the formation of a SAM on gold was verified by XPS. **Figure 6.8**(a) shows high-resolution spectra of the S2p region. We can see that there is no sulphur present in the bare gold substrate (black line), but a peak appears in all subsequent samples, confirming successful formation of a SAM.

High-resolution spectra of the N1s region are presented in **Figure 6.8**(b). No nitrogen is detected in the bare gold substrate as expected. When trying to determine whether the GNF attachment onto SAM has been successful, we compare the shape of the peak. In our case both Au+cysteine and Au+cysteine+GNF-amide are best fitted with just one peak at ca. 400 eV and with FWHM of ca 3 eV. Irrespective of peak fitting, visual inspection of the spectra suggests that going from Au+cysteine (red) to Au+cysteine+GNF-amide (blue) the peak shifts to a higher binding energy, consistent with inclusion of amide functionalities in the sample. Correspondingly, comparison of Au+cysteamine (green) and Au+cysteamine+GNF-COOH (light blue) shows a shift to

higher binding energy in line with conversion of some amine groups to amides upon attachment of GNF-COOH.

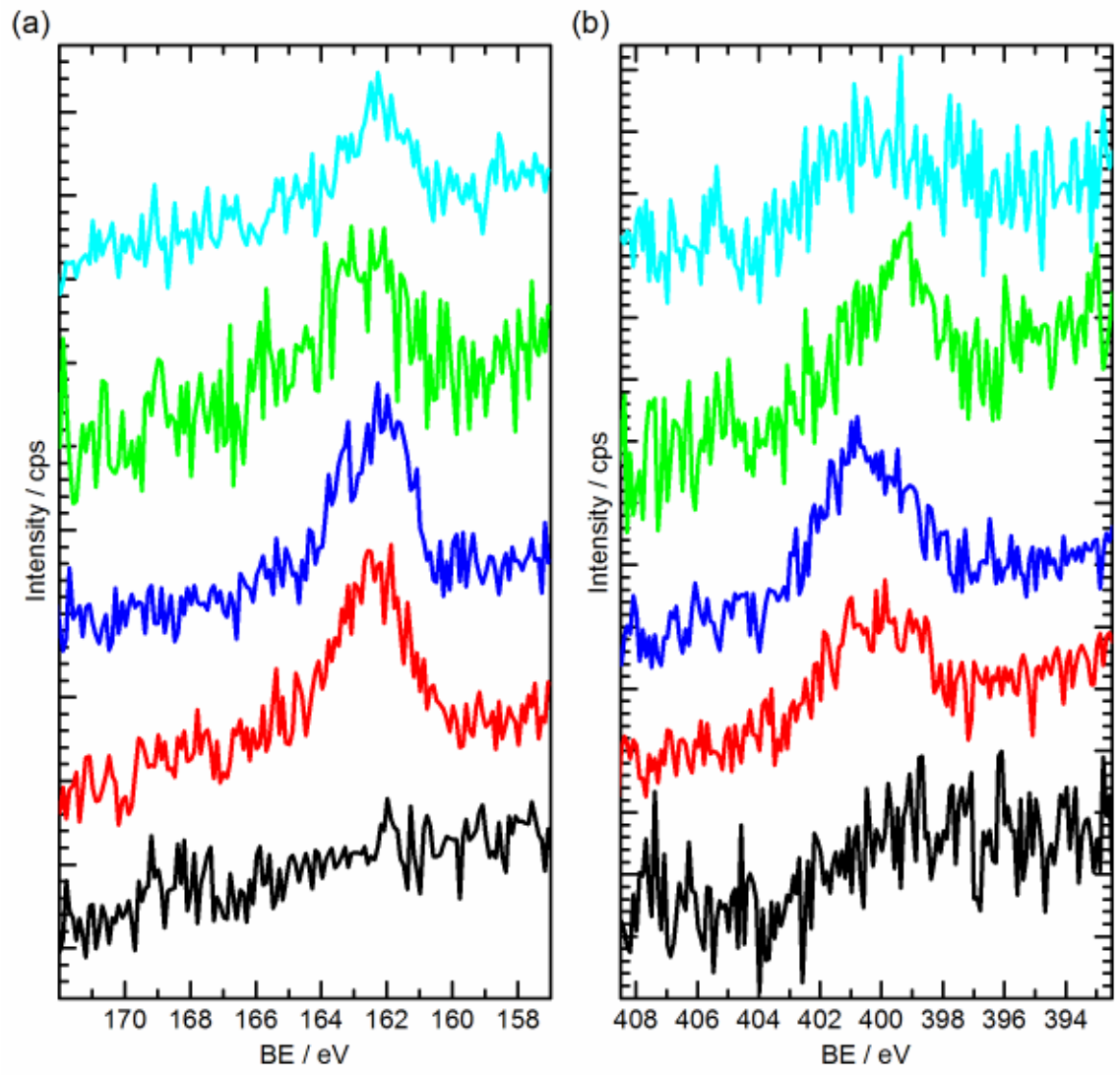

Figure 6.8 High-resolution spectra of (a) S2p and (b) N1s regions. Au (black), Au+cysteine (red), Au+cysteine+GNF-amide (blue), Au+cysteamine (green), Au+cysteamine+GNF-COOH (light blue). Spectra are offset for clarity.

To corroborate the information gleaned from the N1s region spectra, high-resolution spectra of the C1s region was examined. The results are presented in **Figure 6.9** and peak parameters are summarised in **Table 6.4**.

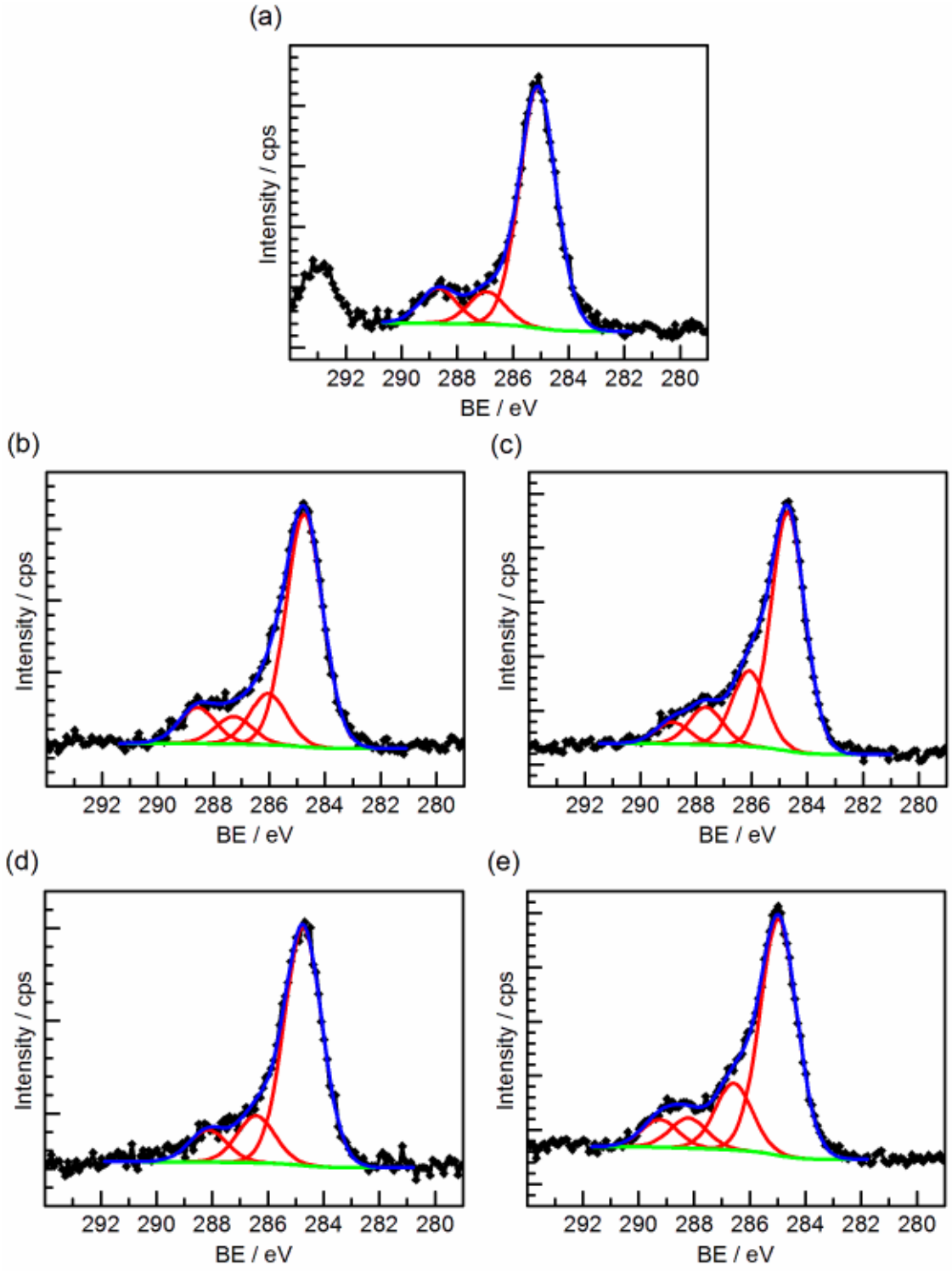

Figure 6.9 Narrow scan XPS spectra of the C1s region. (a) Unmodified Au; (b) Au+cysteine; (c) Au+cysteine+GNF-amide; (d) Au+cysteamine; (e) Au+cysteamine+GNF-COOH. Black squares: experimental data; green: baseline; red: peak fits; blue: cumulative peak fit.

Table 6.4: Peak parameters extracted from peak fits in **Figure 6.9**.

Sample	Name	Position / eV	FWHM / eV	Line shape	%Area
Unmodified Au	C–C	285.1	1.55	GL(30)	78.1
	C–O	286.9	1.55	GL(30)	10.5
	COOH	288.7	1.55	GL(30)	11.4
Au+cysteine	C–C	284.7	1.56	GL(30)	67.0
	C–N, C–S	286.0	1.56	GL(30)	14.7
	N–C=O	287.3	1.56	GL(30)	7.9
	COOH	288.6	1.56	GL(30)	10.3
Au+cysteine+ GNF-amide	C–C	284.7	1.43	GL(30)	63.9
	C–N, C–S	286.1	1.43	GL(30)	20.2
	N–C=O	287.7	1.43	GL(30)	10.1
	COOH	288.9	1.43	GL(30)	5.8
Au+cysteamine	C–C	284.7	1.60	GL(30)	75.0
	C–O , C–N, C–S	286.4	1.60	GL(30)	14.9
	COOH	288.1	1.60	GL(30)	10.1
Au+cysteamine+ GNF-COOH	C–C	285.0	1.56	GL(30)	65.5
	C–N, C–S	286.6	1.56	GL(30)	18.5
	N–C=O	288.2	1.56	GL(30)	8.3
	COOH	289.2	1.56	GL(30)	7.6

Comparison of the C1s region spectra of cysteine SAM and Au+cysteine+GNF-amide shows small changes in the peak area ratios (**Figure 6.9**(b)-(c)). The amount of COOH decreases and the amount of N–C=O increases, as expected when carboxylic acid groups on the cysteine SAM are converted into amides upon reaction with the GNF. The number of C–N groups increases as well upon GNF attachment due to the amine groups on GNF.

C1s region of cysteamine SAM (**Figure 6.9**(d)) must be fitted with a COOH peak, even though there aren't any carboxylic acid groups in the sample. This is most likely due to adventitious carbon being present in detectable amounts, interfering with the quantification of the carbon functionalities and making it difficult to compare Au+cysteamine and Au+cysteamine+GNF-COOH (**Figure 6.9**(e)) samples. However, we do see that upon attachment of GNF-COOH a component for N–C=O functionalities

appears, in agreement with the formation of a covalent bond between the SAM and GNF. This indicates that we have successfully grafted GNF particles onto the substrate.

Au+SAM+GNF samples were also tagged with an electrochemically active ferrocene derivative (ferrocene carboxaldehyde or ferrocene carboxylic acid) for electrochemical detection. First, in order to analyse the samples with XPS, they were prepared on thin films of gold. Iron was not detected in the survey spectra, so high-resolution spectra of the Fe2p region were collected for these samples. The results are presented in **Figure 6.10**.

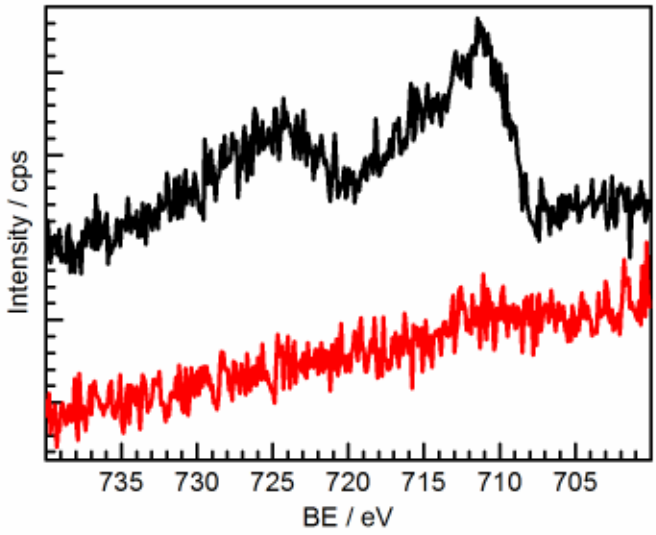

Figure 6.10 Narrow scans of the Fe2p regions of Au+cysteamine+GNF-COOH (black) and Au+cysteine+GNF-amide+FcCHO (red). Spectra are offset for clarity.

The presence of FcCOOH in Au+cysteamine+GNF-COOH is confirmed by the appearance of peaks in the Fe2p region (**Figure 6.10**, black line). The spin-orbit splitting of Fe2p is 13.1 eV, meaning that the $2p_{3/2}$ and $2p_{1/2}$ peaks are well resolved. The experimental spectrum shows significant asymmetry to the features and if peak fitting were attempted, it would be necessary to add two more components to the fit. Additional components could arise from satellite features, but FcCOOH is a low-spin compound and Fe2p spectra from low-spin compounds do not exhibit multiplet splitting.

Barring spin crossover, satellite peaks can be ruled out as FcCOOH is a low-spin compound with the iron centre in the 2+ oxidation state. Contamination seems unlikely as no features are observed in the Fe2p spectrum of Au+cysteine+GNF-amide-FcCHO (**Figure 6.10**, red line). We must therefore assume that some oxidation of the surface has occurred and that we have Fe(III) species present in our sample. Fe(III) compounds always contain unpaired electrons and will therefore show satellite features. Peak fitting was not attempted as the complex multiplet structure and overlapping binding energies [33] make Fe2p region problematic to fit.

The Fe2p region of Au+cysteine+GNF-amide-FcCHO does not show significant peaks (**Figure 6.10**, red line), indicating that on this occasion the synthesis method has not worked and that the procedure needs optimisation for successful attachment of FcCHO onto GNF.

6.3.2.1 Electrochemical Studies of Au + SAM + GNF Assembly

The deposition method described above was repeated with a polycrystalline gold electrode as substrate. Differential pulse voltammograms were recorded of Au+cysteamine+GNF-COOH and Au+cysteamine+GNF-COOH+FcCOOH and the results are compared in **Figure 6.11**(a). With only GNF attached onto the SAM (red line), no voltammetric peaks are observed in the DPV. After FcCOOH attachment to the assembly (blue line), clear voltammetric peaks can be seen at 0.33 and 0.34 V for oxidation and reduction, respectively. The peak potentials are in agreement with $E^{0\prime}$ of FcCOOH reported in literature [25, 26] and the very small peak separation indicates reversible, fast kinetics.

Figure 6.11(b) shows DPV current traces of Au+cysteine and Au+cysteine+GNF-amide+FcCHO. There are no voltammetric peaks present in the DPVs when the working electrode is Au+cysteine (red curves). Upon GNF-amide+FcCHO attachment (blue curves) the ferrocene tag can be detected as evidenced by voltammetric peaks

centred at 0.2 V. The fast, reversible ET is not affected by being immobilised onto the Au+cysteine+GNF-amide+FcCHO assembly as the peak separation between oxidation and reduction peaks is very small.

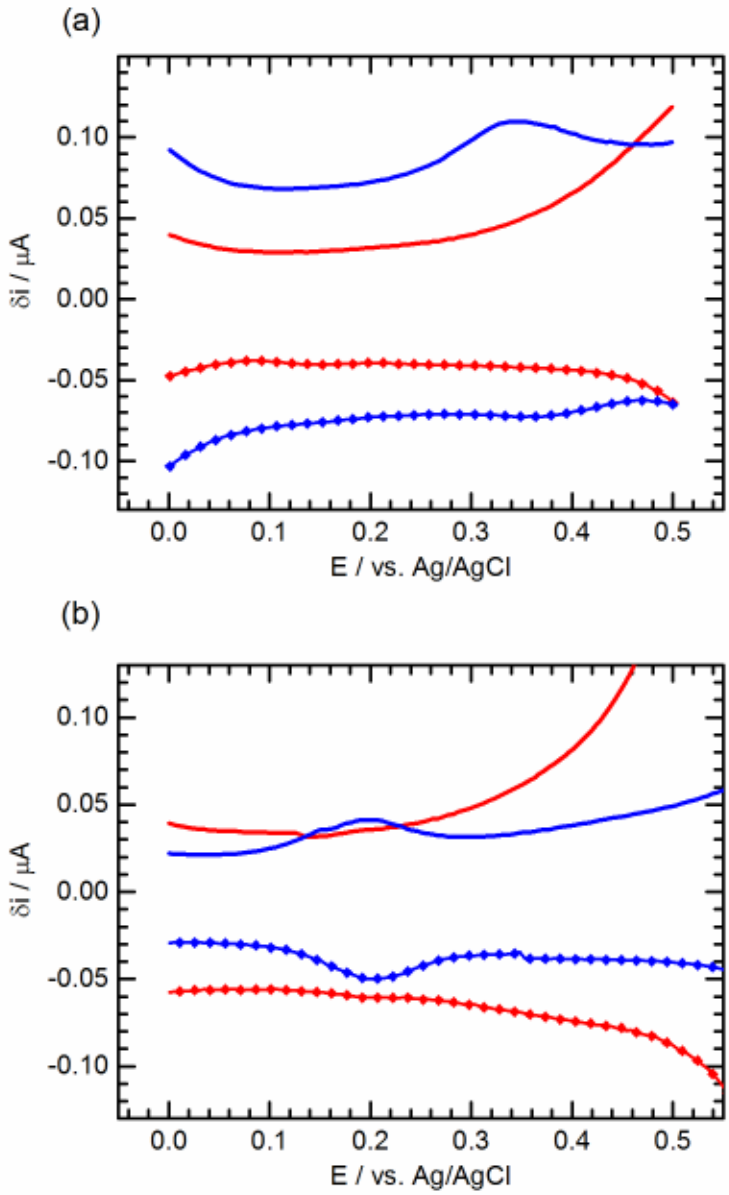

Figure 6.11 Differential pulse voltammograms of (a) Au+cysteamine+GNF-COOH (red) and Au+cysteamine+GNF-COOH+FcCOOH (blue); (b) Au+cysteine (red) and Au+cysteine+GNF-amide+FcCHO (blue). Solid line: oxidation; line and symbols: reduction.

The differential pulse voltammograms presented in **Figure 6.11** clearly indicate the presence of Fc derivatives in both samples. However, the covalent nature of the bond between ferrocene derivative and GNF in the Au+cysteine+GNF-amide+FcCHO

assembly is considered more promising for initial studies and it was therefore investigated further with cyclic voltammetry. A scan rate study was carried out, the results of which are presented in **Figure 6.12**.

Figure 6.12(a) shows cyclic voltammograms of Au+cysteine+GNF-amide+FcCHO at different scan rates. Clear voltammetric peaks can be seen in the CVs with E_p independent of scan rate in the range studied here (50 mV–1 V s^{-1}). E_{pa} was found to be 0.236 V and E_{pc} 0.162 V, giving ΔE_p = 75 mV. The theoretical value of ΔE_p of adsorbed species exhibiting fast, reversible kinetics is zero due to the absence of diffusion. A non-zero ΔE_p is usually found experimentally as some resistance is introduced into the system by the solution and other components. In our case the modification layer on the electrode may inhibit the electron transfer.

To further characterise the modification of the electrode, the peak currents extracted from CVs in **Figure 6.12**(a) were plotted against the scan rate and fitted with a linear regression line (**Figure 6.12**(b)). i_{pc} (blue symbols) depends linearly on scan rate, indicating absence of diffusion as expected of a surface-immobilised redox species. However, the oxidation currents (red symbols) are less well fitted with a linear regression line. To investigate this further, log i_p was plotted against log v and fitted with a linear regression line as shown in **Figure 6.12**(c). The reduction current fit (blue) has a slope of 0.86, close to the theoretical value of 1 for a surface-confined redox process. The slope of the oxidation current fit (red) is 0.62, closer to the theoretical value of 0.5 for a diffusion-controlled redox species.

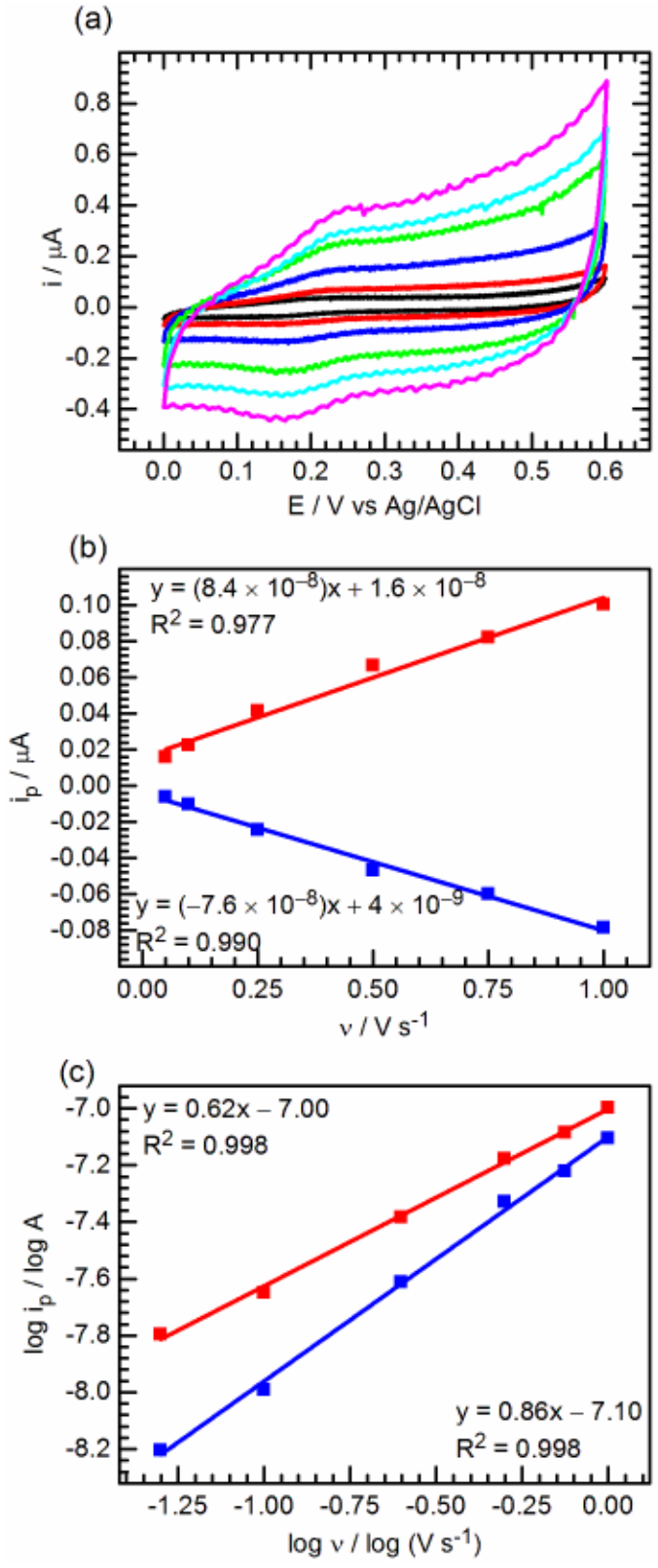

Figure 6.12 (a) Cyclic voltammograms at Au+cysteine+GNF-amide+FcCHO in 0.1 M PBS pH 7; scan rate 50 (black), 100 (red), 250 (blue), 500 (green), 750 (light blue) and 1000 (pink) mV s^{-1}; 5th scans shown; (b) i_{pa} (red) and i_{pc} (blue) plotted against v; (c) log i_{pa} (red) and log $|i_{pc}|$ (blue) plotted against log v.

The log-log plot presented in **Figure 6.12**(c) suggests poor immobilisation of the reduced species onto the electrode surface. On the other hand, the oxidised species is clearly confined to the surface. It is possible that the redox probe is physisorbed onto the surface rather than covalently bonded onto the GNF. The oxidised species carries positive charge and may therefore be more strongly adsorbed than the neutral reduced FcCHO. A possible physisorption site is the basal plane of the graphene flakes via π–π interactions, although no evidence of physisorption of another ferrocene derivative, ferrocenemethanol, onto GNF-COOH was found in experiments described in Section 3.3.7.

The amount of charge passed was calculated for each CV and converted to number of moles of ferrocene groups at the electrode. The data is tabulated in **Table 6.5**.

Table 6.5: Peak currents found from cyclic voltammograms in **Figure 6.12**(b), amount of charge q calculated by integrating peak areas under CV curve in Coulombs and corresponding number of FcCHO molecules in moles.

v / V s^{-1}	**i_{pa} / 10^{-9} A**	**q / 10^{-8} C**	**FcCHO / 10^{-13} mol**	**i_{pc} / 10^{-9} A**	**q / 10^{-8} C**	**FcCHO / 10^{-13} mol**
0.05	−6.24	−1.33	1.38	16.0	4.49	4.65
0.10	−10.2	−1.13	1.17	22.5	3.49	3.61
0.25	−24.4	−1.11	1.15	41.4	2.30	2.38
0.50	−46.9	−1.13	1.18	66.6	2.15	2.22
0.75	−60.0	−1.03	1.06	82.2	1.72	1.78
1.0	−78.4	−1.03	1.07	100	1.37	1.42

The number of moles of Fc groups calculated from the reduction peak decreases slightly as the scan rate increases. When the corresponding number is calculated from the oxidation peak, the values decrease rapidly. This supports the conclusion that the covalent bond formation has failed and we are instead seeing physisorption onto the GNF, where the positively charged $FcCHO^+$ species is more tightly adsorbed than the neutral FcCHO species.

6.4 Conclusion

The majority of work presented in this thesis was conducted after immobilising GNF onto the electrode surface by drop-coating, which is quick and convenient but offers little control over the surface coverage and morphology of the drop-coated layer. In this Chapter, different methods of attaching GNF onto electrodes were discussed.

Thiol-functionalised GNF have been successfully deposited onto gold substrate by self-assembly and the chemisorption was verified by XPS. Individual GNF were imaged on Au(111) substrate using STM, however, high resolution images proved elusive. A significant amount of time was dedicated to STM imaging, and many hours were spent varying the main imaging parameters, bias voltage and tunnelling current. Despite our best efforts, we were unable to find settings that would have allowed us to image the basal plane of a GNF with atomic resolution. Although not attempted in this work, STM under UHV conditions or low temperature conditions could facilitate the imaging of GNF.

Because the bulk of our STM experiments were directed towards imaging individual flakes, only sub-monolayer coverages were investigated. At these very low coverages GNF were found to preferentially adsorb on or near edge sites on Au(111) and lie flat on the surface. This type of orientation would not necessarily be seen for higher surface coverage. Further work would be needed to study self-assembly from higher concentration or at longer deposition times to see how closely packed a GNF monolayer would be and to determine the kinetics of adsorption.

GNF decorated with amide and COOH functionalities have also been deposited onto Au by attachment onto a self-assembled monolayer of a short-chained thiol on a gold substrate. Gold sputter-coated onto FTO glass was used for XPS studies and polycrystalline gold electrodes for electrochemical experiments. Narrow scan C1s

spectra indicated successful attachment and bond formation between the SAM end groups and the GNF.

The SAM-GNF assembly was also tagged with an electrochemically active ferrocene derivative. Narrow scan Fe2p spectra showed the presence of a ferrocene moiety in Au+cysteamine+GNF-COOH+FcCOOH sample but not in Au+cysteine+GNF-amide+FcCHO. Electrochemical experiments suggested the presence of ferrocene moieties in both Au+cysteamine+GNF-COOH+FcCOOH and Au+cysteine+GNF-amide+FcCHO samples, but in-depth analysis of cyclic voltammograms showed poor immobilisation of FcCHO, indicating a lack of covalent bond formation. Further optimisation of the deposition method is therefore needed in order to achieve covalent attachment of ferrocene onto GNF.

References for Chapter 6

1. Rahman, M. M., Fabrication of Self-Assembled Monolayer Using Carbon Nanotubes Conjugated 1-Aminoundecanethiol on Gold Substrates. *Natural Science* **2011,** *3*, 208-217.
2. Smith, K. L.; Black, K. M., Characterization of the Treated Surfaces of Silicon Alloyed Pyrolytic Carbon and SiC. *Journal of Vacuum Science & Technology A* **1984,** *2* (2), 744-747.
3. Bachman, B. J.; Vasile, M. J., Ion Bombardment of Polyimide Films. *Journal of Vacuum Science & Technology A* **1989,** *7* (4), 2709-2716.
4. Mérel, P.; Tabbal, M.; Chaker, M., et al., Direct Evaluation of the sp3 Content in Diamond-Like-Carbon Films by XPS. *Appl. Surf. Sci.* **1998,** *136* (1–2), 105-110.
5. Morar, J. F.; Himpsel, F. J.; Hollinger, G., et al., C 1s Excitation Studies of Diamond (111). I. Surface Core Levels. *Physical Review B* **1986,** *33* (2), 1340-1345.
6. Schmieg, S. J.; Belton, D. N., Polycrystalline Diamond Film on Si(100) by XPS. *Surf. Sci. Spectra* **1992,** *1* (4), 329-332.
7. Ramanathan, T.; Fisher, F. T.; Ruoff, R. S., et al., Amino-Functionalized Carbon Nanotubes for Binding to Polymers and Biological Systems. *Chem. Mater.* **2005,** *17* (6), 1290-1295.
8. Techane, S. D.; Gamble, L. J.; Castner, D. G., Multitechnique Characterization of Self-Assembled Carboxylic Acid-Terminated Alkanethiol Monolayers on Nanoparticle and Flat Gold Surfaces. *The Journal of Physical Chemistry C* **2011,** *115* (19), 9432-9441.
9. Zorn, G.; Liu, L.-H.; Árnadóttir, L., et al., X-Ray Photoelectron Spectroscopy Investigation of the Nitrogen Species in Photoactive Perfluorophenylazide-Modified Surfaces. *The journal of physical chemistry. C, Nanomaterials and interfaces* **2014,** *118* (1), 376-383.
10. Tang, X.-Z.; Li, W.; Yu, Z.-Z., et al., Enhanced Thermal Stability in Graphene Oxide Covalently Functionalized with 2-Amino-4,6-Didodecylamino-1,3,5-Triazine. *Carbon* **2011,** *49* (4), 1258-1265.
11. Hammond, J. S.; Holubka, J. W.; deVries, J. E., et al., The Application of X-Ray Photo-Electron Spectroscopy to a Study of Interfacial Composition in Corrosion-Induced Paint De-Adhesion. *Corros. Sci.* **1981,** *21* (3), 239-253.
12. Johansson, E.; Nyborg, L., XPS Study of Carboxylic Acid Layers on Oxidized Metals with Reference to Particulate Materials. *Surf. Interface Anal.* **2003,** *35* (4), 375-381.
13. Rosillo-Lopez, M.; Lee, T. J.; Bella, M., et al., Formation and Chemistry of Carboxylic Anhydrides at the Graphene Edge. *RSC Advances* **2015,** *5* (126), 104198-104202.
14. França, R.; Mbeh, D. A.; Samani, T. D., et al., The Effect of Ethylene Oxide Sterilization on the Surface Chemistry and in Vitro Cytotoxicity of Several Kinds of Chitosan. *Journal of Biomedical Materials Research Part B: Applied Biomaterials* **2013**.

15. Baker, S. E.; Cai, W.; Lasseter, T. L., et al., Covalently Bonded Adducts of Deoxyribonucleic Acid (DNA) Oligonucleotides with Single-Wall Carbon Nanotubes: Synthesis and Hybridization. *Nano Lett.* **2002,** *2* (12), 1413-1417.
16. Liu, Z.; Shen, Z.; Zhu, T., et al., Organizing Single-Walled Carbon Nanotubes on Gold Using a Wet Chemical Self-Assembling Technique. *Langmuir* **2000,** *16* (8), 3569-3573.
17. Minati, L.; Speranza, G.; Torrengo, S., et al., Characterization of Thiol-Functionalized Carbon Nanotubes on Gold Surfaces. *Surf. Sci.* **2010,** *604* (17–18), 1414-1419.
18. Kim, Y.-R.; Bong, S.; Kang, Y.-J., et al., Electrochemical Detection of Dopamine in the Presence of Ascorbic Acid Using Graphene Modified Electrodes. *Biosens. Bioelectron.* **2010,** *25* (10), 2366-2369.
19. Yu, Q.; Jauregui, L. A.; Wu, W., et al., Control and Characterization of Individual Grains and Grain Boundaries in Graphene Grown by Chemical Vapour Deposition. *Nat Mater* **2011,** *10* (6), 443-449.
20. Gottardi, S.; Müller, K.; Bignardi, L., et al., Comparing Graphene Growth on Cu(111) Versus Oxidized Cu(111). *Nano Lett.* **2015,** *15* (2), 917-922.
21. Feng, X.; Wu, J.; Bell, A. T., et al., An Atomic-Scale View of the Nucleation and Growth of Graphene Islands on Pt Surfaces. *The Journal of Physical Chemistry C* **2015,** *119* (13), 7124-7129.
22. Huang, K.; Delport, G.; Orcin-Chaix, L., et al., Single Layer Nano Graphene Platelets Derived from Graphite Nanofibres. *Nanoscale* **2016,** *8* (16), 8810-8818.
23. Abeed, F. A.; Al-Allaf, T. A. K.; Sulaiman, S. T., Electroanalytical Studies of Ferrocene and Substituted Ferrocene in Non-Aqueous Solvents by Rotating Disc Voltammetry. *Analyst* **1988,** *113* (2), 333-336.
24. Sharp, M.; Petersson, M.; Edström, K., Preliminary Determinations of Electron Transfer Kinetics Involving Ferrocene Covalently Attached to a Platinum Surface. *J. Electroanal. Chem.* **1979,** *95* (1), 123-130.
25. McCormack, S.; Russell, N. R.; Cassidy, J. F., Cyclic Voltammetry of Ferrocene Carboxylic Acid Cyclodextrin Inclusion Complexes. *Electrochim. Acta* **1992,** *37* (11), 1939-1944.
26. Raoof, J. B.; Ojani, R.; Kolbadinezhad, M., Electrocatalytic Characteristics of Ferrocenecarboxylic Acid Modified Carbon Paste Electrode in the Oxidation and Determination of L-Cysteine. *Electroanalysis* **2005,** *17* (22), 2043-2051.
27. Ma, W.; Ying, Y.-L.; Qin, L.-X., et al., Investigating Electron-Transfer Processes Using a Biomimetic Hybrid Bilayer Membrane System. *Nat. Protocols* **2013,** *8* (3), 439-450.
28. Khorana, H. G., The Chemistry of Carbodiimides. *Chem. Rev.* **1953,** *53* (2), 145-166.
29. DeTar, D. F.; Silverstein, R., Reactions of Carbodiimides. I. The Mechanisms of the Reactions of Acetic Acid with Dicyclohexylcarbodiimide1,2. *J. Am. Chem. Soc.* **1966,** *88* (5), 1013-1019.
30. Staros, J. V.; Wright, R. W.; Swingle, D. M., Enhancement by n-Hydroxysulfosuccinimide of Water-Soluble Carbodiimide-Mediated Coupling Reactions. *Anal. Biochem.* **1986,** *156* (1), 220-222.
31. Thermo Scientific, Crosslinking Technical Handbook. https://tools.thermofisher.com/content/sfs/brochures/1602163-Crosslinking-Reagents-Handbook.pdf (accessed 22 September 2016).
32. Xia, N.; Xing, Y.; Wang, G., et al., Probing of EDC/NHSS-Mediated Covalent Coupling Reaction by the Immobilization of Electrochemically Active Biomolecules. *Int. J. Electrochem. Sci* **2013,** *8*, 2459-2467.
33. Biesinger, M. C.; Payne, B. P.; Grosvenor, A. P., et al., Resolving Surface Chemical States in XPS Analysis of First Row Transition Metals, Oxides and Hydroxides: Cr, Mn, Fe, Co and Ni. *Appl. Surf. Sci.* **2011,** *257* (7), 2717-2730.

34. Barr, T. L.; Seal, S., Nature of the Use of Adventitious Carbon as a Binding Energy Standard. *Journal of Vacuum Science & Technology A* **1995,** *13* (3), 1239-1246.
35. Engbæk, J.; Schiøtz, J.; Dahl-Madsen, B., et al., Atomic Structure of Screw Dislocations Intersecting the Au(111) Surface: A Combined Scanning Tunneling Microscopy and Molecular Dynamics Study. *Physical Review B* **2006,** *74* (19), 195434.
36. Salzmann, C. G.; Nicolosi, V.; Green, M. L. H., Edge-Carboxylated Graphene Nanoflakes from Nitric Acid Oxidised Arc-Discharge Material. *J. Mater. Chem.* **2010,** *20* (2), 314-319.
37. Sakurai, T.; Watanabe, Y., *Advances in Scanning Probe Microscopy*. Springer-Verlag: Berlin, 2000.
38. Wei, H.; Kim, S.; Kim, S. N., et al., Patterned Forest-Assembly of Single-Wall Carbon Nanotubes on Gold Using a Non-Thiol Functionalization Technique. *J. Mater. Chem.* **2007,** *17* (43), 4577-4585.
39. Lim, J. K.; Yun, W. S.; Yoon, M.-h., et al., Selective Thiolation of Single-Walled Carbon Nanotubes. *Synth. Met.* **2003,** *139* (2), 521-527.
40. Eigler, D. M.; Lutz, C. P.; Rudge, W. E., An Atomic Switch Realized with the Scanning Tunnelling Microscope. *Nature* **1991,** *352* (6336), 600-603.

7 Concluding Remarks

This thesis set out to achieve three goals: to examine the effect of specific surface functionalities present at carbon electrodes on common redox probes; to study the potential-dependent dissociation of acidic surface functionalities; and to explore different ways of attaching functionalised carbon nanomaterials onto a surface. In this work graphene nanoflakes with well-defined edge functionalities were used as a novel carbon nanomaterial. Characterisation of GNF has been reported before [1], but in this thesis we have added to the existing knowledge of the acid-terminated GNF by performing pH titration and in-situ monitoring of acid dissociation by infrared spectroscopy. Complexation of GNF-COOH was also studied by using different cations.

7.1 Influence of GNF on the Electrochemistry of Redox Probes

Oxidised carbon electrodes will present a range of surface oxygen functionalities; hence it can be difficult to isolate the interaction of redox probes with a specific surface moiety. The strength of this study are the well-characterised and uniform GNF that enabled me to attribute changes in electrochemical response to specific functionalities. The very high density of carboxylic acid groups of the GNF-COOH flakes and the absence of other oxygen-containing functionalities allowed me to specifically investigate the effect of these highly charged and acidic groups on the electrochemical response of GNF.

The presence of an immobilised layer of GNF on the surface of a boron-doped diamond electrode did not inhibit electron transfer of ferrocene methanol, a common outer-sphere redox probe, irrespective of edge termination. When a proton-coupled electron transfer reaction was examined, carboxylic acid –terminated GNF were found to participate in the redox reaction by providing a non-solution proton source and sink.

A whole Chapter was devoted to the $[Fe(CN)_6]^{3-/4-}$ redox couple, which is often used in electrochemical studies as a redox probe despite a large body of evidence showing complex behaviour at electrodes and instability in solution. At BDD electrode, the presence of COOH groups has been shown to have an adverse effect the electron transfer kinetics of $[Fe(CN)_6]^{3-/4-}$ especially in alkaline solutions attributed to electrostatic repulsion between negatively charged carboxylates and the negatively charged redox species [2, 3]. The reversibility and electron transfer rate of the $[Fe(CN)_6]^{3-/4-}$ redox system has been shown by others to depend on the concentration and identity of cations in solution [4, 5]. Additionally, it is known that $[Fe(CN)_6]^{3-/4-}$ can be unstable in solution of low ionic strength and low pH, and cyanide ligand loss and subsequent decomposition and adsorption onto electrodes have been observed by

several groups [5-11]. In this work it is shown that the acid groups at GNF-COOH severely inhibit the redox reaction of $[Fe(CN)_6]^{3-/4-}$ in acidic solution when more acid groups are expected to be protonated; therefore, electrostatic repulsion cannot be used to explain the effect of GNF-COOH on this redox couple. By monitoring the stability of $[Fe(CN)_6]^{3-/4-}$ in the presence of GNF, it is demonstrated that the acid-terminated flakes accelerate the decomposition of the redox species.

7.2 Potential-Driven Deprotonation of Acid Groups

In Chapter 5, the effect of applied potential on carboxylic acid groups at the GNF edge was studied. Numerous reports on the dissociation of self-assembled monolayers exist, but the findings are contradictory. Some groups have reported deprotonation occurring at positive applied potential in response to the electric field at the electrode [12-16], whereas others have observed deprotonation at negative potentials in response to changes in the apparent pK_a of the acid groups due to changes in cation activity at the electrode [17-20].

By complexing COOH-terminated GNF with divalent cations and immobilising them on BDD, a large surface area electrode with a high concentration of acid groups was constructed. The dissociation of carboxylic acid groups at the GNF edge was then monitored in situ by combining potentiostatic control with infrared spectroscopy. Deprotonation was observed on application of a negative potential of the surface-immobilised acid groups as well as the supporting electrolyte. The deprotonation was confirmed to stem from changes in the apparent pK_a of all species near the electrode.

The observation of deprotonation of electrode-immobilised acids is not new; however, in this thesis we have provided convincing evidence of the mechanism behind the observed behaviour. There are few studies that can provide in situ measurement of changes in interfacial speciation as a function of applied potential as has been done in

this thesis. To the best of our knowledge, potential-induced deprotonation of solution species has never previously been reported.

7.3 Immobilisation of GNF

In Chapter 6, different methods of attaching GNF onto a substrate are discussed. The main immobilisation technique used in this work is drop-coating, which is quick and convenient but offers little control over the surface coverage and morphology of the drop-coated layer. To study the immobilisation of GNF onto a substrate in a more controlled fashion, other techniques were used.

Firstly, thiol-terminated GNF were attached onto a gold substrate by self-assembly and the successful attachment was confirmed by XPS. Sub-monolayer coverages were used in order to be able to image the surface with scanning tunnelling microscopy. At low coverages, the GNF were found to orientate horizontally on the surface and adsorb preferentially onto step edges. Secondly, self-assembled monolayers on gold with different head groups were utilised to attach GNF onto the substrate through covalent bonding, and narrow scan C1s spectra indicated successful attachment and bond formation between the SAM end groups and the GNF.

7.4 Future Work

It was not possible to determine the identity of the $[Fe(CN)_6]^{3-/4-}$ decomposition product from the experimental results presented in this thesis. To identify the new species observed in this study, a few techniques could be tried. UV-Vis in the total internal reflection mode would allow further in situ characterisation of the precipitate by discriminating between interfacial and solution species. If the precipitate can be separated from the solution, X-ray diffraction (XRD) could be used to study the crystal structure of the decomposition product.

Although we were unable to achieve atomic resolution STM images of the GNF in this study, the use of UHV conditions or low temperature conditions could facilitate the imaging of GNF. Further work would also be useful to study self-assembly of thiol-terminated GNF from higher concentration or at longer deposition times to see how closely packed a GNF monolayer would be and to determine the kinetics of adsorption. Additionally, scanning electron microscopy (SEM) imaging could be used to probe the orientation on freestanding BDD discs.

Recent developments in the synthesis of functional graphene nanocomposites have led to advances in electrochemical biosensing applications for graphene materials [21], and this is an area in which potential use for GNF can be envisaged. Another field where graphene is expected to be widely utilised is composite materials for energy devices, for example to improve the mechanical stability of NiO [22] or polyaniline [23] in supercapacitor electrodes; hence, GNF are a promising candidate for use in similar applications.

References for Chapter 7

1. Rosillo-Lopez, M.; Lee, T. J.; Bella, M., et al., Formation and Chemistry of Carboxylic Anhydrides at the Graphene Edge. *RSC Advances* **2015,** *5* (126), 104198-104202.
2. Granger, M. C.; Swain, G. M., The Influence of Surface Interactions on the Reversibility of Ferri/Ferrocyanide at Boron-Doped Diamond Thin-Film Electrodes. *J. Electrochem. Soc.* **1999,** *146* (12), 4551-4558.
3. Hutton, L. A.; Iacobini, J. G.; Bitziou, E., et al., Examination of the Factors Affecting the Electrochemical Performance of Oxygen-Terminated Polycrystalline Boron-Doped Diamond Electrodes. *Analytical Chemistry* **2013,** *85* (15), 7230-7240.
4. Peter, L. M.; Dürr, W.; Bindra, P., et al., The Influence of Alkali Metal Cations on the Rate of the $Fe(CN)_6^{4-}/Fe(CN)_6^{3-}$ Electrode Process. *J. Electroanal. Chem.* **1976,** *71* (1), 31-50.
5. Beriet, C.; Pletcher, D., A Microelectrode Study of the Mechanism and Kinetics of the Ferro/Ferricyanide Couple in Aqueous Media: The Influence of the Electrolyte and Its Concentration. *J. Electroanal. Chem.* **1993,** *361* (1-2), 93-101.
6. Więckowski, A.; Szklarzyk, M., The State of the Polycrystalline Platinum Electrode During the Heterogeneous Electron-Transfer Reaction: $Fe(CN)_6^{3-}+e^- Fe(CN)_6^{4-}$. *J. Electroanal. Chem.* **1982,** *142* (1–2), 157-170.
7. Pons, S.; Datta, M.; McAleer, J. F., et al., Infrared Spectroelectrochemistry of the $Fe(CN)_6^{4-}/Fe(CN)_6^{3-}$ Redox System. *J. Electroanal. Chem.* **1984,** *160* (1–2), 369-376.
8. Kawiak, J.; Kulesza, P. J.; Galus, Z., A Search for Conditions Permitting Model Behavior of the $Fe(CN)^{3-/4-}_6$ System. *J. Electroanal. Chem.* **1987,** *226* (1–2), 305-314.
9. Lee, C.; Anson, F. C., Inhibition of the Electroreduction of $Fe(CN)_6^{3-}$ at Microelectrodes in the Absence of Supporting Electrolyte: Mediation of the Inhibited Reduction by Methyl Viologen. *J. Electroanal. Chem.* **1992,** *323* (1–2), 381-389.
10. Pharr, C. M.; Griffiths, P. R., Infrared Spectroelectrochemical Analysis of Adsorbed Hexacyanoferrate Species Formed During Potential Cycling in the Ferrocyanide/Ferricyanide Redox Couple. *Analytical Chemistry* **1997,** *69* (22), 4673-4679.
11. Karyakin, A. A., Prussian Blue and Its Analogues: Electrochemistry and Analytical Applications. *Electroanalysis* **2001,** *13* (10), 813-819.
12. White, H. S.; Peterson, J. D.; Cui, Q., et al., Voltammetric Measurement of Interfacial Acid/Base Reactions. *The Journal of Physical Chemistry B* **1998,** *102* (16), 2930-2934.
13. Burgess, I.; Seivewright, B.; Lennox, R. B., Electric Field Driven Protonation/Deprotonation of Self-Assembled Monolayers of Acid-Terminated Thiols. *Langmuir* **2006,** *22* (9), 4420-4428.

14. Rosendahl, S. M.; Burgess, I. J., Electrochemical and Infrared Spectroscopy Studies of 4-Mercaptobenzoic Acid SAMs on Gold Surfaces. *Electrochim. Acta* **2008,** *53* (23), 6759-6767.
15. Ma, C.; Harris, J. M., Surface-Enhanced Raman Spectroscopy Investigation of the Potential-Dependent Acid−Base Chemistry of Silver-Immobilized 2-Mercaptobenzoic Acid. *Langmuir* **2011,** *27* (7), 3527-3533.
16. Luque, A. M.; Mulder, W. H.; Calvente, J. J., et al., Proton Transfer Voltammetry at Electrodes Modified with Acid Thiol Monolayers. *Analytical Chemistry* **2012,** *84* (13), 5778-5786.
17. Sugihara, K.; Shimazu, K.; Uosaki, K., Electrode Potential Effect on the Surface pK_a of a Self-Assembled 15-Mercaptohexadecanoic Acid Monolayer on a Gold/Quartz Crystal Microbalance Electrode. *Langmuir* **2000,** *16* (18), 7101-7105.
18. Futamata, M., Characterization of the First Layer and Second Layer Adsorbates on Au Electrodes Using ATR-IR Spectroscopy. *J. Electroanal. Chem.* **2003,** *550–551*, 93-103.
19. Goutev, N.; Futamata, M., Attenuated Total Reflection Surface-Enhanced Infrared Absorption Spectroscopy of Carboxyl Terminated Self-Assembled Monolayers on Gold. *Appl. Spectrosc.* **2003,** *57* (5), 506-513.
20. Luque, A. M.; Cuesta, A.; Calvente, J. J., et al., Potentiostatic Infrared Titration of 11-Mercaptoundecanoic Acid Monolayers. *Electrochem. Commun.* **2014,** *45*, 13-16.
21. Song, Y.; Luo, Y.; Zhu, C., et al., Recent Advances in Electrochemical Biosensors Based on Graphene Two-Dimensional Nanomaterials. *Biosens. Bioelectron.* **2016,** *76*, 195-212.
22. Lee, G.; Cheng, Y.; Varanasi, C. V., et al., Influence of the Nickel Oxide Nanostructure Morphology on the Effectiveness of Reduced Graphene Oxide Coating in Supercapacitor Electrodes. *The Journal of Physical Chemistry C* **2014,** *118* (5), 2281-2286.
23. Ma, L.; Su, L.; Zhang, J., et al., A Controllable Morphology GO/PANI/Metal Hydroxide Composite for Supercapacitor. *J. Electroanal. Chem.* **2016,** *777*, 75-84.

Appendix 1: Additional Figures for Chapter 4

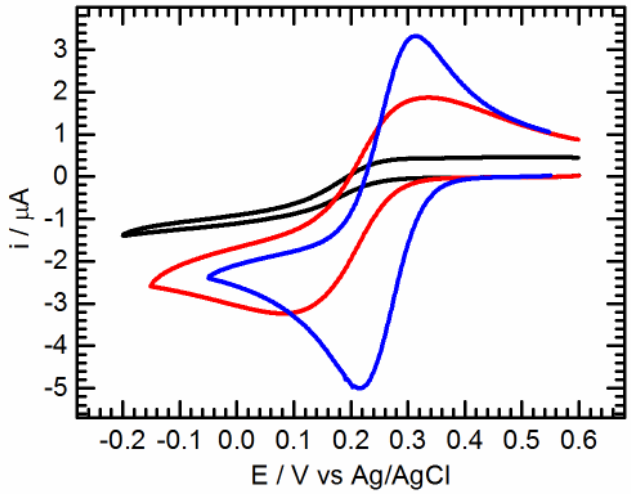

Figure A1.1 Cyclic voltammograms of 0.5×10^{-3} M $K_3[Fe(CN)_6]$ at a BDD modified with GNF-COOH in different concentrations of pH 5 PBS: 1 M (blue); 0.1 M (red); 0.01 M (black). Scan rate 50 mV s^{-1}. First scans shown.

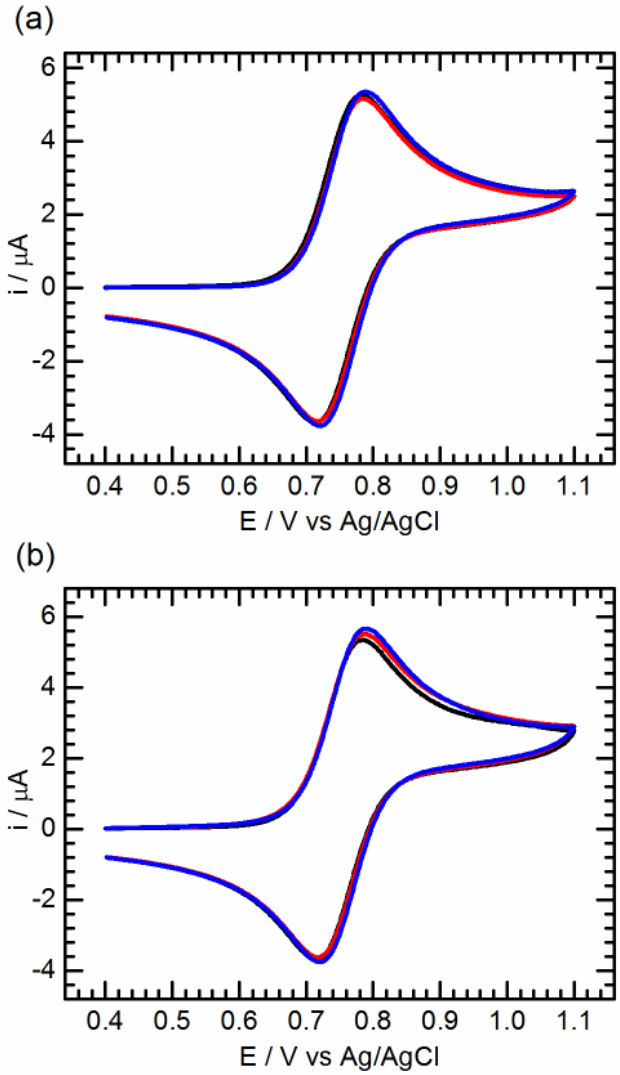

Figure A1.2 Cyclic voltammograms of 0.5×10^{-3} M $K_4[Ru(CN)_6]$ at (a) clean BDD; (b) BDD modified with GNF-COOH. Supporting electrolyte: 0.1 M PBS at pH 6 (black), pH 7 (red), pH 8 (blue). Scan rate 50 mV s^{-1}. First scans shown.

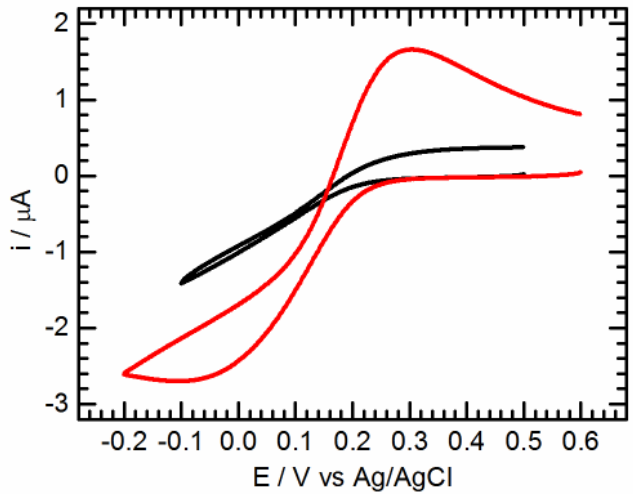

Figure A1.3 Cyclic voltammograms of 0.5×10^{-3} M $K_3[Fe(CN)_6]$ at a BDD modified with GNF-COOH in 0.01 M NaCl at pH 5 (black) and pH 8.4 (red). Scan rate 50 mV s^{-1}. First scans shown.

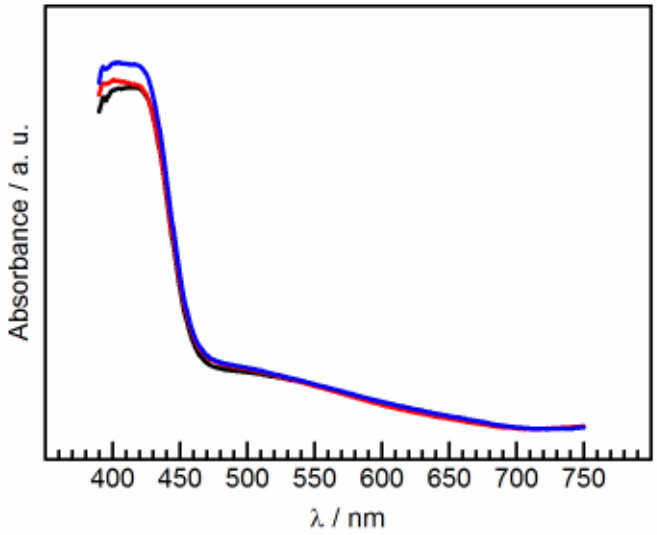

Figure A1.4 UV Vis spectra of 2×10^{-3} M $K_3[Fe(CN)_6]$ and 2×10^{-3} M $K_4[Fe(CN)_6]$ with 30 µg ml^{-1} GNF in H_2O at *t* = 0 h (black), *t* = 7 h (red) and *t* = 24 h (blue).

Appendix 2: Derivation of Equation (5.9)

For an acid *HA*:

$$HA = H^+ + A^- \quad \text{(A.1)}$$

$$K_a = \frac{a_{H^+} a_{A^-}}{a_{HA}} \quad \text{(A.2)}$$

However, if excess cation M^+ is present, this can associate with A^- and change its activity:

$$M^+ + A^- = MA \quad \text{(A.3)}$$

$$K_{as} = \frac{a_{MA}}{a_{M^+} a_{A^-}} \quad \text{(A.4)}$$

From Equation (A.4):

$$a_{A^-} = \frac{a_{MA}}{K_{as}\, a_{M^+}} \quad \text{(A.5)}$$

Substituting into Equation (A.5):

$$K_a = \frac{a_{H^+} a_{MA}}{a_{HA} K_{as} a_{M^+}} \quad \text{(A.6)}$$

Taking logs:

$$\log K_a = \log \frac{a_{H^+} a_{MA}}{a_{HA}} - \log K_{as} - \log a_{M^+} \quad \text{(A.7)}$$

By definition, the first term in Equation (A.7) is pK_a(app), i.e. the measured pK_a when the activity of M^+ is not zero.

Therefore:

$$-pK_a = -pK_a(app) + pK_{as} - \log a_{M^+} \quad \text{(A.8)}$$

Equation (A.8) then rearranges into Equation (5.9).

Appendix 3: Calculation of the values presented in Table 5.6

The asymmetric stretch of sulphate ion absorbs strongly in infrared around 1100 cm^{-1} and this band was found to decrease and increase with applied potential. This change in the activity of sulphate ions, $\Delta a_{SO_4^{2-}}$, at the electrode surface, due to electrostatic migration effects on application of −0.5 V, was quantified with help of calibration experiments in Section 5.7 and it was found to be -3.5×10^{-3} M. Therefore, on application of −0.5 V, it is expected that the change in the activity of potassium cations, Δa_{K^+}, is $2 \times \Delta a_{SO_4^{2-}} = +7 \times 10^{-3}$ M.

a_{K^+} in the equilibrated state and on application of −0.5 V was calculated from the amount of K_2SO_4 used to prepare solutions at specific pH. pK_a(app) values were determined using Equation (5.9), and activity changes in sulphate species on application of −0.5 V were then calculated using the modified Henderson-Hasselbalch equation (Equation (5.10)).

The following assumptions are made in the calculations: Δa_{K^+} is taken to be $+7 \times 10^{-3}$ M regardless of equilibrium concentration of K^+; concentration is approximated with activity; and the increased sulphate concentration at the interface due to pre-concentration is neglected (it is clear from IR spectra in **Figure 5.5** that $a_{SO_4^{2-}}$ is higher at the electrode interface than in the bulk solution).

0.1 M pH 7 K_2SO_4 solution

K_2SO_4 is expected to dissociate fully, thus giving a_{K^+} = 0.200 M at equilibrium. On application of −0.5 V the activity of K^+ increases to a_{K^+} = 0.207 M. Using these activity values, $pK_a(HSO_4^-)$ = 1.92 and assuming pK_{as} = 0, $pK_a(app)$ can be calculated using Equation (5.9): $pK_a(app) = pK_a + pK_{as} - \log(a_{K^+})$.

At equilibrium: $pK_a(app) = 1.92 + 0 - \log(0.200) = 2.619$

At −0.5 V: $pK_a(app) = 1.92 + 0 - \log(0.207) = 2.604$

To determine the speciation at a specific pH Equation (5.10) is used:

$pH = pK_a(app) + \log([a_{SO_4^{2-}}]/[a_{HSO_4^-}])$

At equilibrium: $\frac{a_{SO_4^{2-}}}{a_{HSO_4^-}} = 10^{pH - pK_a(app)} = 24045$

At −0.5 V: $\frac{a_{SO_4^{2-}}}{a_{HSO_4^-}} = 10^{pH - pK_a(app)} = 24887$

Therefore, for 0.1 M pH 7 solution on application of −0.5 V:

$$\Delta a_{SO_4^{2-}} = 0.1\ \text{M} \times \left[\left(\frac{24887}{24887+1}\right) - \left(\frac{24045}{24045+1}\right)\right]$$

$$\Delta a_{SO_4^{2-}} = +0.14 \times 10^{-6}\ \text{M}$$

The above calculation predicts that as a negative potential is applied, 0.14×10^{-6} M HSO_4^- will deprotonate and form SO_4^{2-}. In experimental conditions this value is too small to be detected and we can therefore expect to see no protonation of SO_4^{2-} and all changes in $\Delta a_{SO_4^{2-}}$ will result from migration effects.

0.1 M pH 3.5 K_2SO_4 solution

pH 3.5 K_2SO_4 was prepared by combining 0.1 M H_2SO_4 and 0.1 M K_2SO_4. The final concentrations were 0.0988 M K_2SO_4 and 0.0012 M H_2SO_4, giving 0.198 M K^+.

Therefore, at equilibrium and 1.0 V: $a_{K^+} = 0.198$ M

On application of −0.5 V: $a_{K^+} = 0.205$ M

Using Equation (5.9): $pK_a(app) = pK_a + pK_{as} - \log(a_{K^+})$:

At equilibrium: $pK_a(app) = 1.92 + 0 - \log(0.198) = 2.623$

At −0.5 V: $pK_a(app) = 1.92 + 0 - \log(0.205) = 2.608$

Using $pH = pK_a(app) + \log([a_{SO_4^{2-}}]/[a_{HSO_4^-}])$ to determine speciation:

At equilibrium: $\frac{a_{SO_4^{2-}}}{a_{HSO_4^-}} = 10^{pH - pK_a(app)} = 7.604$

At −0.5 V: $\frac{a_{SO_4^{2-}}}{a_{HSO_4^-}} = 10^{pH - pK_a(app)} = 7.870$

Therefore, on application of −0.5 V: $\Delta a_{SO_4^{2-}} = +0.355 \times 10^{-3}$ M

From the calculation above, in 0.1 M K_2SO_4 solution at pH 3.5 and on application of −0.5 V, we predict 0.36×10^{-3} M HSO_4^- to deprotonate and form SO_4^{2-}.

0.1 M pH 3 K_2SO_4 solution

pH 3 K_2SO_4 solution was prepared by combining 0.1 M H_2SO_4 and 0.1 M K_2SO_4. The final concentrations were 0.096 M K_2SO_4 and 0.004 M H_2SO_4, giving 0.192 M K^+.

Therefore, at equilibrium and 1.0 V: $a_{K^+} = 0.192$ M

On application of −0.5 V: $a_{K^+} = 0.199$ M

As above, Equation (5.9) is used to find pK_a(app):

At equilibrium: $pK_a(app) = 2.637$

At −0.5 V: $pK_a(app) = 2.621$

Using pH = pK_a(app) + log([$a_{SO_4^{2-}}$]/[$a_{HSO_4^-}$]) to determine speciation:

At equilibrium: $\frac{a_{SO_4^{2-}}}{a_{HSO_4^-}} = 10^{pH - pK_a(app)} = 2.405$

At −0.5 V: $\frac{a_{SO_4^{2-}}}{a_{HSO_4^-}} = 10^{pH - pK_a(app)} = 2.489$

Therefore, at −0.5 V: $\Delta a_{SO_4^{2-}} = +0.75 \times 10^{-3}$ M

In 0.1 M K_2SO_4 solution at pH 3 and on application of −0.5 V, we expect to see 0.75×10^{-3} M HSO_4^- deprotonating to form SO_4^{2-}.

Appendix 4: Calculation of the values presented in Table 5.7

Following the same methodology as in Appendix 3, changes in phosphate speciation were calculated using the value of Δa_{K^+} determined in Section 5.7 ($+7 \times 10^{-3}$ M). a_{K^+} in the equilibrated state and on application of −0.5 V was calculated from the amounts of KH_2PO_4 and 0.1 M K_2HPO_4 used to prepare solutions at specific pH. pK_a(app) values were determined using Equation (5.9), and activity changes in sulphate species on application of −0.5 V were then calculated using the modified Henderson-Hasselbalch equation (Equation (5.10)).

<u>0.1 M pH 7 phosphate</u>

pH 7 phosphate solution was prepared by combining 0.1 M KH_2PO_4 and 0.1 M K_2HPO_4 in approximately 1:1 ratio. Assuming that both KH_2PO_4 and K_2HPO_4 dissociate fully to K^+ and HPO_4^-, the concentration of K^+ in equilibrated state is calculated to be 0.15 M.

Therefore, at equilibrium and 1.0 V: $a_{K^+} = 0.150$ M

On application of −0.5 V: $a_{K^+} = 0.157$ M

pK_a(app) is calculated using Equation (5.9): pK_a(app) = pK_a + pK_{as} – log(a_{K^+}) with values $pK_a(H_2PO_4^-) = 7.2$ and $pK_{as} = 0$:

At equilibrium and 1.0 V: $pK_a(app) = 8.033$

On application of −0.5 V: $pK_a(app) = 8.014$

Using $pH = pK_a(app) + \log([a_{HPO_4^{2-}}]/[a_{H_2PO_4^-}])$ to determine speciation:

At equilibrium and 1.0 V: $\frac{a_{HPO_4^{2-}}}{a_{H_2PO_4^-}} = 10^{pH - pK_a(app)} = 0.092$

At −0.5 V: $\frac{a_{HPO_4^{2-}}}{a_{H_2PO_4^-}} = 10^{pH - pK_a(app)} = 0.097$

Therefore, on application of −0.5 V: $\Delta a_{HPO_4^{2-}} = +0.36 \times 10^{-3}$ M.

From the calculation above, in 0.1 M phosphate solution at pH 7 and on application of −0.5 V, we predict 0.36×10^{-3} M $H_2PO_4^-$ to deprotonate and form HPO_4^{2-}.

<u>0.1 M pH 9 phosphate</u>

pH 9 phosphate solution was prepared from 0.1 M K_2HPO_4, which dissociates fully to give 0.2 M K^+ and 0.1 M HPO_4^{2-}. Therefore, at equilibrium and 1.0 V we have $a_{K^+} = 0.200$ M, and on application of −0.5 V we have $a_{K^+} = 0.207$ M.

$pK_a(app)$ is calculated using Equation (5.9): $pK_a(app) = pK_a + pK_{as} - \log(a_{K^+})$ with values $pK_a(H_2PO_4^-) = 7.2$ and $pK_{as} = 0$:

At equilibrium and 1.0 V: $pK_a(app) = 7.909$

On application of −0.5 V: $pK_a(app) = 7.894$

Using $pH = pK_a(app) + \log([a_{HPO_4^{2-}}]/[a_{H_2PO_4^-}])$ to determine speciation:

At equilibrium: $\frac{a_{HPO_4^{2-}}}{a_{H_2PO_4^-}} = 10^{pH - pK_a(app)} = 12.33$

At −0.5 V: $\frac{a_{HPO_4^{2-}}}{a_{H_2PO_4^-}} = 10^{pH - pK_a(app)} = 12.76$

Corresponds to a $\Delta a_{HPO_4^{2-}} = +0.24 \times 10^{-3}$ M

In 0.1 M phosphate solution at pH 9 and on application of −0.5 V, we expect to see 0.24×10^{-3} M $H_2PO_4^-$ deprotonating to form HPO_4^{2-}.

0.1 M pH 3 phosphate

At pH 3, the phosphate will exist as $H_2PO_4^-$ and H_3PO_4. The solution was prepared by combining 0.1 M KH_2PO_4 and 0.1 M H_3PO_4 with final concentrations of 0.08 M KH_2PO_4 and 0.02 M H_3PO_4.

Therefore, at equilibrium and 1.0 V: $a_{K^+} = 0.08$ M

On application of −0.5 V: $a_{K^+} = 0.087$ M

pK_a(app) is calculated using Equation (5.9): pK_a(app) = pK_a + pK_{as} – log(a_{K^+}) with values $pK_a(H_3PO_4) = 2.12$ and $pK_{as} = 0$:

At equilibrium and 1.0 V: $pK_a(app) = 3.217$

On application of −0.5 V: $pK_a(app) = 3.180$

Using pH = pK_a(app) + log([$a_{H_2PO_4^-}$]/ [$a_{H_3PO_4^0}$]) to determine speciation:

At equilibrium: $\frac{a_{H_2PO_4^-}}{a_{H_3PO_4^0}} = 10^{pH - pK_a(app)} = 0.092$

At −0.5 V: $\frac{a_{H_2PO_4^-}}{a_{H_3PO_4^0}} = 10^{pH - pK_a(app)} = 0.097$

Corresponds to a $\Delta a_{H_2PO_4^-} = +2.0 \times 10^{-3}$ M.

From the calculation above, in 0.1 M phosphate solution at pH 3 and on application of −0.5 V, we predict 2.0×10^{-3} M H_3PO_4 to deprotonate and form $H_2PO_4^-$.